CHARACTERISTICS OF NANO-MODIFIED CEMENTITIOUS COMPOSITES INCORPORATING BASALT FIBER PELLETS AND POLYVINYL ALCOHOL FIBERS AND THEIR SUITABILITY FOR SHEAR KEY JOINTS

by

Riham Refaat Abdelsamie Abdelhamid Elhadary

A Thesis Submitted to the Faculty of Graduate Studies of
The University of Manitoba
in partial fulfillment of the requirements for the degree of

Doctor of Philosophy

Department of Civil Engineering
University of Manitoba
Winnipeg

January 2023

Copyright © 2023 by Riham Elhadary

ABSTRACT

The low toughness of normal/conventional concrete (CC) motivated the advent of high-performance fiber-reinforced cementitious composites (HPFRCC) to control cracking and hence extend the service life of infrastructural elements. HPFRCC incorporating various constituents (50% cement, 50% slag, and 6% nano-silica), with single basalt fiber pellets (macro-BFP) or hybrid fiber systems including BFP and polyvinyl alcohol (micro-PVA) fibers at different dosages were extensively studied in this thesis. Fresh, mechanical and durability tests were conducted to investigate the properties of these innovative composites. Moreover, the synergetic evaluation of the flexural performance and single pellet pull-out in various homogenized nano-modified matrices was comprehensively explored using integrated experimental and modeling approaches. To investigate the potential of employing these composites as a filler in shear key bridge joints, the HPFRCC interfacial bonding capacity with CC under shear configurations, as well as its interaction with reinforcement steel rebars were experimentally and numerically studied.

The results showed that nano-silica led to improved performance at early- and later-ages in terms of hardening rates, mechanical capacity, refinement of pore structure, resistance to freezing-thawing cycles, bonding with BFP and interfacial bonding with CC and steel rebars. Reduction in mechanical capacity and interfacial bonding with CC were observed for specimens comprising a higher dosage (4.5%) of BFP (single fiber system); however, the tensile strain hardening behaviour and rebar interfacial bonding capacity were improved with BFP dosage. Comparatively, 1% micro-PVA fibers with 2.5% or 4.5% macro-BFP (hybrid systems) resulted in marked improvement in terms of

mechanical properties, durability to frost action, and interfacial bonding with precast CC and steel rebars.

The synoptic outcomes of this thesis highlighted that nano-silica modified HPFRCC comprising hybrid fibers (G-N-V1-B2.5 and G-N-V1-B4.5) can be a practicable option for shear key joints with enhanced performance in terms of mechanical and durability properties, as well as bonding capacity with CC and shear reinforcing dowels. The developed finite element models herein could efficiently project the expected full-scale behavior of complex composites such as HPFRCC including its shear capacity, crack formation process, and modes of failure, which pave the way for field applications.

CO-AUTHORSHIP

This thesis has been prepared in accordance with the regulation of integrated-article format stipulated by the Faculty of Graduate Studies at the University of Manitoba. Substantial parts of this thesis were either published in or submitted for publication to peer-reviewed technical journals and international conferences as shown below:

Journal Papers

1. **Elhadary, R.** and Bassuoni, M.T. Evaluation of Nano-Modified Cementitious Composites with Basalt Fiber Pellets and Polyvinyl Alcohol Fibers for Shear Key Joints. *Computers and Concrete* (Submitted in January 2023; under revision).

2. **Elhadary, R.** and Bassuoni, M.T. Bonding Evaluation of Nano-Silica Modified Slag-Based Composites Comprising Basalt Pellets and Polyvinyl Alcohol Fibers. *Journal of Materials in Civil Engineering, ASCE, (*Submitted in December 2022: under review).

3. **Elhadary, R.** and Bassuoni, M.T., 2023 (online first). Interfacial Bonding between Basalt Fiber/Polymer Pellets and Various Nano-Modified Cementitious Matrices. *Journal of Materials in Civil Engineering*, 35(3), 0402247, pp. 1-18.

4. **Elhadary, R.** and Bassuoni, M.T., 2022 (online first). Nano-Modified Slag-Based Cementitious Composites Reinforced with Basalt Pellets and Polyvinyl Alcohol Fibers. *Journal of Sustainable Cement-Based Materials*, 12 p.

5. **Elhadary, R.** and Bassuoni, M.T., 2020. Mechanical Properties of Nano-Modified Cementitious Composites Reinforced with Single and Hybrid Fibers. *Transportation Research Record*, 2675(9), pp. 56-64

Conference Proceedings

1. **Elhadary, R**. and Bassuoni, M.T." Pull-out of Basalt Fibre Pellets from Cementitious Composites." *In Proceedings of the 7th International Conference on Civil Structural and Transportation Engineering (ICCSTE'22)*, Niagara Falls, Canada, June 2022.

2. **Elhadary, R**. and Bassuoni, M.T." Interfacial Bonding of Nano-modified Cementitious Composites Incorporating Basalt Pellets to Normal Concrete." *In proceedings of the Canadian society for civil engineering (CSCE) Annual* Conference, Whistler, British Colombia, May 2022.

Dedication

This work is dedicated to:

My Parents, Refaat and Emtyaz,

My Two Siblings, Mai and Mostafa,

My Beloved Husband, Ahmed,

My beloved Son, Hisham, and daughter, Layla

My whole family that has a great influence in my life,

All my heart to you for your support to achieve every success, if any, in my life.

Acknowledgements

First and above all, all praises, thanks, and gratitude to Almighty Allah for the benevolence he has bestowed upon me and the guidance to complete this work.

Finally, I can express my deep sense of gratitude and heartfelt respect to my advisor Dr. Mohamed Bassuoni, for his enthusiasm, mentorship, knowledge, and patience throughout this work. I appreciate his treatment as a supportive older brother to me. I am mainly attributing the quality of this work to his compassion, knowledge, and endless enthusiasm, without holding back any tiny amount of effort.

In addition, I would like to greatly thank the assistance of the McQuade Heavy Structures Laboratory staff, Dr. Chad Klowak and Mr. Samuel Abraha for the valuable technical support during the preparation and testing stages.

I highly appreciate the financial support from Natural Sciences and Engineering Research Council of Canada, Manitoba Transportation and infrastructure (MTI), as well as the Price Scholarship for Women in Engineering. The IKO Construction Materials Testing Facility and Manitoba Institute for Materials at the University of Manitoba at which the experiments were conducted were instrumental for this work.

I would like to express my deepest gratitude to my parents (Refaat Elhadary and Emtyaz Elbadary) for their moral support and inspiration throughout my entire life. I am grateful for their endless love, patience, encouragement, and prayers. Also, I acknowledge my two Siblings (Moustafa and Mai) for their continuous emotional and spiritual support.

I want to express my appreciation to Ahmed Azzam, my wonderful husband, who supported me with all love, and stood with me side by side in finding our path. I also express my gratitude to Hisham, my little young man, and my little daughter Layla, who are a spontaneous motivator for a better future for us all.

TABLE OF CONTENTS

ABSTRACT ..... **II**

TABLE OF CONTENTS ..... **VII**

LIST OF TABLES ..... **X**

LIST OF FIGURES ..... **XII**

NOTATIONS ..... **XXI**

CHAPTER 1: INTRODUCTION **1**

1.1 Overview **1**
1.2 Need for Research **3**
1.3 Objectives of Research **6**
1.6 Structure of the Thesis **10**

CHAPTER 2: LITERATURE REVIEW **12**

2.1. Overview on Cementitious Composites **12**
2.2. Cementitious Composites Composition **13**
2.3. HPCC Properties **15**
2.3.1. Rheological Properties 16
2.3.2. Mechanical Properties 17
2.3.3. Durability Properties 20
2.3.4. Shrinkage 21
2.4. Cementitious Composites Incorporating Basalt Fibers **22**
2.4.1. Fresh Properties 23
2.4.2. Mechanical Properties 23
2.4.3. Durability Properties 25
2.4.4. Shrinkage 27
2.5. Applications **28**
2.5.1. Shear Key Bridge Joints 29
2.5.2. Bonding Evaluation 31
2.5.4.1. Shear Key Bridge Joint 36
2.5.4.2. Interface Modeling 38
2.5. Closure **40**

CHAPTER 3: NANO-MODIFIED SLAG-BASED CEMENTITIOUS COMPOSITES REINFORCED WITH BASALT PELLETS AND POLYVINYL ALCOHOL FIBERS **42**

3.1 Introduction **42**
3.1.1 Research Significance **45**
3.2 Methodology **46**
3.2.1 Materials **46**
3.2.2 Procedures **47**
3.2.3 Tests **48**

3.3 Results and Discussion 50
3.3.1 Fresh Properties 50
3.3.2 Compressive Strength 52
3.3.3 Flexural Strength 58
3.3.4 Resistance to Frost Damage 64

CHAPTER 4: INTERFICIAL BONDING BASALT FIBER/POLYMER PELLETS AND VARIOUS NANO-MODIFIED CEMENTITIOUS MATRICES 68

4.1 Introduction 68
4.1.1 Research Significance 72
4.2 Experimental Program 73
4.2.1 Materials and Mixtures 73
4.2.2 Testing 76
4.3 Finite Element Modeling 79
4.3.1 Phase I: Homogenization Method 79
4.3.1.1 Theoretical Formulation 79
4.3.1.2 Numerical Simulation and Model Parameters 83
4.3.2 Phase II: Single Pellet Pull-out 85
4.3.2.1 Theoretical Formulation 85
4.3.2.2 Numerical Simulation and Model Parameters 87
4.4 Results and Discussion 89
4.4.1 Experimental 89
4.4.1.1 Flexural Behavior 89
4.4.1.2 BFP Pull-Out 97
4.4.2 Modeling 101
4.4.2.1 Phase I 101
4.4.2.2 Phase II 103

CHAPTER 5: BONDING EVALUATION OF NANO-SILICA MODIFIED SLAG-BASED COMPOSITES COMPRISING BASALT PELLETS AND POLYVINYL ALCOHOL FIBERS 110

5.1 Introduction 110
5.1.1 Research Significance 114
5.2 Experimental Program 114
5.2.1 Materials and Mixtures 114
5.2.2 Testing 116
5.3 Results and Discussion 121
5.3.1 Mechanical Capacity of HPFRCC 121
5.3.1.1 Compressive Strength and Hydration Development 121
5.3.1.2 Tensile Strength 124
5.3.2 Bonding Evaluation 129
5.3.2.1 Slant Shear Strength 129
5.3.2.2 Direct Shear Strength 133
5.3.2.3 Coefficient of Friction and Adhesion 136
5.3.2.4 Rebar Pull-Out 137

CHAPTER 6: EVALUATION OF NANO-MODIFIED CEMENTITIOUS COMPOSITES WITH BASALT FIBER PELLETS AND POLYVINYL ALCOHOL FIBERS FOR SHEAR KEY JOINTS 141

6.1 Introduction 141
6.1.1 Research Significance **145**
6.2 Experimental Program 146
6.2.1 Materials and Mixtures **146**
6.2.2 Tests **147**
6.3 Finite-Element Modeling 150
6.3.1 Phase I: Homogenization **150**
6.3.1.1 Theoretical Formulation **150**
6.3.1.2 Model Parameters and Numerical Simulation **151**
6.3.2 Phase II: Bond Evaluation for Laboratory Tests **153**
6.3.2.1 Theoretical Formulation **153**
6.3.2.2 Model Parameters and Numerical Simulation **155**
6.3.3 Phase III: Predictive Model for the Shear Key Bridge Joint **159**
6.3.3.1 Case Description **159**
6.3.3.2 Numerical Simulation and Model Parameters **160**
6.4 Results and Discussion 161
6.4.1 Phase I: Homogenization **161**
6.4.2 Phase II: Bond Evaluation **163**
6.4.2.1 Slant Shear **165**
6.4.2.2 Direct Shear **169**
6.4.2.3 Coefficient of Friction and Adhesion **171**
6.4.2.4 Rebar Pull-Out **172**
6.4.3 Phase III: Predictions of Shear Key Behavior **174**

CHAPTER 7: SUMMARY, CONCLUSIONS, AND RECOMMENDATIONS 180

7.1 Summary 180
7.2 Conclusions 182
7.2.1 Factors Affecting Properties of Nano-Modified Cementitious Composites (Chapter 3) 182
7.2.2 Evaluation of Single Pellet Interfacial Bond Strength with Various Cementitious Composites (Chapters 4) 183
7.2.3 Bonding Evaluation of Nano-Modified Cementitious Composites (Chapter 5). 186
7.2.4 Potential of Nano-Modified Cementitious Composites in Shear Key Joints (Chapter 6) 187

REFERENCES 190

APPENDIX A: SUPPLEMENTAL RESULTS FOR CHAPTER 3 214

APPENDIX B: SUPPLEMENTAL RESULTS FOR CHAPTER 4 217

APPENDIX C: SUPPLEMENTAL RESULTS FOR CHAPTER 5 220

APPENDIX D: SUPPLEMENTAL RESULTS FOR CHAPTER 6 223

LIST OF TABLES

Table 2.1: Exemplar mixtures proportions per cubic meter 15

Table 2.2: Mixtures proportions [Zhu *et al*., 2012] 20

Table 2. 3: Mass proportions of concrete mixtures 28

Table 3.1. Chemical and physical properties of GU cement and slag 47

Table 3.2. Properties of BFP and PVA fibers 47

Table 3.3: Mixtures proportions per cubic meter and fresh properties 52

Table 3. 4: ANOVA of the hardened and durability tests' results 56

Table 3.5: Flexural properties of the cementitious composites at 56 days 61

Table 3.6: Summary of MIP test results at 56 days 66

Table 4.1: Properties of fibers 76

Table 4.2: Mixtures proportions per cubic meter 77

Table 4.3: Summary of MIP test results at 56 days 85

Table 4.4: Flexural properties of the cementitious composites at 56 days 95

Table 4.5: Homogenized engineering properties of RVEs 103

Table 4.6: Experimental versus modeling results for the single pellet pull-out tests 106

Table 5.1: Properties of fibers 119

Table 5.2: Mixtures proportions per cubic meter 120

Table 5.3: Compressive strength (MPa) of composites 123

Table 5.4: Summary of the MIP test results 123

Table 5.5: Tensile properties of the composites..... 127

Table 5.6: Slant shear test parameters..... 132

Table 6.1: Mixtures proportions per cubic meter..... 147

Table 6.2: Mechanical properties of composites at 56 days 152

Table 6.3: MIP test results at 56 days 153

Table 6.4: Homogenized engineering properties of RVEs with a size of 40 mm..... 158

Table 6.5: Experimental slant shear test parameters..... 164

Table 6.6: Experimental versus modeling results for the slant shear test at 33.7°..... 164

Table 6.7: Experimental versus modeling results for the bi-shear test 164

Table 6.8: Experimental versus modeling results for the rebar pull-out test 165

LIST OF FIGURES

Figure 2.1: The stress-strain relationship of SHCC under tension [adapted from Mechtcherine, 2013]. 16

Figure 2.2: The stress–strain curves for four mixtures under tensile load, where notation (1, 2) refers to the mixture, and (A) refers to the modified mixing sequence [adapted from Zhou *et al*., 2012]. 19

Figure 2.3: Exemplar fiber dosage increasing with a reduction in crack area in M4 for fibers length of 25 mm; (a) BD, and (b) FD [adapted from Branston *et al*., 2016].. 27

Figure 2.4: The developed strain over time for fiber dosage (0.1%) of lengths 12 and 25 mm [adapted from Branston *et al*., 2016]. 28

Figure 2.5: Specimens' configurations and corresponding model setups: (a) pull-push I; (b) pull-push II; (c) pull-pull [adopted from Dalalbashi *et al.*, 2018]..... 39

Figure 3.1: Reinforcing fibers: (a) BFP, and (b) PVA..... 47

Figure 3.2: Penetration resistance vs. time for all mixtures..... 52

Figure 3.3: Compressive strength of all composites vs. age..... 57

Figure 3.4: TGA results for the CH contents (at a temperature range of 400°C to 450°C) in the mixtures. (G: slag-based binder, and G-N = nano-modified slag-based binder). 57

Figure 3.5: Exemplar mode of failure of specimens after the compressive strength test at 56 days: (a) G-N-B2.5, and (b) G-N-B2.5-V1. 58

Figure 3.6: Load-deflection (P-δ) curves for the composites with a single fiber system. 62

Figure 3.7: Comparison of load-deflection (P-δ) curves for the composites reinforced with BFP (single fibers) and BFP with PVA fibers (hybrid fibers). 62

Figure 3.8: SEM images for G-N-B2.5 at 56 days showing: (a) hydration products in the longitudinal grooves of BFP, (b) magnified image for the area indicated in (a), and (c) EDX spectrum of the paste at the locations indicated in (b). 63

Figure 3.9: Interaction of BFP with PVA in G-N-B2.5-V1..... 63

Figure 3.10: Relative dynamic modulus of elasticity (RE_d) of all composites vs. number of freezing-thawing cycles. 67

Figure 4.1: Fiber type: (a) NFC, (b) PVA, and (c) BFP. 77

Figure 4.2: Single pellet pull-out test set-up. 79

Figure 4.3: Tensile stress-strain relationships of the different matrices. 85

Figure 4.4: Homogenization RVEs: a) meso-RVE_1 of mixture G-N-NFC0.2, (b) macro-RVE scale, (c) meso-RVE_2 of mixture G-N-V1, (d) LINK 8 element for BFP, and (e) SOLID65 element for the cementitious matrix. 89

Figure 4.5: Load-deflection (P-δ) curves for the composites with single fiber systems. 95

Figure 4.6: Load-deflection (P-δ) curves for the composites with hybrid fiber systems. 96

Figure 4.7: TGA results for the CH contents (at a temperature range of 400 to 450°C) in the mixtures. 96

Figure 4.8: Bond-slip relationships from the single pellet pull-out tests. 99

Figure 4.9: Examplar SEM micrograph for matrix G at 56 days: (a) ITZ with BFP, and (b) EDX spectrum of paste at the indicated location in (a). (SE = standard error for 10 points). 99

Figure 4.10: Exemplar SEM micrograph for matrix G-N at 56 days: (a) ITZ with BFP, and (b) EDX spectrum of paste at the indicated location in (a). (SE = standard error for 10 points). 100

Figure 4.11: Exemplar SEM micrograph for matrix G-NCC at 56 days: (a) ITZ with BFP, and (b) EDX spectrum of paste at the indicated location in (a). (SE = standard error for 10 points). 100

Figure 4.12: Exemplar SEM micrographs at 56 days showing: (a) interaction of BFP with G-N-V1, and (b) deposition of NFC in BFP's micro-grooves in G-NCC-NFC0.2. 101

Figure 4.13: Predicted load-slip curves for the single pellet-pullout from different matrices. 107

Figure 4.14: Examplear stress-strain distributions from the models for the single pellet pull-out tests: (a) G-N-V1, and (b) G-NCC-NFC0.2. 107

Figure 4.15: Predicted crack distributions at the last stage of BFP debonding: (a) plan view of mixture G-N-V1, (b) elevation view of mixture G-N-V1, (c) plan view of mixture G-NCC-NFC0.2, and (d) elevation view of mixture G-NCC-NFC0.2. 108

Figure 4.16: Parametric analysis results: (a) homogenized modulus and bond strength of mixture G-N reinforced with PVA, (b) debonding energy, (c) homogenized modulus and bond strength of mixture G-NCC reinforced with NFC, and (d) debonding energy. 109

Figure 5.1: Tests set-up: (a) slant shear, (b) bi-shear, and (c) rebar pull-out. 120

Figure 5.2: Slant shear stress configuration and Mohr's circle. 120

Figure 5.3: TGA results for the CH contents (at a temperature range of 400 to 450°C) in the mixtures. 123

Figure 5.4: Exemplar mode of failure of specimens after the compressive strength test at 56 days: (a) G-N-B2.5, and (b) G-N-B2.5-V1. 124

Figure 5.5: Stress-strain relationships from the direct tension test. 127

Figure 5.6: Exemplar failure plane after the direct tension test for the G-N-B4.5-V1 specimen. 128

Figure 5.7: Examplar SEM micrograph for matrix G at 56 days: (a) ITZ with BFP, and (b) EDX spectrum of paste at the indicated location in (a). (SE = standard error for 10 points). 128

Figure 5.8: Examplar SEM micrograph for matrix G-N at 56 days: (a) ITZ with BFP, and (b) EDX spectrum of paste at the indicated location in (a). (SE = standard error for 10 points). 128

Figure 5.9: Exemplar SEM micrograph showing the interaction of BFP with PVA in G-N-B4.5-V1 specimen. 129

Figure 5.10: Failure modes of the composite specimes cast with HPFRCC and CC: a) compression failure of CC substrate [45º], b) interface failure [33.7°], and c) localized interfacial bond followed by cracking of CC substrate [33.7°]. 132

Figure 5.11: Load-displacement relationships from the slant shear test specimens at 33.7°. (Note: values in parentheses are standard deviations). 132

Figure 5.12: Examplar SEM micrographs and EDX at the indicated locations of the composite specimens at the HPFRCC/CC interface: (a) binder G, and (b) binder G-N. 133

Figure 5.13: Examplar SEM micrographs at HPFRCC/CC interfaces after the slant shear tests for G-N-B4.5-V1 specimens: (a) PVA bounded to the HPFRCC at the interface with CC, and (b) fracture edges of PVA in the HPFRCC towards the CC layer.... 133

Figure 5.14: Load-displacement relationships for the bi-shear test specimens. (Note: values in parentheses are standard deviations). 135

Figure 5.15: Failure modes of the composite specimes cast with HPFRCC and CC in the bi-shear test: (a) interface failure, and (b) localized interfacial cracking and crushing of the CC layer. 135

Figure 5.16: Coefficient of friction (μ) and adhesion (c) from the slant and bi-shear tests. 137

Figure 5.17: Load-slip relationships of rebar pull-out from the composites. (Note: values in parentheses are standard deviations)..... 140

Figure 6.1: Homogenization RVEs: (a) meso-RVE$_0$ of mixture G-N-V1, (b) meso-RVE$_4$ of mixture G-N-B2.5-V1, (c) meso-RVE$_5$ of mixture G-N-B4.5-V1, and (d) SEM micrograph showing the interaction of BFP with PVA. 153

Figure 6.2: Finite element geometry: (a) slant shear model at 33.7°, (b) slant shear model at 45°, (c) bi-shear model, (d) rebar pull-out model, (e) SOLID65 element for CC, (f) SOLID185 element for HPFRCC, and (g) LINK180 element for the steel rebar. 158

Figure 6.3: Mid-span bridge details: (a) top view, and (b) precast CC beam cross-section. (Note: all dimensions are in millimeter). 162

Figure 6.4: FEM for the bridge mid-span: (a) model's parts and loading, (b) beam boundaries, and (c) shear key meshing. 163

Figure 6.5: Crushing failure in the CC specimen cast with G-N-B2.5 at 45°: (a) experimental failure, (b) modeling simulation, and (c) bond stress (MPa) distribution at the interface. 167

Figure 6.6: Interface failure in specimens cast with G-N-B2.5 at 33.7°: (a) experimental failure, (b) modeling simulation, and (c) bond stress (MPa) distribution at the interface. 167

Figure 6.7: Interfacial and CC failure in specimens cast with G-N-B2.5-V1 at 33.7°: (a) experimental failure, (b) modeling simulation, and (c) bond stress (MPa) distribution at the interface. 168

Figure 6.8: Exemplar SEM micrographs and EDX at the indicated locations in the interface between HPFRCC and CC: (a) G, and (b) G-N specimens. 168

Figure 6.9: Exemplar SEM micrograph of fracture edges of PVA in the HPFRCC towards the CC layer. 168

Figure 6.10: Direct shear failure in specimen G-N-B2.5: (a) experimental failure, and (b) predicted failure associated with shear stress (MPa) distribution at the interface between HPFRCC/CC. 170

Figure 6.11: Direct shear failure in specimen G-N-B2.5-V1: (a) experimental failure, (b) predicted failure associated with shear stress (MPa) distribution at the interface between HPFRCC/CC. 171

Figure 6.12: Shear-normal stresses interaction (fitted to Eq. 6) of the composite HPFRCC/CC specimens: (a) combination of experimental slant shear (at 33.7°) and bi-shear results, (b) FEM predictions for various slant shear angles (25°, 30°, 35°, 40°). 173

Figure 6.13: Rebar pull-out failure from G-N-B4.5-V1: (a) experimental failure, and (b) simulated rebar pull-out associated with bond stress (MPa) distribution around the rebar. 175

Figure 6.14: Predicted crack distributions during debonding of the rebar from HPFRCC: (a) plan view of mixture G-N-B4.5, (b) elevation view of mixture G-N-B4.5, (c) plan view of mixture G-N-B4.5-V1, and (d) elevation view of mixture G-N-B4.5-V1. 176

Figure 6.15: Development of cracking at the interface in shear key joints incorporating HPFRCC with single BFP: (a) initial crack at approximately 55% of ultimate load, and (b) crack propagation up to failure. 179

Figure 6.16: Development of cracking in shear key joints incorporating HPFRCC with PVA/BFP: (a) initial interface crack at approximately 85% of ultimate load, and (b) crack deviation at approximately 45° into CC. 179

Figure 6.17: Shear resistance force relative to the standard truck loading HL-93 vs. vertical deflection for all composites in the shear key joint. 179

Figure A.1: Flexural test setup. 214

Figure A.2: Target flow for all specimens of 170±10 mm. 215

Figure A.3: Resistance to frost damage after 300 cycles: (a) G-N-B4.5 and (b) G-N-B4.5-V1. 215

Figure A.4: Walk-in Environmental Chamber. 216

Figure A.5: Cumulative intrusion vs. Pore size diameter. 216

Figure B.1: The homogenized stiffness coefficients kij equation. 217

Figure B.2: The pellet pull-out test set up. 217

Figure B.3: Examplear stress distributions from the models for the single pellet pull-out tests: (a) G, (b) G-N, and (c) G-NCC. 218

Figure B.4: Nano-fibrillated Cellulose: (a) solid state, (b) homogenizer at 2000 rpm for 4 min and (b) Liquid state (homogenization in water). 219

Figure B.5: The homogenized stiffness coefficients kij equation for G-NCC-NFC0.2 (RVE1). 219

Figure C.1: Preparations for the CC half cylinder for all specimens at 45°. 220

Figure C.2: Preparations for the CC half cylinder for all specimens at 33.7°. 220

Figure C.3: Slant Shear test set up. 221

Figure C.4: Bi-Shear test set up. 221

Figure C.5: Quasi-static tensile test specimen failure in the middle. 222

Figure C.6: Shear-normal stresses interaction of the composite HPFRCC/CC specimens for combination of experimental slant shear (at 33.7°) and bi-shear results. 222

Figure D.1: Cumulative intrusion vs. pore size diameter. 223

Figure D.2: Predicted peak load-embedded rebar length relationships for all composites. 223

Figure D.3: The homogenized stiffness coefficients kij equation for G-B2.5 (RVE1). 224

Figure D.4: The homogenized stiffness coefficients kij equation for G-N-B2.5 (RVE2). 224

Figure D.5: The homogenized stiffness coefficients kij equation for G-N-B4.5 (RVE3). 224

Figure D.6: The homogenized stiffness coefficients kij equation for G-N-B4.5-V1 (RVE5). 224

Figure D.7: Shear stress distribution for shear key bridge joint filled with G-N-B4.5-V1. 225

Figure D.8: Interface failure in specimens cast with G-N at 33.7°: (a) modeling simulation, and (b) bond stress (MPa) distribution at the interface. 225

Figure D.9: Interface failure in specimens cast with G-N at 33.7°: (a) modeling simulation, and (b) bond stress (MPa) distribution at the interface. 226

Figure D.10: Interface failure in specimens cast with G-N-B4.5 at 33.7°: (a) modeling simulation, and (b) bond stress (MPa) distribution at the interface. 226

Figure D.11: Interface failure in specimens cast with G-N-B4.5-V1 at 33.7°: (a) modeling simulation, and (b) bond stress (MPa) distribution at the interface. 227

Figure D.12: Direct shear failure in specimen G-N associated with shear stress (MPa) distribution at the interface between HPFRCC/CC. 227

Figure D.13: Direct shear failure in specimen G-N-B4.5-V1 associated with shear stress (MPa) distribution at the interface between HPFRCC/CC. 227

Figure D.14: Direct shear failure in specimen G-B2.5 associated with shear stress (MPa) distribution at the interface between HPFRCC/CC. 228

Figure D.15: Direct shear failure in specimen G-N-B4.5 associated with shear stress (MPa) distribution at the interface between HPFRCC/CC. 228

NOTATIONS

ANOVA Analysis of Variance

A Cross-section area of cylinder

A_f Cross-sectional areas of the pellet

A_m Cross-sectional areas of the matrix

[A] Area of the interface

BFP Basalt fiber/polymer pellets

b Coefficient parameter of how quickly the damage parameter reaches the value 1

CZM Cohesive zone model

CC conventional concrete

CH Calcium hydroxide

C-S-H Calcium-silicate-hydrate

c Adhesion strength (the pure shear strength)

C_f Interface stiffness tensor

d Steel bar diameter

d_t Debonding parameter

[d_t] Damage evolution parameter

$d\sigma_{ij}$ Volume averaged stress tensors of the RVE

$d\varepsilon_{ij}$ Volume averaged strain tensors of the RVE

EDX Elemental dispersive X-ray

ECC Engineered cementitious composites

E_0 Initial modulus of elasticity of intact material

E_f Moduli of elasticity of the pellet

E_m Moduli of elasticity of the matrix

E_{11} Longitudinal Young's modulus

E_{22} Transverse Young's modulus

E_{33} Transverse Young's modulus

F Vertical compression force of the composite cylinders

FRP Fiber-reinforced polymer

FRCM Fiber reinforced cementitious matrix

FEM Finite element modeling

F_f Forces applied to the pellet

F_m Forces applied to the matrix

g Regularities parameter shape of the curve

G_{12} In plane shear modulus

G_{13} In plane shear modulus

G_{23} Transverse shear modulus

HPFRCC High-performance fiber-reinforced cementitious composites

HRWR High-range water reducer

H Influence of both the interface compliance and morphology of the inclusion

ITZs Interfacial transition zones

K Stiffness parameter (slope of the line)

k_{ij} Effective tensor modulus of homogenized stiffness matrix

Le Embedment rebar length

L_{RVE} Edge side of RVE

L_y The slippage between steel and concrete in the direction of loading (y ordinate)

MIP Mercury intrusion porosimetry

NS Nano-silica

NCC Nano-crystalline cellulose

NFC Nano-cellulose fibers

n normal vector,

PVA Polyvinyl alcohol

RVE Representative volumetric element

PP Polypropylene

P Maximum applied load

$P_{0.5}$ The residual strengths at deflections 0.5 mm (*L/600*)

P_2 The residual strengths at deflections 2 mm (*L/150*)

P_{cr} The peak strength at first-cracking

S Interface surface of RVE

s Local slip at the fiber/pellet–matrix interface

(s) Edge of RVE

R_S The residual strength

SEM Scanning electron microscopy

TGA Thermogravimetric analysis

T Ultimate failure load

T_t^{max} Maximum equivalent tangential contact stress

t The tangential vector

UHPC Ultrahigh performance concrete

u_i Displacement applied in i direction on the boundary s at point x_j

w/b Water-to-binder ratios

x_j^+ The point on the edge s of RVE

α Compliance in tangential directions of the interface

α Angle of inclination with the vertical

β Compliance in normal directions of the interface

Δu_i: Displacement jumps (ε_{inter})

δ_s The relative displacement of steel rebar

δ_c The relative displacement of concrete

δ_m^c The slip at the completion of debonding

δ_t^* Tangential slip at the onset of debonding

δ_t^c Tangential slip at the completion of debonding

δ_t Tangential displacement jump (slip)

δ_{ij} Kronecker's delta

ε_t Axial tensile strain

ε_o Peak-critical strain

ε_t^{ck} The cracking strains

ε_i The crack-deformation strain

ε^{in} The cracking inelastic strain

ε^{pl} The plastic strains

ε_t^{pl} The plastic strains in tension

$\varepsilon_{ij}{}^0$ Constant strain at i-j directions

η Unit outward vector

μ Coefficient of friction

σ Axial tensile stress

σ_n Normal stress on the bond interface

σ_t Axial tensile stress

σ_o Maximum tensile stress

τ Pure shear stress

τ Interfacial shear stresses

τ_n Shear stresses on the bond interface

τ Interfacial shear bond strength

τ_b bond strength

τ_v The rebar shear stress

v_{12} In plane Poisson's ratio

v_{13} In plane Poisson's ratio

v_{23} Transverse Poisson's ratio

CHAPTER 1: INTRODUCTION

1.1 Overview

Numerous studies have been conducted to mitigate the low toughness/ductility of conventional concrete (CC) [e.g. Yang *et al.*, 2010; Bandelt and Billington, 2016; Meng *et al.*, 2017]. This technical limitation may aggravate the nucleation and propagation of cracks in CC, and reduction in its performance and service life, especially in vulnerable locations such as joints in pavements and bridges suffering from extreme loading and environmental conditions in the presence of salt and moisture. High-performance fiber-reinforced cementitious composites (HPFRCC) typically exhibit high toughness under tension and flexural loadings [Pan *et al.*, 2015]. These composites are, for example used in new construction, repairs, and retrofitting of joint to enhance ductility and performance of structural elements under service and extreme conditions [Smith *et al.*, 2010; Lepech and Li, 2010].

In HPFRCC, supplementary cementitious materials (SCMs), e.g., slag: by-product from steel industry, are commonly used to reduce the cement factor/carbon footprint, enhance fiber/matrix interaction, and improve the overall properties of the composites. SCMs react with calcium hydroxide (CH) from the hydration reaction producing additional calcium silicate hydrate gel (C-S-H), and consequently densifying the pore structure of cementitious systems [Neville, 2011]. However, the higher volume use of SCMs in the binder retards the hardening rate and strength development of the cementitious matrix. This limitation can be mitigated by the inclusion of small dosages of ultrafine nanoparticles [e.g. nano-silica (NS), nano-crystalline cellulose (NCC)] in the cement-based matrix to modify its microstructure and enhance hardened properties.

One of the most viable options to improve the ductility of cement-based materials is reinforcing the matrix with fibers. Metallic, natural, and synthetic fibers have been adopted to improve both plastic and hardened properties of HPFRCC through controlling bleeding and impeding the nucleation of cracks [Bentur and Mindess, 2006]. The key advantages of HPFRCC are their increased residual strength beyond first-cracking, deformability and ductility/toughness [Bentur and Mindess, 2006]. Moreover, fibers can restrain the cracks width and intensity, based on the type, geometry, dosage, and properties of the fibers used in the cementitious composites. Accordingly, many studies have been performed on cementitious matrices comprising hybrid fiber systems, as their performance exceeds that of individual fibers [e.g., Loh *et al.*, 2019; Wang *et al.*, 2019; Özkan and Demir, 2020; Wang *et al.*, 2021; Özkan and Çoban, 2021].

Macro-basalt fibers are a relatively a new type of fibers, which are emerging in concrete research due to its high tensile strength (3000 to 4000 MPa), adequate modulus of elasticity (93-110 GPa), high thermal and corrosion resistances, as well as low-cost relative to other alternatives such as glass fibers [Azzam *et al.*, 2021]. At early-age (7 days), basalt fibers had good bond with the matrix; however, this bond was significantly reduced within 90 days. This was attributed to the reaction between alkaline pore solution and silica component in basalt fibers, leading to reduction in the strength and integrity of the reinforced composites [Jiang *et al.*, 2014]. This shortcoming can be alleviated through using a polymeric resin (e.g. polyamide) to protect the fibers [Mahmoud *et al.*, 2017], resulting in the advent of a new class of basalt fibers termed basalt fiber pellets (BFP). At the University of Manitoba, 36 mm long macro-BFP with different dosages (i.e., 2.5%, 4.5%, and 6.9%) were used as a single fiber system to develop nano-modified cementitious composites comprising 50% cement, 50% SCMs (i.e., 50% slag, 50% fly

ash), and 6% nano-silica. These composites improved hardened and durability properties including high ductility, high performance under extreme loadings (e.g., direct tension, impact), excellent bonding and compatibility with sound or cracked parent CC, and resistance to ingress of fluids and frost action with/without de-icing salts, suggesting promising potential for a suite of infrastructural applications [Azzam *et al.*, 2019; Azzam *et al.*, 2021].

1.2 Need for Research

Deterioration of concrete infrastructure, especially in vulnerable locations such as joints of bridges is commonly associated with excessive cracking due to various loading, chemical and environmental schemes. These cracks allow water, salts, or aggressive chemicals to penetrate through the joints, thereby causing further damage to the joint, corrosion of reinforcing dowels and reduction in the transverse load transfer [Russell, 2009; Russell, 2011]. Thereby, high-performance repairs or overlays (e.g., HPFRCC) have been used for protection of concrete infrastructure, which are characterized by high crack resistance, low permeability, and high compatibility with CC.

HPFRCC typically exhibit ductile post-cracking behavior under tension and flexural loadings depending on key mixture design parameters. Different types of binders incorporating General Use cement (GU), slag, fly ash, nano-silica, etc. and a range (0.25 to 0.35) of water-to-binder ratios (*w/b*) have been used with various geometries and types of fibers (e.g., polyvinyl alcohol [PVA], steel, nano-fibrillated cellulose [NFC]) to produce HPFRCC [e.g., Pan *et al.*, 2015; Meng *et al.*, 2017; Da Costa Correia *et al.*, 2018]. Such composites have a compressive strength range from 40 to 150 MPa associated with a ductile behavior (strain softening or hardening) under tensile stresses [e.g., Douglas and Billington, 2005; Mechtcherine *et al.*, 2013; Yang and Li, 2014]. For

example, after first-cracking, these composites have high tensile ductility, within the range of 3 to 7% [Zhou *et al.*, 2012], relative to CC which cracks at approximately 0.01% tensile strain [Wang, 2005]. Different types of ultrafine nanoparticles (e.g. nano-silica, nano-crystalline cellulose) have been incorporated in HPFRCC to modify microstructure and enhance hardened properties. For instance, addition of 6% nano-silica by mass to cement-based binders with/without SCMs creates additional nucleation sites for precipitation of hydration products [Kong *et al.*, 2012; Said *et al.*, 2012], accelerates the pozzolanic reactivity [Kong *et al.*, 2012, Ghazy *et al.*, 2016b], and enhances the particle packing (filler effect) in the hardened paste. Also, it reduces *w/b* in the paste due to water absorption into its ultrahigh surface porosity.

Micro-PVA and NFC fibers have been used in HPFRCC because of their hydrophilic nature and potential for impeding nucleation of cracks in the matrix [Liu *et al.*, 2011; Jongvisuttisun *et al.*, 2013]. PVA fibers have a tensile capacity up to 1600 MPa, with a moderate modulus of elasticity (up to 66 GPa) [Li *et al.*, 2001]; the typical dosage of PVA micro-fibers is 2% by volume of the composite to yield a strain hardening behavior [Li *et al.*, 2001]. Macro-basalt fibers have emerged in concrete research since last decade, owing to their high mechanical properties, high corrosion resistance, high thermal resistance, and lower cost relative to glass and carbon fibers [Ayub *et al.*, 2014; Iyer *et al.*, 2015; Arslan *et al.*, 2016; Iyer *et al.*, 2016; Ghazy *et al.*, 2016a]. A new class of basalt fibers termed basalt fiber pellets (macro-BFP) has been introduced through using a polymeric resin (e.g. polyamide) to encapsulate the fibers [Mahmoud *et al.*, 2017]. Using macro-BFP as a single system with different dosages in nano-modified cementitious matrix resulted in promising results in terms of fresh and mechanical properties [Mahmoud *et al.*, 2017; Azzam *et al.*, 2019]. However, these composites

experienced considerable reduction up to 30% in terms of compressive and first-peak flexural strengths, especially with higher dosages of BFP (4.5% or 6.9% by volume). While the performance of hybrid fiber systems exceeds that of individual fiber components, as of yet, research on BFP in hybrid fibers systems to reinforce cementitious composites has not been commenced.

For fundamental understanding of the performance of HPFRCC, characterization of fiber/matrix interaction is of outmost concern. The fiber/matrix interfacial bonding is a governing factor for bridging cracks and progressive load transfer mechanisms. Limited information has been reported on determining/predicting the fiber/matrix interfacial bonding from HPFRCC. For instance, Azzam *et al.* [2021] investigated the effect of displacement rate and type of binder on the single BFP interfacial bonding with matrix, and the highest bonding results were obtained at the high displacement rate (50 mm/min) and nano-modified based slag matrix [Azzam *et al.*, 2021]; however, no other types of nano/micro-fibers (nano-fibrillated cellulose, micro-PVA) and nanoparticles [i.e., nano-crystalline cellulose NCC)] were included in these matrices. Moreover, with experimental characterization, finite element modeling (FEM) can encompass various analytical methods to simulate heterogeneous composites through optimizing the critical representative volumetric element (RVE) and representation of the thin layer between inclusion (fiber) and surrounding matrix (i.e. interfacial transition zones [ITZs]) [Teng *et al.*, 2007; Sun *et al.*, 2007]. These integrated approaches can be effectively used to study innovative HPFRCC comprising BFP to capture its bonding characteristics with different matrices, and linkage of pellet/matrix interaction to the bulk trends.

The overall performance of cementitious repair/filler for jointing applications depends mainly on the adhesion and coefficient of friction between the repair material

and the precast CC, in order to ensure the integrity of the composite section and load transfer between layers of concrete. The incorporation of BFP (single system) in HPFRCC improved the bond behaviour with uncracked and pre-cracked CC under flexural loading [Azzam *et al.*, 2022]. The HPFRCC had high integrity with the CC, where the two layers of concrete acted as one unit under flexural loading, with no signs of transverse delamination [Azzam *et al.*, 2022]. So far, there is scarce information on exploring the interfacial bonding behavior of HPFRCC comprising single BFP or hybrid BFP/PVA systems with precast CC or reinforcing rebars for shear key applications. In a previous study, Bediwy and El-Salakawy [2021] evaluated the bond behavior of sand-coated glass fiber-reinforced polymer rebars with straight/headed-ends embedded in HPFRCC comprising single BFP [Bediwy and El-Salakawy, 2021]. It was reported that the presence of BFP kept the intactness of concrete blocks with no signs of cracks/crushing [Bediwy and El-Salakawy, 2021]. High rebar interfacial pull-out strength from FRCC comprising hybrid fiber systems were also reported [e.g., Kim *et al.*, 2013; Wang *et al.*, 2019; Özkan and Demir, 2021]. However, there is still no data on exploring the rebar interfacial bonding with innovative HPFRCC comprising hybrid PVA/BFP systems for jointing applications.

1.3 Objectives of Research

The constant demand for resilient cementitious composites in various infrastructural applications prompts continual research efforts to produce innovative composites exploiting recent advancements in materials manufacturing. The objective of this doctoral research is to:

- Develop nano-modified cementitious composites comprising high-volume slag and reinforced with single BFP or hybrid fiber systems to study their fresh, mechanical and durability properties.
- Establish homogenization multi-scale models for randomly distributed fibers in the matrix to determine the homogenized stiffness elastic coefficients k_{ij}, and further verify the modeling predictions with experimental results with parametric analysis of selected variables.
- Evaluate the effect of nano-modified cementitious composites comprising various matrices and fibers on the BFP/matrix interfacial bonding characteristics and correlate it to the bulk properties of the composites through experimental and modeling studies.
- Investigate the interfacial bonding of these composites with CC and steel rebar, to check their suitability for shear key applications through experimental and modeling studies.
- Develop a predictive 3D FEM for full-scale shear key bridge joint with innovative HPFRCC and provide fundamental data on their maximum shear capacity, modes of failures, and crack formation process.

1.4 Scope of Research

To achieve the objectives of this thesis, the research work involves both experimental and modeling studies as described below:

- *Providing fundamental data on nano-modified cementitious composites comprising and reinforced with single (macro-BFP or micro-PVA) and hybrid system (micro-PVA and macro-BFP) fibers*: The effect of nano-silica and fiber systems of single (macro-BFP or micro-PVA) and hybrid system (micro-PVA and macro-BFP) fibers on the fresh (mortar flow test, air content, and setting time), hardened (compressive

strength, flexural strength and toughness) and durability (freeze/thaw cycles and porosity) properties were evaluated. Seven mixtures were cast and tested. Furthermore, thermal and microscopy studies were conducted to correlate the microstructure and hydration evolution of the composites to the bulk trends.

- *Characterization of the fiber/matrix interaction:* The effect of various nano-modified [nano-silica (NS), nano-crystalline cellulose (NCC)] cementitious matrices comprising high volume-slag without/with micro- or nano-fibers [micro-PVA, nano-fibrillated cellulose (NFC)] on the bonding with BFP using integrated experimental (flexure, and single pellet pull-out) and modeling (homogenization/FEM) approaches were evaluated. Fourteen mixtures were prepared, tested and verified against FEM predictions. Furthermore, thermal and microscopy studies were performed to augment the bulk results.
- *Investigating the potential of employing HPFRCC in shear key bridge joints:* The interfacial bonding capacity between HPFRCC and parent CC under shear configurations, as well as its interaction with reinforcing rebars were evaluated. Hence, the compressive and tensile capacity aspects were used to evaluate the bonding performance of HPFRCC by slant shear, bi-shear, rebar pull-out tests. Six mixtures were prepared and tested to evaluate the effect of variable HPFRCC composites with/without nano-silica and reinforced with single BFPs or hybrid PVA/BFP systems. In addition, the bulk trends were corroborated with thermogravimetry and microstructural analyses.
- *Developing 3D FEM for investigating the efficiency of HPFRCC in shear key bridge joints:* The bonding strength distribution, modes of failures, crack pattern/formation process between these composites and precast CC, as well as steel rebar were

analyzed. The bond strength of the composites was investigated through slant shear, bi-shear, and rebar pull-out models using ANSYS software package. The models were then calibrated and validated against the experimental data previously obtained to develop a full-scale 3D FEM for predicting the performance of shear key joint filled with various HPFRCC under HL-93 design truck loads according to AASHTO LRFD [2020].

1.5 Original Contributions

The current Ph.D. thesis introduces an integrated experimental and modeling approaches on high-performance cement-based materials engineered with nano-silica and reinforced with single BFP or hybrid (PVA/BFP) and its suitability to be employed as a filler material in shear key bridge joints. The specific outcomes of this work are as follows:

- Providing a large data set on such composites comprising nano-silica and reinforced with single BFP and hybrid PVA/BFP fiber system with balanced performance in terms of mechanical and durability properties.
- Producing fundamental data on the BFP/matrix interaction in cementitious composites comprising various types of nanoparticles (nano-silica, nano-crystalline cellulose) with/without micro- or nano-fibers (micro-PVA, NFC) to elucidate the post-cracking stage of the composites' performance.
- Developing a homogenization method for predicting the stiffness elastic coefficients k_{ij} of the nano-modified cementitious composites incorporating single BFP dosages and hybrid PVA/BFP fiber system.
- Demonstrating the interfacial shear bonding capacity of the studied cementitious composites with precast CC, as well as presenting the influence of using different inclination shear angles (45°, 33.7°) and fiber systems (i.e., single BFP and hybrid

PVA/BFP) on the interface shear key parameters including adhesion and coefficient of friction for jointing applications.

- Generating data on the interfacial bond slip relationship of the studied cementitious with steel rebars, as well as presenting the influence of using different fiber systems on the rebar interlocking/friction mechanisms.
- Introducing 3D FEM and numerical data for analyzing the bond stress distribution, modes of failure, and crack pattern and formation process of the nano-modified cementitious composites in jointing applications with precast CC and steel rebar.
- Providing predictive information about the maximum shear bond capacity, crack formation process, and modes of failure from a full-scale 3D FEM for a shear key bridge joint grouted with such composites under HL-93 design truck loads.

1.6 Structure of the Thesis

This thesis consists of eight chapters as described below:

- **Chapter One** contains introduction, problem definition/research significance, objectives, scope of work, and contributions of the research.
- **Chapter Two** presents literature review on basalt fibers, HPFRCC and their bond properties to normal concrete/reinforcement rebars, repair systems, shear key bridge joints, and finite element modeling.
- **Chapter Three** describes the results and discussion to evaluate the behavior of the nano-modified cementitious composites comprising nano-silica and reinforced with single BFP or hybrid PVA/BFP fiber system in terms of the fresh and hardened properties as well as the complementary thermal and microscopy studies.

- **Chapter Four** provides the test results and discussion for the developed composites comprising (nano-silica, NCC) with/without micro- or nano-fibers (micro-PVA, NFC) subjected to BFP /matrix pull-out, as well as the complementary thermal and microscopy studies. It describes the homogenization approach for these composites, in addition to 3D FEM and its validation against bulk results, as well as the results of a parametric study.
- **Chapter Five** introduces the test results and discussion for the bonding capacity between HPFRCC and CC under different shear loading configurations, as well as its interaction with reinforcing rebars, as well as the complementary thermal and microscopy studies.
- **Chapter Six** introduces the FEM results and discussion for bonding capacity of developed HPFRCC with precast CC, and steel rebars, as well as a predictive model for a 3D full-scale shear key bridge joint with various innovative HPFRCC.
- **Chapter Seven** provides a summary of the research findings, concluding remarks based on the test and modeling results and recommendations for future research.

CHAPTER 2: LITERATURE REVIEW

Concrete plays an important role in improving the existing infrastructure, owing to its lower cost and acceptable performance, in addition to its flexibility in the production processes. In order to overcome the drawbacks of conventional concrete (CC) and providing materials with higher performance to meet the requirements, various integrated approaches had been utilized to improve the material performance. The technical limitation of cracking, low toughness/ductility of CC represents can be mitigating by incorporating different types of fibers are considered an interesting method [Li, 2004].

2.1. Overview on Cementitious Composites

High performance cement-based materials consisted of two main classes: high-compressive-strength and high-ductility cementitious composites [i.e., strain hardening cement composites (SHCC) and engineered cementitious composite (ECC), in addition to some high-performance cementitious composites reinforced with fiber (HPFRCC)]. High-compressive strength cement composites preserve effectively to decrease the size of structural members, besides providing strength safety for reinforced structural concrete. High ductility cementitious composites can be used under considerable deformation well as improve the structure performance under extreme loading configurations (e.g. earthquakes, impact, etc.) [Li, 2004].

High performance fiber reinforced cementitious composites (HPFRCC) represents one of the family of fiber reinforced concrete (FRC). HPFRCC typically exhibit ductile post-cracking behavior under tension and flexural loadings depending on key mixture design parameters. The production of HPFRCC, incorporating different types and systems of fibers for better performance, of the structural system, reduced energy

demand, and limited maintenance cost during its life cycle. Many studies utilized hybrid fiber systems in HPFRCC, as their performance exceeds that of individual fiber components [e.g. Dawood and Ramli, 2011; Park *et al.*, 2012]. For example, in binary-scale fiber systems, micro-fibers counteract coalescence of micro-cracks, while macro-fibers restrain the growth of macro-cracks in the matrix [Zhang and Cao, 2014; Sindu and Sasmal, 2019; Elhadary and Bassuoni, 2021]. For fundamental understanding of the performance of HPFRCC, characterization of fiber/matrix interaction is of utmost concern. The fiber/matrix interfacial bonding is a governing factor for bridging cracks and progressive load transfer mechanisms. Moreover, the fiber type, strength, orientation, geometry, and volume fraction as well as matrix properties, service temperature and displacement rate are among the key parameters affecting fiber/matrix adhesion.

ECC represents high-tensile-ductile cement-based materials mostly reinforced with 2% by volume of polyvinyl alcohol (PVA) fibers that was introduced by Li and coworkers in 1990s [Li *et al.*, 2001; Ranade *et al.*, 2013; Li *et al.*, 2017; Yu *et al.*, 2018]. ECC has moderate-to-high (4 to 12 MPa) tensile capacity with high ductility (hundred times that of the CC and FRC) and failure strain (3 to 7%). ECC has efficient crack control capabilities (multiple cracking mechanism) that delayed the debonding failure, enhanced the bearing capacities of strengthened structures, and made it a highly durable material in environmental regimes [Sui *et al.*, 2018].

2.2. Cementitious Composites Composition

HPFRCC represents one of the categories of the FRC It typically exhibits ductile post-cracking behavior under tension and flexural loadings depending on key mixture design parameters. Numerical studies have been conducted to introduce a huge amount of mixtures formulation (**Table 2.1**), to understand fiber-matrix interaction performance

associated with a competitive cost material and higher performance. Supplementary cementitious materials (SCMs) are commonly used to reduce the cement content, enhance fiber/matrix interaction and improve the overall properties of the composites. Currently, HPFRCC are used in new construction and retrofitting applications (e.g., pavement, bridges, buildings, etc.) to increase ductility and improve the performance of structure members under service and extreme conditions.

Metallic, natural, and synthetic fibers have been adopted to improve both plastic and hardened properties of HPFRCC through impeding the nucleation of cracks and controlling bleeding [Bentur and Mindess, 2006]. Moreover, fibers such as steel, carbon, polypropylene, and polyvinyl alcohol, can restrain the cracks width and intensity, based on the type, geometry, dosage, and properties of the fibers used in the cementitious composites. Besides, high volume supplementary cementitious materials (SCMs) are commonly used to reduce the cement content in HPFRCC.

Strain hardening cement-based composites (SHCCs) is the most common type of high-performance fiber reinforced cementitious composites (HPFRCC). SHCCs, which are reinforced with short fibers, exhibits pseudo strain hardening under tension loading (i.e., ECC) [**Figure 2.1**]. After first-crack stress, the short fibers start to carry tension load till reaching the tensile strength capacity, and then the gradual multiple cracks formation result in a decrease in the composite stiffness. Subsequently, SHCC fails due to exceeding the tensile strength capacity of the used fibers or even the pullout of the fibers from the matrix at the weakest crack location [Mechtcherine, 2013]. The high ductility/toughness of SHCCs prompt it to be used in various infrastructure applications (i.e., repair and concrete strengthening).

Table 2.1: Exemplar mixtures proportions per cubic meter

Mixture ID.	Cement (kg)	Fly ash (kg)	Slag (kg)	Water* (kg)	Fibers (Volume)	Fine aggregate (kg)	HRWR (l)
1	560	675	---	315	2%	450	3.8
2	381.6	890.4	---	318	2%	462	15.3
3	381.6	763.2	127.2	318	2%	462	15.3
4	381.6	636.0	254.4	318	2%	462	15.3
5	381.6	508.8	381.6	318	2%	462	15.3

1 [Halvaei *et al*., 2014] and 2-5 [Zhu *et al*., 2012]

One of the important crucial issues in the material design is to well homogenize distributed fine fibers within the matrix, in order to improve the strength of the matrix, the interfacial bond between matrix and the fibers, and impeding the crack spreading in the matrix. When the required fibers are well distributed within the matrix, the matrix/fiber interfacial bond is significantly enhanced, the huge risk of early fibers pull-out and leads to premature composite failure is diminished. Moreover, the utilize of fine aggregate will be common instead of coarse aggregate. Polyethylene (PP) and polyvinyl alcohol (PVA) fibers represented the most appropriate reinforced fibers in HPFRCC. PVA fibers have a tensile capacity up to 1600 MPa, with a moderate modulus of elasticity (up to 66 GPa) [Li *et al.*, 2001]; the typical dosage of PVA micro-fibers is 2% by volume of the composite to yield a strain hardening behavior [Li *et al.*, 2001].

2.3. HPCC Properties

The main purpose of using various types and systems of fibers is to control the propagation and nucleation of cracks and hence extend the service life of infrastructural elements. Besides, fibers able to improve the material properties under different loading configuration including ductility/toughness, fatigue, shear strength, and flexural strengths.

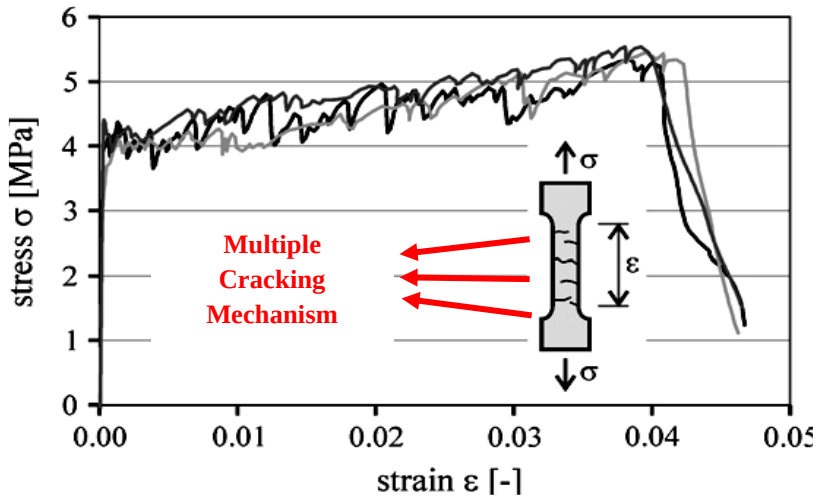


Figure 2.1: The stress-strain relationship of SHCC under tension [adapted from Mechtcherine, 2013].

Moreover, many studies have been performed on cementitious matrices comprising hybrid fiber systems, as their performance exceed that of single fiber systems [e.g. Wang *et al.*, 2019; Wang *et al.*, 2021]. For instance, the combination of both PVA micro-fibers and basalt macro-fibers in the cementitious matrix improved the mechanical and physical properties [Özkan and Demir, 2020], especially at elevated temperatures [Wang *et al.*, 2021] and reduced the apparent void volume (porosity), and capillary water absorption [Özkan and Çoban, 2021]. However, there are different factors affecting the efficiency of using fibers, including the fiber system, type, volume, geometry, size, and matrix properties, where fibers might reduce the workability of cementitious composites. The addition of fibers reduces the workability of the mixture and increases the voids content besides high risk of clumping and fiber clustering. Subsequently, the fresh characteristics of the cementitious composite have to be controlled in order to enhance its fresh and hardened properties [Kuder *et al.*, 2007].

2.3.1. Rheological Properties

The fresh properties of the HPFRCC cementitious composites can be indicated through using rheological parameters, including pumpability, placeability, compactability and finishability, where each application needs specific rheological properties. There were various models exist describing the rheological properties of cement-based systems. Bingham model is the most commonly used, which is given by **Equation 2.1**:

$$\tau = \tau_0 + \mu_0 \gamma \qquad \textbf{(Equation 2.1)}$$

Where τ_0 is the Bingham yield stress, identifying the stress required to start the flow, μ_0 is the Bingham plastic viscosity representing the material resistance to flow, while γ and τ represent the shear rate and stress, respectively. Besides, some tests were conducted in different studies to determine the workability of cementitious composites including flow and flow retention tests using flow table as an indication on the composite's rheological properties [e.g. Mahmoud *et al*., 2017; Azzam *et al.*, 2019].

2.3.2. Mechanical Properties

Unlike parent/conventional concrete (CC) and fiber reinforced concrete (FRC), HPCC are characterized by high ductility, controlled crack width, as well as exhibits strain hardening (i.e., ECC) under tension loads. ECC has moderate-to-high (4 to 12 MPa) tensile capacity with high ductility and failure strain (3 to 7%). The superior mechanical properties of cementitious composites motived the demand of many researchers to improve its mechanical behavior through using different fibers systems (i.e., single and hybrid fiber systems) as well as its types, or even changing the cementitious matrix components and/or proportions.

Many researchers investigated the effect of various nano-particles (fillers) and fine aggregate on the mechanical behavior of cementitious composites such as nano-silica, nano-titanium, nano-carbon tubes, nano-crystalline cellulose (NCC), and other

fillers [e.g. Jongvisuttisun *et al*., 2013; Hoyos *et al.*, 2013; Cao *et al.*, 2015; Hanif *et al*., 2017], in order to modify its microstructure and enhance its hardened properties. Other studies focused on the effect of fiber systems (i.e., hybrid system) and type on the mechanical performance of cementitious composites like steel fibers, carbon fibers, polypropylene fibers (pp), polyvinyl alcohol fibers (PVA), nano-fibrillated cellulose (NFC), and others. Consequently, it was emphasized through different studies that the interfacial zone at the fiber matrix interface is a governing factor for bridging cracks and progressive load transfer mechanisms [e.g. Pan *et al*., 2015; Da Costa Correia *et al.*, 2018; Xu *et al*., 2021].

In hybrid systems, based on different fiber sizes, micro-fibers provide restraint to micro-cracks and deter their coalescence, thus increasing the ultimate capacity, while the macro-fibers control the propagation of macro-cracks in the matrix that enhances the strain limit and toughness in the post-cracking stage. Wang *et al.* [2019] investigated the performance of cementitious composites incorporating hybrid fibers (PVA and basalt fibers). It was concluded that the addition of 1.5% basalt and 0.5% PVA fibers into the cementitious composite led to notable improvement in the post-cracking flexural and uniaxial tensile strengths relative to that of mixtures reinforced with a single system (1.5% PVA) and hybrid system (1.5% PVA and 0.5% steel). This was accompanied with corresponding improvements in toughness and strain capacity as well [Wang *et al.*, 2019].

Many researchers investigated the effect of improving the mixing sequence on the ECC performance. For instance, Zhou *et al*. [2012] studied the effect of mixing sequence on the mechanical properties and fibers distribution. It was reported that the addition of fibers after mixing all liquid and powder materials resulted in a poor distribution of fiber

and low hardened performance (Standard mixing sequence); However, adding fibers in step between two equally divided fraction of solid and liquids materials (modified mixing sequence), led to well distribution of fibers in the matrix, as well as enhancement in the tensile strength and strain capacity of ECC (**Figure 2.2)** [Zhou *et al*., 2012].

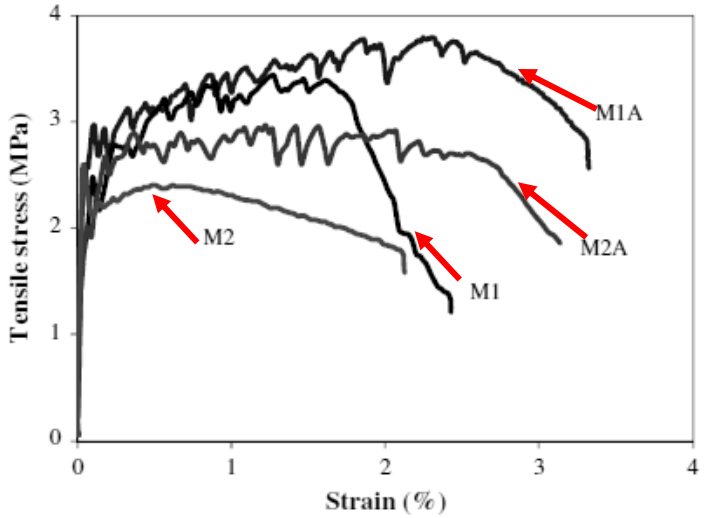


Figure 2.2: The stress–strain curves for four mixtures under tensile load, where notation (1, 2) refers to the mixture, and (A) refers to the modified mixing sequence [adapted from Zhou *et al*., 2012].

One of the alternatives methods used in cementitious composites is to study the effect of supplementary cementitious materials (SCMs) on the mechanical properties. Zhu *et al*. [2012] studied the effect of partially replacement of cement with 70% of powder content (combination of fly ash and ground granulated blast furnace slag) as presented in **Table 2.2**. It was reported that the combination of SCMs in ECC enhanced the tensile strain capacity and strain-hardening performance (more than 2.5%) after 90 days. Moreover, unlike to ECC with only fly ash, the combination of 30% slag and 40% fly ash had a potential effect on increasing the compressive strength by 60%, higher than that of 70% fly ash of the total binder, specifically at early ages [Zhu *et al*., 2012].

Table 2.2: Mixtures proportions [Zhu *et al*., 2012].

Mixture ID	PC (kg)	FA (kg)	Slag (kg)	Sand (kg)	Water (kg)	HRWR (l)	PVA (kg)
ECC 70-0	381.6	890.4	0	462	318	15.3	26
ECC 60-10	381.6	763.2	127.2	462	318	15.3	26
ECC 50-20	381.6	636.0	254.4	462	318	15.3	26
ECC 40-30	381.6	508.8	381.6	462	318	15.3	26

2.3.3. Durability Properties

ECC materials exhibits excellent tensile toughness/ductility, which provide the structures with high strength when the material suffers from multiple micro-cracking associated with strain hardening plateau. Thus, ECC specimens were preloaded in some studies under different strains to nucleate the micro-crack damage as in the cracked state (worst case scenario), to conservatively assess the durability potential of such high-performance mixtures under different exposure conditions [e.g. Şahmaran and Li, 2007; Şahmaran and Li, 2008].

Numerical studies have been conducted in order to understand the performance of HPCC under different durability tests. Li *et al*. [2003] conducted frost resistance test for 14 consecutive weeks on conventional concrete prism (CC) and ECC. It was reported that the CC specimens suffered from severe deterioration after five weeks (110 cycles) before reaching the 60% relative dynamic modulus of elasticity (RE_d) failure limit stipulated by ASTM C666. Conversely, ECC specimens reached to 300 cycles without deterioration. As a result, the durability factor of CC and ECC specimens were 10% and 100% respectively [Li *et al*., 2003].

Sahmaran *et al*. [2012] reported the influence of utilizing PVA micro-fibers, and high volume of SCMs (i.e., fly ash) with 0.27 *w/cm* on the freeze-thaw resistance (300 freeze/thaw cycles [ASTM C666]) and the microstructure properties of the ECC

mixtures. It was reported that the high volume of fly ash improved the durability of ECC materials and exhibits an excellent tensile strain capacity, accompanied by increasing freeze and thaw cycles. While ECC matrix without PVA micro-fibers suffered from severe deterioration and failed before reaching the required number of cycles (300 cycles). This improvement attributed to the role of PVA micro-fiber on improving the freeze-thaw resistance of ECC mixtures. [Şahmaran *et al*., 2012].

2.3.4. Shrinkage

Shrinkage represents one of the most major issues, which influence the mechanical and durability properties of ECC, unlike conventional concrete, where the presence of coarse aggregate restrains the volumetric changes such as shrinkage strains. Numerous studies have been conducted in order to mitigate such technical strain limitation effect [e.g. Zhang *et al*., 2009].

Kawashima and Shah [2011] investigated the effect of incorporating 1% cellulose fibers by mass on the behavior of cementitious materials in sealed and unsealed condition, relative to early-age shrinkage. The unsealed condition is the drying shrinkage and autogenous shrinkage, while the sealed condition was to mimic only the autogenous shrinkage. It was reported that adding 1% cellulose fibers by mass of cement showed significant effect on controlling the nucleation and propagation of drying cracks shrinkage. Moreover, it was found that well fiber dispersion in matrix resulted in the improved properties of cementitious materials [Kawashima and Shah, 2011].

Zhu *et al.* [2012] reported the influence of various SCMs (i.e., 70% of slag and/or fly ash by mass of cement-based binder) on the mechanical behavior and free drying shrinkage properties of ECC mixtures. It was reported that the mixture with 40% fly ash and 30% slag had drying shrinkage of 840 micro-strain at 28 days, while the mixture with

70% fly ash had drying shrinkage of 1000 micro-strain. Moreover, the drying shrinkage marginally increased by using 70% slag; however, mixture of 30% slag and 40% fly ash achieved the lowest dying shrinkage. This could be attributed to the particle packing effect of mixed SCMs (i.e., 30% slag, and 40% fly ash) [Zhu *et al*., 2012].

2.4. Cementitious Composites Incorporating Basalt Fibers

Basalt fibers (BF) are a relatively emerging type of fibers in concrete research due to its high tensile strength (3000 to 4000 MPa), adequate modulus of elasticity (93-110 GPa), high thermal and corrosion resistances, as well as low-cost relative to other alternatives such as glass fibers. BF can be employed in strengthening member exposed to various loading configurations including shear, flexural, and tension stresses; in addition, they are used in strengthening bridges and tunnels as well.

Basalt fibers are made out of crushed basalt rocks, consisting of mineral composition including pyroxene, plagioclase, and olivine. The basalt fiber filaments of diameter range from 9 to 13 μm are produced from basalt rock, (i.e., washed and melted down up to 1,400°C), and then extruded from small nozzles in order to be suitable for asbestos replacement. The processing method of basalt fiber is so complicated, owning to higher melting point required for melting down the rocks. Many studies have been conducted to investigate the effect of mechanical, structural, and physical properties, in order to provide clear basis for various further applications [e.g. Shi, 2012]. Moreover, basalt fibers are biodegradable, and nontoxic materials, in which they do not cause any environmental by-product waste. In addition, it is believed that basalt fiber will motivate the concrete industry owing to its green effect, cheap price, lightweight, as well as thermal and corrosion resistance [Iyer *et al*., 2015].

2.4.1. Fresh Properties

Different studies investigated the effect of basalt fibers on the fresh properties of the developed composites, considering its slump and slump flow as well as the workability of the mixtures. In general, the inclusion of basalt fibers was reported to negatively influence the workability of the mixtures to a certain extent according to the mixture design and components.

For instance, Jiang *et al.* [2014] studied the effect of various basalt fiber dosages on the slump flow of the developed composites. It was found that the inclusion of basalt fibers with volume fraction of 0.05%, 0.1%, 0.3%, and 0.5% diversely affect the slump of the mixtures to fall from 185 mm to 172 mm, 157 mm, 87 mm, and 65 mm, respectively [Jiang *et al*., 2014].

A new class of basalt fiber called basalt fiber pellets (BFPs) were used in concrete research, where encapsulated BF strands with polyamide resin to protect BF from degradation due to high alkali media. Azzam *et al.* [2019] investigated the effect of using high volume of SCMs (i.e., 50% slag or 50% fly ash) in cementitious composites reinforced with BFP with volume fraction 2.5%, 4.5%, and 6.9%. It was reported that the workability enhanced with the increase of BFP dosage and achieved the target mortar flow (200±20 mm), without diverse effect on the initial and setting times of the developed composites [Azzam *et al.*, 2019]

2.4.2. Mechanical Properties

The length of BF had a potential effect on the mechanical characteristics of developed composites. Relative to plain concrete, compressive strength, splitting tensile strength and flexural strength for basalt fiber of length 12 mm with different dosages (0 to 0.5% by volume) improved by 0.18 to 4.68%, 14.08 to 24.34% and 6.30 to 9.58%, respectively.

However, the strengths increase for the 22 mm basalt fiber length relative to the 12 mm length was 0.55 to 5.72%, 14.96 to 25.51% and 7.35 to 10.37%, respectively. Adequate interfacial bond strength between basalt fibers and the matrix was observed at the early ages. However, the bond showed degradation to specific extent at 28 days. Besides, the MIP results showed that the inclusion of basalt fibers increased the porosity of the concrete due to the effect of foaming action of fibers [Jiang *et al*., 2014].

Iyer *et al*. [2015] studied the influence of utilizing basalt fibers in FRC of grade 30 MPa and modulus of rupture 4.1 MPa. It was reported that the compressive strength after 28-days as well as the modulus of rupture were improved. Three different lengths of BF (12, 36 and 50 mm) with three different quantities (4, 8, 12 kg/m^3 of concrete) were cast. It was reported that the basalt fibers (36 mm) of 8 kg/m^3 achieved the highest performance in terms of the compressive strength (38 MPa) and modulus of rupture (5 MPa) [Iyer *et al*., 2015].

Jalasutram *et al*. [2017] studied the influence of using different volume fraction of BF ranged from 0 to 2% on the compressive, splitting tensile and flexural strengths, as well as flexural toughness of FRC. It was reported that increasing the dosage of BF had a marginal effect on decreasing the compressive strength of the developed concrete mixtures; however, the mode of failure was shifted from brittle to ductile failure. Whilst, increasing the dosage of basalt fiber (up to 2% by volume) significantly improved the splitting tensile strength and flexural strength of developed concrete by 15%, 75%, respectively. Moreover, BF improved the flexural toughness of FRC by almost 3 times, relative to that of plain concrete [Jalasutram *et al*., 2017].

In hybrid systems, based on different fiber sizes, micro-fibers provide restraint to micro-cracks and deter their coalescence, thus increasing the ultimate capacity, while the

macro-fibers control the propagation of macro-cracks in the matrix that enhances the strain limit and toughness in the post-cracking stage. Wang *et al.* [2019] investigated the performance of cementitious composites incorporating hybrid fibers system (PVA and basalt fibers). It was reported that the inclusion of 1.5% basalt and 0.5% PVA fibers into the cementitious composite led to notable improvement in the post-cracking flexural and uniaxial tensile strengths with corresponding improvements in toughness and strain capacity, relative to that of mixtures reinforced with either a single system of 1.5% PVA or hybrid fibers of 1.5% PVA and 0.5% steel.

Azzam *et al.* [2019] investigated the effect of different dosage of BFP of 2.5%, 4.5%, and 6.9% by volume (i.e., 1%, 2%, and 3% of BF strands) on the mechanical performance of developed cementitious composites incorporating high volume of SCMs (i.e.., 50% slag). It was reported that increasing the dosage of BFP reduced the compressive strength (up to 11%), and experienced considerable reduction up to 30% in terms of first-peak flexural strength, especially with higher dosages of BFP (6.9% by volume) [Azzam *et al.*, 2019]. Whilst, despite the higher modulus of elasticity of the steel fibers compared with BFP, the 2.5% dosage of BFP (i.e., 1% BF) improved the first tensile-cracking strength and energy absorption by 29% and 8%, respectively, relative to 1% of steel fibers by volume [Azzam *et al*., 2021].

2.4.3. Durability Properties

Durability of cement-based materials is a critical issue for infrastructure elements exposed to aggressive environments, especially jointing application. High ductility and controlling cracks are necessary for their longevity and structural safety. The basalt fibers were found to be vulnerable to alkaline environment, which might affect the mechanical properties and microstructure of cement-based materials incorporating such type of fiber.

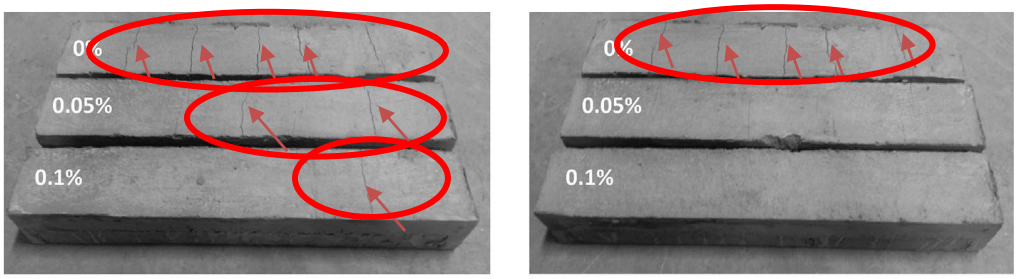
For example, Sim *et al*. [2005] investigated the effect of submerging basalt fibers in 1N NaOH solution at 40°C for a duration ranging between 7 and 28 days. It was reported that the tensile strength of BF reduced by 50% and 80% at 7 and 28 days, respectively [Sim *et al.*, 2005]. Moreover, Jiang *et al.* [2014] reported that basalt fibers have low alkaline resistance that make them vulnerable to degradation in media with pH values from 11 to 13, which is the case in cementitious systems. At early-age (7 days), basalt fibers had good bond with the matrix; however, this bond was significantly reduced within 90 days. This was attributed to the reaction between alkaline pore solution and silica component in basalt fibers, leading to reduction in the strength and integrity of the cementitious system [Jiang *et al.,* 2014]. One of the proposed solutions to alleviate such technical limitation is through using a polymeric resin (e.g. polyamide) to encapsulate the fibers [Mahmoud *et al.*, 2017]. This resulted in the advent of a new class of basalt fibers termed basalt fiber pellets (BFP).

Despite the high alkaline media of the matrix, concrete elements can be exposed to the ingress of external alkaline chemicals (e.g. sodium chloride, hydroxide, and carbonate) from soil, groundwater, or de-icing salts. Few studies investigated the effect of alkaline loading on FRCC. For instance, Sahmaran and Li [Şahmaran and Li, 2009] studied the effect of 1 N sodium hydroxide solution at 38°C for 30 and 90 days on developed composites incorporating 2% PVA micro-fibers. These composites incorporated 55% and 70% fly ash replacement by mass of the binder [1250 kg/m^3], with constant *w/b* of 0.26. It was reported that the pore feature's nature of 2% PVA micro-fibers led to slightly to intermediate loss of tensile ductility (13% to 21%) for un-cracked and pre-cracked specimens.

2.4.4. Shrinkage

Early shrinkage of concrete represents the volumetric change of the member and usually occurs after placement of concrete within first few hours. When the rate of water evaporation exceeds the rate of water bleeding, the volumetric change occurs due to the combinations of autogenous mechanisms and capillary pressure (plastic shrinkage), which is usually created at the pore structure near to the concrete surface. When the shrinkage stresses exceed the concrete tensile strength, concrete will crack and permit the penetration of the ingressive substances, resulting in the rapid deterioration of concrete and accelerated corrosion of embedded steel reinforcement.

There are different internal parameters in the concrete that affected the shrinkage restraints including the aggregate, rebars, etc. Branston *et al*. [2016] investigated the effect of using basalt fiber in controlling crack width and measuring the shrinkage strain magnitude (**Table 2.4**). It was reported that basalt fibers prevent the nucleation of cracks by decreasing the free shrinkage magnitude and impeding the cracks formation process as described in **Figures 2.3** and **2.4** [Branston *et al*., 2016].



(a) (b)

Figure 2.3: Exemplar fiber dosage increasing with a reduction in crack area in M4 for fibers length of 25 mm; (a) BD, and (b) FD [adapted from Branston *et al*., 2016].

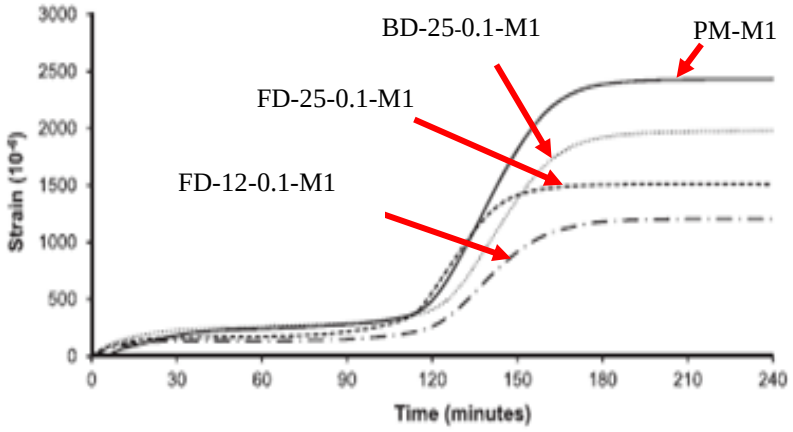


Figure 2.4: The developed strain over time for fiber dosage (0.1%) of lengths 12 and 25 mm [adapted from Branston *et al*., 2016].

Table 2. 3: Mass proportions of concrete mixtures

Mixture ID	Cement (kg)	Fine Aggregate (kg)	Coarse Aggregate (kg)	Water (kg)
M1	1	2	0	0.5
M2	1	2	0	035
M3	1	2	2	0.5
M4	1	1	0	0.5
M5	1	1	0	0.35

2.5. Applications

In order to limit the de-bonding failure of joints such as pavement, bridge decks, flooring, etc. as well as increasing the service life of the infrastructure systems, the interface bond strength evaluation in the design of connections is of outmost concern. AASHTO LRFD Bridge Design Specifications [2020] indicate that transferring loads (pure tension, pure shear, and combination of shear and compression) at joints occurs through adhesive bonding, friction, and doweling action. In the field, the most common issue of joints is longitudinal cracking, resulting in premature deterioration due to infiltration of water and aggressive chemicals leading to corrosion of reinforcement and loss of the monolithic behavior among bridge segments [Russell, 2011; Wang *et al.*, 2019; Fu *et al.*, 2021].

Subsequently, cementitious composites materials incorporating fibers can be employed in a suit of repair/overlay in concrete pavements/bridges joints, or as a filler material in bridge deck shear key joints applications.

2.5.1. Shear Key Bridge Joints

In the 1950s, the prestressed CC box girders were utilized in adjacent precast concrete box girder bridges, due to their simple structure, economy, and ease of construction. The bridge superstructure typically consists of prestressed CC concrete box girders placed sequentially assembled to each other, forming longitudinal shear keys joints. These joints, which are typically cast-in-place and filled with a grout material, help transfer load between the girders during service and under extreme loads. Also, shear dowels or tie rods at the joints are used to enhance the load transfer mechanism, in which the combination between shear and tension applied load transfer at the interface is ensured by the shear dowels and the contact area between precast CC-cast in-place grouted materials according to American Association of State Highway and Transportation Officials (AASHTO) load and resistance factor design (LRFD) Bridge Design Specification [AASHTO,2020]. However, poor compatibility with the existing precast CC segments, cracking behaviour, premature deterioration due to water infiltration and chemical agents, corrosion of reinforcing steel and reduction in the monolithic behavior of the segments remain challenging issues for these types of connections. (Hanna *et al.,* 2009; Russell, 2009; Grace *et al.*, 2010; Fu *et al.,* 2011; Russell, 2011; Hussein *et. al,* 2017a and 2017b).

Numerous experimental studies have been conducted to evaluate the shear key bonding capacity using various filler materials (e.g., non-shrinking grouts, magnesium-ammonium phosphate mortars, epoxy, polymer concrete, fiber reinforced concrete, ultra-high-performance concrete [UHPC]) [Ma *et al.*, 2012; Weber *et al.*, 2015; Arafa *et al.*,

2016; Hu *et al.*, 2021]. Issa *et al.* [2003] evaluated the performance of shear key filled with four different types of grouts: Set-grout, Set-grout-45 for normal temperature, Set-45 for hot weather, and polymer concrete under various loading tests including direct shear, direct tension, and flexural tests. It was reported that these tests have the capability to evaluate the grout material performance in terms of bond strength and ultimate capacity. Other studies evaluated the performance of shear keys between adjacent box girders grouted using two different materials, non-shrink grout material and magnesium ammonium phosphate mortars using direct tension, and shear forces. The authors recommended that these testing methods could evaluate the joint performance and obtain the ultimate strength capacity of shear keys [Issa *et al.*, 2003].

Weber *et al.* [2015] investigated the behavior of a non-shrinking grouted joint without/with post-tensioned carbon-fiber-reinforced polymer (CFRP) reinforcing rods under concentrated double-tire ASSHTO HL-93 design truck load. They reported that the use of CFRP post-tensioned rods increased the initial joint cracking load from 58% to 65% of the ultimate load compared with the specimen without posttensioned rods. However, significant cracking occurred in the grouted material or at the bonded interface with precast CC, likely due to the lower compressive strength of the non-shrinking grout material [Weber *et al.*, 2015].

Porter *et al.* [2011] studied the connections between precast deck panels with shear dowels force by using the shear test to determine the ultimate shear strength. Results showed that the shear test can be used to evaluate the performance of the connections. Also, this test setup could allow the shear dowels to pull out of the connection when diagonal cracks were formed [Porter *et al.*, 2011]. Arafa *et al.* [2016] assessed the performance shear key joint reinforced with glass fiber-reinforced polymer

bars and jointed with ultra-high-performance concrete (UHPC). It was reported that UHPC enhanced the behaviour of bridge joint because of its superior mechanical properties by 32%, relative to non-shrinking grout materials [Arafa *et al.*, 2016]. Semendary *et al.* [2017] investigate a new field developed precast conventional concrete (CC) shear key joints grouted with UHPC according to AASHTO LRFD Bridge Design Specification [2020] under HL-93 design truck loads for different loading case scenario, in order to conduct the live-load moment-distribution factors (LLMDFs). It was reported that the LLMDFs of the loaded beams and adjacent beam were higher compared with unloaded beams. Besides, loading the bridge with one truck on the right side for both the interior and exterior beams improved the LLMDFs, which were 0.179 and 0.222, compared with loading the bridge with two trucks or even one truck on the left side.

Hu *et al.* [2021] tested 30 UHPC-connection conventional concrete (CC) shear keys under shear loads to investigate the effect of UHPC on shear key capacity, relative to that of non-shrinking grout material. It was observed a shear-off failure mode (interfacial bonding failure followed by diagonal cracks towards CC or UHPC) of the UHPC connection, similar to that of the non-shrinking grout shear key joint. In particular, UHPC improved the shear key capacity by 32% relative to that of non-shrink grout. Besides, the shear capacity increased linearly with the displacement until visible crack formation up to 78% of the ultimate load for the UHPC-connection. [Hu *et al.*, 2021].

2.5.2. Bonding Evaluation

The bonding behavior between concrete layers is one of the most important factors that evaluate the compatibility of the new layer with the old substrate as well as it guarantees monolithic behavior of the system in order to increase the structure capacity of the existing pavement. Numerous studies have been conducted to enhance the overall

performance of infrastructure system under different loading configurations. For instance, Wagner *et al.* [2013] investigated the performance of interfacial bonding stress between cementitious composites incorporating 0.5% and 1% PVA micro-fibers of length 8 mm and 12 mm and conventional concrete (CC). It was reported that 1% of length 12 mm PVA micro-fibers were able to deviate the interfacial micro-crakes outside the interface as well as impede the nucleation of micro-cracks at the interfacial bond zone [Wanger *et al.*, 2013].

Carbonell *et al.* [2013] used the pull-off test to find the bond strength between UHPC overlay and normal strength concrete (NSC). Almost all of the specimens failed in the normal strength concrete as opposed to the bond line or UHPC overlay. The authors concluded that this testing method does not represent the actual strength of the interface bond because of the failure mode. In addition, the results of splitting tensile tests demonstrated a higher bond strength than the pull-off test [Carbonell *et al.*, 2013].

Using the slant shear test, Zanotti *et al.* [2018] investigated the interfacial bonding between parent concrete with fiber reinforced repair concrete comprising 0.5% and 1% PVA micro-fibers of length 8 mm and 12 mm, and steel fibers of length 13 mm. Three different bonding plane inclinations: 30°, 25°, and 20° with the vertical axis were applied. It was reported that 1% PVA micro-fibers (12 mm) and 0.5% of steel fibers (13 mm) were able to deviate the micro-cracks away from the interfacial zone and increased the adhesion (c) up to 103% and 98%, respectively. However, increasing the volume fraction of steel fibers from 0.5% to 1% reduced adhesion due to formation of additional interfacial transitional zones (ITZs), which acts as a weak links at the interface [Zanotti *et al.*, 2018].

Al-Madani *et al.* [2017] studied the interfacial bond between normal concrete substrate and ultrahigh performance concrete (UHPC) concrete comprising a mixture of 1% straight and hooked end steel fibers with a diameter of 0.2 mm and 0.35 mm, and a length of 13 mm, and 25 mm, respectively, using the bi- shear (direct shear) test as well as slant shear test at an inclination angle of 30° with the vertical. It was reported that the bond strength in the slant shear test was much higher relative to the bi-shear test (approximately 4.5 times) due to the combined normal stress, which increased the friction between the contact layers in the slant shear test [Al-Madani *et al.*, 2017]. Semendary and Svecova [2020] investigate the effect of concrete substrate strength (normal strength concrete NCS and high strength concrete HSC), aggregate types and surface preparation (dry and saturated surface dry SSD) on the interfacial bond strength between UHPC and substrate concrete through using different loading test configurations, including direct tension, slant shear and bi-shear tests. The results indicate that the UHPC resulted in a marginal increase in the bond strength for NSC and a significant increase in the bond strength of the HSC specimens by 23%. The cohesion and shear friction coefficients were determined using different loading tests, in which he cohesion value was 2.78 MPa for dry and SSD conditions, and the friction coefficients were1.33 and 1.32 for dry and the SSD specimens, respectively [Semendary and Svecova, 2020].

Gomaa *et al.* [2020] studied the effect of using alkali-activated concrete (AAC) mixtures synthesized using five different class C fly ash (FA) and conventional portland cement concrete (PCC) on the interfacial bond with PCC. The interfacial bond was examined under different slant shear inclination angles (45° and 22.5°), and pull-off tests with sand blasting treatment, bonding adhesive treatment, as well as no surface treatment. It was reported that the adhesion increased with an increase in the calcium content of the

FA. Moreover, three different failure modes occurred depending on the inclination angle of the interface joint between the repair and PCC materials shifted from compression failure at 45° angle to sliding along the interface at 22.5° angle. Moreover, the pull-off test results were sensitive to the surface treatment with sandblasting, which yielded the highest direct tensile strength [Gomaa *et al.*, 2020].

Azzam *et al.* [2022] studies the effect of nano-modified cementitious composites reinforced with single dosage of BFP on the bond strength with the substrate concrete under pull-off test. The authors reported that the mode of failure for all composites under pure tension stresses (up to 1.89 MPa), regardless of binder type and fibers' dosage, which assembly took place in the CC layer of compressive strength 45 MPa (10 to 70 mm below the interface). In addition, these tests did not represent the actual strength of the interface bond with the substrate concrete [Azzam *et al.*, 2022].

Moreover, number of studies have been conducted to investigate the cracking phenomena at the bonding interface. For instance, Azzam *et al.* [2022] evaluated the bond behaviour of nano-modified cementitious composites comprising single dosages of basalt fiber pellets (BFP) with cracked and un-cracked substrate concrete under flexural configurations. The cementitious composites showed efficient performance in fibers' restraining ability to control the crack opening width within the repair layer. This helped to minimize the stresses at the substrate-repair interface, in which the two layers behaved monolithically under the applied flexural loading, without any signs of transverse delamination [Azzam *et al.*, 2022].

2.5.3. Rebar Bonding Evaluation

For fundamental understanding of the performance of cementitious composites, characterization of rebar/concrete interaction is of outmost concern. The rebar bond slip

relationship is a governing factor for bridging cracks and progressive load transfer mechanisms. Various experimental (e.g., pull-out tests) methods have been used to determine/predict the rebar interfacial bond with repair materials [Kim *et al.*, 2013; Wang *et al.*, 2015; Khaksefidi *et al.*, 2021]. The chemical bond, interlocking, friction, compressive strength of concrete, rebar structure, rebar type and embedded length, as well as the rebar diameter are among the key parameters affecting rebar adhesion. For instance, Ahmad *et al.* [2011] investigate the interfacial bond behaviour between carbon fiber-reinforced polymer (CFRP) rebars and UHPC. Different parametric studies such as embedment length, rebar diameter and concrete strength had been investigated. It was also found that ultimate bond strength decreases with rebar diameter, concrete strength, and embedment length. Moreover, the bond strength can be expected during early age (3 days) [Ahmad *et al.* ,2011].

Other studies investigate the effect of structural fibers on the interfacial bonding mechanism between GFRP bar and concrete. Kim *et al.* [2013] studied the interfacial bonding between glass fiber reinforced polymer rebars and fiber-reinforced concrete with two different dosages (0.5%, 1% by volume) of fibers (i.e., steel, polypropylene (PP), and PVA). It was reported that 1% PVA or steel fibers improved the pull-out bond strength by 25%, and 14%, respectively, as these fibers impeded the creation and propagation of cracks and their growth in the matrix [Kim *et al.*, 2013]. Similarly, Wang *et al.* [2015] investigated the interfacial bonding behavior between basalt fiber reinforced polymer rebars and engineered cementitious composites containing PVA micro-fibers (2% by volume) of length 12 mm, where the addition of PVA fibers controlled micro-cracking and improved the bond strength between rebars and the matrix by 35% [Wang *et al.*, 2015].

Khaksefidi *et al.* [2021] investigate the rebar interfacial bond with concrete through preparing two types of rebars (high-strength and normal strength) embedded in the centre of cubic UHPC and normal strength concrete NSC with three bonded lengths (2, 4, and 6 timed the diameter). The results show that the concrete strength, the ratio of concrete cover to the diameter (c/d), bond length, and rebar yield strength play an important role in determining the failure mode. The bond strength increased by using a high-strength rebar (AIV) in comparison with normal strength (AIII) rebars. UHPC reduces the embedded length of rebars by increasing bond strength relative to NSC. Besides, increasing the bond length led to significant improvement in the maximum bond stress of NSC; However, the maximum bond stress decreases in UHPC [Khaksefidi *et al.*, 2021]. Moreover, the bond behavior of sand-coated glass fiber-reinforced polymer rebars with straight/headed-ends embedded in HPFRCC comprising BFP was evaluated [Bediwy and El-Salakawy, 2021]. It was reported that the presence of BFP kept the intactness of concrete blocks with no signs of cracks/crushing [Bediwy and El-Salakawy, 2021].

2.5.4. Modelling

2.5.4.1. Shear Key Bridge Joint

Recently, several academic research teams in the United States and Canada have been developed to study different infrastructure joints between concrete layers with/without shear dowels (i.e.., shear key bridge joints). Small-or full-scale of experimental and numerical shear key joints have been conducted to investigate the joint performance by applying either static or cyclic loads under truck loads and/or environmental loads. The researchers concluded that the bond strength along the interface plays a vital role in transferring loads. In addition, several finite element modeling (FEM) has been calibrated

using small-or full-scale experimental results in terms of load transfer mechanisms. It was reported that FEM could be used for the design of shear key connections.

For example, Hussein *et al.* [2017] conducted experimental and FEM studies to evaluate the ultimate shear key capacity between precast CC and UHPC under direct shear, tension, and flexural loading configurations. It was reported that the UHPC shear key configurations can be optimized using FEM [Hussein *et al.*, 2017]. Another study investigates a new analytical FEM for developed PC key shear joints grouted with UHPC under HL-93 design truck loads for different loading case scenario, in order to conduct the live-load moment-distribution factors (LLMDFs). It was reported that the FEM showed a good agreement with the field application, in which loading the bridge with one truck on the right side for both the interior and exterior beams improved the LLMDFs, relative to loading the bridge with two trucks or even one truck on the left side [Semendary *et al.*, 2017].

Hu *et al.* [2021] developed two shear key configurations using experiments and FEM to predict the shear capacity of joints filled with UHPC comprising hook-end steel fibers (0.07% by weight of premix) at length 16 mm under shear loading (compressive load at the shear key interface). It was indicated that the models had good agreement (maximum 15% error) with experimental results, and thus they could be used for the design of shear key connections. In particular, UHPC improved the shear key capacity by 32% relative to that of non-shrink grout. Besides, the shear capacity increased linearly with the displacement until visible crack formation up to 78% of the ultimate load for the UHPC-connection. However, the models predicted a shear-off failure mode (interfacial bonding failure followed by diagonal cracks towards CC or UHPC) of the UHPC connection, similar to that of the non-shrinking grout shear key joint. [Hu *et al.*, 2021].

Fu *et al.* [2021] used experiments and finite element modeling (FEM) to assess the performance of single and double shear key joints and filled with fiber reinforced concrete (FRC) comprising steel fibers (2% by volume) under combined bending and shear loads. It was reported that the double shear key joint increased the initial cracking and ultimate loads by up to 68%, and 105%, respectively, compared with the single shear key joint. Moreover, the average initial cracks and ultimate loads for the shear key at 30° and 60° joints increased by approximately 127%, 54%, and 107%, 91%, respectively for the single and double shear key joints. The initial crack appeared at the bottom corner of the shear key and propagated along the vertical direction till reaching the ultimate load [Fu *et al.*, 2021].

2.5.4.2. Interface Modeling

With experimental characterization, finite element modeling (FEM) approach can encompass various analytical methods (e.g., homogenization [Mori and Tanaka, 1973], generalized self-consistency [Christensen and Lo, 1979]) methods through optimizing the critical representative volumetric element (RVE) and representation of the thin layer between inclusion (fiber) and surrounding matrix (i.e. interfacial transition zones [ITZs]) [Teng *et al.*, 2007; Sun *et al.*, 2007]. Besides, this integrated approach can be effectively used to better understand the bonding performance, dealing with the factors that might lead to the de-bonding failure [Grace *et al.*, 2013; Hussein *et al.*, 2017; Hu *et al.*, 2021].

Tran *et al.* [2007] focused on experimental and analytical approaches to evaluate the propagation of de-bonding along with the interface between overlay and substrate materials under three-point flexural fatigue setup. Two types of overlay materials were investigated (fiber reinforced and plain mortars). A video-microscope with a magnification of 175x was utilized to monitor the de-bonding propagation along the

interface. It was reported that the model was an efficient tool to predict interfacial failure and cracking behaviour [Tran *et al*., 2007].

Dalalbashi *et al.* [2018] addressed the analytical pull-out investigation on the single PVA micro-fiber from tensile-reinforced mortar (TRM). Three different pull-out model setups, consisting of one pull-pull and two pull-push configurations, were simulated (**Figure 2.5**). As the output of the analytical modeling, it was reported that the analytical modeling helped in extraction of the bond-slip laws from the experimental results corresponding to each test set up. Besides, the differences in the load-slip curves obtained from different models setups leads to different bond-slip laws [Dalalbashi *et al.*, 2018].

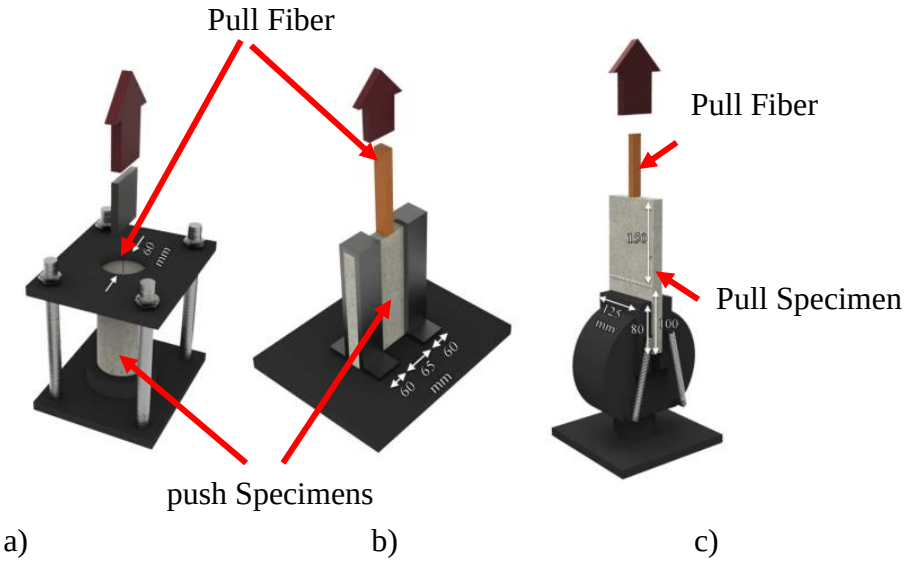


Figure 2.5: Specimens' configurations and corresponding model setups: (a) pull-push I; (b) pull-push II; (c) pull-pull [adopted from Dalalbashi *et al.*, 2018].

Haile *et al.* [2019] developed a six multi-level homogenization analytical models for the prediction of the elastic moduli and mechanical properties at a smaller length scale for UHPC. The multi-scale analysis combines the modeling of the material properties at micro-scale (10^{-6} m), meso-scale (10^{-3} m), and finally macro-scale for UHPC, in which

the matrix is homogenized with carbon fiber (CF) and steel fiber (SF) that acts as inclusions embedded in the matrix separately. It was reported that fiber type, orientation, and volume fraction play an important role in the material properties. Besides, the predicted values of UHPC with fibers with an error of less than 15% relative to that of the experimental test results, substantiating the accuracy of numerical predictions [Haile *et al.*, 2019].

2.5. Closure

The constant demand for resilient cementitious composites in various infrastructural applications prompts continual research efforts to produce innovative composites incorporating different types and systems of fibers, in order to mitigate the technical limitation (e.g. cracking, low toughness/ductility) of traditional concrete. Hence, various types and sizes of metallic, synthetic, and natural fibers have been used to improve the plastic and hardened properties of HPFRCC. Moreover, the hybrid fiber systems have been utilized in HPFRCC, as their performance exceeds that of individual fiber components. Besides, macro-basalt fibers have emerged in concrete research since last decade, owing to their excellent performance. However, research on the use of single BFP in HPFRCC is still at early stages, with many unexplored areas such as the pellet/matrix interaction.

Moreover, different mixtures with/without fiber reinforcement are being employed in jointing application (i.e., shear key bridge joints); HPFRCC typically exhibit ductile post-cracking behavior under tension and flexural loadings depending on key mixture design parameters. HPFRCC reinforced with single BFP and/or hybrid PVA/BFP systems might be a good candidate for these application, which warrants focused research in this area. As of yet, there is no data focused on evaluating the effect

of combinations of macro-BFP with micro-fibers such as PVA (hybrid fiber system) in cementitious composites to assess the efficacy of this combination on the properties of the composites through using integrated experimental and modeling (homogenization/FEM) approaches, as well as environmental freeze exposures. Such data is crucial to identify the functionality of these composites for safe and resilient use in jointing applications (i.e., shear key bridge joints). Hence, further investigations are required to identify the effect of different parameters including the fiber dosage, type, and systems, as well as the loading and exposure regimes on the performance of these composites.

CHAPTER 3: NANO-MODIFIED SLAG-BASED CEMENTITIOUS COMPOSITES REINFORCED WITH BASALT PELLETS AND POLYVINYL ALCOHOL FIBERS

3.1 Introduction

Numerous studies [e.g. Yang *et al.*, 2010; Bandelt and Billington, 2016; Meng *et al.*, 2017] have been introduced to mitigate the technical limitation (e.g. cracking, low toughness/ductility) of traditional concrete, leading to the development of high-performance fiber-reinforced cementitious composites (HPFRCC) using different fiber types and binders. HPFRCC typically exhibit high toughness under tension and flexural loadings [Pan *et al.*, 2015]. For example, engineered cementitious composites (ECC), offer superior ductility/toughness associated with pseudo strain hardening performance [Pan *et al.*, 2015]. Li and coworkers [Li *et al.*, 2001; Ranade *et al.*, 2013; Li *et al.*, 2017; Yu *et al.*, 2018] developed ECC reinforced with polyvinyl alcohol (PVA) fibers that have moderate-to-high (4 to 12 MPa) tensile capacity with high ductility and failure strain (3 to 7%). Currently, HPFRCC are used in new construction and retrofitting applications (e.g., pavement, bridges, buildings, etc.) to enhance ductility and performance of structural elements under service and extreme conditions.

In HPFRCC, supplementary cementitious materials (SCMs), e.g. slag: by-product from steel industry, are commonly used to reduce the cement factor/carbon footprint, enhance fiber/matrix interaction and improve the overall properties of the composites. SCMs react with calcium hydroxide from the hydration reaction producing additional high stiffness calcium silicate hydrate (C-S-H), and consequently densifying the pore

Elhadary, R. and Bassuoni, M.T., 2022. Nano-modified slag-based cementitious composites reinforced with basalt pellets and polyvinyl alcohol fibers. *Journal of Sustainable Cement-Based Materials*, pp.1-12.
Elhadary, R. and Bassuoni, M.T., 2020. Mechanical Properties of Nano-Modified Cementitious Composites Reinforced with Single and Hybrid Fibers. *Transportation Research Record*, 2675(9), pp.56-64

structure of cementitious systems [Neville, 2011]. Nevertheless, when used at high volumes in the binder, the slower reactivity of SCMs retard the strength and hardening rate of the cementitious matrix. This can be mitigated by the inclusion of small dosages (4-6% by mass of binder) of ultrafine nano-silica in cement-based matrix [Ghazy *et al.*, 2016; Azzam *et al.*, 2019]. Nano-silica positively influences the microstructure of the cementitious matrices through multiple mechanisms, including precipitation of hydration products at the newly created nucleation sites [Kong *et al.*, 2012; Said *et al.*, 2012], pozzolanic reactivity [Kong *et al.*, 2012; Ghazy *et al.*, 2016], filling effect due to its ultrafine nature, and reducing the apparent water-to-binder ratio (*w/b)* in the paste [Kong *et al.*, 2012] due to the water absorption into its ultrahigh nano-pores.

Metallic, natural, and synthetic fibers have been adopted to improve both plastic and hardened properties of HPFRCC through impeding the nucleation of cracks and controlling bleeding [Bentur and Mindess, 2006]. Moreover, fibers can restrain the cracks width and intensity, based on the type, geometry, dosage, and properties of the fibers used in the cementitious composites. Accordingly, many studies have been performed on cementitious matrices comprising hybrid fiber systems, as their performance exceed that of single fiber systems [e.g. Loh *et al.*, 2019; Özkan *et al.*, 2020; Wang *et al.*, 2021; Özkan *et al.*, 2021; Wang *et al.*, 2019]. In hybrid systems, based on different fiber sizes, micro-fibers provide restraint to micro-cracks and deter their coalescence, thus increasing the ultimate capacity, while the macro-fibers control the propagation of macro-cracks in the matrix that enhances the strain limit and toughness in the post-cracking stage. For instance, the combination of both PVA and basalt fibers in the cementitious matrix improved the mechanical and physical properties [Özkan *et al.*, 2020], especially at elevated temperatures [Wang *et al.*, 2021] and reduced the apparent void volume

(porosity) and capillary water absorption [Özkan *et al.*, 2021]. Wang *et al.* [2019] investigated the performance of cementitious composites incorporating hybrid fibers (PVA and basalt fibers). It was concluded that the addition of 0.5% basalt and 1.5% PVA fibers into the cementitious composite led to notable improvement in the post-cracking flexural and uniaxial tensile strengths with corresponding improvements in toughness and strain capacity, relative to that of mixtures reinforced with a single system of 1.5% PVA or hybrid fibers of 1.5% PVA and 0.5% steel.

Basalt fibers are a relatively emerging type of fibers in concrete research due to its high tensile strength (3000 to 4000 MPa), adequate modulus of elasticity (93-110 GPa), high thermal and corrosion resistances, as well as low cost relative to other alternatives such as glass fibers [Azzam *et al.*, 2021]. Concrete/mortar reinforced with basalt fibers showed increasing in tensile strength, flexural strength, and ductility [Ayub *et al.*, 2014; Iyer *et al.*, 2015; Iyer *et al.*, 2016; Azzam *et al.*, 2021]. While mixtures' toughness was enhanced by increasing the dosage of the fibers, the post-cracking stage showed strain softening trends. Reduction of workability of fresh concrete and fiber balling at basalt fibers dosages of more than 0.5% by volume were also reported [Ayub *et al.*, 2014; Jiang *et al.*, 2014; Iyer *et al.*, 2016]. Jiang *et al.* [2014] reported that basalt fibers have low alkaline resistance that make them vulnerable to degradation in media with pH values from 11 to 13, which is the case in cementitious systems. At early-age (7 days), basalt fibers had good bond with the matrix; however, this bond was significantly reduced within 90 days. This was attributed to the reaction between alkaline pore solution and silica component in basalt fibers, leading to reduction in the strength and integrity of the cementitious system [Jiang *et al.*, 2014]. This technical limitation can be alleviated through using a polymeric resin (e.g. polyamide) to encapsulate the fibers [Mahmoud *et*

al., 2017], resulting in the advent of a new class of basalt fibers termed basalt fiber pellets (BFP). However, research on BFP, especially in hybrid fibers systems, in cementitious composites is still at early stages, which warrants further investigation, before its safe application in the field.

3.1.1 Research Significance

There is a continual demand for the advent of resilient and sustainable cementitious composites incorporating high-volume SCMs for various infrastructure applications. Using macro-BFP as a single fiber system with different dosages in nano-modified cementitious composites showed promising results in terms of fresh and mechanical properties [Azzam *et al.*, 2019; Mahmoud *et al.*, 2017; Bediwy and Salakawy, 2021]. However, these composites experienced considerable reduction up to 30% in terms of first-peak flexural strength, especially with higher dosages of BFP (4.5% by volume). Moreover, no data is available on the combination of macro-BFP with micro-fibers such as PVA (hybrid fiber system) in cementitious composites to assess the efficacy of this combination on the properties of the composites. Thus, the current study focused on the development of nano-modified cementitious composites comprising high replacement of cement with 50% slag, 6% nano-silica as an additive, and reinforced with single (macro-BFP or micro-PVA) and hybrid system (micro-PVA and macro-BFP) fibers. The results of fresh, mechanical and durability properties for these composites were studied and corroborated by thermal and microstructural analyses. This data is essential to informatively assess the potential of these composites for multiple field applications, especially in harsh environments of cold regions.

3.2 Methodology

3.2.1 Materials

In this study, the used binder comprised 50% General Use (GU) cement and 50% Grade 100 slag, meeting the requirements of CSA-A3001 [2018] (**Table 3.1**). A single dosage of 6% nano-silica solution (NS), which consists of 50% SiO_2 particles dispersed in an aqueous solution, was used as an additive. Nano-silica product is commercially available at a cost of $1/liter, when bought in bulk amounts. The specific surface area, pH, mean particle size, density, and viscosity values of nano-silica are 80,000 m^2/kg, 9.5, 35 nm, 1.1 g/cm^3, and 8 cP, respectively. Continuous gradation of fine aggregate from 0 to 600 μm was used in the mixtures, and its fineness modulus, absorption and specific gravity were 2.9, 1.5% and 2.6, respectively. In order to enhance the mixtures' workability, poly-carboxylic high-range water reducer (HRWR), complying with ASTM C494 Type F [2017], was added. Two sizes and types of fibers (BFP and PVA) were utilized to reinforce the mixtures. Macro-BFP were used at two different dosages of 2.5% and 4.5% by volume, equivalent to basalt fibers component of 1% and 2% by volume, respectively. The BFP have length of 36 mm and diameter of 1.8 mm [**Figure 3.1(a)** and **Table 3.2**], and they consist of 16 μm basalt roving (60% by mass) encapsulated by polyamide resin (40% by mass). The micro-PVA fibers were used at a fixed dosage of 1% by volume, with a length of 12 mm and diameter of 38 μm [**Figure 3.1(b)** and **Table 3.2**].

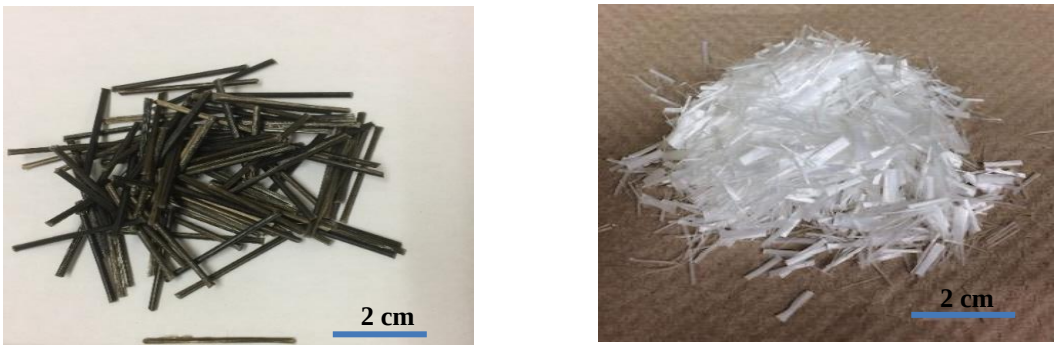
Table 3.1. Chemical and physical properties of GU cement and slag

Oxide Analysis/Physical Property	GU Cement	Slag
SiO_2 (%)	19.22	33.40
Al_2O_3 (%)	5.01	13.40
Fe_2O_3 (%)	2.33	0.76
CaO (%)	63.22	42.70
MgO (%)	3.31	5.30
SO_3 (%)	3.01	2.40
Na_2Oeq. (%)	0.12	0.30
Specific Gravity	3.15	2.87
Fineness (m^2/kg)	390[a]	492[a]

[a]Blaine fineness

Table 3.2. Properties of BFP and PVA fibers

Property	BFP	PVA
Length (mm)	36	12
Diameter/dimensions(mm)	1.8	38×10-3
Aspect ratio	20	315
Specific gravity	1.74	1.3
Tensile strength (MPa)	2,300	1600
Elastic modulus (GPa)	65	66



(a) (b)

Figure 3.1: Reinforcing fibers: (a) BFP, and (b) PVA.

3.2.2 Procedures

Seven mixtures were prepared comprising 50% cement and 50% slag with a total base binder of 700 kg/m^3 and constant *w/b* of 0.3, meeting the requirement for high-volume supplementary cementitious materials (HVSCM-1) concrete, according to Annex K in CSA A23.1 [30], as listed in **Table 3.3**. Nano-silica at a constant dosage of 6% (42 kg/m^3

by mass of the binder), was used as an additive in six mixtures (i.e. ternary binder content of 742 kg/m^3), where this dosage led to marked improvement of mechanical properties as reported in previous studies [Azzam *et al.*, 2019; Ghazy *et al.*, 2016]. Different fiber systems of either micro-PVA, macro-BFP or hybrid BFP/PVA were used to reinforce six mixtures. Mixtures incorporating single fiber systems comprised 2.5% BFP, 4.5% BFP, or 1% PVA, while the mixtures reinforced with hybrid fiber systems included 2.5% or 4.5% BFP combined with PVA at 1% by volume of the composite. For the mixtures' ID, the letters B, V, N, and G refer to BFP, PVA, nano-silica, and slag, respectively, while the numbers refer to the dosage of fibers.

A concrete pan mixer (60 rpm) was used to mix all the constituent materials. Initially, the dry constituents were added followed by gradual addition of the liquid phase (nano-silica, water, and admixtures) until reaching homogeneity. Subsequently, fibers were introduced and mixed with the ingredients for 7-10 minutes till reaching uniform distribution of fibers. All specimens were compacted in molds using a vibrating table and covered with polyethylene sheets for 24 h. The specimens were then demolded and cured in a standard curing room (temperature of 22$\pm$2°C and relative humidity of more than 95%) until testing.

3.2.3 Tests

The flowability, fresh air content and rate of hardening tests were conducted to investigate the fresh properties of the developed composites. The mortar flow test and air content were carried out according to ASTM C230 [2020] and ASTM C231 [2017], respectively, while the setting time of the mixtures was determined using standard needles at regular time intervals according to ASTM C403 [2016].

The compressive strength of the developed mixtures was determined according to ASTM C39 [2018], by testing triplicate cylinders (100×200 mm) at 3, 7, 28, 56, and 90 days of curing. The first-peak flexural load and the post-cracking performance of the mixtures were studied using triplicate prisms (100×100×350 mm) according to ASTM C1609 [2019] at 56 days, in a four-point bending test configuration. A servo controlled closed-loop testing machine was used, in which the displacement rate relied on the measured net mid span deflection of the prism. The flexural toughness represented is the area under the load-deflection curve (P-δ) up to 2 mm deflection (span/150), and the residual post-cracking index (R_i) was calculated according to **Equation 3.1** [2019]:

$$R_i = \frac{\frac{(P_{0.5}+P_{0.75}+P_1+P_{1.25})}{4}}{P_{cr}} \qquad \textbf{(Equation 3.1)}$$

where, $P_{0.5}$, $P_{0.75}$, P_1, and $P_{1.25}$ are the residual loads at deflections 0.5, 0.75, 1, and 1.25 mm, respectively and P_{cr} is the peak load at first-cracking.

The durability of the composites was evaluated according to ASTM C666 Procedure A, [2015] after 56 days of standard curing, in which the specimens were subjected to consecutive and rapid freeze-thaw cycles (total of 300 cycles) in an environmental chamber. The resistance to freezing-thawing cycles of the different mixtures was assessed based on the durability factor (*DF*) of triplicate prisms (50×50×285 mm). The *DF* of the developed mixtures was calculated based on dynamic modulus of elasticity according to ASTM C215 [2019].

Thermal and microscopy tests were performed to corroborate the trends from the bulk tests. Thermogravimetric analysis (TGA) was done for powder samples (pulverized by a mechanical grinder and passing sieve #200 [75 μm]) extracted from the triplicate cylinders used in compressive strength at a constant heating rate of 10°C/min, to

determine the portlandite (calcium hydroxide CH) contents in the matrix with age. In addition, elemental dispersive X-ray (EDX) with scanning electron microscopy (SEM) was carried out on fracture pieces comprising PVA and BFP fibers at 56 days, and the specimens were coated with carbon to improve their conductivity for the SEM imaging. The features of pore structure of the different mixtures were determined after 56 days by mercury intrusion porosimetry (MIP), where two cylinders from each mixture were used to produce 5-7 test samples of small pea-sized chunks (around 4-6 mm). Preconditioning of samples was carried out by oven drying at 45±2°C and silica gel until a constant mass was achieved; this procedure was adopted to reduce the potential of drying shrinkage cracks and decomposition of some hydration products associated with higher temperatures. The pressure of apparatus ranges from sub-ambient to 228 MPa. Considering a cylindrical shape of pores, a surface tension of 0.485 N/m and 130° of mercury contact angle with high-pressure limit up to 228 MPa yields a pore radius of about 3 nm, implying intrusion of all capillary pores.

3.3 Results and Discussion

3.3.1 Fresh Properties

All composites achieved the target flow of 170±10 mm (more than 170±10% the original base diameter of the mold, which was 100 mm), as listed in **Table 3.3**. The mixtures required high dosages (6 to 11 l/m^3) of the HRWR to achieve the required flowability. This can be linked to the mixtures design variables including low *w/b* (0.30), presence of nano-silica, high binder content (700 or 742 kg/m^3) and high content (50%) of angular slag particles in the binder, thus increasing the friction among constituents in the plastic state. Moreover, the dosage of HRWR increased (11 l/m^3) in the mixtures containing

PVA fibers (single and hybrid systems) compared with corresponding composites incorporating single dosages of BFP (approximately 7 to 8 l/m^3), due to the hydrophilic nature of PVA fibers, resulting in reduction of the free water needed for lubrication and workability of fresh composites.

For the air content (**Table 3.3**), the range varied between 3 to 8%, which mainly depended on the inclusion of pellets and/or PVA fibers. The mixtures incorporating BFP had increased air contents with dosage. For instance, the air content for mixture G-N-B4.5 was 118% and 14% higher, compared with that of mixtures G-N and G-N6-B2.5, respectively. The increased viscosity and friction between macro-BFP fibers and matrix might have led to a foaming action during mixing as implicated by the increased air content values. On the other hand, using 1% micro-synthetic PVA fibers led to marginal increase (less than 1% by volume) in the air content of fresh mixtures. Such trends were reflected on the hardened and durability results, as discussed in the succeeding sections.

High-volumes of slow reactivity SCMs (e.g. slag) typically extend the final setting time of mortar/concrete up to 12 h, as shown herein by the extended setting time (approximately 9 h) of the reference mixture G-B2.5 without nano-silica (**Figure 3.2**). However, the final setting times of all the nano-modified composites developed herein remained within the normal range of 4.6 to 5.1 h, despite the high-volume of slag incorporated in the base binder and high dosages of HRWR to attain the target flowability. This can be linked to the presence of ultrafine silica particles (80,000 m^2/kg), resulting in accelerated rates of reactivity, and thus skeletal rigidity, which was mainly due the nucleation effect within the first few hours, as also observed in previous studies [Zhang *et al.*, 2012; Ghazy *et al.*, 2016; Azzam *et al.*, 2019]. This suggests the suitability

of the developed nano-modified cementitious composites for most infrastructure systems, as they have plausible rates of rigidity.

Table 3.3: Mixtures proportions per cubic meter and fresh properties

Mixture ID	Cement (kg)	Slag (kg)	Water* (kg)	NS (kg)	Fine Aggregate (kg)	PVA (kg)	BFP (kg)	Air Content (%)	HRWR (I)	Flow Table (mm)
G-N	350	350	180	84	1232	--	--	3.4	5.5	180
G-B2.5	350	350	210	--	1288	--	43.3	6.9	6.5	163
G-N-B2.5	350	350	180	84	1167	--	43.3	6.5	7.6	170
G-N-B4.5	350	350	180	84	1115	--	78.3	7.4	8	165
G-N-V1	350	350	180	84	1206	13	--	4.0	11	180
G-N-V1-B2.5	350	350	180	84	1142	13	43.3	7.4	11	170
G-N-V1-B4.5	350	350	180	84	1090	13	78.3	8.2	11	165

*The amount of water was adjusted considering the water content of nano-silica (aqueous solution with 50 % solid content of SiO_2).

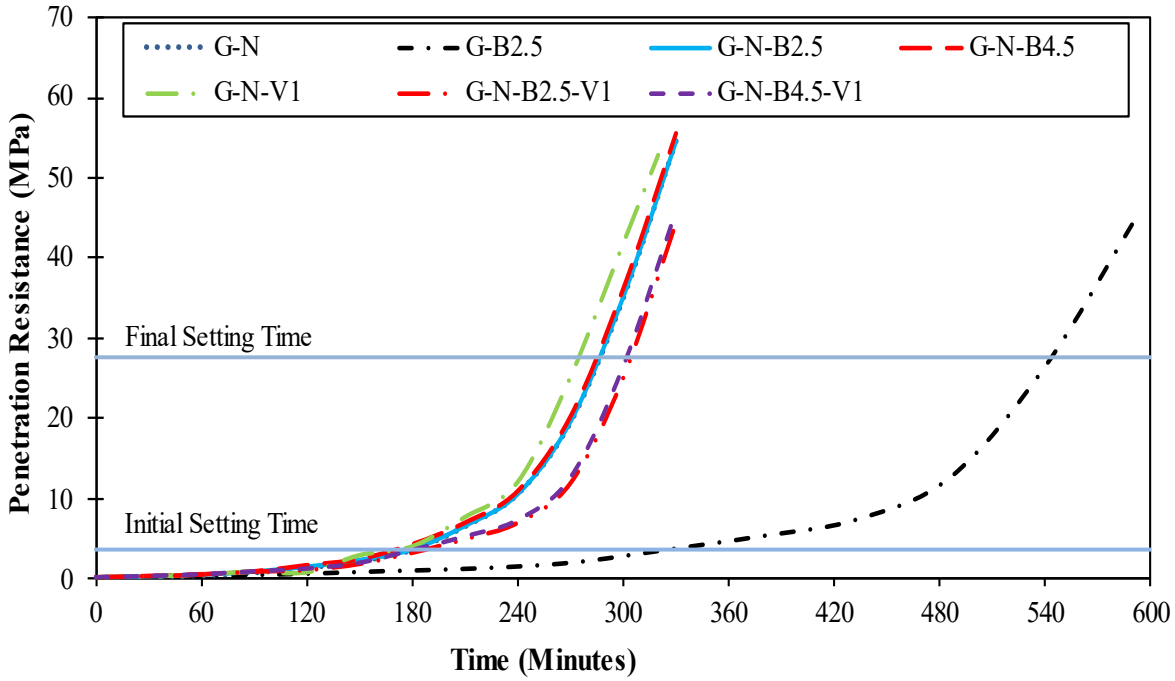


Figure 3.2: Penetration resistance vs. time for all mixtures.

3.3.2 Compressive Strength

The compressive strength results of the composites at different ages are shown in **Figure 3.3** Most codes and standards (e.g., CSA-A23.1/A23.2 [2019]) require the properties of cement-based materials comprising slow reactivity SCMs (e.g., slag) to be assessed at 56

or 91 days. Despite the higher percentage of slag (50%) in the base binder, the compressive strength of all mixtures comprising 6% nano-silica was improved, especially at early ages. For example, the compressive strength of G-N-B2.5 was increased by 32%, 26% and 15%, respectively, relative to G-B2.5 at 1, 3 and 7 days; however, the significance of this trend diminished with time (e.g. 6% increase at 28 days).

These trends can be explained by the thermal analysis data (**Figure 3.4**), which shows the calcium hydroxide (CH) contents in mixture G-N relative to that in the reference mixture G (without nano-silica) at different ages. At early-age, the normalized CH contents in mixture (G-N) relative to mixture G were 0.82, 0.64 and 0.52 at 1, 3 and 7 days, respectively. This improved performance can be ascribed to the contribution of nano-silica, which had ultrafine particles with specific surface of 80,000 m^2/kg. This catalyzed the hydration process via securing nucleation sites for the hydration products to precipitate on [14], as indicated by faster initial and final setting times. Moreover, the early consumption of CH (starting within 1 day) corresponded to the boosted pozzolanic reactivity of nano-silica at early-age that precipitated additional calcium silicate hydrate (C-S-H) gel in the matrix, even with the coexistence of high-volume slag in the binder. The slope of the normalized CH contents was almost constant between 28 and 90 days (average of 0.32), indicating a slow pozzolanic activity that can be attributed to the contribution of slag. In addition, nano-silica agglomerates have a physical contribution to the strength development of the matrix through its filling effect, and absorption of water within their nano-pores, leading to reduction in the content of free water within the paste [Kong *et al.*, 2012]. Thus, inclusion of 6% nano-silica mitigated the delay in hardening and strength development of the cementitious composites incorporating high-volume slag.

Addition of BFP to the nano-modified matrix decreased the compressive strength of the composites, especially with increasing the BFP dosage (4.5%). For instance, at 56 days the compressive strength of mixtures G-N-B2.5 and G-N-B4.5 were 6% and 21%, respectively, lower than that of the counterpart mixture G-N, which was 87 MPa. Statistical analysis by analysis of variance (ANOVA; **Table 3.4**) showed that this reduction in the compressive strength of composite was insignificant (F value of 5.7 vs. F_{cr} of 7.7) in the case of 2.5% BFP and significant (F value of 172.2 vs. F_{cr} of 7.7) in the case of 4.5% BFP. According to Montgomery (2017), if the F-distribution density function exceeds its critical value (F_{cr}), the tested variable has a significant effect on the mean value of the results. A similar trend was reported with the increase of basalt fiber mini-bars dosage (0.3, 1, and 2 % by volume) in normal strength concrete of 37 MPa [Branston *et al.*, 2016]. This behavior could be linked to the increase in air content of the matrix (**Table 3.3**) and the additional creation of interfacial transitional zones (ITZs), especially with higher dosages of BFP that acted as stress concentrators and weak links in the matrix, leading to reduction in compressive strength.

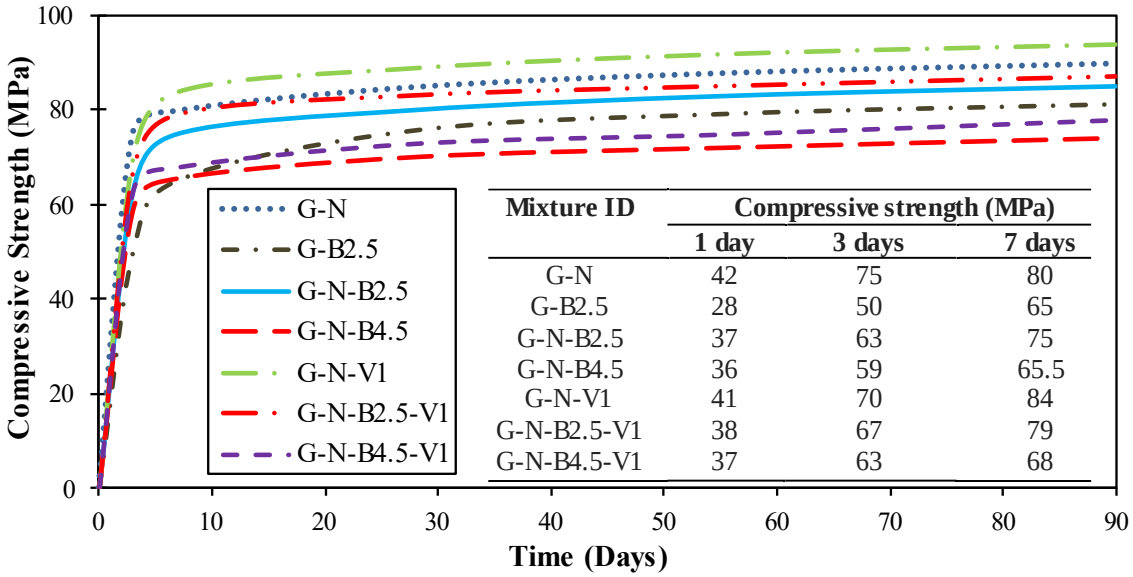
Comparatively, 1% PVA in the single fiber system (G-N-V1) led to increasing the compressive strength of the nano-modified composite compared to the corresponding composites without fibers or with single BFP. For instance, at 56 days, the compressive strength of mixture G-N-V1 was 5%, 11% and 27%, respectively higher compared with that of G-N, G-N-B2.5 and G-N-B4.5, with statistical significance relative to the mixtures incorporating BFP (**Table 3.4**). Previous studies typically used higher volumes of micro-PVA fibers (e.g. 2% by volume) to improve the mechanical properties of composites [Pan *et al.*, 2015; Li *et al.*, 2016]; however, a higher PVA dosage was not used here to avoid balling and clustering effects when adding PVA to BFP.

Regarding the hybrid system, 1 % micro-PVA fibers was used in combination with macro-BFP fibers to attain the required flowability of the composites. The compressive strength of G-N-B2.5-V1 and G-N-B4.5-V1 was improved compared with that of the corresponding mixtures without micro-PVA fibers (G-N-B2.5 and G-N-B4.5), with statistical significance (**Table 3.4**). Moreover, micro-PVA fibers led to changing the failure mode of the composites from abrupt crushing of the matrix to incremental development of macro-cracks, where the matrix remained intact after reaching its capacity (e.g. **Figure 3.5**). The positive effect of PVA on strength of composites can be attributed to its hydrophilic nature, resulting in reducing the *w/b* in the paste, especially at the ITZ with the cementitious matrix [Liu *et al.*, 2011]. In addition, hydroxyl groups (OH^-) on the PVA surface may have a potential for creating hydrogen bonds between molecules and forming new compounds at the boundaries with cement paste (chemical effect), leading to improving interfacial bonding with the matrix [Toutanji *et al.*, 2008; Noushini *et al.*, 2013]. Moreover. the bridging function of micro-PVA fibers can impede the nucleation and coalescence of micro-cracks in the matrix, acting as uniformly distributed reinforcing system in the composites, which was able to consume fracture energy as indicated by transforming failure of composites to a ductile mode.

Table 3. 4: ANOVA of the hardened and durability tests' results

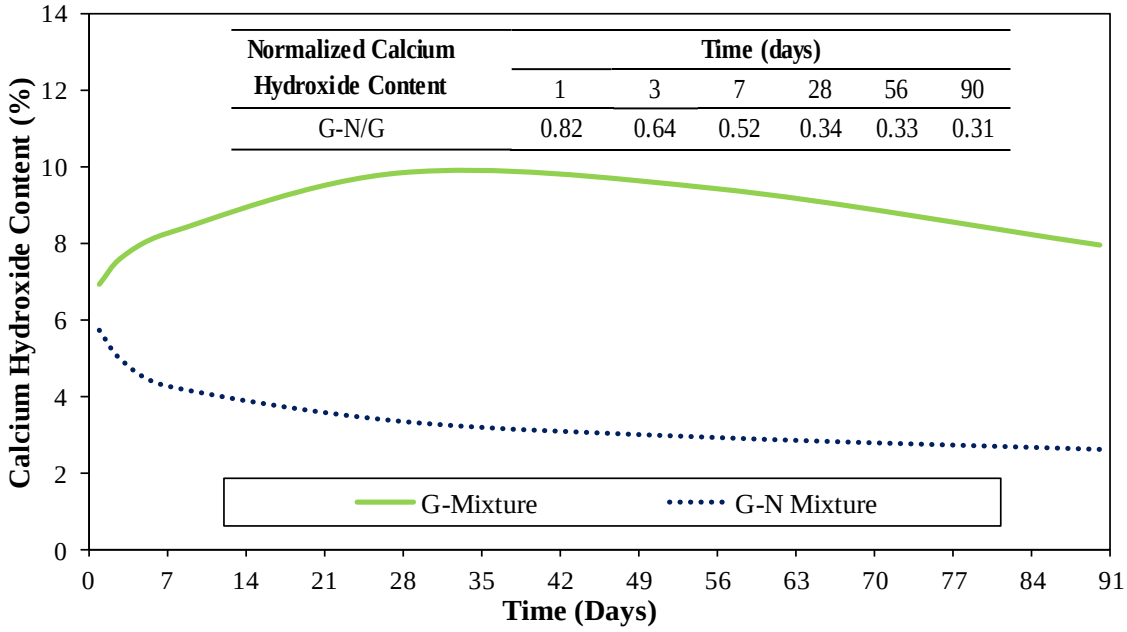
Comparative Parameters	Compressive Strength	First-Peak Flexural Strength	Toughness	Freeze/Thaw Resistance (*DF*)
		F-Values*		
Nano-silica				
G-B2.5 vs. G- N-B2.5	13.3$^{\alpha}$	101.9$^{\alpha}$	94. 7$^{\alpha}$	111. 5$^{\alpha}$
BFP				
G-N vs. G-N-B2.5	5.7	20.5$^{\alpha}$	591.4 $^{\alpha}$	96$^{\alpha}$
G-N vs. G-N-B4.5	172.2$^{\alpha}$	60.7$^{\alpha}$	711 $^{\alpha}$	273. 4$^{\alpha}$
G-N-B2.5 vs. G-N-B4.5	55.1$^{\alpha}$	87.3$^{\alpha}$	108.7$^{\alpha}$	40.7 $^{\alpha}$
PVA				
G-N vs. G-N-V1	5.4	1.3	222.3$^{\alpha}$	0.8
G-N-B2.5 vs. G-N-V1	139.3$^{\alpha}$	39.4$^{\alpha}$	337.5 $^{\alpha}$	108. 4$^{\alpha}$
G-N-B4.5 vs. G-N-V1	297.3$^{\alpha}$	113.2$^{\alpha}$	637.5 $^{\alpha}$	294$^{\alpha}$
Hybrid system				
G-N-B2.5 vs. G-N-B2.5-V1	8.9$^{\alpha}$	0.2	145.2$^{\alpha}$	24.3$^{\alpha}$
G-N-B4.5 vs. G-N-B4.5-V1	9.3 $^{\alpha}$	109.9$^{\alpha}$	156. 2$^{\alpha}$	118.1$^{\alpha}$

Notes: ANOVA for compressive strength, flexural strength and toughens were at 56 days.
*The critical value for the *F*-distribution density function (F_{cr}) was 7.7. $^{\alpha}$Denotes statistical significance.



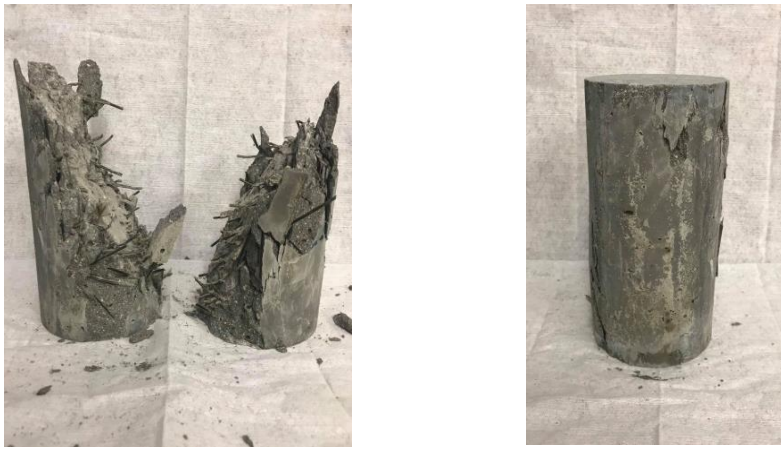
Mixture ID	Compressive strength (MPa)		
	1 day	3 days	7 days
G-N	42	75	80
G-B2.5	28	50	65
G-N-B2.5	37	63	75
G-N-B4.5	36	59	65.5
G-N-V1	41	70	84
G-N-B2.5-V1	38	67	79
G-N-B4.5-V1	37	63	68

Figure 3.3: Compressive strength of all composites vs. age



Normalized Calcium Hydroxide Content	Time (days)					
	1	3	7	28	56	90
G-N/G	0.82	0.64	0.52	0.34	0.33	0.31

Figure 3.4: TGA results for the CH contents (at a temperature range of 400°C to 450°C) in the mixtures. (G: slag-based binder, and G-N = nano-modified slag-based binder).



(a) (b)

Figure 3.5: Exemplar mode of failure of specimens after the compressive strength test at 56 days: (a) G-N-B2.5, and (b) G-N-B2.5-V1.

3.3.3 Flexural Strength

The flexural performance parameters (flexural strength, residual strength and toughness) for all composites are listed in **Table 3.5**, while **Figures 3.6** and **3.7** show representative load-deflection (P-δ) curves. Complying with the trends drawn from compressive strength, the inclusion of nano-silica in the binder led to noticeable increase in the flexural performance of composites. For instance, the first-peak flexural strength and toughness of mixture G-N-B2.5 increased by 41% and 34% respectively, compared with G-B2.5 (**Table 3.5**), with statistical significance (**Table 3.4**). This improvement can be explained by the functions of nano-silica in densifying the cementitious composites microstructure by producing additional C-S-H (pozzolanic effect) in addition to physically filling out the pore spaces in the paste.

Conforming to the trends of compressive strength, the addition of BFP to the nano-modified matrix decreased the first-peak flexural strength of the composites, especially with higher dosage of the macro-BFP. The first-peak flexural strength of G-N-B2.5 and G-N-B4.5 specimens were 33% and 50% respectively lower compared with that

of the reference mixture G-N (**Table 3.5**), with statistical significance (**Table 3.4)**. This can be linked to the higher content of air voids and intensity of ITZs, as discussed earlier, with increasing the BFP dosage. Comparatively, addition of PVA fibers to the composite (G-N-V1) led to achieving the highest first-peak flexural strength (11.1 MPa), which was 7%, 58% and 111% higher relative to that of mixtures G-N, G-N-B2.5 and G-N-B4.5, respectively (**Table 3.5** and **Figure 3.6**), with statistical significance relative to the mixtures comprising only BFP (**Table 3.4**). Moreover, using 1% micro-PVA fibers with macro-BFP forming hybrid system improved the first-peak flexural strength of composites by offsetting the adverse effects imparted by BFP, especially with the 4.5% BFP dosage. For example, the first-peak flexural strength of mixture G-N-B4.5-V1 was 46% higher compared with G-N-B4.5 (**Table 3.5** and **Figure 3.7**), with statistical significance (**Table 3.4**). As discussed earlier, this can be ascribed to the hydrophilic and chemical effects of the micro-PVA fibers, which improved the quality of the matrix especially at the ITZs and interfacial bonding. Moreover, the crack-bridging function of micro-PVA have potential for reducing stress concentration at the tips of micro-cracks, thus delaying the coalescence of these cracks in the cementitious matrix, and consequently increasing its first-peak flexural strength [Liu *et al.*, 2011; Thong *et al.*, 2016].

After the first-peak load, the load-deflection curves of the composites reinforced with fibers exhibited mixed trends depending on the type and dosage of fibers. Regarding the mixture reinforced with single PVA fibers (G-N-V1), which had the highest flexural strength, it did not show appreciable ductility after the first-peak cracking and fractured in a brittle manner (**Figure 3.6**), with R_i and toughness of 0.15 and 15.5 J, respectively. This behavior might be ascribed to the low dosage of micro-PVA fibers relative to the

critical dosage (2% by volume) utilized in previous research [Li *et al.*, 2001; Xu *et al.*, 2011]. Conversely, after a sudden load reduction up to a deflection of approximately 0.2 mm (**Figure 3.6**), mixtures comprising single BFP continued to resist the load progressively up to the target deflection limit (2 mm). For instance, G-N-B2.5 showed a post-cracking plateau (R_i of 0.64), whilst G-N-B4.5 exhibited a deflection-hardening trend (R_i of 1.1) with 33% higher toughness relative to G-N-B2.5 (**Table 3.5**).

The post-cracking behavior of composites reinforced with BFP can be ascribed to the high tensile capacity associated with reasonable modulus of elasticity of BFP that efficiently mitigated the propagation of macro-cracks in the composites and carried the load capacity till reaching a second peak load, especially in the case of 4.5% dosage due to the abundance of the pellets in the failure plane at the middle-third span of the specimens. In addition, the composites comprising BFP benefited from improved bonding between the pellets and matrix, owing to the high contact surface area of the textured longitudinal micro-grooves. This trend was verified by SEM and EDX [e.g. **Figures 3.8(a)-(c)**] which showed the deposition of hydration products in these grooves cross-linking BFP and matrix; the average *Ca/Si* for the cement gel at the interface had a lower value (1.18) compared to the conventional C-S-H typically generated from the hydration reaction of cement (1.7) [Detwiler *et al.*, 1996], which suggested that it was generated from the efficient pozzolanic effect induced by nano-silica to the slag-based binder, conforming to the TG results (**Figure 3.4**). Furthermore, there was no degradation observed on the pellets' surface due to the protective role of the polyamide resin from the surrounding alkaline matrix.

Regarding the mixtures reinforced with the hybrid system (PVA/BFP), it was observed that there was a minimum reduction in the bearing load; subsequently, they

continued to carry significant load till reaching the designated deflection, relative to the corresponding mixtures comprising single BFP. For instance, specimens from mixture G-N-B4.5-V1 showed a pseudo deflection-hardening behavior (R_i of 1.4), as depicted in **Table 3.5** and **Figure 3.7**. Correspondingly, the toughness of mixtures G-N-B2.5-V1 and G-N-B4.5-V1 were 61% and 46%, respectively higher relative to that of mixtures G-N-B2.5 (40.3 J) and G-N6-B4.5 (30.3 J), with statistical significance (**Table 3.4**). This enhancement can be ascribed to the interaction and synergistic effects of the randomly distributed micro-PVA fibers and macro-BFP (e.g., **Figure 3.9)**, as the former constrained the coalescence and nucleation of micro-cracks and the latter restrained macro-cracks propagation in the matrix, thus enhancing the composites' ductility.

Table 3.5: Flexural properties of the cementitious composites at 56 days

Mixture ID	First-Peak Strength (MPa)	Residual Strength at *L/600* (MPa)	Residual Strength at*L/150* (MPa)	Residual Post-Cracking index (R_i)	Toughness (J)
G-N	10.7	--	--	--	1.8
G-B2.5	5.1	4.1	3.4	0.95	22.7
G-N-B2.5	7.2	4.3	4.5	0.64	30.3
G-N-B4.5	5.4	4.8	5.1	1.10	40.3
G-N-V1	11.4	3.0	0.2	0.15	15.5
G-N-B2.5-V1	7.8	8.2	6.6	0.98	48.8
G-N-B4.5-V1	7.9	9.8	8.2	1.40	58.9

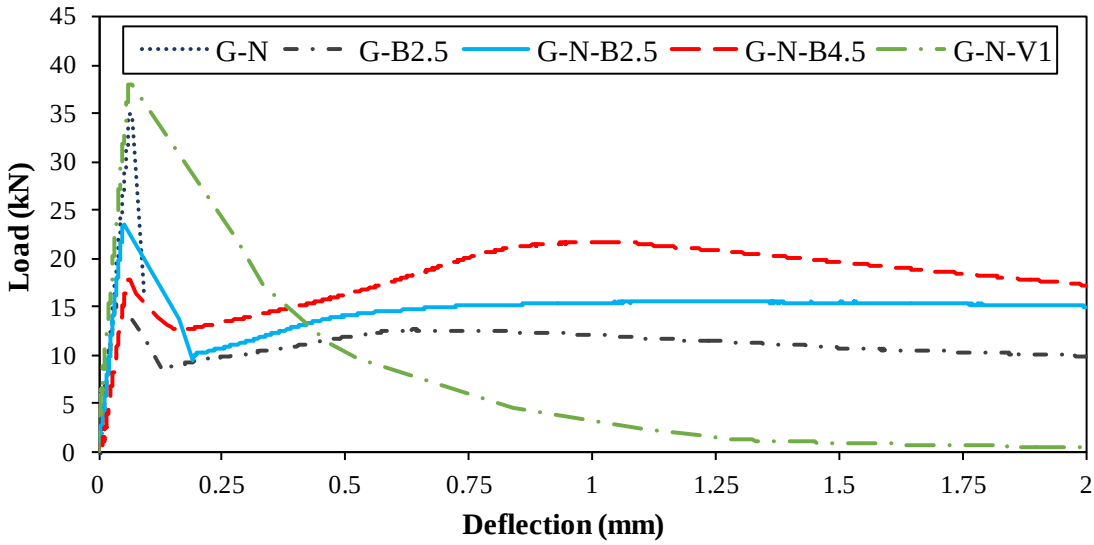


Figure 3.6: Load-deflection (P-δ) curves for the composites with a single fiber system.

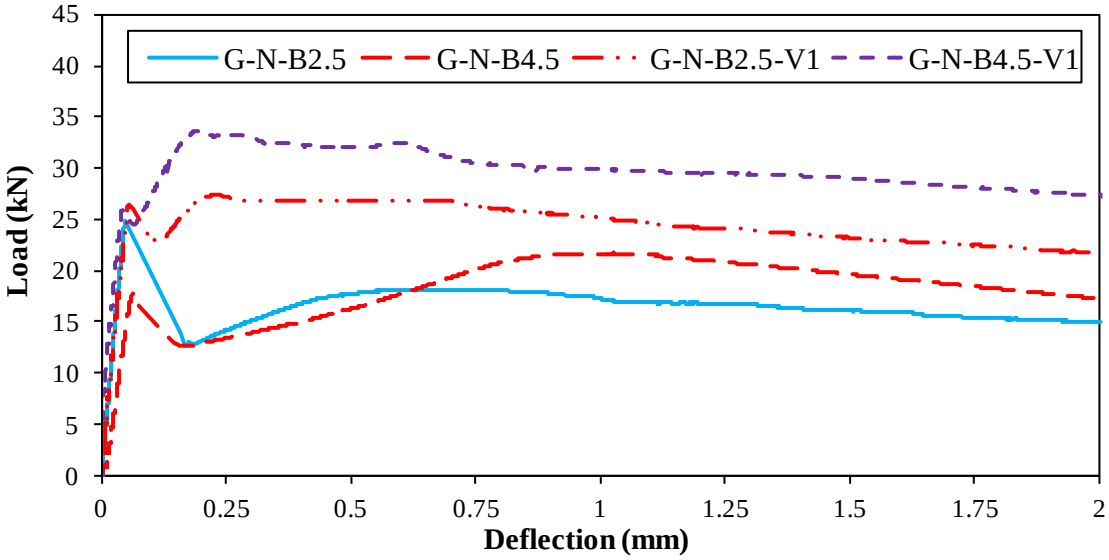
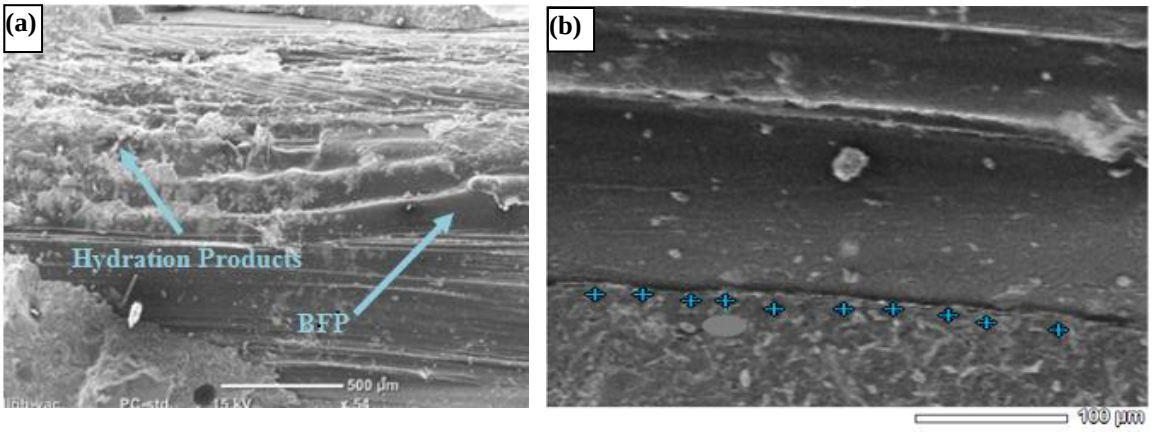
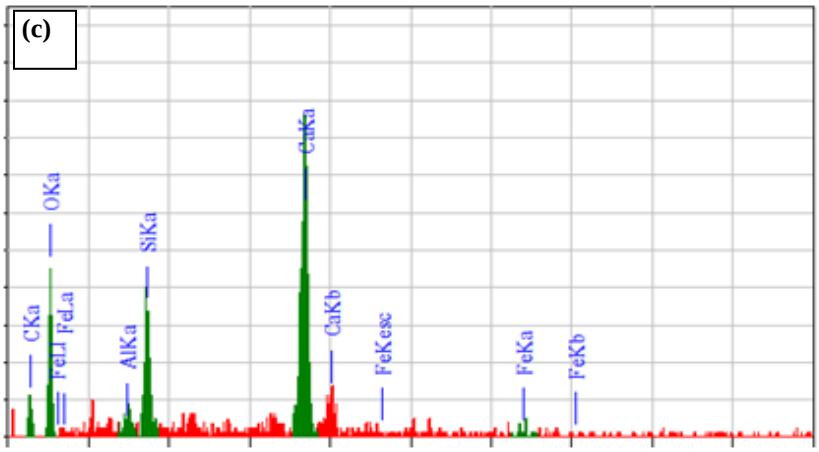


Figure 3.7: Comparison of load-deflection (P-δ) curves for the composites reinforced with BFP (single fibers) and BFP with PVA fibers (hybrid fibers).





Element	C	O	AL	Si	Ca	Fe	Mean Ca/Si	SE N=10
Atomic Weight %	14.44	71.50	1.33	5.22	6.17	0.74	1.18	0.07

Figure 3.8: SEM images for G-N-B2.5 at 56 days showing: (a) hydration products in the longitudinal grooves of BFP, (b) magnified image for the area indicated in (a), and (c) EDX spectrum of the paste at the locations indicated in (b).

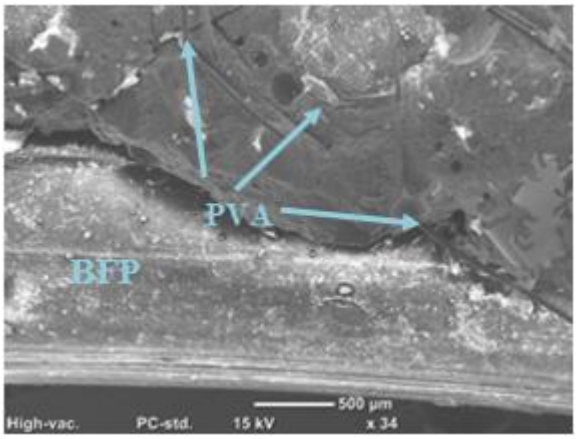


Figure 3.9: Interaction of BFP with PVA in G-N-B2.5-V1.

3.3.4 Resistance to Frost Damage

The relative dynamic modulus of elasticity (RE_d) and the durability factor (*DF*) were calculated to assess possible risk of frost damage of composites, which intentionally did not comprise an air entraining agent, to clearly capture the effects of nano-silica and fibers/pellets on the matrix. **Figure 3.10** shows the results of RE_d and *DF* of the composites, and **Table 3.6** summarizes the MIP results characterizing the pore structure of these composites before being exposed to freezing-thawing cycles.

Conforming to the trends of hardened properties, the inclusion of nano-silica in the base binder had conspicuous effect on increasing the durability of composites. For instance, specimens from mixture G-N, which had a low air content of 3.4%, achieved the highest *DF* of 93% after 300 cycles. This superior performance can be ascribed to the mixture design of this nano-modified binder, which incorporated 50% cement, 50% slag and 6% nano-silica at a low *w/b* (0.3), resulting in efficient hydration and pozzolanic reactivity (**Figure 3.4**) and high strength (**Figure 3.3, Table 3.5**). This matrix had refined pore structure (**Table 3.6**; low porosity: 10%, low threshold pore diameter: 0.08 μm, and high proportion of micro-pores: 58%). Correspondingly, incorporating nano-silica in mixture G-B2.5 to produce mixture G-N-B2.5 increased the number of accommodated freezing/thawing cycles from 130 to 200 to reach the the 60% RE_d failure limit stipulated by ASTM C666 (**Figure 3.10**), with statistical significance (**Table 3.4**). This complied with the improved pore structural features of mixture G-N-B2.5 relative to that of mixture G-B2.5 (**Table 3.6)**, The synergistic pozzolanic and filler effects of nano-silica produced denser matrix, which discounted the penetrability of water and consequent saturation of cement paste, thus increasing the resistance of specimens to frost damage.

Despite improving the post-cracking flexural performance, addition of BFP to the nano-modified matrix adversely affected the resistance of composites to frost damage. For instance, specimens from G-N-B2.5 and G-N-B4.5 had low *DF* of 41% and 33% after 200 and 165 cycles, respectively (**Figure. 3.10**), with statistical significance (**Table 3.4**). The MIP results showed that the pore structural features were altered with increasing BFP dosage in the matrix. For example, increasing the BFP dosage in mixture G-N-B2.5 to produce mixture G-N-B4.5, increased the total porosity and threshold pore diameter by 22% and 47%, respectively, and reduced the proportion of micropores by 25% (**Table 3.6**). This corresponded to the observed increase in fresh air contents and creation of additional of ITZs zones between macro-size pellets and mortar, which reduced the compressive and flexural capacities. Thereby, the mixtures comprising single BFP had coarser pore structure (**Table 3.6**), with more susceptibility to fluid penetration, saturation, and damage by frost action.

Comparatively, the nano-modified composite reinforced single micro-PVA (G-N-V1) fibers had high resistance (*DF* of 92% after 300 cycles) to freezing–thawing cycles. This can be ascribed to maintaining the quality of the matrix, due to the hydrophilic and chemical effects of PVA as discussed earlier, as suggested by the comparable pore structural features of G-N-V1 to that of the corresponding nano-modified binder without fibers (G-N) [**Table 3.6]**. Moreover, adding 1% micro-PVA fibers to macro-BFP (hybrid system) offset the adverse effects imparted by the pellets on the frost resistance of the composites. For instance, adding 1% micro-PVA fibers in mixture G-N-B4.5 to produce mixture G-N-B4.5-V1 significantly increased the *DF* from 33% to 82%, with statistical significance (**Table 3.4**). This improvement could be attributed to the potential effect of PVA fibers on shifting the characteristics of pore structure from coarse to fine. For

example, the total porosity of mixture G-N-B4.5-V1 (hybrid system) increased by 9% relative to that of mixture G-N-B4.5 (single BFP), which corresponded to the increase in air content (**Table 3.3**); however, its threshold pore diameter and proportion of micro-pores decreased and increased, by 57% and 63%, respectively. This suggested that randomly distributed micro-PVA fibers interrupted the coarser pore network resulting from the addition of BFP, which led to more discrete network with larger proportion of micro-pores. Thus, the higher tortuosity of this pore structure could discount fluid penetration and saturation of the specimens; in addition, the role of micro-PVA fibers on impeding the nucleation of micro-cracks, resulting from the aggravated freezing-thawing cycles, in the matrix led to improving the durability of composites comprising hybrid fibers to frost action.

Table 3.6: Summary of MIP test results at 56 days

Mixture ID	Apparent Total Porosity (%)	Threshold Pore Diameter (μm)	Proportion of Micro-pore (<0.1 μm)
G-N	10.0	0.08	58
G-B2.5	13.5	0.67	30
G-N-B2.5	12.1	0.43	40
G-N-B4.5	14.8	0.63	30
G-N-V1	10.5	0.10	59
G-N-B2.5-V1	14.1	0.21	52
G-N-B4.5-V1	16.1	0.27	49

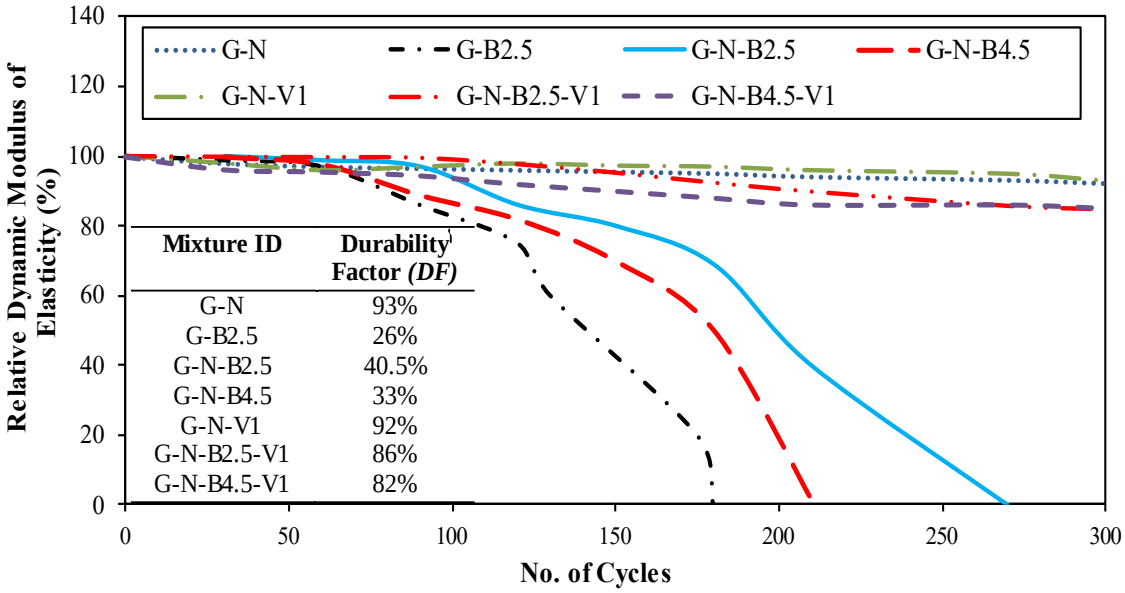


Figure 3.10: Relative dynamic modulus of elasticity (RE_d) of all composites vs. number of freezing-thawing cycles.

CHAPTER 4: INTERFICIAL BONDING BASALT FIBER/POLYMER PELLETS AND VARIOUS NANO-MODIFIED CEMENTITIOUS MATRICES

In Chapter 3, the fresh, mechanical and durability properties, of nano-modified cementitious composites comprising high-volume slag and reinforced with single BFP and hybrid PVA/BFP fiber systems were investigated to study the potential of employing the developed composites in jointing applications. The cementitious composites reinforced with hybrid PVA/BFP showed promising performance in terms of mechanical and durability properties. In this chapter, the synergetic evaluation of the flexural performance and single pellet pull-out of BFP in homogenized nano-modified (nano-silica, NS; nano-crystalline cellulose, NCC) cementitious matrices, without/with micro- (polyvinyl alcohol fibers, PVA) or nano-fibers (nano-fibrillated cellulose, NFC) were investigated. Thus, integrated experimental (flexure, single pellet pull-out, thermogravimetry, microstructure) and modeling (homogenization/FEM) approaches were conducted to evaluate the effect of BFP interfacial bonding with various nano-modified cementitious matrices.

4.1 Introduction

Deterioration of concrete infrastructure (e.g. pavements, bridges, etc.) is commonly associated with excessive cracking due to various loading, chemical and environmental schemes. The low toughness of ordinary concrete motivated the advent of high-performance fiber-reinforced cementitious composites (HPFRCC) [e.g. Yang *et al.*, 2010;

Elhadary, R. and Bassuoni, M.T., 2023. Interfacial Bonding between Basalt Fiber/Polymer Pellets and Various Nano-Modified Cementitious Matrices. *Journal of Materials in Civil Engineering*, 35(3), p.04022471-18.

Ranade *et al.*, 2013; Bandelt and Billington, 2016] to control cracking and hence extend the service life of infrastructural elements. HPFRCC typically exhibit ductile post-cracking behavior under tension and flexural loadings depending on key mixture design parameters. Different types of binders incorporating General Use cement (GU), slag, fly ash, nano-silica, etc. and a range (0.25 to 0.35) of water-to-binder ratios (*w/b*) have been used with various geometries and types of fibers (e.g. polyvinyl alcohol [PVA], steel, nano-fibrillated cellulose [NFC]) to produce HPFRCC [e.g. Pan *et al.*, 2015; Meng *et al.*, 2017; Da Costa Correia *et al.*, 2018].

Different types of ultrafine nanoparticles (e.g. nano-silica, nano-crystalline cellulose) have been incorporated in HPFRCC to modify microstructure and enhance hardened properties. For instance, addition of 6% nano-silica by mass to cement-based binders without/with supplementary cementitious materials creates additional nucleation sites for precipitation of hydration products [Kong *et al.*, 2012; Said *et al.*, 2012], accelerates the pozzolanic reactivity [Kong *et al.*, 2012, Ghazy *et al.*, 2016b], and enhances particle packing (filler effect) in the hardened paste. Also, it reduces *w/b* in the paste due to water absorption into its ultrahigh surface porosity. Incorporation of 0.5% NCC by mass of cementitious binders positively affects the microstructural evolution of hardened paste. Its hydrophilic nature and chemical reactivity with cement paste through its hydroxyl groups (OH^-) led to additional deposition of hydration products in the matrix [Jongvisuttisun *et al.*, 2013; Hoyos *et al.*, 2013; Cao *et al.*, 2015]. In addition, NCC in the form of spindle shapes might be able to impede the nucleation of nano-cracks in the matrix [Flores *et al.*, 2017; Fu *et al.*, 2017].

Many studies utilized hybrid fiber systems in HPFRCC, as their performance exceeds that of individual fiber components [e.g. Dawood and Ramli, 2011; Park *et al.*,

2012]. For example, in binary-scale fiber systems, micro-fibers counteract coalescence of micro-cracks, while macro-fibers restrain the growth of macro-cracks in the matrix [Zhang and Cao, 2014; Sindu and Sasmal, 2019; Elhadary and Bassuoni, 2021]. Hence, various types and sizes of metallic, synthetic, and natural fibers have been used to improve the plastic and hardened properties of HPFRCC. For instance, micro-PVA and NFC fibers have been used in cement-based composites because of their hydrophilic nature and potential for impeding nucleation of cracks in the matrix [Liu *et al.*, 2011; Jongvisuttisun *et al*., 2013]. PVA fibers have a tensile capacity up to 1600 MPa, with a moderate modulus of elasticity (up to 66 GPa) [Li *et al.*, 2001]; the typical dosage of PVA micro-fibers is 2% by volume of the composite to yield a strain hardening behavior [Li *et al.*, 2001]. NFC consists of cellulose bundles of micrometric length (100-2000 µm), nanometric diameter (30-400 nm) and high aspect ratios (average of 1000). They typically exhibit moderate tensile strength (up to 120 MPa) and low modulus of elasticity (up to 11 GPa) [Hisseine *et al.*, 2018]. Few studies reported that the incorporation of 0.1 to 0.2% NFC by volume of cementitious binder improved the compressive strength (up to 16%), flexural strength (up to 22%), and splitting tensile strength (up to 34%) of ordinary strength mortar/concrete [Onuaguluchi *et al.*, 2014; Hisseine *et al.*, 2018; Hisseine *et al.*, 2019]. However, there is still dearth of information on the use of NFC in various HPFRCC applications, including its interaction with other types of fibers.

Macro-basalt fibers have emerged in concrete research since last decade, owing to their high tensile strength (up to 4,000 MPa), adequate modulus of elasticity (93-110 GPa), high thermal and corrosion resistances, and lower cost compared with other alternatives such as glass and carbon fibers [Ayub *et al.*, 2014; Iyer *et al.*, 2015; Arslan *et al.*, 2016; Iyer *et al.*, 2016; Ghazy *et al.*, 2016a]. While basalt fibers initially have

adequate bonding with the cementitious matrix, this bond diminishes within a relatively short period of time (approximately 90 days) due to alkali-silica reactions between the pore solution and silicate component of basalt [Jiang *et al.*, 2014]. This motivated the development of a new fiber type termed (BFP), where basalt fiber strands are encapsulated with a polymeric resin (e.g. polyamide [Mahmoud *et al.*, 2017]) for protection against alkaline media. Yet, research on the use of BFP in HPFRCC is still at early stages.

For fundamental understanding of the performance of HPFRCC, characterization of fiber/matrix interaction is of outmost concern. The fiber/matrix interfacial bonding is a governing factor for bridging cracks and progressive load transfer mechanisms. Various experimental (e.g., pull-out tests) and analytical (e.g., homogenization [Mori and Tanaka, 1973], generalized self-consistency [Christensen and Lo, 1979]) methods have been used to determine/predict the fiber/matrix interfacial bonding [Laranjeira *et al.*, 2010; Al-Jaberi *et al.*, 2018; Sui *et al.*, 2018; Al-Jaberi and Myers, 2019]. The fiber type, strength, orientation, geometry, and volume fraction as well as matrix properties, service temperature and displacement rate are among the key parameters affecting fiber/matrix adhesion. For instance, the bonding capacity, ultimate slip, and energy consumption capacity of fiber-reinforced polymer (FRP) with engineered cementitious composites (ECC) and concrete interface improved with the addition of an ECC layer comprising PVA fibers (2% by volume); ECC has efficient crack control capabilities that delayed the debonding of FRP and enhanced the bearing capacities of FRP-strengthened structures [Sui *et al.*, 2018]. Al-Jaberi et al. [2019] investigated the effect of service temperature on the FRP-epoxy bond system and fiber-reinforced cementitious matrix (FRCM) bond system on strengthening structural elements. It was reported that there was a high

reduction in FRP-epoxy bond properties when exposed to high service temperature, compared with the FRCM bond system. The reduction of the FRP-epoxy bond was linked to rapid deterioration of the epoxy-substrate adhesion when the temperature was close to or exceeded the heat distortion temperature of the epoxy [Al-Jaberi *et al.*, 2019; Al-Jaberi and Myers, 2019]. Moreover, Azzam *et al.* [2021] investigated the effect of displacement rate and type of binder on the single BFP interfacial bonding with matrix, and the highest results were obtained with the high displacement rate (50 mm/min) and nano-modified based slag matrix [Azzam *et al.*, 2021]; however, no other types of fibers were included in these matrices. Also, Azzam *et al.* [2022] evaluated the bond behaviour of nano-modified cementitious composites comprising single dosages of BFP in terms of their flexural configurations with/without pre-cracked substrate concrete. The cementitious composites showed efficient integrity with the intact substrate concrete layer, where the two layers behaved monolithically under the applied flexural loading, without any signs of transverse delamination [Azzam *et al.*, 2022]. With experimental characterization, finite element modeling (FEM) can encompass various analytical methods to simulate heterogeneous composites through optimizing the critical representative volumetric element (RVE) and representation of the thin layer between inclusion (fiber) and surrounding matrix (i.e. interfacial transition zones [ITZs]) [Teng *et al.*, 2007; Sun *et al.*, 2007]. This integrated approach can be effectively used to study innovative HPFRCC comprising BFP to capture its bonding characteristics with different matrices.

4.1.1 Research Significance

The constant demand for resilient cementitious composites in various infrastructural applications prompts continual research efforts to produce innovative composites

exploiting recent advancements in materials manufacturing. Ongoing research at the University of Manitoba led to developing nano-silica modified cementitious composites with high-volume slag and reinforced with single BFP [Mahmoud *et al.*, 2017; Azzam *et al.*, 2019; Azzam *et al.*, 2021] or hybrid BFP/PVA systems [Elhadary and Bassuoni, 2021]. These composites showed improved hardened and durability properties including high ductility, high performance under extreme loadings (e.g. direct tension, impact) and resistance to ingress of fluids and frost action without/with deicing salts. Yet, focused research is still needed on other aspects such as exploring the effect of nano-modified cementitious composites comprising various matrices and fibers on the BFP/matrix interfacial bonding characteristics. Such data is crucial to identify the functionality of these composites for safe and resilient use in various applications. Hence, the primary objective of the current study was to evaluate the interaction of BFP with different nano-modified (nano-silica, NCC) cementitious matrices comprising high volume-slag without/with micro- or nano-fibers (PVA, NFC) using integrated experimental (flexure, single pellet pull-out, thermogravimetry, microstructure) and modeling (homogenization/FEM) approaches.

4.2 Experimental Program

4.2.1 Materials and Mixtures

General use cement (GU) and Grade 100 slag meeting CSA-A3001 [2018] requirements were used as the main components of the base binder (700 kg/m^3). Two different types of nanoparticles were used as additives to the base binders: 6% nano-silica solution (NS) or 0.5% nano-crystalline cellulose powder (NCC) by mass of the base binder. The NS solution comprises 50% SiO_2 particles well dispersed in an aqueous solution, with a

specific surface area of 80,000 m^2/kg, mean particles size of 35 nm, and density of 1.1 g/cm^3. It was reported that 6% of this NS solution had a positive effect at improving the pore structure and hardened properties of concrete comprising supplementary cementitious materials [Ghazy *et al.*, 2016b; Mahmoud *et al.*, 2017]. The NCC powder has a specific surface area of 430,000 m^2/kg, 5-40 nm width, 50-800 nm length, and density of 1.5 g/cm^3. According to previous studies [Cao *et al.*, 2016; Flores *et al.*, 2017; Fu *et al.*, 2017], 0.5% NCC by mass of the binder had favorable effects on the hardened properties of mortar/concrete.

Fine aggregate with continuous gradation of 0 to 600 μm was used in the mixtures, and its fineness modulus, absorption and specific gravity were 2.9, 1.5% and 2.6, respectively. In order to improve the workability of all mixtures, poly-carboxylic high-range water reducer (HRWR), complying with ASTM C494 Type F [2017], was used at a dosage of 100 to 150 ml per 10 kg of binder to achieve a constant flow table diameter of 180±20 mm. Three different types and sizes of fibers were used to reinforce the mixtures: NFC (nano-fibers), PVA (micro-fibers) and BFP (macro-fibers) [**Figure 4.1**]. The properties and dosages of the fibers are summarized in **Table 4.1**. These dosages were selected based on the ranges reported in previous studies [e.g. Cao *et al.*, 2016; Hisseine *et al.*, 2019; Sindu and Sasmal, 2019] for improving the hardened properties of concrete/composites.

Fourteen mixtures were prepared at 0.30 *w/b* with 50% cement and 50% slag (base binder: 700 kg/m^3) meeting the requirements of high-volume supplementary cementitious materials (HVSCM-1) concrete in Annex K, CSA 23.1 [2019]. Nano-modified binders comprised either 6% NS or 0.5% NCC by mass of base binder. Mixtures reinforced with the single fiber systems comprised either 2.5% BFP, 4.5% BFP (by volume of

composite), 1% PVA (by volume of composite), or 0.2% NFC (by volume of binder), while mixtures reinforced with the hybrid systems included 2.5% or 4.5% BFP combined with either 1% PVA or 0.2% NFC. The proportions of all mixtures are listed in **Table 4.2**. For the mixtures' IDs, the letters G, N, NCC, NFC, V and B refer to slag, nano-silica, nano-crystalline cellulose, nano-fibrillated cellulose, polyvinyl alcohol fibers and basalt fiber pellets, respectively, while the numbers indicate the dosage of fibers.

The NS sol or NCC powder was directly dispersed into the mixing water using a homogenizer at 2000 rpm for 4 min. Initially, the dry constituents (sand, cement, slag) were added to a concrete pan mixer (60 rpm), followed by gradual addition of required mixing water containing either NS sol or NCC with half the amount of HRWR while constantly mixing until the homogeneity of the mixture was achieved. In mixtures comprising NFC, the NFC was dispersed into one half of the required mixing water using a homogenizer at 3000 rpm for 10 min; all the dry constituents were mixed with a gradual addition of the first half of mixing water containing NCC with half amount of HRWR, followed by addition of the remaining half of mixing water comprising NFC. PVA and/or BFP were added last with the remaining amount of HRWR, and the ingredients were mixed for additional 8 to 10 min to achieve uniform distribution of fibers. After casting the composites in moulds, all specimens were consolidated using a vibrating table. Polyethylene sheets were used to cover the surface of the specimens for 24 h. Subsequently, the specimens were demolded and cured in a standard room maintained at a 22±2°C and a relative humidity of more than 95% until testing.

Table 4.1: Properties of fibers

Property	NFC	PVA	BFP
Length (mm)	100×10^{-3}	12	36
Diameter/width (mm)	80×10^{-6}	38×10^{-3}	1.8
Aspect ratio	1250	315	20
Specific gravity	1.5	1.3	1.7
Tensile strength (MPa)	115	1600	2,300
Elastic modulus (GPa)	12	66	65
Volume fraction [V_f] (%)*	0.2	1	2.5, 4.5

*NFC is expressed by volume of binder, whereas PVA and BFP are expressed by volume of composite.
*The mechanical properties of BFP (macro-fiber), PVA (micro-fiber), and NFC (nano-fiber) was provided by the manufacturers

4.2.2 Testing

The flexural strength and post-cracking behavior of composites at 56 days were determined using triplicate prisms (100×100×350 mm) for each mixture in **Table 4.4**, according to ASTM C1609 [2019] in a four-point bending configuration. A servo controlled closed-loop testing machine was used at an average displacement rate of 0.075 mm/min up to L/900 net mid-span deflection of the prisms, and 0.2 mm/min beyond deflection of L/900, according to ASTM C1609 [2019]. The flexural toughness was calculated as the area under the load-deflection curve (P-δ) up to a deflection of span/150 (2 mm) using the trapezoidal rule described in Al-khafaji et al. [1986], and the residual strength (R_S) was calculated according to **Equation 4.1** [2019], where, $P_{0.5}$ and P_2 are the residual strengths at deflections 0.5 mm (*L/600*) and 2 mm (*L/150*), respectively and P_{cr} is the peak strength at first-cracking.

$$R_S = \frac{P_{0.5}\ or\ P_2}{P_{cr}} \qquad \textbf{(Equation 4.1)}$$

To evaluate the flexural post-cracking stage of the composites reinforced with either 2.5% or 4.5% of BFP through the interfacial characteristics between BFP and matrix, the single pellet pull-out test was conducted for G, G-N, G-NCC, G-N-V1, and G-NCC-NFC matrices at 56 days. Six replicate blocks (100×100×50 mm) including a single

Table 4.2: Mixtures proportions per cubic meter

Mixture ID	Cement (kg)	Slag (kg)	Water* (kg)	NS (kg)	NCC (kg)	Fine Aggregate (kg)	NFC (kg)	PVA (kg)	BFP (kg)	Air Content (%)	Compressive Strength (MPa) at 56 days
G-B2.5	350	350	210	--	--	1288	--	--	43.3	6.9	79 ± 2.7
G-N-B2.5	350	350	180	84	--	1167	--	--	43.3	6.5	83 ± 3.0
G-N-B4.5	350	350	180	84	--	1115	--	--	78.3	7.4	72 ± 2.3
G-N-V1-B2.5	350	350	180	84	--	1142	--	13	43.3	7.4	85 ± 3.4
G-N-V1-B4.5	350	350	180	84	--	1090	--	13	78.3	8.2	75 ± 2.6
G-NCC-B2.5	350	350	211	--	3.5	1279	--	--	43.3	6.3	86 ± 3.6
G-NCC-B4.5	350	350	211	--	3.5	1226	--	--	78.3	7.2	74 ± 2.4
G-NCC-B2.5-NFC0.2	350	350	208	--	3.5	1279	3.5	--	43.3	6	90 ± 3.2
G-NCC-B4.5-NFC0.2	350	350	208	--	3.5	1228	3.5	--	78.3	6.8	83 ± 3.2

*Adjusted amount of mixing water considering the water content of NS (50% solid content) or NFC (20% solid content).



Figure 4.1: Fiber type: (a) NFC, (b) PVA, and (c) BFP.

BFP, with an embedded length of 18 mm in the middle of the blocks (**Figure 4.2**), were tested for each matrix. The displacement rate was 0.2 mm/min, in order to match the range used in the flexural tests [Azzam *et al.*, 2021].

BFP, with an embedded length of 18 mm in the middle of the blocks (**Figure 4.2**), were tested for each matrix. The displacement rate was 0.2 mm/min, in order to match the range used in the flexural tests [Azzam *et al.*, 2021].

Thermal and microstructural tests were performed to corroborate the trends obtained from the bulk tests. Thermogravimetric analysis (TGA) was conducted at a constant heating rate of 10°C/min on powder samples, obtained from pulverized chunks passing Sieve #200 [75 μm], to determine the calcium hydroxide (CH) quantities in the various matrices up to 90 days. The portlandite content was calculated by determining the decrease of the ignited mass percentage in a temperature range from 400°C to 450°C, and multiplying the result by 4.11 (the ratio of the molecular mass of CH to that of water). Scanning electron microscopy (SEM) with elemental dispersive X-ray (EDX) was carried out at 56 days on extracted fracture pieces comprising BFP and adjacent matrix to capture morphological features at the ITZ. First, the fracture samples were coated with carbon to improve their conductivity for imaging. Subsequently, it was mounted in the SEM chamber under the high-vacuum mode (10^{-4} Pa), where the accelerating voltage and working distance were 15 kV and 18 mm, respectively. The features of pore structure for the different matrices were determined at 56 days by mercury intrusion porosimetry (MIP). Six pea-sized (4 to 7 mm) chunks taken from at least two concrete cylinders from each mixture were used as test samples. Preconditioning of samples was carried out by oven drying at 50±2°C and silica gel until a constant mass was achieved; this procedure was adopted to reduce the potential of drying shrinkage cracks and decomposition of

some hydration products associated with higher temperatures. The apparatus has a pressure range from sub-ambient to 228 MPa. By assuming a cylindrical geometry of pores, a mercury contact angle of 130° and surface tension of 0.485 N/m, the high-pressure limit (228 MPa) yields a pore radius of about 3 nm, implying intrusion of all capillary pores.

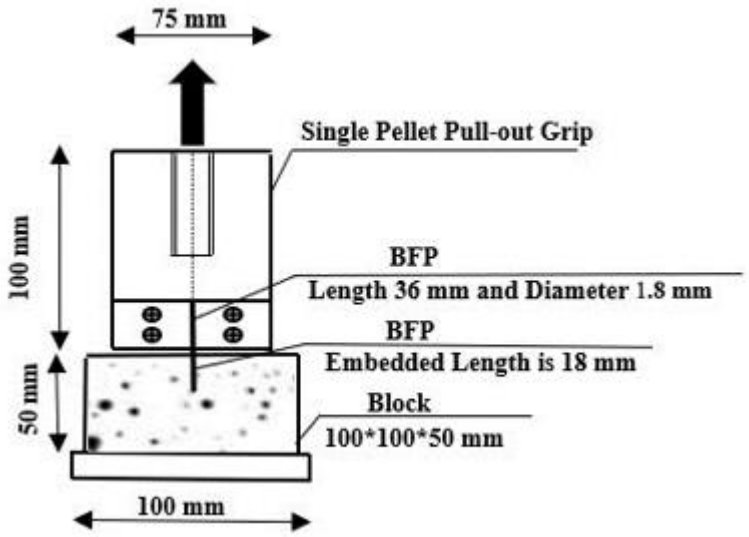


Figure 4.2: Single pellet pull-out test set-up.

4.3 Finite Element Modeling

4.3.1 Phase I: Homogenization Method

4.3.1.1 Theoretical Formulation

The classical elastic-plastic damage model for concrete is widely used in FEM [Lubliner *et al.*, 1989; Li and Li *et al.*, 2019]. This method was adopted herein to model the behavior of different matrices without fiber inclusions (G, G-N, and G-NCC). The bond between different materials in each matrix (i.e., cement, slag, fine aggregate, nano-particles, and water) without nano/micro-fibers inclusions are considered as one unit element [Li and Li *et al.*, 2019]. The tensile stress-strain relationship of the matrix can be

expressed by **Equation 4.2,** whereas the plastic tensile strain can be determined from **Equation 4.3** [Balamirzoev *et al.*, 2021], which reduces to ε_t^{ck} in case of no damage to concrete.

$$\sigma_t = (1 - [dt])\, E_o\, (\varepsilon_t - \varepsilon_t^{pl}) \qquad \textbf{(Equation 4.2)}$$

$$[d_t] = \begin{cases} 0 & \varepsilon < \varepsilon_o \\ 1 - e^{-b(\varepsilon - \varepsilon_o)^g} & \varepsilon \geq \varepsilon_o \end{cases}$$

$$\varepsilon_t^{ck} = \varepsilon_i - \varepsilon_o = \varepsilon_i - \frac{\sigma_o}{E_o}$$

$$\varepsilon_t^{pl} = \varepsilon_t^{ck} - \frac{d_t}{(1-d_t)} \frac{\sigma_t}{E_o} \qquad \textbf{(Equation 4.3)}$$

where, σ_t and ε_t are the axial tensile stress and strain, respectively, σ_o , E_0 are the maximum tensile stress and initial modulus of elasticity of intact material, [d_t] is the damage evolution parameter, ε_o, ε_t^{ck} , ε_i , and ε_t^{pl} are the peak-critical strain, cracking strain, crack-deformation strain, and plastic strain, respectively, b is the coefficient parameter of how quickly the damage parameter reaches the value 1, g is the regularities parameter for the shape of the curve.

The multi-scale theory adopted in this work to model matrices as one unit element with nano- and micro-fibers (NFC and PVA) as inclusions is governed by the hierarchical non-linear computational homogenization method [Kanit *et al.*, 2003; Li and Li *et al.*, 2019; Balamirzoev *et al.*, 2021]. This method is used to solve mechanics problems at the meso-scale, which is linked to the macro-scale by the representative volume element (RVE). At the meso-scale, heterogeneous materials with various mechanical and geometric characteristics are considered in the RVE. The center of the RVE represents each solid point at the macro-scale, and thus the RVE should have sufficient size to encompass the inhomogeneous microstructure. The general constitutive relation of a

heterogeneous material in terms of computational non-linear homogenization can be expressed by [Kanit *et al.*, 2003]:

$$d\sigma_{ij} = k_{ij}\, d\varepsilon_{ij} \qquad \textbf{(Equation 4.4)}$$

where, k_{ij} is the effective tensor modulus of homogenized stiffness matrix, $d\sigma_{ij}$ and $d\varepsilon_{ij}$ are the volume averaged stress and strain tensors of the RVE, respectively, and *i* and *j* are equal to 1, 2 or 3 with respect to the global axes *x*, *y*, and *z*, respectively. The homogenization method averages the mesoscopic stress-strain field based on the single inclusion theory to express the effective properties of composite materials, based on the properties of different components and volume fraction of inclusions (fibers). Mori and Tanaka (M-T method) [1973] introduced the theory of single inclusion, which is widely used to predict the elastic properties of homogenized materials. Considering RVE_H with the volume *V* of the two-phase composite consisting of matrix H_m with volume V_m and volume fraction $v_m = V_m/V$, and the inclusion H_f with volume V_f and volume fraction $v_f = V_f/V = 1\text{-}v_m$, the volume averages are defined as [Mori and Tanaka,1973]:

$$(\mathfrak{f}) = \frac{1}{V}\int_H \mathfrak{f}(x)\, dV \;, (\mathfrak{f})_L = \frac{1}{V_L}\int_{H_L} \mathfrak{f}(x)\, dV_L \;,\; L = m, f \qquad \textbf{(Equation 4.5)}$$

where, $\mathfrak{f}$ represents the meso-stress or meso-strain tensor over the RVE_H, and the integration is carried out with respect to the micro-coordinate *x* in the RVE_H. The volume averages over the RVE, matrix phase and inclusion phase are related by:

$$(\mathfrak{f}) = v_m\,(\mathfrak{f})_m + v_f\,(\mathfrak{f})_f \qquad \textbf{(Equation 4.6)}$$

Benveniste [1987] modified this theory to obtain the average stress and strain in terms of local elemental stresses and strains as follows:

$$(d\sigma_{ij}) = \frac{1}{V}\left[\int_{H_m} \sigma_{ij}^{m}\ dV_m + \int_{H_f} \sigma_{ij}^{f}\ dV_f\right] \quad \textbf{(Equation 4.7)}$$

$$(d\varepsilon_{ij}) = \frac{1}{V}\left[\int_{H_m} \varepsilon_{ij}^{m}\ dV_m + \int_{H_f} \varepsilon_{ij}^{f}\ dV_f\right] \quad \textbf{(Equation 4.8)}$$

The non-linear homogenization is carried out by imposing a pure axial strain increment $d\varepsilon_{ij}$ such that the corresponding homogenized stress increment $d\sigma_{ij}$ can be computed from (**Equation 4.7**). Accordingly, the effective modulus k_{ij} of homogenized matrix can be computed analytically from **Equation 4.4** [Kanit *et al.*, 2003].

Based on Elshebly tensor method [Qu, 1993], the interaction between concrete matrix and fiber can be represented such that the short fiber is considered a prolate spheroid (needle shaped) bonded to the matrix. Thus, the effective interface stiffness tensor between matrix and fibers can be obtained through lengthy, albeit straightforward algebraical method, which is described by compliance tensor (η_{ij}) as shown in **Equation 4.9** [Qu, 1993]. Therefore, the displacement jumps Δu_i can be expressed by **Equation 4. 10**. Qu [1993] modified the M-T formula for imperfect interface (**Equation 4.11**), which considers a displacement jump (**Equation 4.10**) for another term (ε_{inter}) corresponding to the third term of the global strain ε (**Equation 4.11**).

$$\eta_{ij} = \alpha\,\delta_{ij} + (\beta - \alpha)\,\eta_i\ \eta_j \quad \textbf{(Equation 4.9)}$$

$$\Delta u_i = [\,u_i\,(S^+) - u_i\,(S^-)] = \eta_{ij}\,\sigma_{ik}\,\eta_k \quad \textbf{(Equation 4.10)}$$

$$\varepsilon = v_m\,\varepsilon_m + v_f\,\varepsilon_f + v_f\,H : C_f : \varepsilon_f \quad \textbf{(Equation 4.11)}$$

$$H = \alpha\,P + (\beta - \alpha)\,Q$$

where, α and β represent the compliance in tangential and normal directions of the interface, respectively, η represent the unit outward vector, δ_{ij} is the kronecker's delta. S, C_f, and H represent the interface surface of RVE, interface stiffness tensor, and influence

of both the interface compliance and morphology of the inclusion, respectively. P is $\frac{1}{r}$, and Q is $\frac{3}{4r}$ for a cylindrical geometry assumption of inclusion radius r.

4.3.1.2 Numerical Simulation and Model Parameters

Based on the elastic-plastic damage parameter model, the mechanical properties of matrices without fiber inclusions were identified into 3D FEM using ANSYS R19.2 workbench [2020] environment as one unit element and integrated into modeling Phases I and II. The input parameters for this model included the tensile stress-strain relationships, Young's modulus and peak stress and strain, which were obtained experimentally for all matrices using a quasi-static direct tension test (**Figure 4.3**). In this test, triplicate cylinders (75×250 mm) were tested under axial tensile loading at 56 days at a displacement rate of 0.2 mm/min, such that the bonded length of the specimen to each sleeve was 75 mm and the remaining/free length was 100 mm [Azzam *et al.*, 2021]. This rate was selected to comply with the one used in the flexural and single pellet pull-out tests.

Using the computational non-linear homogenization method, two-scale cubic RVE were developed herein in ANSYS R19.2 workbench [2020] to determine the homogenized stiffness coefficients k_{ij} for matrices with inclusions/fibers (i.e. G-NCC-NFC0.2 and G-N-V1). To determine the size effect of RVE comprising randomly distributed fibers on the homogenized stiffness coefficient value, four different sizes for two-scale RVE were modeled: RVE_1 (G-NCC-NFC0.2) at 0.5 mm, 1 mm, 1.5 mm, and 2 mm, and RVE_2 (G-N-V1) at 12 mm, 15 mm, 18 mm, and 21 mm. **Figure 4.4** shows exemplar homogenized RVE with cubic dimensions of 0.5 and 12 mm. Each meso-scale

RVE includes the matrix and randomly distributed nano- or micro-fibers (NFC or PVA fibers) oriented randomly in space (*x, y, z*), assuming anisotropic properties.

Both RVE_1 and RVE_2 were modeled with a mesh size of 100 μm, and thus the total number of elements ranged from 3,778 to 7,556 and 8,669 and 15,170, respectively. The elements were subjected to uniaxial tensile stress and shear deformation along the principal coordinates to determine the components of k_{ij} (**Equation 4.4**) for different boundary conditions/matrices interacting with BFP through periodic boundary condition displacement on RVE boundaries (**Equation 4.12**) [Sun *et al.*, 1996; Kanit *et al.*, 2003]:

$$u_i\,(s^+) - u_i(s^-) = \varepsilon_{ij}{}^0\left(x_j^+ - x_j^-\right) = \varepsilon_{ij}{}^0\,L_{RVE} \qquad \textbf{(Equation 4.12)}$$

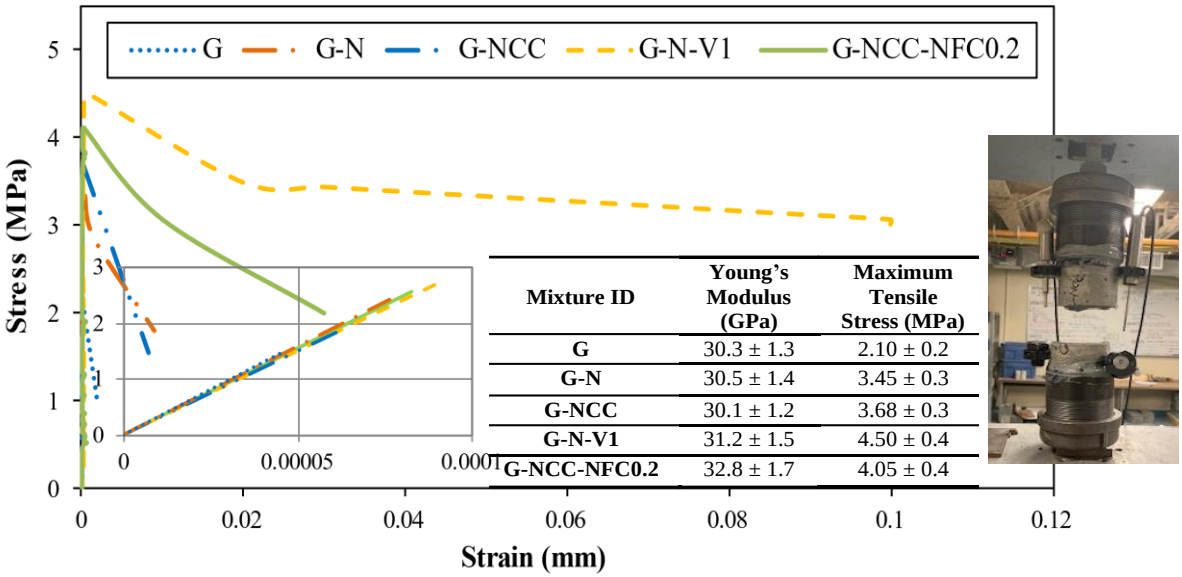
where, (s) and x_j^+ represent the edge of RVE and a point on the edge *s* of RVE, respectively, u_i is the displacement applied in *i* direction on the boundary *s* at point x_j, $\varepsilon_{ij}{}^0$ and L_{RVE} represents the constant strain at *i-j* directions, and edge side of RVE, respectively, and *i* or *j* = 1, 2 and 3 corresponding to *x*, *y* and *z* axes.

The input parameters for **Equations 4.7** and **4.8** involved NFC or PVA properties (**Table 4.1**), the volume fractions of matrix and fibers (**Table 4.2**), and tensile stress-strain relationships obtained experimentally using the quasi-static direct tension test (**Figure 4.3**). Poisson's ratio was 0.2 and the total volume of porosity (V_p) was determined from the MIP test (**Table 4.3**). The interaction bonding between the NFC and PVA fibers and matrix was modeled through the cohesive zone model (CZM) of vanishing thickness. The values of *α, β, and Δu*$_i$ were zero in **Equations 4.9** and **4.10**, representing strong bonding with minimal slip [Haile *et al.*, 2019] of NFC and PVA fibers in the matrix. This was based on the hydrophilic nature and chemical effects of

these fibers, resulting in reducing the *w/b* in the paste at interface with the matrix; thus, the ITZ was considered as rigid as the bulk matrix.

Table 4.3: Summary of MIP test results at 56 days

Mixture ID	Apparent Total Porosity (%)	Threshold Pore Diameter (µm)	Proportion of Micro Pores (<0.1 µm)
G	11.6	0.11	44
G-N	10.3	0.08	58
G-NCC	10.5	0.06	63
G-N-V1	10.4	0.07	64
G-NCC-NFC0.2	9.2	0.05	67



Mixture ID	Young's Modulus (GPa)	Maximum Tensile Stress (MPa)
G	30.3 ± 1.3	2.10 ± 0.2
G-N	30.5 ± 1.4	3.45 ± 0.3
G-NCC	30.1 ± 1.2	3.68 ± 0.3
G-N-V1	31.2 ± 1.5	4.50 ± 0.4
G-NCC-NFC0.2	32.8 ± 1.7	4.05 ± 0.4

Figure 4.3: Tensile stress-strain relationships of the different matrices.

4.3.2 Phase II: Single Pellet Pull-out

4.3.2.1 Theoretical Formulation

The interfacial bonding between macro-fiber (BFP) and matrix is based on a local stress-strain criterion describing the relation between the interfacial shear stress (τ) and the local slip (s) at the fiber/pellet-matrix interface. **Equation 4.13** shows the assumption that BFP is sufficiently stiff enough with no deformation while the load p is applied.

$$s\,(y = L) = \delta \qquad \textbf{(Equation 4.13)}$$

where, y is the coordinate along the length L of BFP, and δ is the total displacement.

The force equilibrium across an infinitesimal element of the pellet-matrix (*dy*) can be expressed by:

$$F_f + F_m = 0 \quad \textbf{(Equation 4.14)}$$

$$\frac{dF_f}{dy} = \pi d\tau s \quad \textbf{(Equation 4.15)}$$

where, F_f and F_m are the forces applied to the pellet and matrix, respectively. Hence, the local slip s can be expressed as a function of the pellet and matrix displacements u_f and u_m, respectively, [Banholzer *et al.*, 2005]:

$$s = u_f - u_m \quad \textbf{(Equation 4.16)}$$

Differentiating the local slip function with respect to *y*, where ε_f and ε_m are, respectively the pellet and matrix strains at a location *y*, and substituting in **Equation 4.14** gives**:**

$$\frac{ds}{dy} = \varepsilon_f - \varepsilon_m \quad \textbf{(Equation 4.17)}$$

$$\frac{ds}{dy} = \left[\frac{1}{A_f E_f} + \frac{1}{A_m E_m}\right] F_f \quad \textbf{(Equation 4.18)}$$

where, E_f, E_m, A_f and A_m are moduli of elasticity and cross-sectional areas of the pellet and matrix, respectively. **Equation 4.19** is the first derivative of **Equation 4.18**, and $T_{(s)}$ is the normalized bond flow, based on the circumferential shear stress τ acting at the contact surfaces between the pellet and matrix as follows [Banholzer *et al.*, 2005]:

$$\frac{ds''}{dy''} = \gamma\pi d\tau s = T_{(s)} \quad \textbf{(Equation 4.19)}$$

$$\gamma = \left[\frac{1}{A_f E_f} + \frac{1}{A_m E_m}\right]$$

The matrix displacement can be neglected due to its high area and low internal stresses compared to that of BFP, and thus **Equation 4.20** can be obtained. Accordingly, the contact surface between the two materials can be modeled analytically by a force-slip relationship between the second-order derivative of the local slip:

$$\frac{ds^{''}}{dy^{''}} = \left[\frac{1}{A_f E_f}\right] \pi d\tau s \qquad \textbf{(Equation 4.20)}$$

where, τ is the shear stress, s is the slippage between BFP and matrix in y direction (direction of loading), while d and A_f are the BFP diameter and cross-sectional area, respectively.

4.3.2.2 Numerical Simulation and Model Parameters

Five 3D models were developed in ANSYS R19.2 Workbench [2020] to simulate the effect of different matrices on the interaction with the single pellet. Elastic-plastic damage (G, G-N, and G-NCC) and homogenization (G-NCC-NFC0.2 and G-N-V1) were implemented to model the behavior of different types of matrices (Phase I) and integrated in Phase II.

The BFP was modeled as a linear-elastic media using LINK8 element, which is a 3D spar (bar) element defined by two nodes with three translational degrees of freedom at each node [**Figure 4.4(d)**]. The matrix block surrounding BFP was modeled as non-linear elastic media by SOLID65 brick element, with eight nodes located at corners [**Figure 4. 4(e)**]; each node has three translational degrees of freedom in the *x*, *y*, and *z* directions. The specific gravity, Young's modulus, and maximum tensile strength for BFP were 1.74 kg/m^3, 65 GPa and 2300 MPa, respectively (**Table 4.1**). The Poisson's ratio for BFP and cementitious matrices were taken as 0.3 and 0.2, respectively. The block model was simulated with dimensions of 100×100×50 mm including a single pellet embedded at a

length 18 mm and diameter of 1.8 mm in the middle of the block [**Figure 4.4(b)]**. The movement of block was restrained by fixing the bottom, and the displacement rate of the applied load was 0.2 mm/min at to the free end of the BFP similar to the experimental scheme. The model was meshed with a mesh size of 10 mm resulting in a total of 2660 nodes and 922 elements.

The interfacial behavior between the pellet and cementitious matrices was modeled as a bonded pair using CONTA175 and TARGE170 by CZM governed by a bilinear-mode-II, with a total of 408 contact elements. The general profile for the traction-separation CZM mode-II cohesive law can be expressed by **Equation 4.21:**

$$\tau_t = K\,\delta_t\,(1 - d_t) \qquad \textbf{(Equation 4.21)}$$

$$K = \frac{T_{max}^t}{\delta_t^*}$$

$$d_t = \begin{cases} 0 & \delta_t^{max} \le \delta_t^* \\ \left(\frac{\delta_t^{max} - \delta_t^*}{\delta_t^{max}}\right)\left(\frac{\delta_t^c}{\delta_t^c - \delta_t^*}\right) & \delta_t^* \le \delta_t^{max} \le \delta_t^c \\ 1 & \delta_t^{max} > \delta_t^c \end{cases}$$

where, T_{max}^t, δ_t^*, δ_t^c, K, δ_t and d_t are the maximum equivalent tangential contact stress, tangential slip at the onset of debonding, tangential slip at the completion of debonding, stiffness parameter (slope of the line), tangential displacement jump (slip) and the debonding parameter, respectively. In the five models, the range of parameter d_t is from 0 to 1 at the completion of debonding. Once debonding is initiated at the interface, friction is engaged until the fiber is pulled-out from the cementitious composite. The CZM parameters were determined from the single pellet pull-out test results.

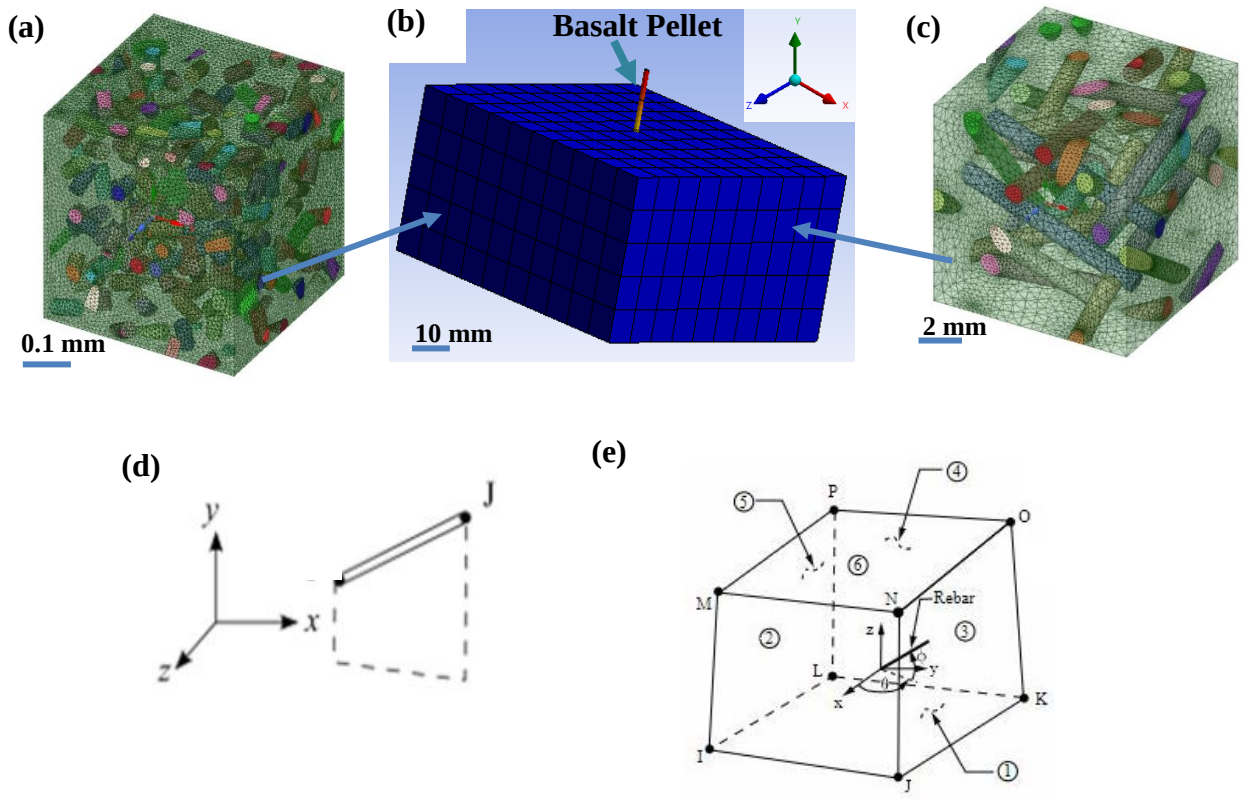


Figure 4.4: Homogenization RVEs: a) meso-RVE$_1$ of mixture G-N-NFC0.2, (b) macro-RVE scale, (c) meso-RVE$_2$ of mixture G-N-V1, (d) LINK 8 element for BFP, and (e) SOLID65 element for the cementitious matrix.

4.4 Results and Discussion

4.4.1 Experimental

4.4.1.1 Flexural Behavior

The flexural test was conducted for all composites at 56 days reinforced with single fiber systems comprising 2.5%/4.5% BFP (by volume of composite), or hybrid systems including 2.5%/4.5% BFP combined with either 1% PVA or 0.2% NFC (**Table 4.2**), in order to investigate the effect of different types of matrices and fiber systems on the flexural performance. Thermal analysis (**Figure 4.7**) and MIP (**Table 4.3**) trends were performed for the five base binders (i.e., G, G-N, G-NCC, G-N-V1, and G-NCC-NFC0.2)

to characterize the pore structure and maturity of matrices, thus elucidating the flexural strength results. **Table 4.4** lists the flexural and residual strengths as well as toughness for all composites at 56 days through using triplicate specimens, and **Figures 4.5-4.6** show representative load-deflection (P-δ) curves. Incorporation of nanoparticles (6% NS or 0.5% NCC) into the cementitious matrix led to marked improvement in the flexural strength of composites. For instance, the first-peak flexural strength of G-N-B2.5 specimens was 41% higher than that of G-B2.5 specimens. This trend can be explained by the improvement of the matrix maturity and pore structure. Thermal analysis (**Figure 4.7**) showed that the normalized CH contents of G-N relative to the refence binder G continuously decreased from 0.82 at 1 day to 0.33 at 90 days. This was associated with refined pore structure in G-N matrix (**Table 4.3:** lower porosity: 10%, lower threshold pore diameter: 0.08 µm, and higher proportion of micro-pores: 58%). While the high surface area of NS particles (80,000 m^2/kg) acts as additional nucleation sites for precipitation of hydration products [Kong *et al.*, 2012], this process is coupled with vigorous pozzolanic reactivity (consumption of CH with time to precipitate additional/secondary C-S-H), as indicated by the TG trends. In addition, the particle packing/filling effect of nano-silica densified the microstructure. This behavior was also observed in previous studies on the use of nano-silica with high-volume fly ash and slag binders [Ghazy *et al.*, 2016b; Mahmoud *et al.*, 2017].

The inclusion of NCC in mixture G-B2.5 to produce mixture G-NCC-B2.5 increased the first-peak flexural strength by 84% compared with that of mixtures G-B2.5. This trend can be linked to the more refined pore structure of G-NCC matrix relative that of the G matrix, as the proportion of micro-pores increased by 43% (**Table 4.3**). Unlike mixture G-N (continuous consumption of CH), the thermal analysis showed that CH

contents in G-NCC followed a similar pattern to that of G; the increasing branch was due to hydration of the blended binder, whereas the decreasing branch was due to the long-term pozzolanic reactivity of slag. However, the normalized CH contents in G-NCC relative to that in the reference mixture G were consistently above 1.0 from 1 to 90 days, indicating improved hydration development and maturity of this matrix. This could be ascribed to the omnipresence of hydroxyl groups (OH^-) on NCC surface promoting chemical interactions with cement particles and spindle geometry of ultrafine NCC (430,000 m^2/kg) creating a pathway for water transport to the inner un-hydrated cement regions, resulting in precipitation of C-S-H, reduction of water content in the paste [Cao *et al.*, 2015; Fu *et al.*, 2017], and thus refining the pore structure of the hardened matrix (**Table 4.3**). In addition, the spindle shapes might be able to impede the nucleation of nano-cracks in the matrix, increasing its flexural capacity.

The incorporation of higher dosage of single BFP (macro-fibers) in the nano-modified matrix decreased the first-peak flexural strength of the composites (**Table 4.4**). For instance, the flexural strength of G-N-B4.5 and G-NCC-B4.5 specimens were 25% and 38%, respectively lower than that of G-N-B2.5 and G-NCC-B2.5 specimens, which were 7.2 MPa and 9.4 MPa, respectively. This can be linked to the increase in the air content associated with 4.5% BFP (**Table 4.2**) resulting from the higher viscosity of these mixture and friction between BFP and matrix (foaming action), in addition to creation of additional ITZs, which acted as weak links and stress concentrators in the matrix, thus reducing its capacity [Elhadary and Bassuoni, 2021].

Adding 1% PVA micro-fibers to BFP (hybrid system) led to increasing the first-peak flexural strength of the nano-silica modified composites. For example, the first-peak flexural strength for G-N-B4.5-V1 specimens was 46% higher than that of G-N-B4.5

specimens, which was 5.4 MPa (**Table 4.4**). While the CH consumption trends of G-N and G-N-V1 were comparable (**Figure 4.7**) due to the role of nano-silica explained earlier, which can be linked to the further microstructural improvement brought by the addition of 1% PVA. MIP results (**Table 4.3**) showed that G-N-V1 had more refined pore structure (relatively lower threshold pore diameter and higher proportion of micro-pores), compared with that of mixture G-N. This could be attributed to the combined hydrophilic and chemical effects (surface OH^- groups) of PVA, resulting in reduction of *w/b* in the paste and creation of cross links at the boundaries between PVA and matrix, resulting in improving the quality of ITZ and interfacial bonding [Liu *et al.*, 2011]. In addition, the randomly distributed PVA micro-fibers segmented the capillary system in the matrix, which led to more discrete pore network with larger proportion of micro-pores (64%). Moreover, the crack-bridging function of PVA had a positive effect at reducing the stress concentration at the tips of micro-cracks in the matrix, and consequently increasing its capacity.

The combination of 0.2% NFC fibers with BFP in the cementitious composites modified with NCC led to noticeable increase in the first-peak flexural strength compared to corresponding composites reinforced with single BFP and hybrid BFP/PVA systems. For example, the first-peak flexural strength for G-NCC-B4.5-NFC0.2 specimens were 72% and 60%, respectively higher than that of G-NCC-B4.5 and G-N-B4.5-V1 specimens, which were 5.4 MPa and 7.9 MPa, respectively (**Table 4.4**). This conformed to the thermal analysis (**Figure 4.7**) and MIP (**Table 4.3**) trends, which showed that mixture G-NCC-NFC0.2 had consistently higher normalized CH contents above 1.0 at all ages relative to mixture G-NCC, and densified pore structure (proportion of micro-pores was 67%). In addition to the effect of NCC at enhancing the matrix as explained earlier,

NFC has surface hydroxyl groups (OH^-) that promote interactions with cement particles. Its hydrophilic/hygroscopic features serve as an internal curing agent owing to its water affinity and retention/release capacity, thereby improving the hydration development/maturity of the matrix with time, ITZ and interfacial bonding [Hisseine *et al.*, 2018; Hisseine *et al.*, 2019]. Moreover, NFC acted as a randomly distributed nano-reinforcing system in the composites, which might delay the nucleation of cracks in the matrix, thus increasing its capacity.

After the first-peak load, the load-deflection curves (**Figure 4.5-4.6)** of the composites reinforced with fibers exhibited mixed trends depending on the contribution of different dosages, and types of fibers with surrounding matrices. For instance, mixtures G-N-B2.5 (average R_s of 4.4 MPa) and G-NCC-B2.5 (average R_s of 4.3 MPa) showed deflection-softening followed by a plateau, whilst mixtures G-N-B4.5 (average R_s of 4.9 MPa) and G-NCC-B4.5 (average R_s of 4.5 MPa) exhibited a deflection-hardening trend with 33% and 18% higher toughness, respectively (**Table 4.4**). This can be ascribed to the high tensile capacity of BFP and its adequate modulus of elasticity (**Table 4.1**), which controlled growth of macro-cracks in the matrix and restored the load carrying capacity till reaching a second peak load, especially in the case of 4.5% dosage owing to the abundance of the pellets in the middle-third span of specimens (failure plane). Also, the type of nano-modification of the matrix affected the post-peak behavior of BFP; the inclusion of 6% NS in mixtures led to improvement in toughness compared with mixtures incorporating 0.5% NCC. For example, the toughness of G-N-B2.5 and G-N-B4.5 composites were 6% and 20%, respectively higher than that of G-NCC-B2.5 and G-NCC-B4.5 composites, which were 28.5 J and 33.6 J, respectively. This trend could be linked to the relative resistance of BFP to pull-out from each type of matrix, which is the main

toughening mechanism of the composites. This is substantiated by the interfacial bonding characteristics obtained from the single pellet pull-out tests discussed in the succeeding section.

Regarding the hybrid systems, it was observed that 1% PVA in combination with BFP had a positive effect at improving the post-cracking behavior of composites (**Figure 4.6**). Such composites had no or little drop in the load after the first-peak, and they continued to carry significant load up to the designated deflection limit, relative to the corresponding mixtures comprising BFP or NFC/BFP. For instance, mixture G-N-B4.5-V1 showed a pseudo deflection-hardening behavior (**Figure 4.6**) with average R_s of 9 MPa (**Table 4.4**). Correspondingly, the toughness of mixtures G-N-B4.5-V1 was 46% and 87%, respectively higher than that of mixtures G-N-B4.5 (40.3 J) and G-NCC-B4.5-NFC0.2 (31.5 J). This could be linked to the synergistic effects of the randomly distributed micro-PVA and macro-BFP fibers, as the former impeded the nucleation and coalescence of micro-cracks and the latter controlled/restrained the propagation of macro-cracks in the composite. This complied with the increase in BFP interfacial bonding in this matrix, as discussed later in the single pellet pull-out section. Conversely, a sudden decline of load (55 to 65%) after reaching the first-peak occurred for mixtures comprising hybrid NFC/BFP, which then continued to carry load up to the designated deflection limit. This was indicative of faster slippage of BFP from the matrix comprising NCC and NFC, as verified by the single pellet pull-out trends.

Table 4.4: Flexural properties of the cementitious composites at 56 days

Mixture ID	First-Peak Strength (MPa)	Residual Strength at *L/600* (MPa)	Residual Strength at *L/150* (MPa)	Residual Post-Cracking index (R_i)	Toughness (J)
G-B2.5	5.1 ± 0.4	4.1 ± 0.4	3.4 ± 0.3	0.95 ± 0.1	22.7 ± 1.1
G-N-B2.5	7.2 ± 0.5	4.3 ± 0.4	4.5 ± 0.4	0.64 ± 0.1	30.3 ± 1.3
G-N-B4.5	5.4 ± 0.4	4.8 ± 0.4	5.1 ± 0.4	1.10 ± 0.1	40.3 ± 2.2
G-N-B2.5-V1	7.8 ± 0.5	8.2 ± 0.8	6.6 ± 0.5	0.98 ± 0.1	48.8 ± 2.2
G-N-B4.5-V1	7.9 ± 0.5	9.8 ± 0.9	8.2 ± 0.8	1.40 ± 0.2	58.9 ± 2.3
G-NCC-B2.5	9.4 ± 0.8	4.2 ± 0.4	4.4 ± 0.4	0.47 ± 0.1	28.5 ± 1.2
G-NCC-B4.5	5.8 ± 0.4	4.3 ± 0.4	4.6 ± 0.4	0.91 ± 0.1	33.6 ± 1.3
G-NCC-B2.5-NFC0.2	11.5 ± 0.9	3.5 ± 0.3	4.5 ± 0.4	0.35 ± 0.1	28.9 ± 1.3
G-NCC-B4.5-NFC0.2	9.3 ± 0.9	4.5 ± 0.4	5.2 ± 0.4	0.56 ± 0.1	31.5 ± 1.3

Note: Values in parentheses represent standard deviations.

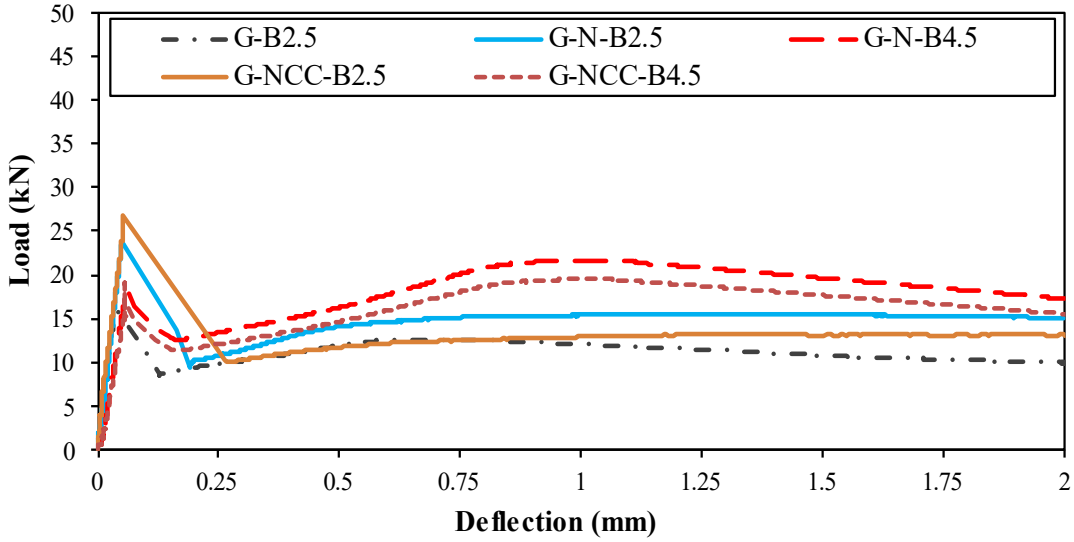


Figure 4.5: Load-deflection (P-δ) curves for the composites with single fiber systems.

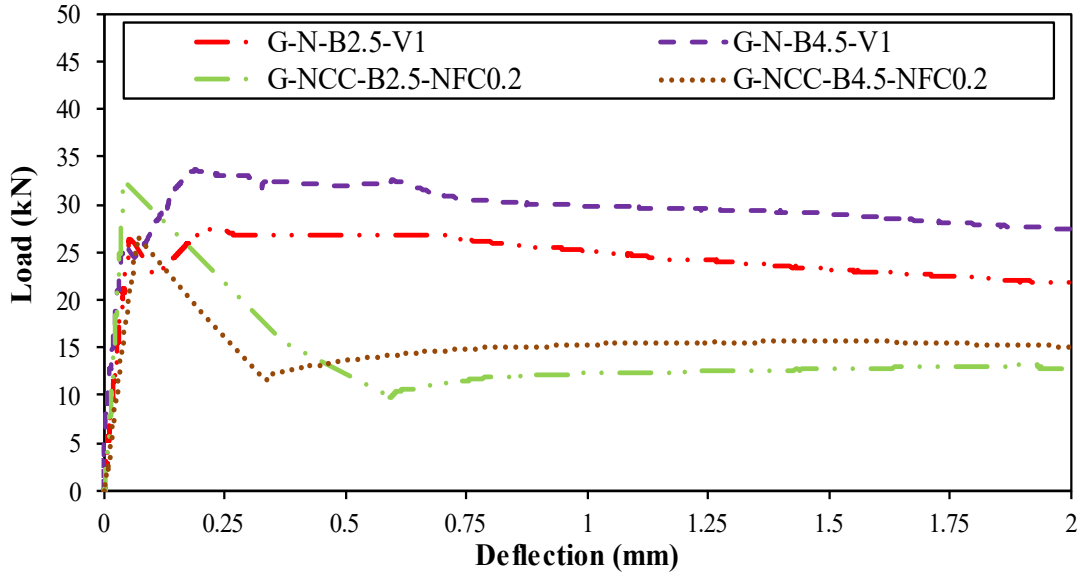


Figure 4.6: Load-deflection (P-δ) curves for the composites with hybrid fiber systems.

Normalized Calcium Hydroxide Content	Time (days)					
	1	3	7	28	56	90
G-N/G	0.82	0.64	0.52	0.34	0.31	0.33
G-NCC/G	1.10	1.10	1.10	1.13	1.09	1.05
G-N-V1/G-N	1.02	1.02	1.02	1.01	1.01	1.01
G-NCC-NFC0.2/G	1.21	1.21	1.23	1.28	1.18	1.13
G-NCC-NFC0.2/G-NCC	1.10	1.10	1.12	1.13	1.08	1.05

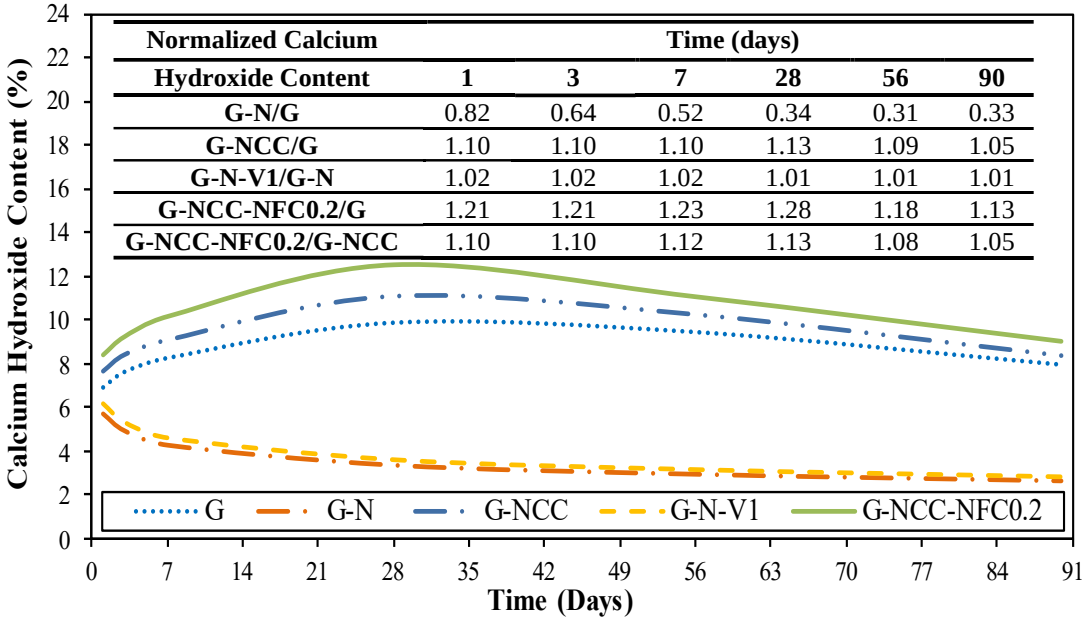


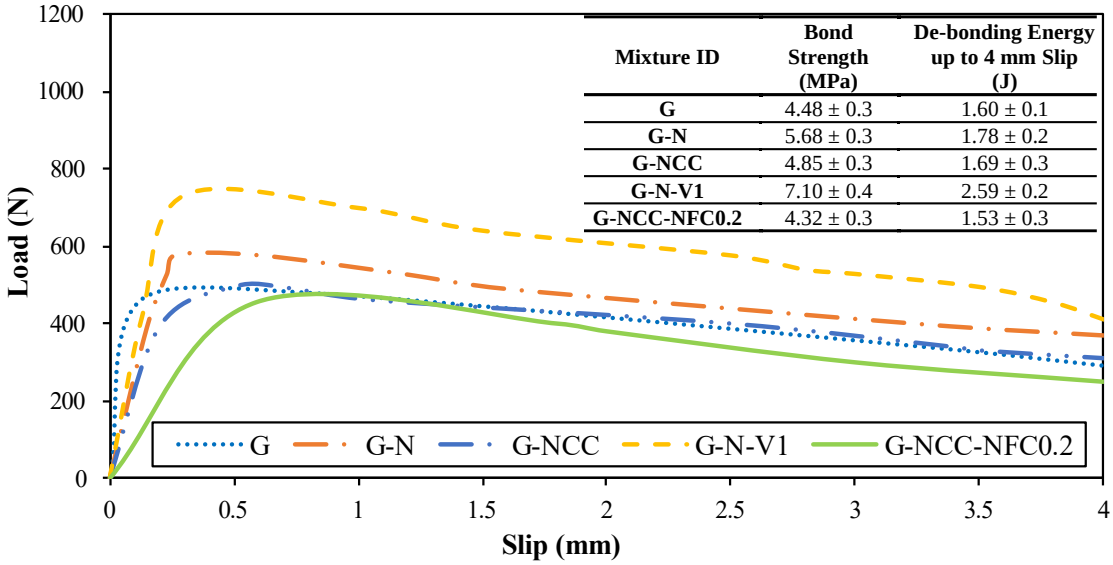
Figure 4.7: TGA results for the CH contents (at a temperature range of 400 to 450°C) in the mixtures.

4.4.1.2 BFP Pull-Out

The flexural post-cracking performance of the composites was governed by the BFP pull-out process form the base matrices (i.e., G, G-N, G-NCC, G-N-V1, and G-NCC-NFC0.2), which was captured by the single pellet-pull out tests (**Figure 4.8**) and substantiated by SEM. The matrix comprising NS had improved interfacial bonding with BFP. For instance, the pull-out strength of BFP from G-N and its de-bonding energy were 27% and 17% and 11% and 5%, respectively higher than that of the reference matrix without nano-silica (G) and mixture modified with NCC (G-NCC). This led to high contact surface area between BFP and matrix and consequently enhancement in BFP/matrix friction and interfacial bonding, which conformed to the higher flexural toughness of these composites (**Table 4.4**). Complying with this trends, SEM and EDX images showed that unlike the reference matrix (G), the inclusion of 6% NS led to perspicuous deposition of cementitious gel/products in the BFP micro-groves cross-linking the pellet with matrix [e.g. **Figure 4.9** and **4.10]**;the average *Ca/Si* of the paste at the interface between BFP and G-N was 1.18 compared to 1.75 in the reference binder G, substantiating efficient filling effect and pozzolanic reactivity of the former resulting in the participation of additional and stiffer pozzolanic C-S-H in the contact zone with BFP. According to Detwiler *et al.* [Detwiler *et al.*, 1996], pozzolanic C-S-H has *Ca/Si* of 1.1, whereas this ratio in primary/hydration C-S-H tends to 1.7. Although 0.5% NCC relatively improved the hydration development of the slag-based matrix with respect to the reference matrix G (**Figure 4.7**), it had a comparable deposition pattern at the interface with BFP at 56 days, suggesting similar resistance to pull-out after first-cracking. SEM analysis showed patchy deposition of cement gel products with *Ca/Si* of 1.70 in the BFP microgrooves (e.g. **Figure 4.11)**, resulting in comparable bond strength and de-bonding energy to that of the

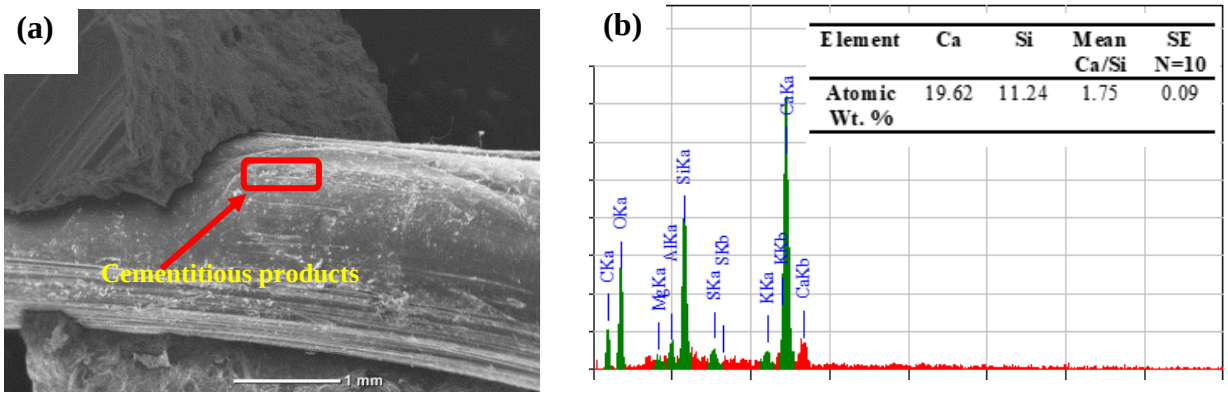
reference binder G, which were 4.48 MPa and 1.60 J, respectively. This conformed to the similar post-cracking plateau of composites G-NCC-B2.5 and G-B2.5 in the flexural tests (**Figure 4.5**).

Adding 1% of PVA fibers led to further improvement of the resistance of BFP to pull-out from the NS-modified cementitious matrix; the pull-out strength and de-bonding energy of G-N-V1 were 25% and 46%, respectively higher than that of mixture G-N (**Figure 4.8)**. PVA micro-fibers in the matrix could control the nucleation and coalescence of micro-cracks. PVA fibers create hydrogen bonds between molecules forming new compounds at the boundaries with cement paste (chemical effect) [Liu *et al.*, 2011], resulting in compact structure around BFP. Also, randomly distributed micro-PVA clusters in the paste surrounding BFP [e.g. **Figure 4.12(a)**], increased the chance of interlocking, friction, and in turn bonding capacity. Hence, this was reflected by the deflection-hardening behavior of these composites (**Figure 4.6**). Conversely, addition of 0.2% NFC to the NCC-modified matrix adversely affected the resistance of BFP to pull-out from the matrix. The bonding strength of BFP with G-NCC-NFC0.2 was 24%, 39%, and 11% respectively less than that with G-N, G-N-V1 and G-NCC. SEM analysis [e.g. **Figure 4.12(b)**] showed deposition of free NFC patches within the longitudinal micro-grooves of BFP due to their nano- and micro-dimensions, and electrostatic attraction since the polyamide resin (Nylon 6) is positively charged [Wu *et al.*, 2010] and NFC has surface hydroxyl groups (OH^-). This partially discounted the deposition of cement gel into the microgrooves, thus making the pellet less tightly adhering to the matrix. These separation zones/weak links led to easier slippage of the pellet from the matrix, which decreased the toughness of these composites as shown by the post-cracking flexural behavior (**Figure 4.7**).



Mixture ID	Bond Strength (MPa)	De-bonding Energy up to 4 mm Slip (J)
G	4.48 ± 0.3	1.60 ± 0.1
G-N	5.68 ± 0.3	1.78 ± 0.2
G-NCC	4.85 ± 0.3	1.69 ± 0.3
G-N-V1	7.10 ± 0.4	2.59 ± 0.2
G-NCC-NFC0.2	4.32 ± 0.3	1.53 ± 0.3

Figure 4.8: Bond-slip relationships from the single pellet pull-out tests.



Element	Ca	Si	Mean Ca/Si	SE N=10
Atomic Wt. %	19.62	11.24	1.75	0.09

Figure 4.9: Examplar SEM micrograph for matrix G at 56 days: (a) ITZ with BFP, and (b) EDX spectrum of paste at the indicated location in (a). (SE = standard error for 10 points).

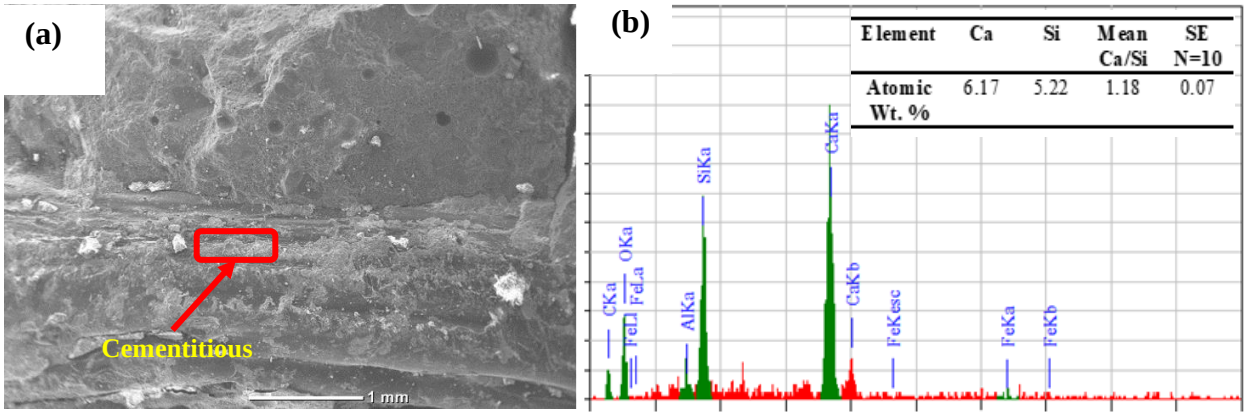


Figure 4.10: Exemplar SEM micrograph for matrix G-N at 56 days: (a) ITZ with BFP, and (b) EDX spectrum of paste at the indicated location in (a). (SE = standard error for 10 points).

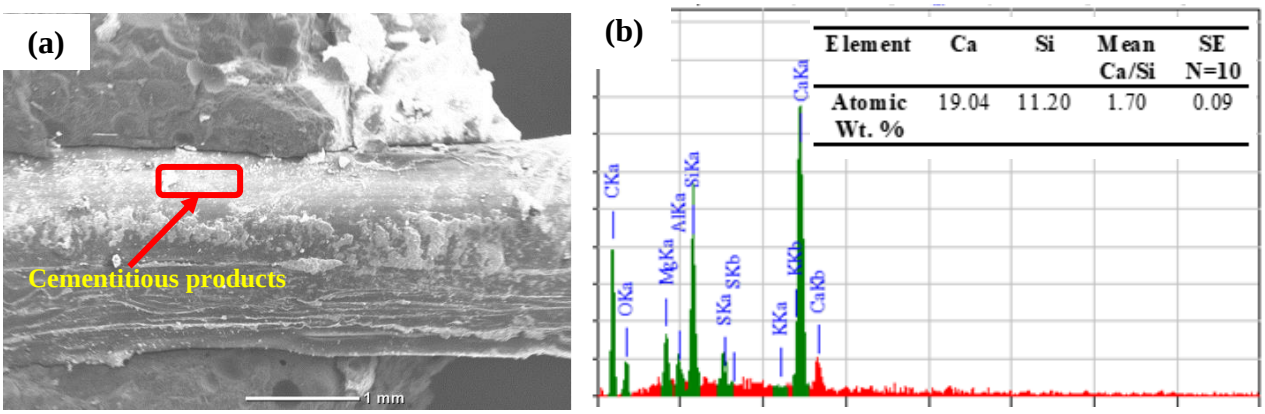


Figure 4.11: Exemplar SEM micrograph for matrix G-NCC at 56 days: (a) ITZ with BFP, and (b) EDX spectrum of paste at the indicated location in (a). (SE = standard error for 10 points).

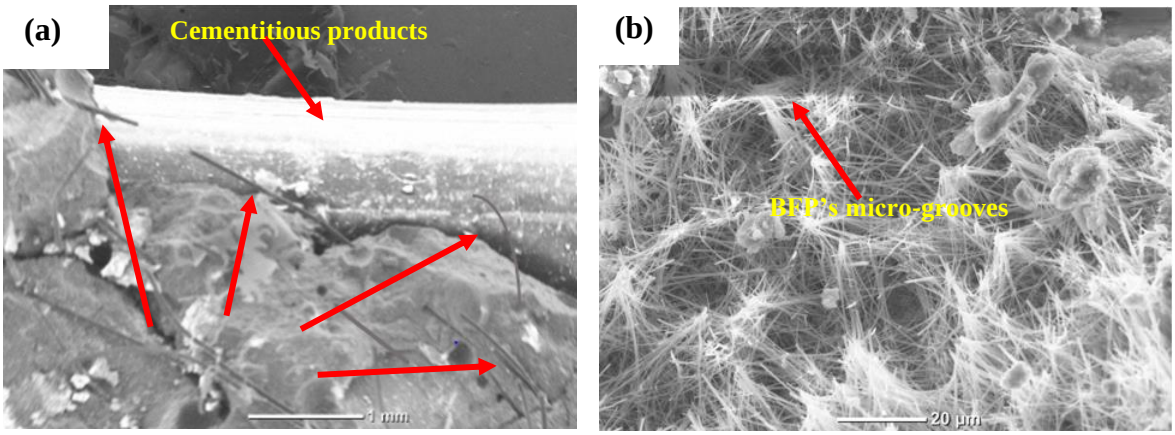


Figure 4.12: Exemplar SEM micrographs at 56 days showing: (a) interaction of BFP with G-N-V1, and (b) deposition of NFC in BFP's micro-grooves in G-NCC-NFC0.2.

4.4.2 Modeling

The FEM approach introduced herein had high reliability with the experimental data (maximum error of 10%). The models were able to capture evolution of micro-cracks, and stress-strain distributions around the pellet for the nano-modified matrices comprising PVA and NFC, respectively. Hence, parametric analyses were conducted to show the effect of different fibers volume fractions on the homogenized stiffness coefficient k_{ij} and BFP interfacial bond strength τ_t, without the need for experimental tests, as discussed later in Phases I and II sections.

4.4.2.1 Phase I

The homogenized stiffness coefficients k_{ij} were determined for matrices G-NCC-NFC0.2 and G-N-V1 using **Equations. 4.4, 4.7** and **4.8**. For example, **Equation 4.22** shows the results of k_{ij} for a 12 mm RVE_2 (comprising PVA). The coupling terms for k_{ij} indicated that the value of extension-shear (E-S) and shear-shear (S-S) components were much

lower than that of the extension-extension (E-E) component, and thus they were negligible.

$$k_{ij} = \begin{bmatrix} & E-E & & & E-S & \\ 31.23 & 8.91 & 8.12 & 0.07 & 0.09 & 0.32 \\ & 31.23 & 8.18 & 0.02 & -0.10 & 0.17 \\ & & 31.23 & -0.03 & 0.02 & 0.28 \\ & Symmetry & & 10.64 & 0.03 & 0.02 \\ & & & & 10.64 & 0.01 \\ & & & S-S & & 10.64 \end{bmatrix} \quad \textbf{(Equation 4.22)}$$

In addition, the elastic moduli *E_{11}*, *E_{22} and E_{33}* were comparable, which was related to the even dispersion of fibers in space. It was observed that 0.5 mm and 12 mm sizes were adequate to yield stable elastic moduli, and thus they were considered as representative volume elements for RVE_1 and RVE_2, respectively.

Nye *et al.* [**Equation 4.23 a**] reported that when $[(k_{11}-k_{12})] = 2\,k_{44}$, a basic definition of anisotropy ratio (α) was achieved; thus, the material can be considered as isotropic [Nye, 1985].

$$k_{ij} = \begin{bmatrix} k_{11} & k_{12} & k_{13} & 0 & 0 & 0 \\ & k_{22} & k_{23} & 0 & 0 & 0 \\ & & k_{33} & 0 & 0 & 0 \\ & Symmetry & & k_{44} & 0 & 0 \\ & & & & k_{44} & 0 \\ & & & & & k_{44} \end{bmatrix} \quad \textbf{(Equation 4.23a)}$$

$$k_{ij} = \begin{bmatrix} 31.23 & 8.91 & 8.12 & 0 & 0 & 0 \\ & 31.23 & 8.18 & 0 & 0 & 0 \\ & & 31.23 & 0 & 0 & 0 \\ & Symmetry & & 10.64 & 0 & 0 \\ & & & & 10.64 & 0 \\ & & & & & 10.64 \end{bmatrix} \quad \textbf{(Equation 4.23b)}$$

where, k_{11}, k_{12}, k_{44} are coefficients of the homogenized stiffness matrix. In the current model, a cubical symmetry was achieved (**Equations 4.23a-b)** from which the homogenized stiffness k_{ij} of the RVEs was determined (i.e. 0.5 mm for RVE_1 and 12 mm

for RVE_2). In this case, the anisotropy ratio (α) was close to 1, suggesting that RVEs of nano-modified cementitious composites comprising PVA or NFC (i.e., G-N-V1 and G-NCC-NFC0.2) can be considered as isotropic.

Table 4.5 lists the results of homogenized Young's modulus, shear modulus, Poisson's ratio, and maximum normal/shear stresses for two-scale meso-RVE in different directions (1, 2, 3), relative to the global axes *x*, *y*, *z*, respectively. The homogenized Young's modulus and tensile stress of RVE_1 (G-NCC-NFC0.2) and RVE_2 (G-N-V1) were and 32.8 GPa and 4.3 MPa and 31.2 GPa and 4.9 MPa, respectively, with an error of less than 10% relative to that of the direct tension test results (**Figure 4.3**) substantiating the accuracy of numerical predictions.

Table 4.5: Homogenized engineering properties of RVEs

Homogenized Matrix	Size (mm)	E_{11} (GPa)	E_{22} (GPa)	E_{33} (GPa)	G_{12} (GPa)	G_{13} (GPa)	G_{23} (GPa)	υ_{12}	υ_{13}	υ_{23}	(σ) MPa	(τ) MPa
G-NCC-NFC0.2 (RVE_1)	0.5	32.8	32.8	32.7	11.6	11.5	11.8	0.21	0.20	0.20	4.3	7.3
G-N-V1 (RVE_2)	12	31.2	31.2	31.2	10.6	10.6	10.6	0.20	0.20	0.21	4.9	7.8

4.4.2.2 Phase II

The parameters implemented in Phase II included the experimental tensile stress-strain relationships, and Young's modulus for the plain matrices (i.e., G, G-N, and G-NCC) using a quasi-static direct tension test (**Figure 4.3**), and the homogenized results obtained from Phase I for the matrices comprising PVA micro-fibers and NFC nano-fibers (i.e., G-N-V1 and G-NCC-NFC0.2). The predicted bond strength and de-bonding energy up to 4 mm slip for the single pellet pull-out tests were in good agreement (maximum 6% and 10% error, respectively) with the corresponding experimental values (**Table 4.6**), indicating the reliability of the modeling approaches implemented in this study.

Accordingly, the models were capable of simulating the bond-slip relationships for all mixtures before and after interface de-bonding as well as during pellet pullout/slip process (**Figure 4.13**).

The modeling results conformed to the experimental trends. The predicted pull-out strength of BFP from G-N and its de-bonding energy were 13% and 18% and 8% and 5%, respectively higher than that from the reference matrix (G) and matrix modified with NCC (G-NCC). This was ascribed to the role of NS in producing extensive deposition of cementitious products in the BFP micro-groves as discussed earlier. Moreover, inclusion of 1% micro-PVA fibers in the matrix modified with NS (G-N-V1) achieved the highest estimations for bonding strength and de-bonding energy compared with that of the other mixtures (**Table 4.6**), owing to the clustering, interlocking and friction effects of well distributed micro-PVA around BFP. Conversely, addition of 0.2% NFC to the NCC-modified matrix reduced predictions for interfacial bond strength by 3%, 27%, and 8%, respectively compared with G-NCC, G-N-V1, and G-N, due to competing with the deposition of cement gel into BFP micro-grooves, thus reducing friction and interfacial bonding with the matrix.

Figure 4.14(a)-(b) show exemplar stress and strain distributions around the pellet for the nano-modified matrices comprising PVA and NFC, respectively, where the load was transferred from the pellet to the surrounding matrix zone with corresponding increase in the cumulative displacement. It was observed that the load reached its peak value at the last stage of debonding (red zone in the contour plot) and just before the initiation of the pellet pull-out/slippage process. The matrix comprising NS and PVA had larger crack processing zone and strain at failure than that of the matrix comprising NCC and NFC. The developed models also simulated the propagation and distribution of

micro-cracks in the matrix during the single pellet-out tests, as for example depicted in **Figure 4.15**. The patterns indicated that the de-bonding failure of BFP from G-N-V1 occurred after generation of multiple and sequential micro-cracks parallel and perpendicular to the loading direction in plan and elevation views [**Figure 4.15(a-b)**], which conformed to the wider crack processing zone in **Figure 4.14(a)**. This was related to the abundance of PVA micro-fibers and their interlocking effect with BFP as well as restraining the growth of micro-cracks in the matrix (toughening mechanism). This led to a ductile mode of failure of these composites, i.e. high consumption of energy was required for the pull-out process, which corresponded to the deflection-hardening post-cracking flexural trend. Comparatively in mixture G-NCC-NFC0.2, fewer perpendicular and parallel micro-cracks to the loading direction appeared simultaneously in different views [**Figure 4.15(c-d)**], indicating a faster debonding failure of BFP at the interface, which corresponded to a smaller crack processing zone [**Figure 4.14(b)**]. This was ascribed to the NFC smaller dimensions that were inadequate to control growth of micro-cracks at the BFP/matrix interface. Also, the precipitation of NFC patches in BFP microgrooves discounted deposition of cement gel leading to reduction of friction and interfacial bonding.

Figure 4.16(a-d) show the effect of different fibers volume fraction on the homogenized stiffness coefficient k_{ij} and BFP interfacial bond strength τ_t. The parametric analysis indicated that increasing the volume fraction of PVA fibers would have a positive effect at increasing homogenized stiffness coefficient and bond strength of matrix G-N, in comparison to increasing the volume of NFC in matrix G-NCC. For instance, the predicted homogenized stiffness of the G-N matrix was 31.2, 35.6, and 38.4 GPa respectively with PVA volumes of 1%, 1.5% and 2% (practical range for PVA fibers

in cement-based materials) [**Figure 4.16(a)**]. Correspondingly, the bond strength and de-bonding energy for the mixture incorporating 2% PVA fibers with BFP would increase by 29% and 33%, respectively compared with that of the mixture comprising 1% of PVA fibers [**Figure 4.16(a)** and **(b)**]. The inclusion of NFC at higher dosages would increase the homogenized stiffness coefficient. The homogenized stiffness modulus of the G-NCC matrix would yield 31.6, 32.8, and 35.6 GPa respectively with NFC volumes of 0.1%, 0.2% and 0.3% (practical range for NFC fibers in cement-based materials) [**Figure 4.16(c)]**, respectively; however, there was appreciable reduction in BFP interfacial bonding and de-bonding energy at these dosages by up to 17%, and 20%, respectively relative to that of the matrix without NFC (G-NCC) [**Figure 4.16(c)** and **(d)]**.

Table 4.6: Experimental versus modeling results for the single pellet pull-out tests

Mixture ID	Bond Strength (MPa)		Error (%)	De-bonding Energy up to 4 mm Slip (J)		Error (%)
	Experimental	Modeling		Experimental	Modeling	
G	4.48	4.73	6	1.60	1.59	1
G-N	5.68	5.34	6	1.78	1.87	5
G-NCC	4.85	4.93	2	1.69	1.78	5
G-N-V1	7.10	6.87	3	2.59	2.35	10
G-NCC-NFC0.2	4.32	4.68	8	1.53	1.68	10

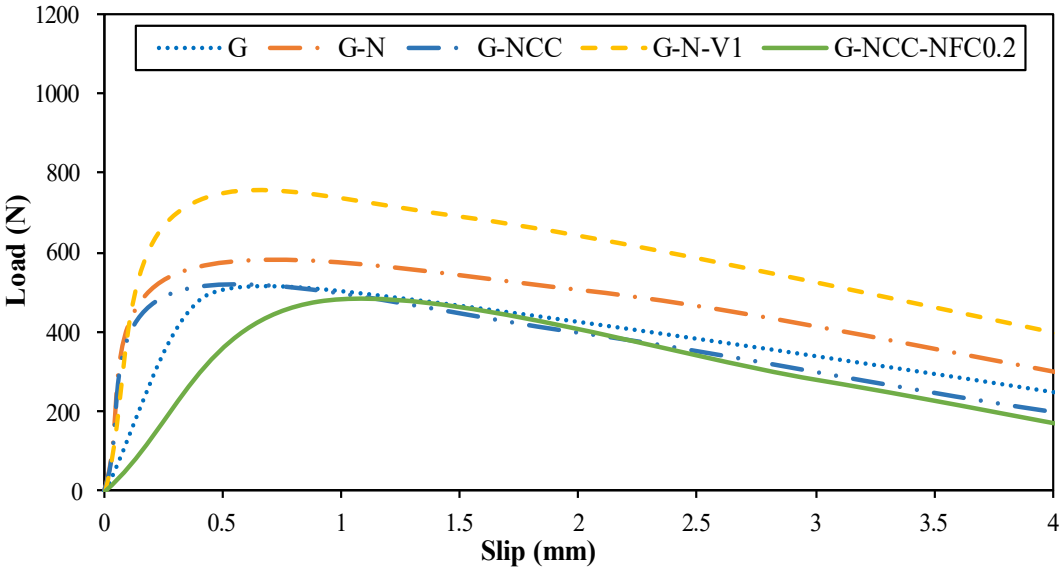


Figure 4.13: Predicted load-slip curves for the single pellet-pullout from different matrices.

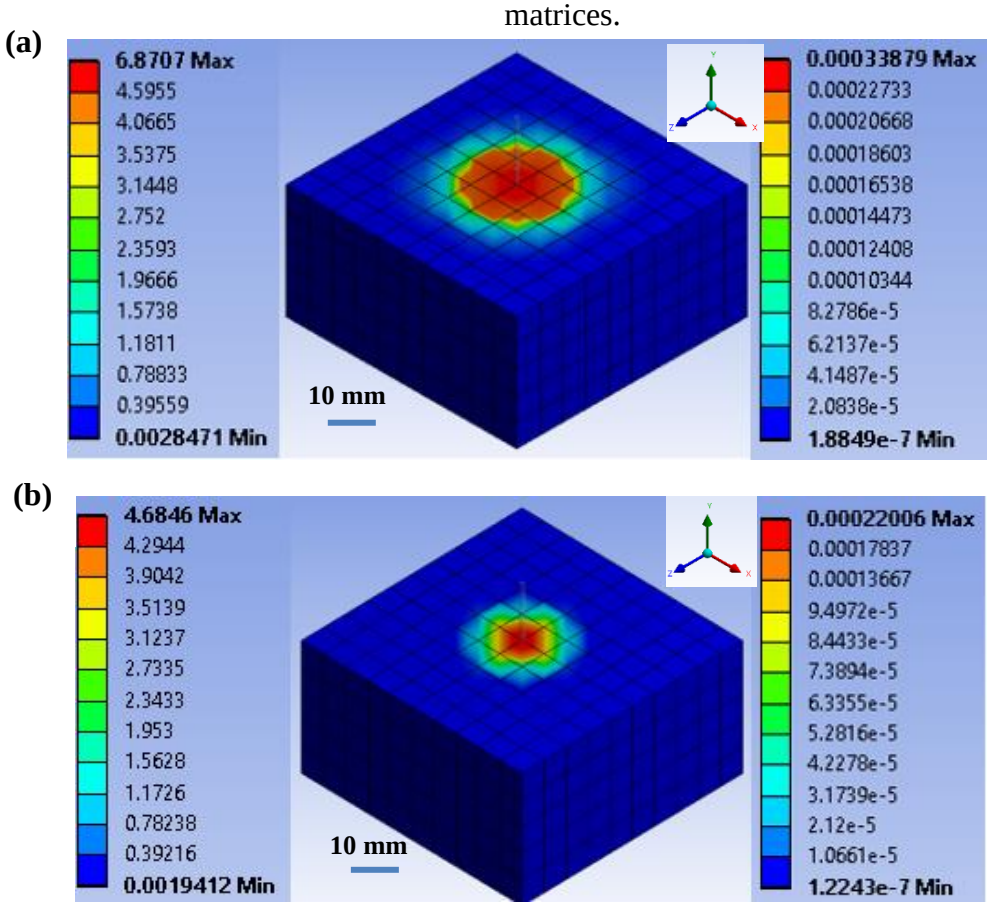


Figure 4.14: Examplear stress-strain distributions from the models for the single pellet pull-out tests: (a) G-N-V1, and (b) G-NCC-NFC0.2.

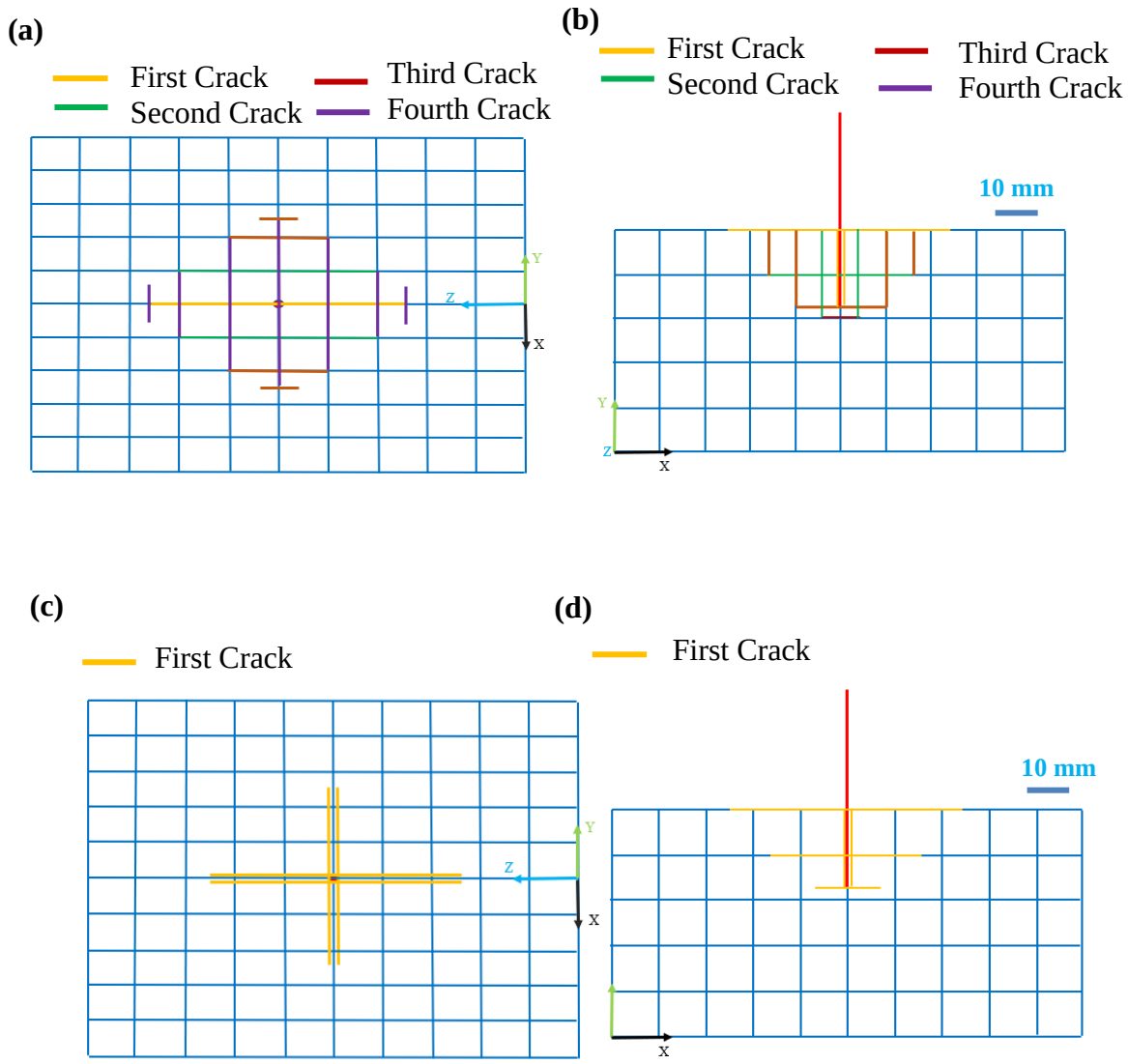


Figure 4.15: Predicted crack distributions at the last stage of BFP debonding: (a) plan view of mixture G-N-V1, (b) elevation view of mixture G-N-V1, (c) plan view of mixture G-NCC-NFC0.2, and (d) elevation view of mixture G-NCC-NFC0.2.

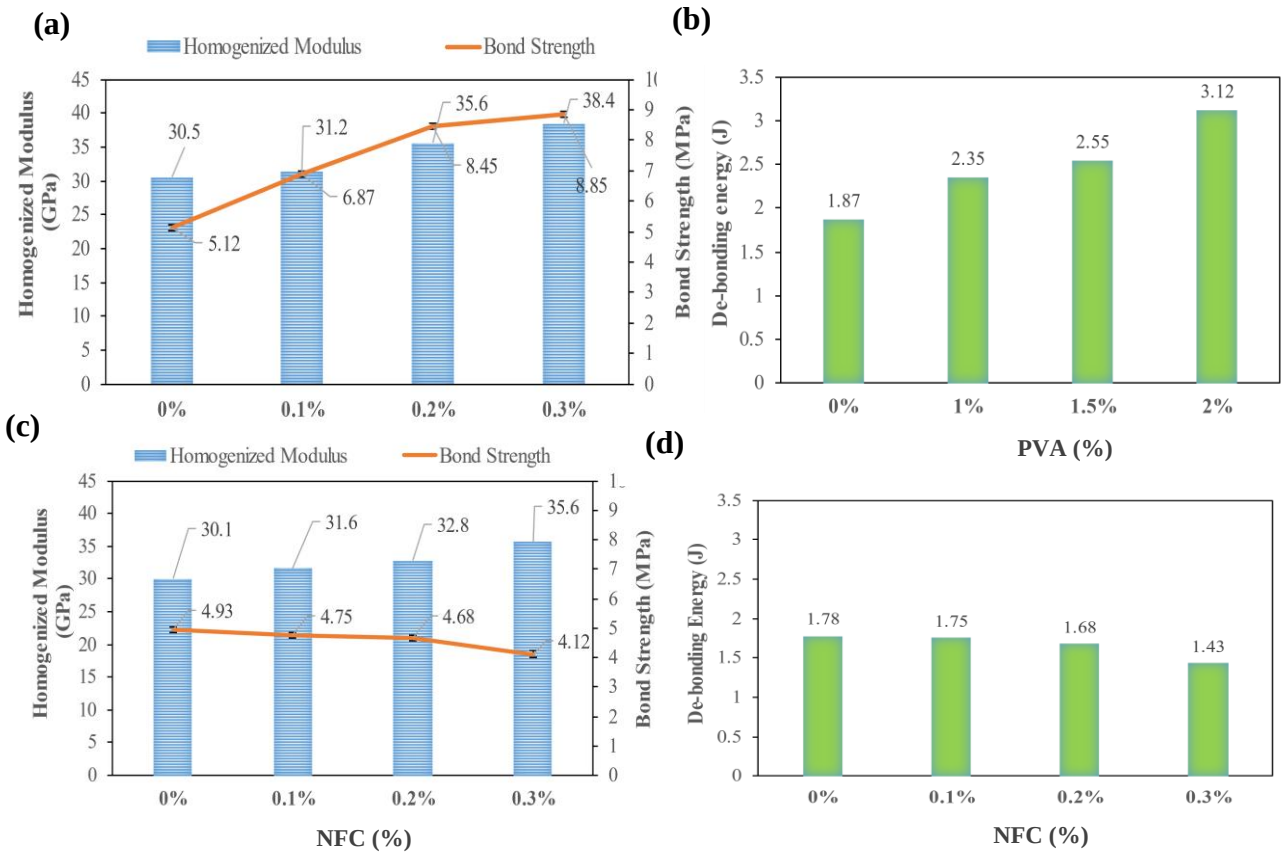


Figure 4.16: Parametric analysis results: (a) homogenized modulus and bond strength of mixture G-N reinforced with PVA, (b) debonding energy, (c) homogenized modulus and bond strength of mixture G-NCC reinforced with NFC, and (d) debonding energy.

CHAPTER 5: BONDING EVALUATION OF NANO-SILICA MODIFIED SLAG-BASED COMPOSITES COMPRISING BASALT PELLETS AND POLYVINYL ALCOHOL FIBERS

In Chapters 3 and 4, the general properties, and the fundamental performance of the developed composites in terms of mechanical properties, durability performance, load transfer, toughening and BFP/matrix interaction were studied. In this chapter, the synergetic evaluation of the mechanical capacity of HPFRCC (comprising nano-silica, cement, slag, PVA and BFP), and its bonding capacity (slant shear, bi-shear, pull-out) with precast conventional concrete and steel rebars were studied. These results were essential to determine the suitability of these composites as a filler material in jointing applications.

5.1 Introduction

The use of cementitious composites as fillers [e.g., shear key joints] between precast normal/conventional concrete segments [e.g., in bridges] is common due to their rapid assembly and high-performance [Jiang *et al.*, 2015; Wang *et al.*, 2019; Jia *et al.*, 2020]. These joints, which are typically cast-in-place, comprise reinforcing bars to ensure the continuity and load transfer between segments. According to AASHTO (LRFD) Bridge Design Specification [2020], load transfer at these joints is obtained by efficient bonding between cementitious composites, rebars and precast concrete. At these joints, there are various stress configurations such as direct tension, direct shear, and a combination of compression and shear. Hence, poor bonding of materials in these connections my lead to cracking, premature deterioration and loss of monolithic behavior among concrete segments [Russell, 2011]. A viable way to mitigate these detrimental effects is to fill the

joints with high-performance materials that are able to control the nucleation, coalescence, and spreading of cracks [e.g. Yang *et al.*, 2010; Ranade *et al.*, 2013; Bandelt and Billington, 2016].

Numerous experimental studies have focused on improving the bond behavior of shear key joints with different types of filler materials (e.g., non-shrinking grouts, magnesium-ammonium phosphate mortars, epoxy, polymer concrete) [e.g., Julander *et al.*, 2012; Weber *et al.*, 2015; Arafa *et al.*, 2016]. High-performance fiber-reinforced cementitious composites (HPFRCC) can be adopted as joint fillers, owing to its stable behavior in terms of durability and mechanical properties. HPFRCC has received increased attention due to its superior ductile post-cracking behavior under tension, flexural, impact loading, and compatibility with parent concrete, depending on mixture parameters. Various types of binders (General Use cement [GU], fly ash, slag, etc. with water-to-binder [*w/b*] ratios ranging from 0.25 to 0.35) have been utilized in HPFRCC with different geometries and types of fibers (e.g., steel, polyvinyl alcohol [PVA]) [e.g. Pan *et al.*, 2015; Meng *et al.*, 2017]. Moreover, nano-silica have been used in HPFRCC to modify hardened properties and improve the microstructure. For example, nano-silica (6% by mass of cement-based binders) with/without supplementary cementitious materials nucleates as additional sites for deposition of hydration products [Kong *et al.*, 2012; Said *et al.*, 2012], accelerates the pozzolanic reactivity [Kong *et al.*, 2012, Ghazy *et al.*, 2016b], improves the filler effect in the hardened paste, and decreases *w/b* in the paste (ultrahigh surface porosity absorption) [Kong *et al.*, 2012].

Different sizes and types of natural, synthetic, and metallic fibers have been utilized to enhance the hardened and plastic characteristics of HPFRCC. For example, PVA micro-fibers have a modulus of elasticity up to 66 GPa, with tensile capacity (up to

1600 MPa) [Li *et al.*, 2001]. For instance, using the slant shear test, Zanotti *et al.* [2018] investigated the interfacial bonding between parent concrete with fiber reinforced repair concrete comprising 0.5% and 1% PVA micro-fibers of length 8 mm and 12 mm, and steel fibers of length 13 mm. Three different bonding plane inclinations: 30°, 25°, and 20° with the vertical axis were applied. It was reported that 1% PVA micro-fibers (12 mm) and 0.5% of steel fibers (13 mm) were able to deviate the micro-cracks away from the interfacial zone and increased the adhesion (c) up to 103% and 98%, respectively. However, increasing the volume fraction of steel fibers from 0.5% to 1% reduced adhesion due to formation of additional interfacial transitional zones (ITZs), which acts as a weak links at the interface [Zanotti *et al.*, 2018]. Al-Madani *et al.* [2017] studied the interfacial bond between normal concrete substrate and ultrahigh performance concrete (UHPC) concrete comprising a mixture of 1% straight and hooked end steel fibers with a diameter of 0.2 mm and 0.35 mm, and a length of 13 mm, and 25 mm, respectively, using the bi- shear (direct shear) test as well as slant shear test at an inclination angle of 30° with the vertical. It was reported that the bond strength in the slant shear test was much higher relative to the bi-shear test (approximately 4.5 times) due to the effect of normal stress, which increased the friction between the contact layers in the slant shear test [Al-Madani *et al.*, 2017].

Kim *et al.* [2013] studied the interfacial bonding between glass fiber reinforced polymer rebars and fiber-reinforced concrete with two different dosages (0.5%, 1% by volume) of fibers (i.e., steel, polypropylene (PP), and PVA). It was reported that 1% PVA or steel fibers improved the pull-out bond strength by 25%, and 14%, respectively, as these fibers impeded the creation and propagation of cracks and their growth in the matrix [Kim *et al.*, 2013]. Similarly, Wang *et al.* [2015] investigated the interfacial

bonding behavior between basalt fiber reinforced polymer rebars and engineered cementitious composites containing PVA micro-fibers (2% by volume) of length 12 mm, where the addition of PVA fibers controlled micro-cracking and improved the bond strength between rebars and the matrix by 35% [Wang *et al.*, 2015].

Basalt fibers are deemed to be a relatively type of fibers that have emerged in the concrete research owing to their mechanical properties (modulus of elasticity up to 110 GPa and high tensile strength up to 4000 MPa), non-corrosive nature, thermal resistance, and reduction in cost relative to other alternative fibers such as carbon and glass fibers [Ayub et al., 2014; Iyer et al., 2015; Arslan et al., 2016; Iyer et al., 2016; Ghazy et al., 2016a]. Initially, basalt fibers have excellent adhering with the cementitious matrix, but this bond diminishes with time due to alkali-silica reactions between the pore solution in the paste and the silicate component of basalt. To mitigate this technical limitation, a new form termed basalt fiber pellets (BFP) has been introduced, in which basalt strands are covered with a polymeric resin (e.g. polyamide [Mahmoud et al., 2017]) for protection against alkaline media. Few studies reported that the incorporation of BFP (single system) in HPFRCC improved the bond behaviour with uncracked and pre-cracked normal/conventional concrete (CC) under flexural [Azzam *et al.*, 2022]. The HPFRCC had high integrity with the CC, where the two layers acted as one unit under flexural loading, with no signs of transverse delamination [Azzam *et al.*, 2022]. Moreover, the bond behavior of sand-coated glass fiber-reinforced polymer rebars with straight/headed-ends embedded in HPFRCC comprising BFP was evaluated [Bediwy and El-Salakawy, 2021]. It was reported that the presence of BFP kept the intactness of concrete blocks with no signs of cracks/crushing [Bediwy and El-Salakawy, 2021]. While many studies reported that the performance of hybrid fiber systems exceeds that of the individual fibers

in HPFRCC [e.g., Wang *et al.*, 2019; Özkan and Demir, 2020; Özkan and Demir, 2021; Elhadary and Bassuoni, 2021]. So far, there is scarce data on exploring the bonding behavior of HPFRCC comprising single BFP or hybrid BFP/PVA systems for jointing applications, hence the motive for this study.

5.1.1 Research Significance

Ongoing efforts at the University of Manitoba led to developing HPFRCC composites reinforced with BFP [Mahmoud *et al.*, 2017; Azzam *et al.*, 2019; Azzam *et al.*, 2021] and hybrid BFP/PVA systems [Elhadary and Bassuoni, 2021]. These composites showed improved mechanical and durability properties including high ductility under static and dynamic loadings, and resistance to ingress of fluids and frost action without/with deicing salts. Yet, focused research is still needed on other aspects such as exploring the bonding capacity between repair/filler HPFRCC and parent (conventional) concrete under shear configurations, as well as its interaction with reinforcing rebars. Considering the compressive and tensile capacity aspects, the main objective of the study herein was to evaluate the bonding performance of HPFRCC comprising high volume-slag and nano-silica with single BFP or hybrid BFP/PVA by slant shear, bi-shear, rebar pull-out tests. The bulk trends were corroborated with thermogravimetry and microstructural analyses. Such results are critical to determine the suitability of these composites for jointing applications.

5.2 Experimental Program

5.2.1 Materials and Mixtures

The base binder of 700 kg/m^{2}consists of cement (GU) and slag (grade 100) according to the requirement of CSA-A3001 [2018]. Also, nano-silica solution (NS) was used as an

additive to the base binder; where the used solution comprises 50% SiO_2 dispersed particles in an aqueous solution with a density of 1.1 g/cm^3, and its mean particle size, specific surface area, pH values, and viscosity are 35 nm, 80,000 m^2/kg, 9.5, and 8 cP, respectively. The used fine aggregate in the mixtures has a continuous gradation of 0 to 600 μm, and its specific gravity, absorption, and fineness modulus are 1.5%, 2.6, and 2.9. The workability of the mixtures was enhanced through utilizing a high-range water reducer (HRWR): poly-carboxylic acid-based complying with ASTM C494 Type F [2017], to realize a target flow table diameter of 180±20 mm. Two different fiber types were used in the mixtures: PVA micro-fibers and BFP macro-fibers (**Table 5.1).**

Six mixtures comprising 50% GU cement and 50% slag by mass of the base binder (700 kg/m^3) at *w/b* of 0.3 were prepared, complying with HVSCM-1 (high volume supplementary cementitious materials category 1), according to Annex K in CSA 23.1 [2019]. The nano-silica was incorporated in the binder at a fixed dosage of 6% by mass in (i.e., ternary binder content of 742 kg/m^3) five mixtures, as this dosage improved the mechanical properties as described in previous studies [e.g., Ghazy *et al.*, 2016b; Azzam *et al.*, 2019]. The mixtures included either single macro-BFP or hybrid PVA/BFP fibers. Mixtures reinforced with single fiber system encompassed 2.5% or 4.5% BFP, while the mixtures with the hybrid fiber system consisted of 2.5% or 4.5% BFP mixed with 1% PVA. **Table 5.2** lists the proportions of all mixtures. For the mixtures' ID., the letters B, G, V, and N denote BFP, slag, PVA, and nano-silica, respectively while the dosages of fibers were indicated by numbers.

Initially, the dry ingredients were put in the concrete pan mixer (60 rpm), and then a gradual addition of liquid phases (NS, water, and admixtures). Subsequently, PVA and/or BFP fibers were mixed with the ingredients for 7-10 minutes until achieving

uniform distribution of fibers. A vibrating table was utilized to compact HPFRCC in the molds. After that the surface of each specimen were covered using polyethylene sheets for 24 h. All specimens were then demolded and kept in a standard curing room at a temperature of 22±2°C with a relative humidity of at least 95%.

5.2.2 Testing

Triplicate cylinders of 100 diameter and 200 mm height were used to determine the compressive strength of HPFRCC at 56 days as per ASTM C39 [2018]. The tensile properties of HPFRCC materials were assessed by a quasi-static direct tension test. In this test, triplicate cylinders (75×250 mm) were tested under axial tensile loading at 56 days at a displacement rate of 0.2 mm/min, in which 75 mm represents the bonded length of each specimen between sleeves with 100 mm free length [Azzam *et al.*, 2021]. In this test, the tangent's slope was used to calculate the strain hardening modulus in the post-cracking stage, while the area underneath the stress–strain curves was used to determine the energy absorption capacity (toughness) up to a limit of 4%.

To study the interfacial bond strength of HPFRCC with conventional concrete (CC) and steel reinforcement, the slant shear (combination of compressive and shear stresses at the interface plane), bi-shear (pure shear at the interface plane, and rebar pull-out tests were conducted. The CC mixture (GU cement 400 kg/m^3 with 15% Type F fly ash replacement at 0.4 *w/b*) is typical of the superstructure (decks and girders) in concrete bridges in Manitoba with a 45 MPa compressive strength at 28 days.

In the slant shear test, triplicate composite cylinders (100 diameter and 200 mm height) were tested at 56 days according to ASTM C39 [2018]. First, the CC was placed in inclined wooden form to fill out half of the cylinder at 45º and 33.7º with the vertical. The 45º inclination angle was selected to achieve the maximum shear stresses [Craig and

Taleff, 1996; Lubliner, 2016], whilst the 33.7º represented the critical angle (the theoretical bond angle) combining shear and normal stresses at the interfacial plane, according to ASTM C882 [2020]. The CC half cylinders were kept in a standard curing room (kept at a temperature of 22±2°C and a minimum relative humidity of 95%) for 28 days. After curing, the inclined surface was wire brushed, cleaned with compressed air, and misted with water to act as a substrate layer; the HPFRCC was then cast to fill the other half of the inclined molds. The specimens were then kept in the standard curing room until testing at 56 days.

Figure 5.1(a) shows the slant shear set-up, including the linear variable differential transducers (LVDT) to measure the resultant displacement (perpendicular and parallel) at the interfacial plane during loading. The adhesion and coefficient of friction can be determined using Mohr's circle (**Equation 5.1)** and **(Figure 5.2)**, where: τ_n and σ_n are the shear and normal (positive for compression) stresses acting on the bond interface; c is the adhesion strength (the pure shear strength), $\mu = \tan(\phi)$ is the coefficient of friction, ϕ is the internal friction angle, F is the measured vertical compression force of the composite cylinders, α is the angle of inclination with the vertical, and A is the cross-section area.

$$\tau_n = c + \mu\ \sigma_n \qquad \textbf{(Equation 5.1)}$$

$$\sigma_0 = F/A \qquad \textbf{(Equation 5.2)}$$

$$\sigma_n = \sigma_o\ sin^2\ (\alpha) \qquad \textbf{(Equation 5.3)}$$

$$\tau_n = 0.5\ \sigma_o\ sin\ (2\alpha) \qquad \textbf{(Equation 5.4)}$$

To evaluate the adhesion behavior between HPFRCC and CC under direct shear, the bi-shear test was conducted at 56 days at a stress rate of 0.25 MPa/s matching that in

the slant shear test. Triplicate CC cubes (150 mm) were prepared, cured for 28 days and prepared in a similar manner to the slant shear specimens. Subsequently, the HPFRCC was cast over the prepared surface (roughened, cleaned, misted) to form an additional thickness of 50 mm. The concrete block was supported at the outside edge by two steel plates, whilst the loading plates rested on the CC at the interface with HPFRCC; the interface slip was measured by attaching LVDT at the interface during loading [**Figure 5. 1(b)]**. The direct bond strength was calculated by **Equation 5.5**, where: τ = interfacial shear bond strength, P = maximum applied load, and $[A]$ = Area of the interface.

$$\tau = P/2[A] \qquad \textbf{(Equation 5.5)}$$

In the rebar pull-out test [**Figure 5.1(c**)], triplicate cubes (200) mm were tested at 56 days following RILEM 7-II-128 [1994] guidelines. Each cube contained a 15M (16 mm) deformed steel re-bar with an embedment length 3 times the bar diameter, i.e., 48 mm. Many studies [e.g., Yuan and Graybeal, 2015; Ronanki *et al.*, 2018; Khaksefidi *et al.*, 2021] reported that the rebar pull-out mode is dominant when the embedded length ranges from 2 to 4 times the diameter. Moreover, polyvinyl chloride tubing was utilized for the remaining bar length (152 mm) to decrease the contact area between concrete and steel and keep the failure load below the machine capacity. The slippage of the free and loaded ends of steel bar in each specimen was monitored using LVDTs under a constant loading rate of 0.5 kN/s. Data aquisition system was utilized to collect the readings of LVDT and loading machine. The bond strength (τ_b) was calculated by **Equation 5.6**, where T is the ultimate failure load, d is the steel bar diameter and Le is the embedment length in contact with concrete (48 mm).

$$\tau_b = T/\pi dLe \qquad \textbf{(Equation 5.6)}$$

Mercury intrusion porosimetry (MIP) tests were conducted for the three matrices (G, G-N, and G-N-V1) comprising the BFP to study their pore structure at 56 days. Two concrete cylinders were cast for each mixture to extract small pea-sized chunks (4-7 mm) as test samples. After that samples were dried in an oven at 50±2°C with silica gel till attainment of a constant mass, in order to decrease the effect of hydration products decomposition and drying cracks at higher temperatures. The apparatus has a pressure range from sub-ambient to 228 MPa. By assuming a cylindrical geometry of the pores, mercury contact angle of 130° and surface tension of 0.485 N/m, the high-pressure limit (228 MPa) yields a pore radius of approximately 3 nm, implying intrusion of all capillary pores. The results from the bulk tests were corroborated with microscopy and thermal tests. For thermogravimetric analysis (TGA), powder samples extracted from cylinders, crushed by a mechanical grinder and passing through #200 [75 μm] sieve, were heated at a constant rate 10°C/min, to evaluate the content of CH calcium hydroxide in the matrix versus age. Besides, fracture carbon coated pieces at the interfacial plane between HPFRCC/CC were investigated by EDX (elemental dispersive X-ray) along with SEM (Scanning Electron Microscope) at 56 days.

Table 5.1: Properties of fibers

Property	PVA	BFP
Length (mm)	12	36
Diameter/width (mm)	38×10^{-3}	1.8
Aspect ratio	315	20
Specific gravity	1.3	1.7
Tensile strength (MPa)	1,600	2,300
Elastic modulus (GPa)	66	65
Volume fraction [V_f] (%)*	1	2.5, 4.5

*PVA and BFP are expressed by volume of composite.
**The mechanical properties of BFP (macro-fiber), and PVA (micro-fiber) were provided by the manufacturers.

Table 5.2: Mixtures proportions per cubic meter

Mixture ID	Cement (kg)	Slag (kg)	Water* (kg)	NS (kg)	Fine Aggregate (kg)	PVA (kg)	BFP (kg)	Air Content (%)
G-N	350	350	180	84	1232	--	--	5.4
G-B2.5	350	350	210	--	1288	--	43.3	6.9
G-N-B2.5	350	350	180	84	1167	--	43.3	6.5
G-N-B4.5	350	350	180	84	1115	--	78.3	7.4
G-N-B2.5-V1	350	350	180	84	1142	13	43.3	7.4
G-N-B4.5-V1	350	350	180	84	1090	13	78.3	8.2

*Adjusted amount of mixing water considering the water content of NS (50% solid content).

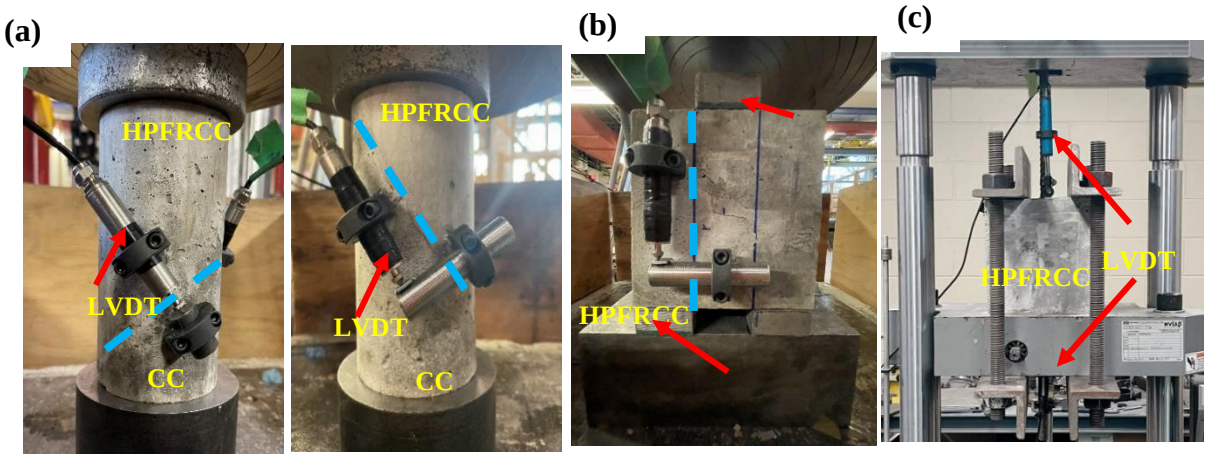


Figure 5.1: Tests set-up: (a) slant shear, (b) bi-shear, and (c) rebar pull-out.

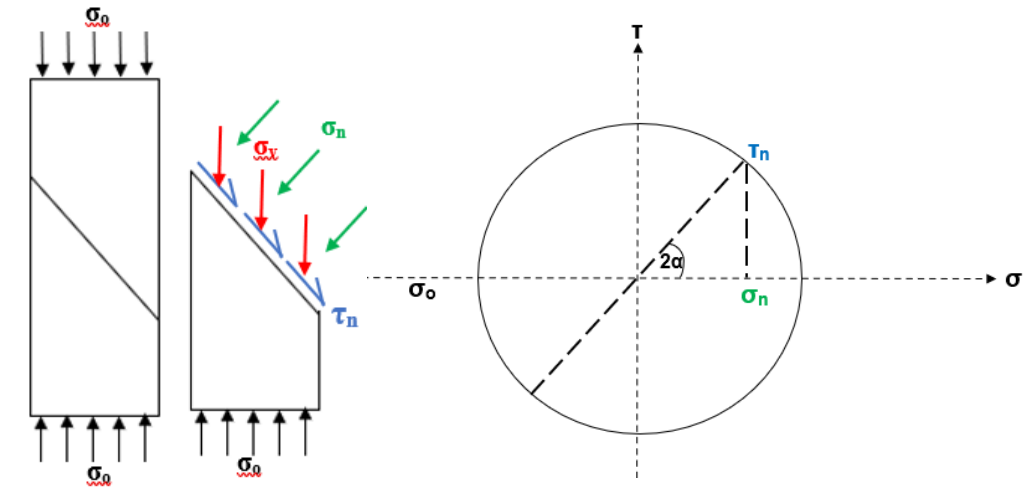


Figure 5.2: Slant shear stress configuration and Mohr's circle.

5.3 Results and Discussion

5.3.1 Mechanical Capacity of HPFRCC

5.3.1.1 Compressive Strength and Hydration Development

Table 5.3 lists the compressive strength of the full cylinders made from HPFRCC, which ranged from 65 to 87 MPa. The improvement for the nano-modified mixtures was more tangible (up to 15%) at 7 and 28 days than that at 56 days (5%), which is the stipulated age to assess the performance of concrete comprising SCMs [CSA A23.1, 2019]. This corresponded to the pore structure refinement in the G-N compared with reference matrix G (**Table 5.4:** reduction in porosity and threshold pore diameter: 11% and 27%, respectively, and increase [32%] in the proportion of micro-pores). The thermal analysis (**Figure 5.3**) showed that the normalized CH contents in the G-N binder compared with reference G binder continuously decreased from 0.82 at one day to 0.33 at 90 days, with almost constant values between 28 and 90 days. This can be ascribed to the ultrahigh specific surface of NS (80,000 m^2/kg), which acts as nucleation sites for early precipitation of hydration products [Kong *et al.*, 2012]. This process was coupled with vigorous pozzolanic reactivity (consumption of CH from early-age to precipitate additional/secondary C-S-H) up to 28 days, as indicated by the steeper slopes of the TG curve in **Figure 5.3**. Subsequently, the CH reduction in the G-N binder continued at a lower rate up to 90 days matching that in the G (reference) binder due to the long-term slow reactivity of slag (latent hydraulic binder). In addition, the particle packing/filling effect of nano-silica contributed to densifying the microstructure.

Adding BFP to the nano-modified cementitious composites reduced their compressive strength at 56 days. For example, the compressive strengths of G-N-B4.5 and G-N-B2.5 and specimens were 17% and 5%, respectively lower than G-N specimens

(87 MPa). This behavior could be linked to the interaction between BFP macro-fibers and the matrix at the mixing stage, resulting in increased air contents (**Table 5.2**). This behavior could be linked to the stress concentration effect of the created ITZs due to the BFP, especially with the higher dosage of BFP, resulting in reduction in the compressive capacity.

Regarding the hybrid fiber system, combining 1% micro-PVA fibers with macro-BFP fibers (i.e., G-N-B2.5-V1 and G-N-B4.5-V1) slightly (average of 4%) increased the compressive strength of composites compared with that of the reference mixture with no PVA fibers (G-N-B2.5 and G-N-B4.5). However, the inclusion of the PVA micro-fibers changed the mode of failure from sudden crushing of the matrix to gradual evolution of multiple cracking, where the matrix stayed intact after reaching its capacity [**Figure 5.4(a) vs. Figure 5.4(b)]**. This trend can be explained by the microstructural modification brought about by the supplement of PVA micro-fibers to the matrix. While the hydration/pozzolanic development of mixtures G-N-V1 and G-N are comparable (same base binder) as shown by the TG curves and normalized CH contents of approximately 1.0 (**Figure 5.3**), the MIP results (**Table 5.4**) showed that mixture G-N-V1 had relatively denser pore structure as the proportion of micro-pores increased to 64%. PVA micro-fibers interrupted the continuity of capillary pores; in addition, the hydrophilic effect of PVA might have led to a reduction of apparent *w/b*, and thus enhancing their ITZ with the matrix [Liu *et al.*, 2011]. Moreover, the syngenetic interaction between PVA micro-fibers and BFP macro-fibers led to impeding the creation of micro-cracks and controlling spreading of macro-cracks in the matrix, and consequently improving the matrix integrity.

Table 5.3: Compressive strength (MPa) of composites

Mixture ID	Age (Days)		
	7 days	28 days	56 days
G-N	80 (8.1)	85 (8.3)	87 (8.5)
G-B2.5	65 (6.8)	76 (7.3)	79 (7.4)
G-N-B2.5	75 (7.3)	80 (7.9)	83 (8.1)
G-N-B4.5	66 (6.7)	70 (6.9)	72 (8.0)
G-N-B2.5-V1	79 (7.4)	83 (8.1)	85 (8.3)
G-N-B4.5-V1	68 (6.8)	73 (7.2)	75 (7.3)

Note: Values in parentheses are standard deviations.

Table 5.4: Summary of the MIP test results

Mixture ID	Apparent Total Porosity (%)	Threshold Pore Diameter (μm)	Proportion of Micro Pores [<0.1 μm] (%)
G	11.6	0.11	44
G-N	10.3	0.08	58
G-N-V1	10.4	0.07	64

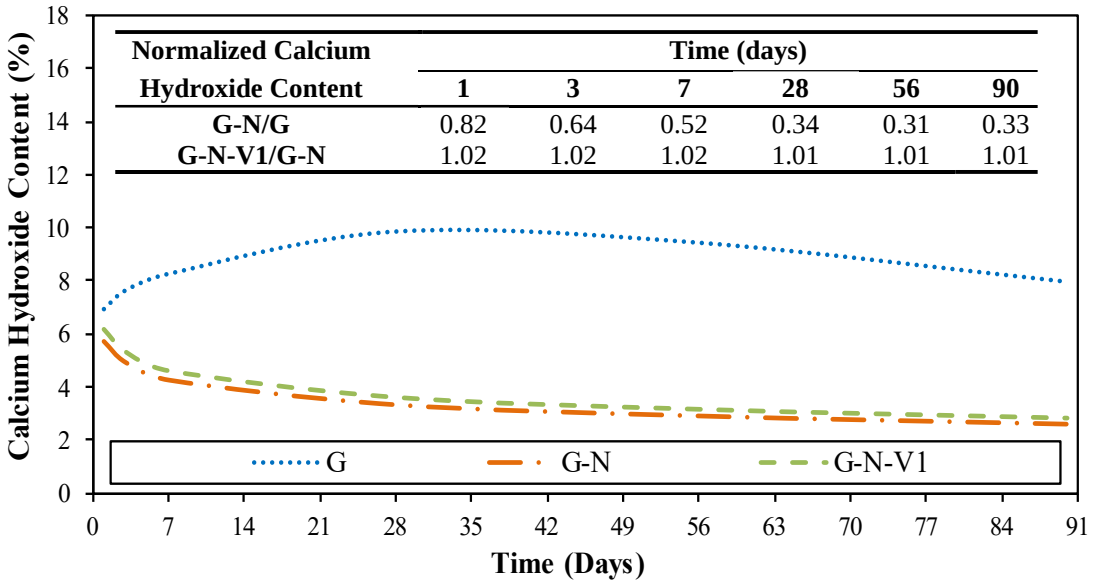


Figure 5.3: TGA results for the CH contents (at a temperature range of 400 to 450°C) in the mixtures.

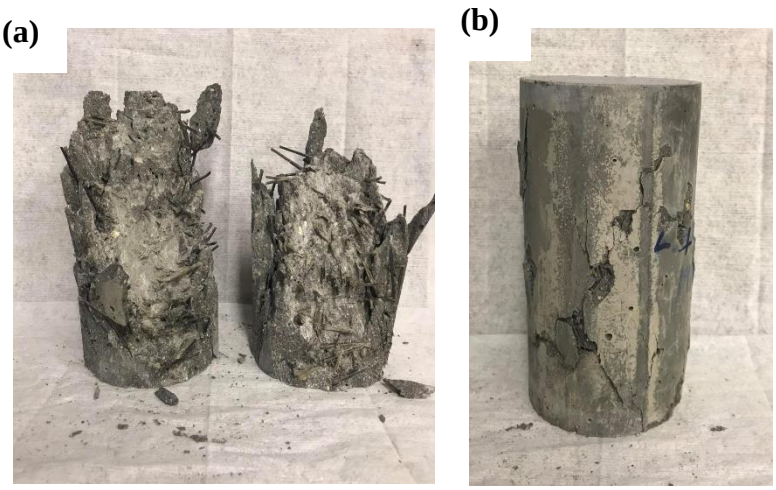


Figure 5.4: Exemplar mode of failure of specimens after the compressive strength test at 56 days: (a) G-N-B2.5, and (b) G-N-B2.5-V1.

5.3.1.2 Tensile Strength

Table 5.5 lists the tensile properties of the composites at 56 days depending on the stress-strain behavior of the quasi-static direct tension test (**Figure 5.5**). The failure of all specimens took place within the middle section due to transverse cracks (e.g., **Figure 5.6**), because of the consistent geometry of the specimens, which alleviated the concentration of stress near the ends. The incorporation of nanoparticles (6% NS) into the cementitious matrix led to marked enhancement in the tensile capacity of composites. The first-cracking strength of G-N-B2.5 specimens was 52% higher than that of G-B2.5 specimens; correspondingly, the modulus of elasticity of G-N-B2.5 specimens was 24% higher than that of G-B2.5 specimens (**Table 5.5**). This trend can be explained by the improvement of the matrix degree of maturity and pore structure refinement brought about by the chemical and physical effects of nano-silica as explained in Section 3.1.1.

Similar to the compressive strength trends, the incorporation of BFP reduced the tensile strength of the composites (**Table 5.5**). For instance, the first-cracking strength and modulus of elasticity of G-N-B2.5 and G-N-B4.5 specimens were 13% and 6% and

20% and 10%, respectively lower than that of G-N specimens, which were 4 MPa and 32.9 GPa, respectively. This was linked to the increase in the air content associated with BFP (**Table 5.2**) and the creation of additional ITZs. Comparatively, the addition of 1% PVA micro-fibers resulted in improving the tensile capacity of the nano-silica-modified composites. For instance, the first-cracking strength and elastic modulus for G-N-B2.5-V1 and G-N-B4.5-V1 specimens were 11% and 4%, and 19% and 5%, respectively higher than that of G-N-B2.5 and G-N-B4.5 specimens, which were 3.5 MPa and 31.1 GPa, and 3.2 MPa and 29.6 GPa, respectively (**Table 5.5**). This could be attributed to the combined chemical and hydrophilic effects (surface OH^- groups) of PVA, led to discounting *w/b* in the paste and creation of cross links at the boundaries between PVA and matrix, associated with improving the quality of ITZs and interfacial bonding [Liu *et al.*, 2011]. In addition, PVA micro-fibers segmented the capillary pore system (**Table 5.4**) as discussed in Section 3.1.1, and synergistically complemented BFP macro-fibers to bridge and control the initiation and spreading of cracks in the matrix, thus improving its tensile capacity.

Beyond the first-cracking strength, various trends were obtained depending on nano-modification and the dosage and type of fibers for the composites (**Figure 5.5**). The inclusion of 6% NS with BFP (i.e., G-N-B2.5 specimens) improved the interfacial bonding between the pellets and matrix as indicated by the significant increase (179%) in toughness with a strain hardening modulus of 3.5 MPa, relative to the corresponding mixture without nano-silica (i.e., G-B2.5) [**Table 5.5**]. SEM and EDX analysis indicated that the addition of NS led to intense accumulation of cementitious products in the micro-groves of BFP (e.g., **Figure 5.8)** cross-linking the pellets to matrix, compared with the reference matrix (G) [e.g., **Figure 5.7]**. Accordingly, significant amount of energy was

consumed to pull-out the fibers from this matrix, which is the main toughening mechanism after first-cracking. The structure of the cementitious gel at the interface zone had average *Ca/Si* of 1.18 relative to 1.75 in the reference binder G, indicating efficient pozzolanic reactivity associated with filling effect of the former leading to deposition of additional and stiffer [Kong *et al.*, 2012, Ghazy *et al.*, 2016b] pozzolanic C-S-H in the contact zone with BFP. This conformed to the high interfacial bond strength obtained from the rebar pull-out tests from the nano-modified composites (6% NS) as will be discussed in the Section 3.2.4. G-N-B2.5 specimens showed strain-softening (50% drop after first cracking) followed by a plateau, whilst G-N-B4.5 specimens showed a strain-hardening behavior (modulus of 17.3 MPa with 41% higher toughness (**Table 5.5)**. In addition to restraining/arresting the nucleation of macro-cracks in the matrix, this can be ascribed to the higher dosage (4.5%) of BFP in the matrix, which had high contact surface area of textured micro-grooves with enhanced adhering between the pellets and matrix (**Figure 5.8)**, which impeded the pull-out process with failure in a more ductile manner.

Addition of 1% PVA in combination with BFP had a positive effect at increasing the post-cracking tensile behavior of composites. Such hybrid fiber-reinforced composites had no or little drop in the load after the first-cracking, and they continued to sustain tensile load, relative to the corresponding composites comprising single BFP (**Figure 5.5**). For example, G-N-B4.5-V1 specimens showed a pseudo strain-hardening performance with a high hardening modulus of 30.8 MPa (**Table 5.5**). Correspondingly, the toughness of G-N-B4.5-V1 specimens was 47% and 20%, respectively higher than that of G-N-B4.5 (82.2 kJ/m^3) and G-N-B2.5-V1 (100.7 kJ/m^3) specimens. This is linked to the interactive effects of the micro-PVA surrounding macro-BFP fibers (e.g., **Figure**

5.9), as the former impeded the nucleation and coalescence of micro-cracks, and the latter controlled/arrested the spreading of macro-cracks in the composite. In addition, the PVA clusters in the matrix had a frictional/interlocking effect, which further enhanced the resistance of the matrix to pellet pull-out, resulting in significant improvement in ductility. This was indicative of higher interfacial bond strength of pulling-out rebar from the nano-modified composites comprising PVA fibers with higher dosage of BFP, as shown by the rebar pull-out trends.

Table 5.5: Tensile properties of the composites

Mixture ID	First-cracking Strength (MPa)	Elastic Modulus (GPa)	Strain Hardening Modulus (MPa)	Energy Absorption Capacity (kJ/m^3)
G-N	4.0 (0.3)	32.9 (0.3)	--	5.82 (1.4)
G-B2.5	2.3 (0.4)	25.1 (0.4)	--	20.9 (2.1)
G-N-B2.5	3.5 (0.5)	31.1 (0.3)	3.5 (1.4)	58.2 (4.2)
G-N-B4.5	3.2 (0.5)	29.6 (0.6)	17.3 (1.4)	82.2 (8.5)
G-N-B2.5-V1	3.9 (0.6)	32.4 (0.8)	22.8 (2.3)	100.7 (9.1)
G-N-B4.5-V1	3.8 (0.9)	31.2 (0.9)	30.8 (2.9)	120.7 (10.9)

Note: Values in parentheses are standard deviations.

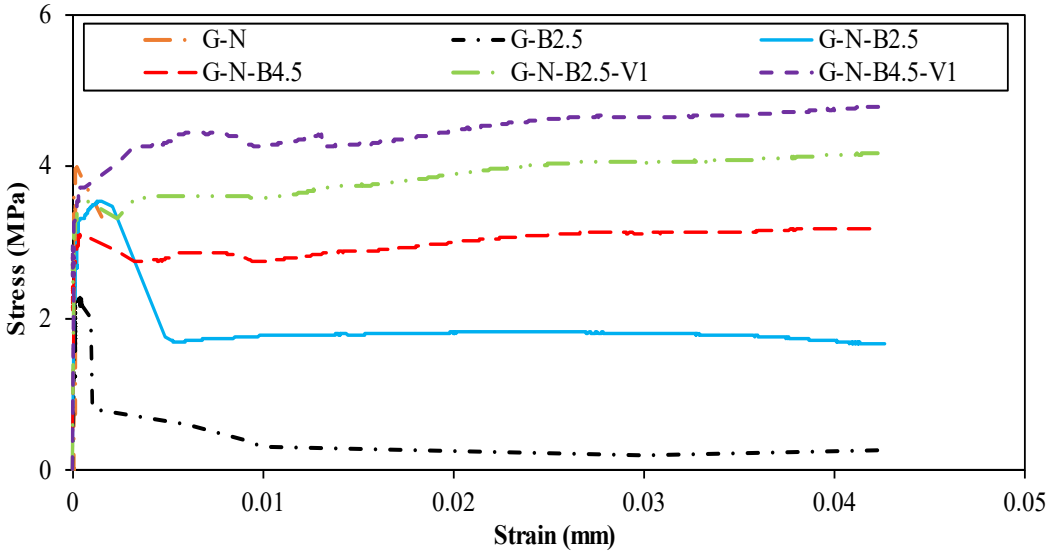


Figure 5.5: Stress-strain relationships from the direct tension test.



Figure 5.6: Exemplar failure plane after the direct tension test for the G-N-B4.5-V1 specimen.

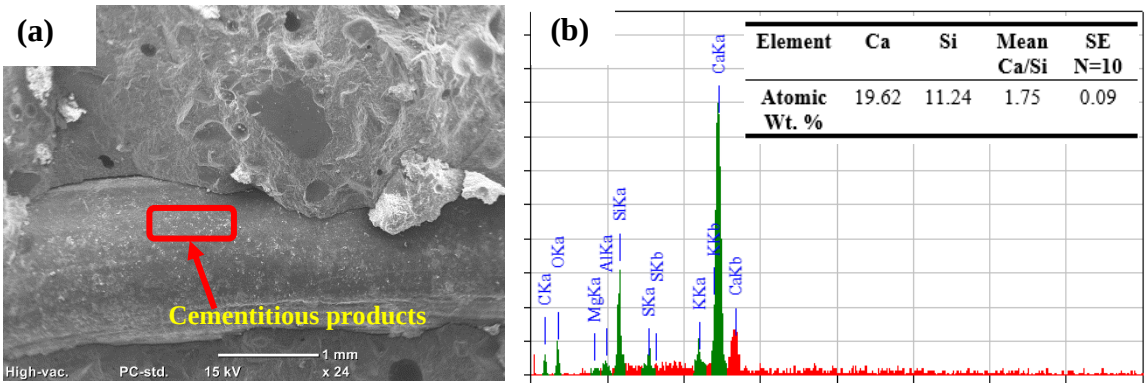


Figure 5.7: Examplar SEM micrograph for matrix G at 56 days: (a) ITZ with BFP, and (b) EDX spectrum of paste at the indicated location in (a). (SE = standard error for 10 points).

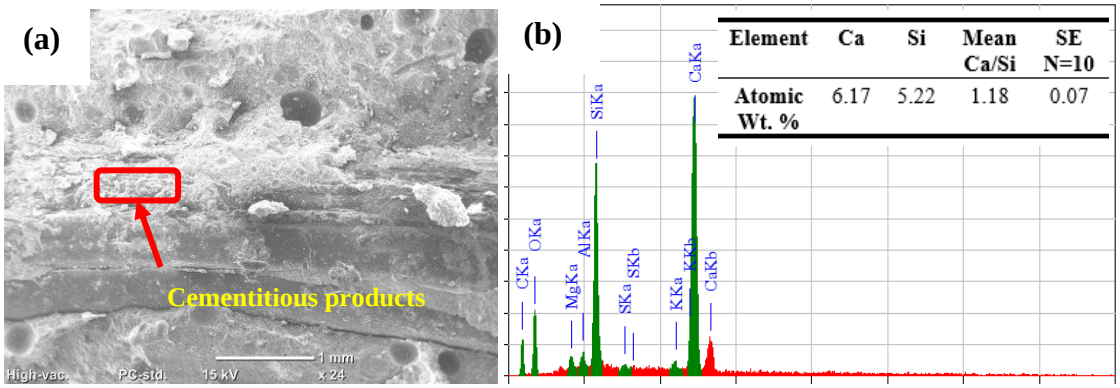


Figure 5.8: Examplar SEM micrograph for matrix G-N at 56 days: (a) ITZ with BFP, and (b) EDX spectrum of paste at the indicated location in (a). (SE = standard error for 10 points).

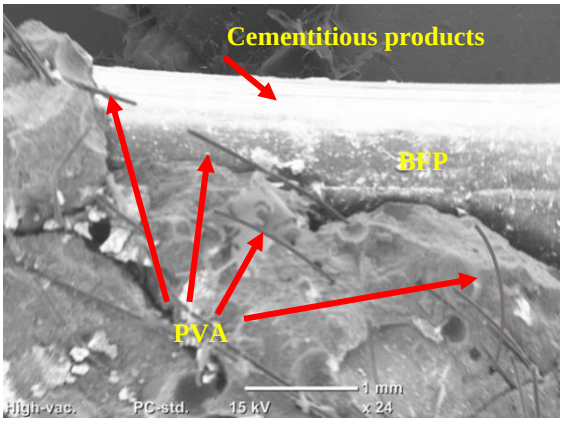


Figure 5.9: Exemplar SEM micrograph showing the interaction of BFP with PVA in G-N-B4.5-V1 specimen.

5.3.2 Bonding Evaluation

5.3.2.1 Slant Shear Strength

Three different modes of failure occurred in the composite HPFRCC/CC specimens (**Figure 5.10**). A compression failure was observed in the specimens bonded at 45º [**Figure 5.10(a)**], at an average strength (σ_o) of 45 MPa with equivalent shear and normal strength components at the interface (average value of 21.7±0.7 MPa, **Table 5.6**). Hence, at that the maximum possible shear stress (45º), the weakest link in the assembly was limited by the capacity of the CC substrate, indicating high degree of bonding with the HPFRCC layer irrespective of its mixture design. Comparatively, the other two modes of failure in the composite assemblies cast at 33.7° were either interface debonding or localized interfacial bond failure followed by cracking in the CC substrate depending on the mix design of HPFRCC [e.g., **Figure 5.10(b)-(c)**]. In these cases, the critical inclination angle used at 33.7° with the vertical, according to ASTM C882 [2020] created a higher shear stress component relative to the normal stress component by approximately 50% (**Table 5.6**) at the interfacial plane, resulting in critical sliding shear

with bonding failure at a lower strength ranging from 10 to 13 MPa, compared with the specimens bonded at 45° (equivalent shear and normal components at the interface). Accordingly, the succeeding analysis is done for this critical angle scenario.

Figure 5.11 shows representative load-displacement curves for the composite specimens cast at 33.7º. The slant bond strength (σ_o) was calculated from **Equation 5.2,** and it was in the range of 16.5 to 28.5 MPa. On the other hand, the debonding energy from the slant shear tests was determined as the area under the load-displacement curves. The mode of failure for the specimens cast without/with NS and single BFP reinforcement (i.e., G-B2.5 and G-N-B2.5) assemblies displayed interface failure [**Figure 5.10(b)**]. However, the nano-modified matrix achieved higher bonding parameters (e.g., 41% higher debonding energy) in the slant shear test (**Table 5.6** and **Figure 5.11**). This improvement could be attributed to the effective pozzolanic reactivity of NS (consumption of CH contents at the interfacial zone), resulting in deposition of additional/secondary C-S-H at the HPFRCC/CC interface, which led to improving the adhesion in this region. This was substantiated by the SEM and EDX analyses, which showed that unlike the reference matrix (G) [e.g., **Figure 5.12 (a),** *Ca/Si* of 1.80], the inclusion of NS in the HPFRCC layer led to the deposition of pozzolanic cementitious gel/at the interface with an average *Ca/Si* of 1.24 [**Figure 5.12(b)**]. This led to refined interface similar to the analogy observed from MIP trends (**Table 5.4).**

Utilizing single BFP in the matrix reduced the slant bond strength and de-bonding energy of the composites [**Figure 5.11**], according to the mechanical capacity of the HPFRCC layer. For instance, the slant bond strength and de-bonding energy of the G-N-B4.5 specimens were 15% and 10%, respectively lower than that of the G-N-B2.5 specimens, which were 20.8 MPa, and 14.0 J. In addition, the mode of failure in the

assemblies displayed interface failure [**Figure 5.10(b)**]. This behavior could be linked to the stress concentration effect of the created ITZs due to the alignment of BFP at the interface with the CC layer, resulting in a reduction in the adhesion capacity. However, the addition of PVA to BFP, forming a hybrid system significantly enhanced the interfacial bonding parameters. The slant bond strength and de-bonding energy of the G-N-B2.5-V1 and G-N-B4.5-V1 specimens were 37%, 82%, and 40%, 76%, respectively higher than that of the G-N-B2.5 and G-N-B4.5 specimens, which were 20.8 MPa, 14.0 J, and 17.8 MPa, 12.7 J, respectively. Moreover, inclusion of PVA led to a more ductile mode of failure involving localized interfacial bond followed by cracking in the CC substrate [**Figure 5.10(c)**]. This trend could be linked to the functional hydroxyl groups (OH^-) on the PVA surface, which enhanced the interaction with cement paste forming chemical bonding at the HPFRCC/CC contact surface [Zanotti *et al.*, 2018]. Accordingly, SEM micrographs [e.g., **Figure 5.13(a)-(b)**] showed that PVA micro-fibers were bound to the HPFRCC layer with fracture edges towards the CC zone; this led to increasing the chance of adhesion, friction, interlocking, and in turn bonding capacity in these assemblies. Besides, the coexistence of PVA micro-fibers with BFP macro-fibers contributed to micro-crack deviation and blunting at the interface, which enhanced interfacial bonding of the two layers and deviating the failure towards the CC substrate (weaker link).

Table 5.6: Slant shear test parameters

Mixture ID	33.7°		Mode of Failure	45°		Mode of Failure
	Shear Stress τ_n (MPa)	Normal Stress σ_n (MPa)		Shear Stress τ_n (MPa)	Normal Stress σ_n (MPa)	
G-N	10.1	6.8	Interface	21.3	21.3	CC
G-B2.5	7.5	5.1	Interface	21.1	21.1	CC
G-N-B2.5	9.5	6.4	Interface	21.6	21.6	CC
G-N-B4.5	8.2	5.5	Interface	21.5	21.5	CC
G-N-B2.5-V1	13.3	8.8	Interface +CC	22.5	22.5	CC
G-N-B4.5-V1	11.5	7.6	Interface +CC	22.6	22.6	CC

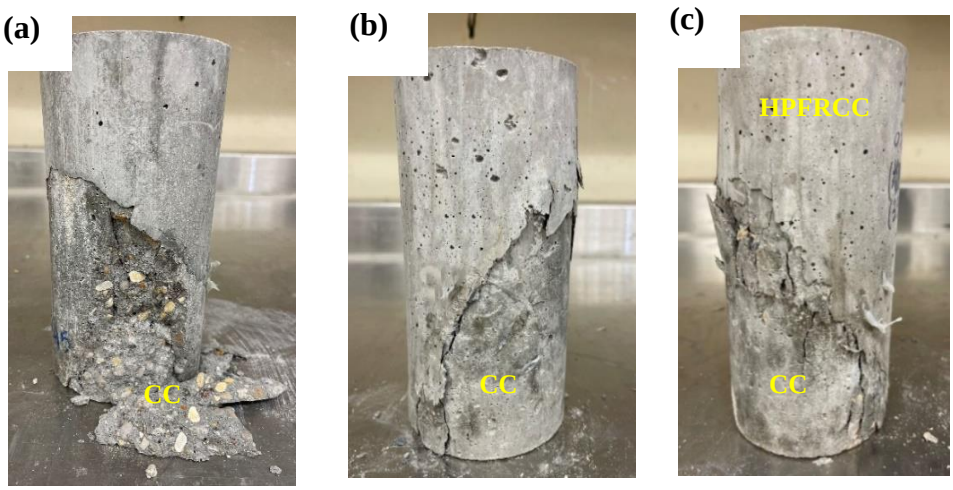


Figure 5.10: Failure modes of the composite specimes cast with HPFRCC and CC: a) compression failure of CC substrate [45º], b) interface failure [33.7°], and c) localized interfacial bond followed by cracking of CC substrate [33.7°].

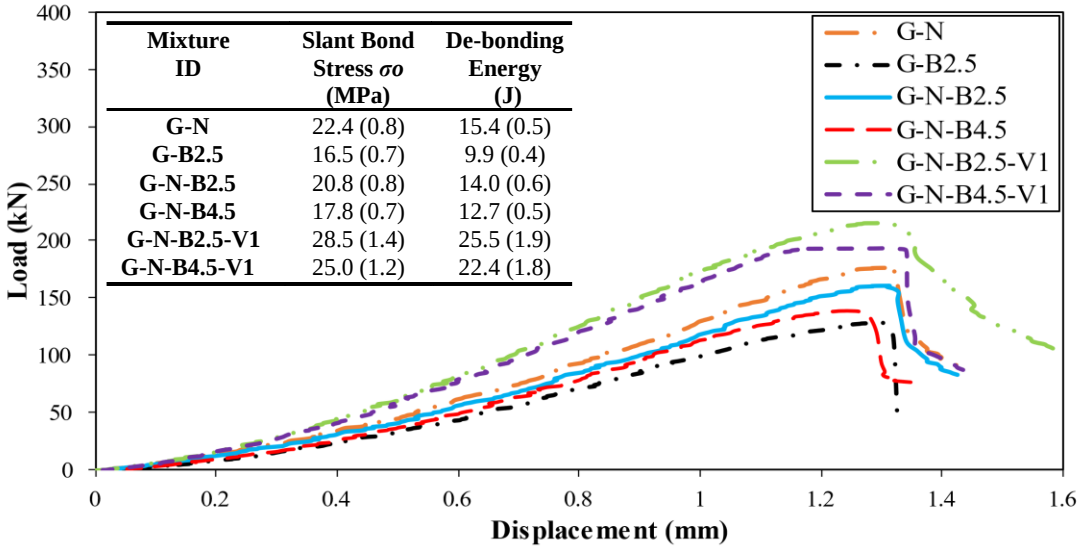


Figure 5.11: Load-displacement relationships from the slant shear test specimens at 33.7°. (Note: values in parentheses are standard deviations).

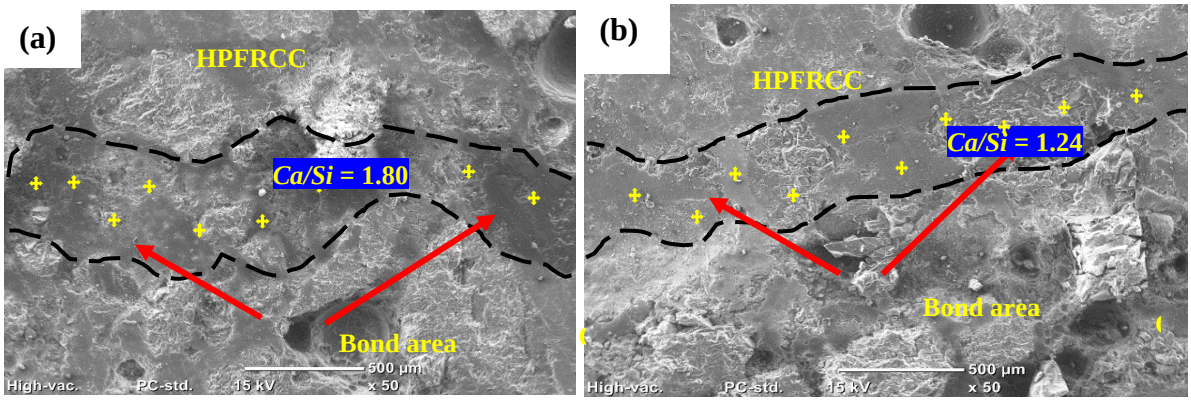


Figure 5.12: Examplar SEM micrographs and EDX at the indicated locations of the composite specimens at the HPFRCC/CC interface: (a) binder G, and (b) binder G-N.

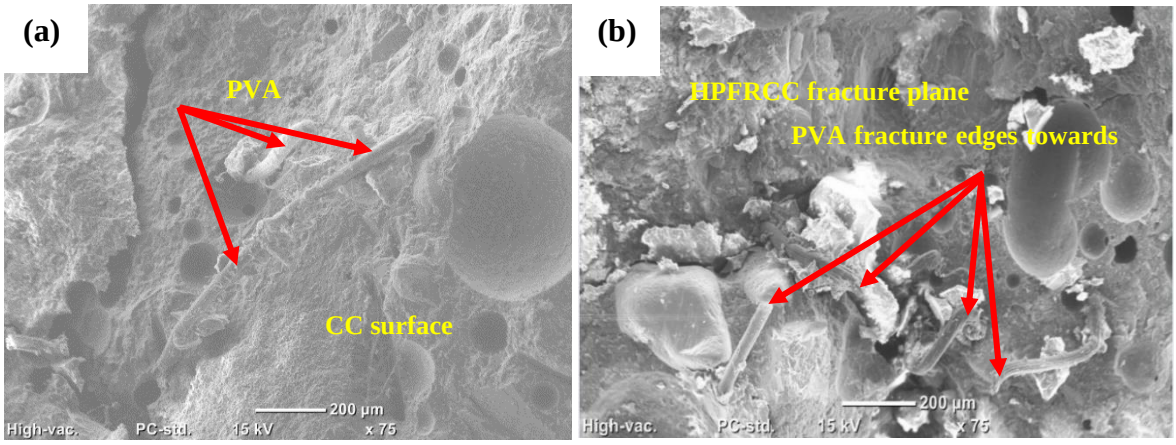


Figure 5.13: Examplar SEM micrographs at HPFRCC/CC interfaces after the slant shear tests for G-N-B4.5-V1 specimens: (a) PVA bounded to the HPFRCC at the interface with CC, and (b) fracture edges of PVA in the HPFRCC towards the CC layer.

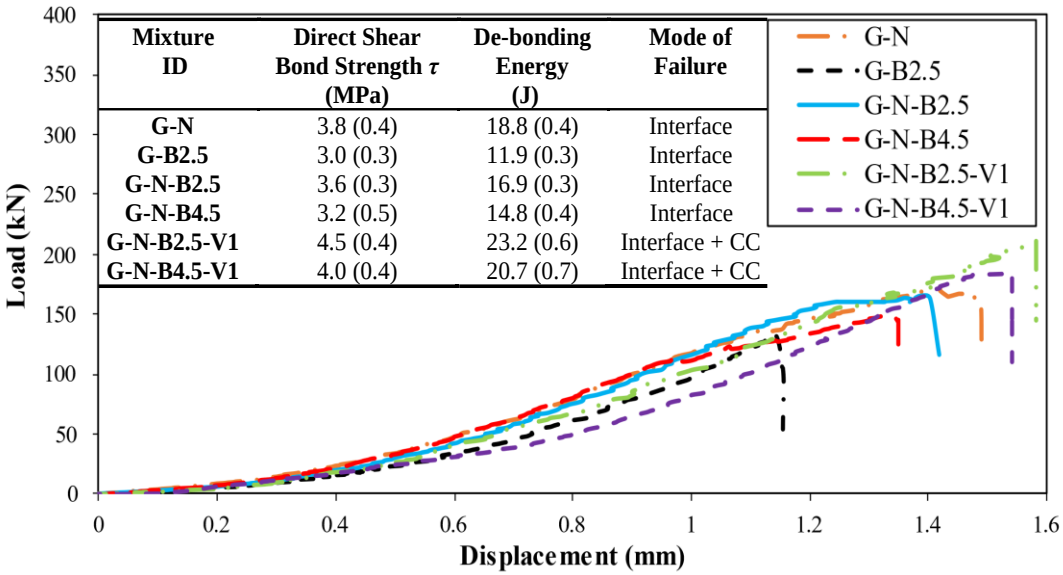
5.3.2.2 Direct Shear Strength

Figure 5.14 shows the load-displacement for all specimens cast with HPFRCC side-by-side with CC under direct shear loading. The direct shear bond strength (τ) represents the adhesion (c) in **Equation 5.1** and was calculated from **Equation 5.5**. On the other hand, the debonding energy from the bi-shear test was determined as the area under the load-displacement curve. A directly proportional load-displacement relationship up to a maximum deformation of approximately 1.6 mm was observed, which mainly depended

on the adhesion improvement due to HPFRCC mix design. All trends were confirmatory to the slant shear test. The mode of failure for all specimens cast without/with nano-silica and single BFP assemblies displayed interface failure [e.g., **Figure 5.15(a**)]. The incorporation of 6% NS into the cementitious matrix led to marked enhancement in the adhesion with the CC surface, owing to the functionality of nano-silica at the interfacial zone as explained earlier [**Figure 5.12(b)**]. For example, the direct shear bond strength and the de-bonding energy for mixtures G-N-B2.5 were 20% and 42%, respectively higher than that of the G-B2.5 specimens, which were 3.0 MPa and 11.9 J, respectively.

The incorporation of a higher dosage of single BFP macro-fibers in the nano-modified matrix reduced the adhesive capacity of the composites under direct shear (**Figure 5.14**). For instance, the direct shear strength and de-bonding energy for the G-N-B2.5 and G-N-B4.5 composites were 5%, 10%, and 16%, 21% respectively lower than that of the G-N composite, which were 3.8 MPa, and 18.8 J, respectively. This was associated with a reduction in the displacement to 1.38 mm for specimens cast with the higher dosage of BFP (i.e., G-N-B4.5). Conforming to the previous observations, this trend was linked to the additional ITZs, especially with the 4.5% BFP that acted weak links at the contact interface between the HPFRCC and CC, leading to a reduction in adhesive capacity. However, using 1% PVA micro-fibers with BFP had a significant effect at improving the adhesive capacity of the composite specimens. The direct shear bond strength and de-bonding energy for the G-N-B2.5-V1 and G-N-B4.5-V1 composite specimens were 25%, 37%, and 25%, 40%, respectively higher than that of G-N-B2.5 and G-N-B4.5 specimens, which were 3.6 MPa, 16.9 J, and 3.2 MPa, 14.8 J, respectively. Moreover, 1% PVA promoted deviation of the fracture plane from interface failure to localized interfacial cracking and crushing of CC layer [e.g., **Figure 5.15 (b)**], due to the

role of PVA in improving the adhesive capacity at the contact zone and friction between two layers, as discussed in the slant shear test. This was reflected by the larger displacement at failure and de-bonding energy.



Mixture ID	Direct Shear Bond Strength τ (MPa)	De-bonding Energy (J)	Mode of Failure
G-N	3.8 (0.4)	18.8 (0.4)	Interface
G-B2.5	3.0 (0.3)	11.9 (0.3)	Interface
G-N-B2.5	3.6 (0.3)	16.9 (0.3)	Interface
G-N-B4.5	3.2 (0.5)	14.8 (0.4)	Interface
G-N-B2.5-V1	4.5 (0.4)	23.2 (0.6)	Interface + CC
G-N-B4.5-V1	4.0 (0.4)	20.7 (0.7)	Interface + CC

Figure 5.14: Load-displacement relationships for the bi-shear test specimens. (Note: values in parentheses are standard deviations).

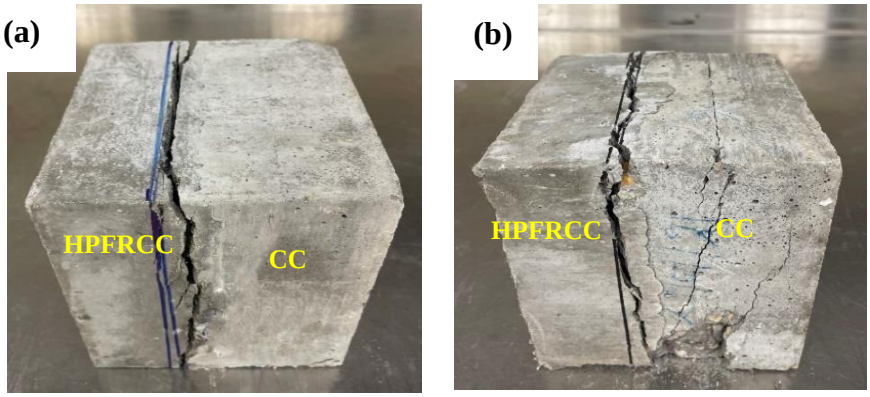


Figure 5.15: Failure modes of the composite specimes cast with HPFRCC and CC in the bi-shear test: (a) interface failure, and (b) localized interfacial cracking and crushing of the CC layer.

5.3.2.3 Coefficient of Friction and Adhesion

Table 5.6 lists the slant shear bonding parameters (normal stress σ_n and shear stress τ_n). The normal and shear stress were calculated using **Equations 5.3** and **5.4**, respectively. The ratio between the shear-to-normal stresses (τ_n/σ_n) for all specimens was approximately 1.5 and 1 at 33.7° and 45°, respectively. The coefficient of friction (μ) and adhesion (c) are important design parameters in connections such as shear key as stipulated in various design codes. For instance, AASHTO LRFD Bridge Design Specifications [2020] stipulate that the coefficient of friction and adhesion between two concrete layers subject to shear stresses can be taken as 1 and 1.65 MPa, respectively for intentionally roughened surfaces and 0.6 and 0.52 MPa, respectively for surfaces without intentional roughness. CEB-FIB code [2010] states that the coefficient of friction and adhesion are influenced by the roughness of the contact zone which is classified from smooth to rough based on average roughness and adhesion values in range of 0.7–1.0 and 1.5–2.5 MPa, respectively.

In order to determine the coefficient of friction, combinations between the slant and bi-shear results were made based on Mohr's principle and fitted to **Equation 5.1**. The coefficient of friction ranged from 0.9 to 1 (**Figure 5.16**), whereas the corresponding friction angle [$\tan^{-1}(\mu)$] ranged between 41.3° to 45.3°. Indeed, the internal friction angle increased with the adhesion capacity (due to inclusion of nano-silica and PVA, as explained earlier) between the HPFRCC and CC. Moreover, it was observed that all mixtures achieved high adhesion values ranging from 3 to 4.5 MPa relative to the codes' (AASHTO LRFD and CEB-FIB) values, indicating high degree of surface bonding between HPFRCC, irrespective of its mixture design variables, and CC. Conforming to the previous observations, the inclusion of 6% nano-silica into the cementitious matrix

(i.e., G-N-B2.5) led to marginal improvement in the coefficient of friction by 5% relative to the reference specimen G-B2.5 (μ = 0.88), owing to the functionality of nano-silica at the interfacial zone as explained earlier. The combination of single BFP into nano-modified cementitious matrix (i.e., G-N) to produce G-N-B2.5 and G-N-B4.5 decreased the coefficient of friction slightly by 1%, and 3% respectively, relative to the G-N specimens (μ = 0.93). Comparatively, the nano-modified specimens incorporating BFP/PVA hybrid fibers (i.e., G-N-B2.5-V1 and G-N-B4.5-V1) met the interface code design parameters in term of coefficient of friction (0.99 and 1.00), respectively for rough

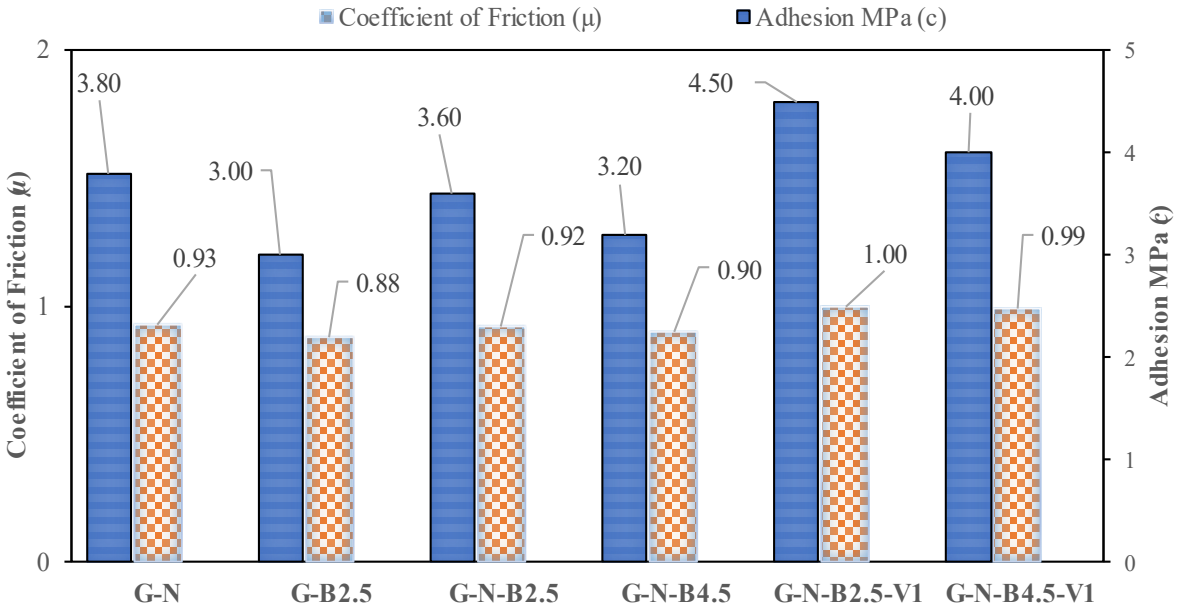


Figure 5.16: Coefficient of friction (μ) and adhesion (c) from the slant and bi-shear tests.

5.3.2.4 Rebar Pull-Out

Figure 5.17 shows the load-slip relationships of the rebar pull-out from all mixtures, in which the bond strength (τ_b) was calculated from **Equation 5.6**. In addition, the debonding energy up to 12 mm was determined as the area under the load-slip curves. The failure load varied between 34.2 to 80.1 kN corresponding to bond strength of 14.2

to 33.2 MPa, and debonding energy of 5.4 to 18.8 J. All specimens failed by rebar pull-out with no signs of damage to the composites (**Figure 5.17**).

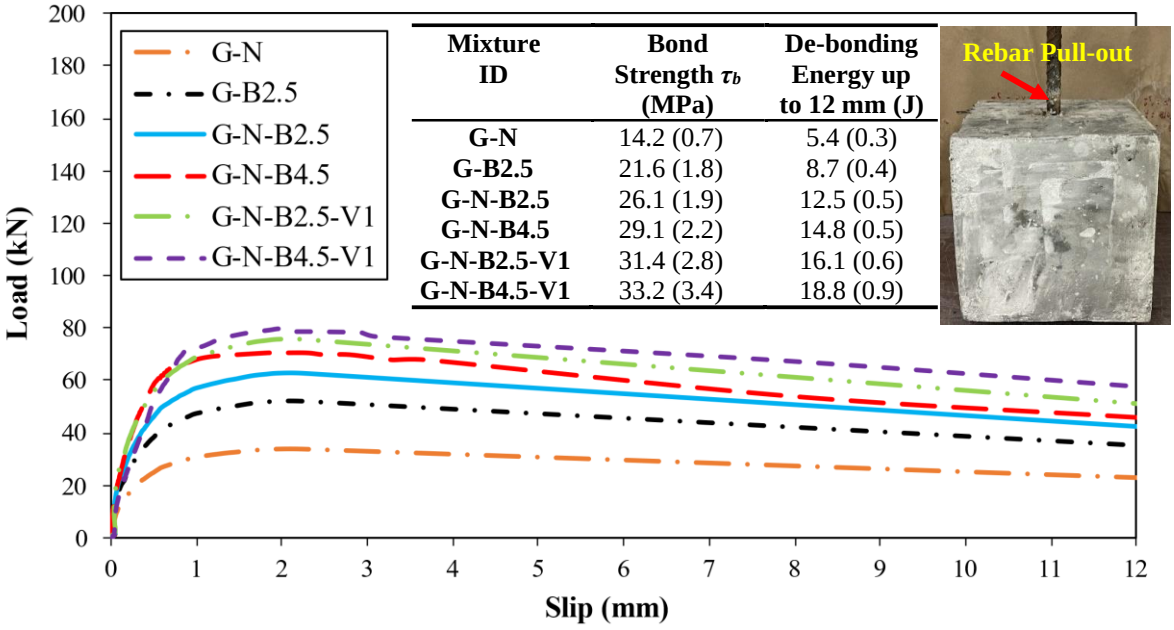
The rebar bond strength to concrete is a function of the adhesion, friction, interlocking, and tensile properties of surrounding concrete [Kim *et al.*, 2013; Khaksefidi *et al.*, 2021]. At the start of loading, adhesion and static friction transferred the applied loads from the steel rebar to the cementitious composites till reaching a load of approximately 18 kN. Subsequently, the slip of the rebar began, and the friction became dynamic. At this stage, the interlocking mechanism between the ribs of the rebar and the surrounding cementitious composites played an important role in the bonding behavior, where the load increased until reaching its maximum value with a slippage of approximately 2 mm. After exceeding the stress corresponding to the tensile capacity of the surrounding cementitious composites (descending branch), internal cracking resulted in a gradual reduction in mechanical interlocking and then the rebar slippage increased up to 12 mm.

The inclusion of 6% NS in the cementitious composites resulted in remarkable improvement in the interfacial bond stress of the steel rebar with its surrounding composites. For example, the pull-out bonding strength of G-N-B2.5 and its de-bonding energy were 21% and 44%, respectively higher relative to the reference matrix without nano-silica (G-B2.5), which were 21.6 MPa and 8.7 J. This conforms to the previously discussed vigorous physical filling and pozzolanic reactivity of NS in densifying the microstructure and enhancing the matrix maturity around the rebar, which was reflected by the high tensile properties of these composites (**Table 5.5:** strain hardening modulus of 3.5 MPa, and high energy absorption capacity: 58.2 kJ/m^3), resulting in improving adhesion, friction, and in turn the bonding capacity.

The incorporation of BFP macro-fibers resulted in further improvement of the rebar pull-out resistance from the NS-modified cementitious matrix, especially with higher BFP dosage. For instance, the bond strength and de-bonding energy of G-N-B4.5 and G-N-B2.5 were 105%, 84%, and 174%, 132%, respectively higher than that of mixture G-N, which were 14.2 MPa and 5.4 J. BFP macro-fibers impeded the spread of macro-cracks within the matrix, resulting in contribution to composites' confinement surrounding the steel rebar. This complies with the high tensile strain-hardening modulus and toughness of the nano-modified composites with BFP, especially G-N-B4.5 specimens, which achieved 17.3 MPa and 82.2 kJ/m^3, respectively (**Table 5.5**). In addition, randomly distributed macro-BFP clusters in the composites, increased the opportunity of friction, mechanical interlocking, and thus enhanced the bonding capacity with the steel rebar.

Utilizing 1% PVA resulted in further enhancement of the resistance of rebar to pull-out from the NS-modified cementitious composites compared with the composites incorporating single BFP. The pull-out bonding strength and de-bonding energy of G-N-B2.5-V1 and G-N-B4.5-V1 were 20%, 29%, and 14%, 27%, respectively higher than that of mixture G-N-B2.5 and G-N-B4.5, which were 26.1 MPa, 12.5 J, and 29.1 MPa, 14.8 J, respectively. This can be attributed to the very high strain hardening capacity and ductility of these composites as substantiated by the direct tension test (**Figure 5.5** and **Table 5.5**). The contribution of randomly distributed PVA micro-clusters surrounding BFP (**Figure 5.9**) synergistically controlled the nucleation of micro-cracks, and then BFP macro-fibers restrained the spreading of macro-cracks in the cementitious composites. This increased likelihood of concrete confinement surrounding the ribs of the steel rebar,

besides surface adhesion/friction complying with the shear tests (**Figure 5.16**), and hence enhancing the resistance to rebar pull-out from the composites.



Mixture ID	Bond Strength τ_b (MPa)	De-bonding Energy up to 12 mm (J)
G-N	14.2 (0.7)	5.4 (0.3)
G-B2.5	21.6 (1.8)	8.7 (0.4)
G-N-B2.5	26.1 (1.9)	12.5 (0.5)
G-N-B4.5	29.1 (2.2)	14.8 (0.5)
G-N-B2.5-V1	31.4 (2.8)	16.1 (0.6)
G-N-B4.5-V1	33.2 (3.4)	18.8 (0.9)

Figure 5.17: Load-slip relationships of rebar pull-out from the composites. (Note: values in parentheses are standard deviations).

CHAPTER 6: EVALUATION OF NANO-MODIFIED CEMENTITIOUS COMPOSITES WITH BASALT FIBER PELLETS AND POLYVINYL ALCOHOL FIBERS FOR SHEAR KEY JOINTS

The preceding chapters provided an extensive evaluation of the performance for nano-silica modified slag-based cementitious composites including hybrid fibers (G-N-V1-B2.5 and G-N-V1-B4.5) which can be a feasible option for applications requiring balance of mechanical capacity, interfacial bonding and ductility, such as shear key joints. In this chapter, the work was focused on developing 3D FEM analysis for investigating the efficiency of the cementitious composites as a filler material in shear key bridge joints. Thus, the bonding strength distribution, modes of failures, crack patterns/formation between these composites and precast normal/conventional (CC), as well as reinforcement steel rebar were analyzed. The models were then calibrated and validated against the experimental data obtained to develop a full-scale 3D FEM for shear key filled with various HPFRCC under HL-93 design truck loads according to AASHTO LRFD [2020]. These results are essential to before future field trials.

6.1 Introduction

Adjacent box beam reinforced concrete girders is a popular method in bridge construction owing to its structural performance and rapid assembly [Jia *et al.*, 2020; Flores *et al.*, 2021]. Shear key joints are required to connect pre-cast box beam girders, which are typically cast-in-place concrete comprising shear dowels to achieve monolithic behavior and load transfer across the bridge superstructure. AASHTO LRFD Bridge Design Specifications [2020] indicate that transferring loads (pure tension, pure shear, and combination of shear and compression) at these joints occurs through adhesive bonding,

friction, and doweling action. In the field, the most common issue of shear key joints is longitudinal cracking, resulting in premature deterioration due to infiltration of water and aggressive chemicals leading to corrosion of reinforcement and loss of the monolithic behavior among bridge segments [Russell, 2011; Wang *et al.*, 2019; Fu *et al.*, 2021].

This technical limitation can be mitigated by filling these joints with high-performance fiber-reinforced cementitious composites (HPFRCC) to control and restrain growth of cracks [e.g., Bandelt and Billington, 2016; Wang *et al.*, 2019; Liu *et al.*, 2019]. HPFRCC has gained much attention due to its post-cracking ductile behavior under tension, flexural and impact loading configurations, as well as compatibility with substrate concrete. Different binders including cement, slag, fly ash, etc. with water-to-binder ratios (*w/b*) ranging between 0.25 and 0.35 have been utilized to produce HPFRCC. Moreover, nanoparticles, such as nano-silica, have been integrated in HPFRCC in order to densify the microstructure of hardened paste through their filling/packing effect, pozzolanic reactivity [Kong *et al.*, 2012, Ghazy *et al.*, 2016b], creation of nucleation sites for hydration products deposition [Kong *et al.*, 2012; Said *et al.*, 2012], and ultrahigh surface porosity absorption (reduction in *w/b*). In addition, different sizes and types of fibers have been employed to enhance hardened characteristics of HPFRCC [Poorhosein and Nematzadeh, 2018]. For example, PVA micro-fibers have adequate modulus of elasticity (66 GPa) as well as tensile capacity (up to 1600 MPa) [Li *et al.*, 2001]. Zanotti *et al.* [2018] investigated the interfacial bonding between substrate conventional concrete (CC) with fiber reinforced concrete using the slant shear test. Two different dosages (0.5%, and 1%) of PVA micro-fibers of length 8 mm and 12 mm, and steel fibers of length 13 mm were used. It was reported that 0.5% steel and 1% PVA fibers (12 mm) were able to deviate the micro-cracks away from the

interfacial zone and increased the adhesion by up to 98%, and 103%, respectively [Zanotti *et al.*, 2018]. Wang *et al.* [2015] evaluated the bonding behavior between cementitious composites including 2% by volume PVA micro-fibers and basalt fiber reinforced polymer rebars, where the addition of PVA fibers controlled micro-cracking and increased the bond strength between the rebars and matrix by 35% [Wang *et al.*, 2015].

Numerous studies (experimental and numerical) have been carried out to evaluate the shear key bonding capacity using various filler materials (e.g., non-shrinking grouts, magnesium-ammonium phosphate mortars, fiber reinforced concrete, polymer concrete, epoxy, ultra-high-performance concrete [UHPC]) [e.g., Smolcic and Ozbolt, 2017; Wu, 2019; Tayeh and Magbool, 2021; Hu *et al.*, 2021]. Weber *et al.* [2015] investigated the behavior of a non-shrinking grouted joint without/with post-tensioned carbon-fiber-reinforced polymer (CFRP) reinforcing rods under concentrated double-tire ASSHTO HL-93 design truck load. They reported that the use of CFRP post-tensioned rods increased the initial joint cracking load from 58% to 65% of the ultimate load compared with the specimen without posttensioned rods. However, significant cracking occurred in the grouted material or at the bonded interface with precast CC, likely due to the lower compressive strength of the non-shrinking grout material [Weber *et al.*, 2015]. Fu *et al.* [2021] used experiments and finite element modeling (FEM) to assess the performance of single and double shear key joints and filled with fiber reinforced concrete (FRC) comprising steel fibers (2% by volume) under combined bending and shear loads. It was reported that the double shear key joint increased the initial cracking and ultimate loads by up to 68%, and 105%, respectively, compared with the single shear key joint. Moreover, the average initial cracks and ultimate loads for the shear key at 30° and 60°

joints increased by approximately 127%, 54%, and 107%, 91%, respectively for the single and double shear key joints. The initial crack appeared at the bottom corner of the shear key and propagated along the vertical direction till reaching the ultimate load [Fu *et al.*, 2021].

Hussein *et al.* [2017] conducted experimental and FEM studies to evaluate the ultimate shear key capacity between precast CC and UHPC under direct shear, tension, and flexural loading configurations. It was reported that the UHPC shear key configurations can be optimized using FEM [Hussein *et al.*, 2017]. Hu *et al.* [2021] developed two shear key configurations using experiments and FEM to predict the shear capacity of joints filled with UHPC comprising hook-end steel fibers (0.07% by weight of premix) at length 16 mm under shear loading (compressive load at the shear key interface). It was indicated that the models had good agreement (maximum 15% error) with experimental results, and thus they could be used for the design of shear key connections. UHPC improved the shear key capacity by 32% relative to that of non-shrink grout. Besides, the shear capacity increased linearly with the displacement until visible crack formation up to 78% of the ultimate load for the UHPC-connection. However, the models predicted a shear-off failure mode (interfacial bonding failure followed by diagonal cracks towards CC or UHPC) of the UHPC connection, similar to that of the non-shrinking grout shear key joint. [Hu *et al.*, 2021].

Basalt fibers have considerable tensile strength up to 4,000 MPa, and modulus of elasticity up to110 GPa, besides its high thermal and corrosion resistance, and lower cost compared with carbon and glass fibers [Ayub *et al.*, 2014; Iyer *et al.*, 2015; Arslan *et al.*, 2016; Iyer *et al.*, 2016; Ghazy *et al.*, 2016a]. A new form termed basalt fiber pellets (BFP) has been developed by covering basalt fibers with a polymeric resin (e.g.,

polyamide [Mahmoud et al., 2017]), to protect them from decomposition in the cementitious matrix due to the chemical reaction between alkalis in the pore solution of hydrated paste and silicate component of basalt). The addition of BFP (single system) in HPFRCC improved the bond behaviour with pre-cracked and uncracked CC under a flexural loading configuration [Azzam *et al.*, 2022]. The HPFRCC had high bonding with the CC, where the two layers of concrete acted monolithically, with no signs of transverse cracking [Azzam *et al.*, 2022]. Moreover, the bonding performance of sand-coated glass fiber reinforced polymer rebars with straight/headed-ends embedded in HPFRCC comprising BFP was evaluated [Bediwy and El-Salakawy, 2021]. It was reported that the presence of BFP kept the intactness of concrete blocks with no signs of cracks/crushing [Bediwy and El-Salakawy, 2021]. Many studies reported that the performance of hybrid fiber systems exceeds that of the individual fibers in HPFRCC [e.g., Wang *et al.*, 2019; Özkan and Demir, 2020; Özkan and Demir, 2021; Elhadary and Bassuoni, 2021]. However, there is still a dearth of information on the applicability of innovative HPFRCC comprising single BFP or hybrid PVA/BFP systems for jointing applications such as shear key joints, thus the motive for the study herein.

6.1.1 Research Significance

Ongoing efforts at the University of Manitoba resulted in the development of nano modified HPFRCC comprising single fiber system of BFP [Mahmoud *et al*. 2017; Azzam *et al*. 2019] and hybrid fiber system of PVA/BFP [Elhadary and Bassuoni, 2021]. The developed composites showed promising characteristics, including high ductility under static and dynamic loadings, resistance to ingression of fluids as well as frost action with/without de-icier, where it showed elastic and thermal compatibility with CC. Yet,

there is no data on evaluating their bonding capacity and failure/crack pattern for jointing applications (e.g., shear key). Hence, this study focused on evaluating the bonding capacity between CC (representing adjacent pre-cast box girders) and HPFRCC (representing cast-in place shear key joint filler) comprising nano-silica, high slag volume with/without single (BFP) and hybrid (PVA/BFP) fiber systems using integrated experimental (slant shear, bi-shear, rebar pull-out, thermogravimetry, and microstructure) as well as modeling (homogenization/FEM) approaches. In addition, 3D FEM for full-scale box beam bridge girders was developed to predict the various HPFRCC shear key behaviour under concentrated ASSHTO HL-93 design truck load. These results are critical to determine the suitability of these composites for shear key jointing applications.

6.2 Experimental Program

6.2.1 Materials and Mixtures

Six mixtures comprising 50% GU cement and 50% slag by mass of base binder (700 kg/m^3) meeting CSA-A3001 [2018] requirements with 0.30 *w/b* were prepared, classified as cementitious composites with high-volume supplementary cementitious materials (HVSCM-1), according to Annex K in CSA 23.1 [2019]. Constant dosage of nano-silica [6% by mass of the binder] was added to five mixtures (i.e., ternary binder content of 742 kg/m^3), where this dosage resulted in remarkable improvement of mechanical properties of concrete [e.g., Ghazy *et al.*, 2016b; Azzam *et al.*, 2019]. The fine aggregate used in the mixtures has a continuous gradation between 0 and 600 μm, as well as its fineness modulus, specific gravity, and absorption are 2.9, 2.6, and 1.5%, respectively. A high-range water reducer (HRWR), compliant with ASTM C494 Type F [2017], was added to

achieve a flow table diameter of 180±20 mm. Five mixtures were reinforced with macro-BFP (i.e., 2.5%, 4.5% by volume), or hybrid PVA/BFP fibers incorporating 1% by volume PVA (length of 12 mm, elastic modulus of 66 GPa) combined with 2.5% or 4.5% BFP. The length, diameter, and modulus of elasticity of BFP are 36 mm, 1.8 mm, and 65 GPa, respectively. **Table 6.1** lists the proportions of the mixtures. For the mixtures' ID, the letters G, N, B and V denote to slag, nano-silica, BFP as well as PVA respectively, where the numbers refer to the dosage of fibers.

Initially, the concrete pan mixer (60 rpm) contained the dry ingredients (cement, slag, fine aggregate), followed by adding gradually the liquid phases (water, NS, and admixtures). Subsequently, the fiber portion (PVA and/or BFP) were mixed with the ingredients till achieving homogenous distribution. After casting, a vibrating table was used to consolidate specimens. The surface of specimen was then covered with polyethylene sheets for 24 h. Afterwards, specimens were demolded then kept in a standard curing room at constant temperature of 22±2°C with relative humidity of minimum 95% until testing.

Table 6.1: Mixtures proportions per cubic meter

Mixture ID	Cement (kg)	Slag (kg)	Water* (kg)	NS (kg)	Fine Aggregate (kg)	PVA (kg)	BFP (kg)	Air Content (%)
G	350	350	210	--	1352	--	--	6.2
G-N	350	350	180	84	1232	--	--	5.4
G-B2.5	350	350	210	--	1288	--	43.3	6.9
G-N-B2.5	350	350	180	84	1167	--	43.3	6.5
G-N-B4.5	350	350	180	84	1115	--	78.3	7.4
G-N-B2.5-V1	350	350	180	84	1142	13	43.3	7.4
G-N-B4.5-V1	350	350	180	84	1090	13	78.3	8.2

*Adjusted amount of mixing water considering the water content of NS (50% solid content).

6.2.2 Tests

The compressive strength was determined by testing triplicate cylinders (100 diameter and 200 mm height) at 56 days according to ASTM C39 [2018]. In the tension test,

triplicate cylinders (75 mm diameter and 250 mm length) were tested under axial tensile loading at 56 days at a displacement rate of 0.2 mm/min using a quasi-static direct tension test. The bonded length of the specimen to each sleeve was 75 mm and the remaining/free length was 100 mm [Azzam *et al.*, 2021], In addition, the modulus of elasticity was calculated based on the elastic part of the tensile stress-strain relationship.

To evaluate the interfacial bond strength of HPFRCC with CC, slant shear (a combination of compressive and shear stresses at the interface) and bi-shear (pure shear at the interface plane), were conducted. The CC mix design (400 kg/m^3 GU cement with 15% fly ash replacement at *w/b* 0.4) was typical of the pre-cast box beams used in Manitoba bridge superstructure with a compressive strength 45 MPa at 28 days. In addition, the bonding between HPFRCC and reinforcement was evaluated by a rebar pull-out test.

In the slant shear test, triplicate cylinders of 100 mm (diameter) and 200 mm (length) were tested at 56 days at a loading rate of 0.25 MPa/s similar to ASTM C39 [2018]. Initially, the inclined half-filled cylinder was cast with CC and kept in a standard curing room for 28 days, followed by placing HPFRCC on the prepared CC surface (roughened, cleaned, misted) at 33.7º and 45º with the vertical and then cured until testing at 56 days. The 33.7° signified the theoretical critical bond angle according to ASTM C882 [2020], whilst the 45° represents the maximum shear stress case [Craig and Taleff, 1996; Lubliner, 2016]. Linear variable differential transducers (LVDT) were used to record the resultant deformation (parallel and perpendicular to the interfacial plane).

In the bi-shear test, triplicate CC cubes (100 mm) were cast, cured, and prepared in the same manner to the slant shear specimens. Subsequently, an additional thickness of 50 mm HPFRCC was poured over the prepared CC surface and cured till testing at 56

days at a loading rate of 0.25 MPa/s. Two steel plates were used to support the edges of concrete block, whilst the loading plates was placed on the CC surface at the interfacial bond with HPFRCC. Moreover, the interface slip was recorded by attaching LVDTs at the interface.

In the rebar pull-out test, triplicate 200 mm blocks comprising 15M (16 mm) steel rebar with an embedded length of 48 mm (3 times the bar diameter) [Ronanki *et al.*, 2018; Arjomandi and Asl, 2021; Khaksefidi *et al.*, 2021]. The remaining length of bar (152 mm) was enclosed in a polyvinyl chloride tube to reduce the contact area between steel and concrete. At 56 days, the free end of steel rebar was loaded in tension at a rate of 0.5 kN/s [RILEM 7-II-128 (1994)], while recording the slippage of the free and loaded ends slippage by LVDTs.

The pore structure of the main matrices (i.e., G, G-N, and G-N-V1) were assessed using mercury intrusion porosimetry (MIP), Small pea-sized chunks (diameter ranged from 4 mm to 7 mm) were used to perform the test. In addition, thermogravimetry analysis (TGA) was performed at 10°C/min constant heating rate on powder samples passing from 75 µm sieve [sieve #200], to specify the quantity of calcium hydroxide (CH) in the matrix. Moreover, scanning electron microscope (SEM) equipped with EDX (elemental dispersive X-ray) at 56 days were conducted on fracture pieces extracted from the HPFRCC/CC interfacial zone surface to corroborate the bulk trends.

6.3 Finite-Element Modeling

6.3.1 Phase I: Homogenization

6.3.1.1 Theoretical Formulation

The bond behaviour of plain matrices without fibers (i.e., G and G-N) was simulated using the classical elastic-plastic damage model for cement-based materials (e.g., concrete) as one-unit element [Lubliner *et al.*, 1989]. The stress-strain relation of the specimens without fibers can be expressed through **Equation 6.1**, in which the damage evolution parameter can be specified from **Equation 6.2** [Balamirzoev *et al.*, 2021]; where, σ and ε are the stress as well as strain, respectively, E_0 , ε_o , ε^{pl}, and ε^{in} are initial elastic modulus of elasticity of intact material, and peak-critical strain, plastic strain, and cracking inelastic strain respectively, d is the damage evolution parameter, b is a coefficient, and g is the regularities parameter for the shape of the curve.

$$\sigma = (1-d)\, E_o\, (\varepsilon - \varepsilon^{pl}) \qquad \textbf{(Equation 6.1)}$$

$$d = \begin{cases} 0 & \varepsilon < \varepsilon_o \\ 1 - e^{-b(\varepsilon-\varepsilon_o)^g} & \varepsilon \geq \varepsilon_o \end{cases} \qquad \textbf{(Equation 6.2)}$$

$$\varepsilon^{pl} = \varepsilon^{in} - \frac{d}{(1-d)}\frac{\sigma}{E_o}, \qquad \varepsilon^{in} = \varepsilon - \varepsilon_o \qquad \textbf{(Equation 6.3)}$$

The hierarchical non-linear multi-scale computational homogenization theory was used to predict the mechanical properties of heterogeneous matrices reinforced with micro- and/or macro-fibers (BFP and PVA/BFP) as inclusions [Li and Li, 2019; Balamirzoev *et al.*, 2021], by the representative volume element (RVE). The RVE should have enough size to embrace the inhomogeneous microstructure, and thus each solid element at macro-scale represents the center of RVE. This theory can be expressed through **Equation 6.4** [Kanit *et al.*, 2003], where, $d\varepsilon_{ij}$ and $d\sigma_{ij}$ are the volume averaged

strain and stress tensors, respectively, of the RVE. k_{ij} is the effective tensor modulus of homogenized stiffness matrix, where *i* and *j* are equal to 1, 2 or 3 relative to the global axes *x*, *y*, and *z*, respectively. Moreover, the compliance tensor (η_{ij}) described the effective interfacial bond between fibers and matrix, as depicted in **Equation 6.5** [Qu, 1993]; where, η represents the unit outward vector, δ_{ij} is the kronecker's delta, where α and β represent the compliance in the tangent and normal directions, respectively, with respect to the interface.

$$d\sigma_{ij} = k_{ij}\, d\varepsilon_{ij} \qquad \textbf{(Equation 6.4)}$$

$$\eta_{ij} = \alpha\, \delta_{ij} + (\beta - \alpha)\, \eta_i\, \eta_j \qquad \textbf{(Equation 6.5)}$$

6.3.1.2 Model Parameters and Numerical Simulation

With regards to the elastic-plastic damage parameter model, the mechanical characteristics of all the matrices with no fibers (G and G-N) including compressive and tensile strength, as well as Young's modulus, which were determined experimentally (**Table 6.2**), were used as input data for the 3D FEM using ANSYS R19.2 workbench [2020].

The homogenization method was used to develop five-scale cubic RVEs of dimension 40 mm using ANSYS R19.2 workbench [2020], to calculate the homogenized stiffness coefficients k_{ij} for all matrices reinforced with fibers (G-B2.5, G-N-B2.5, G-N-B4.5, G-N-B2.5-V1, as well as G-N-B4.5-V1). The hybrid PVA/BFP multiscale inclusion was simulated using two-scale cubic RVE levels, in which PVA micro-fibers are homogenized in a cubic RVE of 12 mm with matrix G-N to form G-N-V1 (RVE_0), and then integrated as a matrix unit (i.e, G-N-V1) in a cubic RVE of 40 mm homogenized with BFP macro-fibers (2.5%, and 4.5%) to form RVE_4 and RVE_5, respectively (**Figure**

6.1). Each meso-scaled RVE comprises the matrix and random distributed micro- and/or macro-fibers in the space (*x, y, z*), assuming anisotropic characteristics. All RVEs were modeled with a mesh size 100 µm, hence, the total number of elements for RVE_0, RVE_1, RVE_2, RVE_3, RVE_4, and RVE_5 were 8,669, 10,775, 13,995, 15,267, 25,160, and 29,550, respectively. Each element was subjected to shear and tensile stresses along the principal coordinates, to specify the components of k_{ij} (**Equation 6.4**) for various specimens comprising single inclusion (i.e., PVA, BFP) and multiscale inclusions (PVA/BFP) through periodic boundary condition displacement at RVE boundaries. Volume fraction for the fibers was integrated as an input parameter. In addition, the used Poisson's ratio was 0.2 for all matrices, and the porosity was specified based on MIP test (**Table 6.3**). The interfacial bond between matrix and BFP macro-fibers and PVA micro-fibers was analysed using the cohesive zone model (CZM) of vanishing thickness (considering α *and* β equal to zero in **Equation 6.5**). This assumption can be linked to the chemical and hydrophilic effects of PVA micro-fibers with the paste, and BFP (macro-fibers) longitudinal micro-grooves to sustain sufficient amount of gel in the contact zone with the matrix [Elhadary and Bassuoni, 2021].

Table 6.2: Mechanical properties of composites at 56 days

Mixture ID	Compressive Strength (MPa)	Tensile Strength (MPa)	Young's Modulus (GPa)
G	82	2.8	28.5
G-N	87	4.0	32.9
G-B2.5	79	2.3	25.1
G-N-B2.5	83	3.5	31.1
G-N-B4.5	72	3.2	29.6
G-N-B2.5-V1	85	3.9	32.4
G-N-B4.5-V1	75	3.8	31.2

Table 6.3: MIP test results at 56 days

Mixture ID	Apparent Total Porosity (%)	Threshold Pore Diameter (μm)	Proportion of Micro Pores [<0.1 μm] (%)
G	11.6	0.11	44
G-N	10.3	0.08	58
G-N-V1	10.4	0.07	64

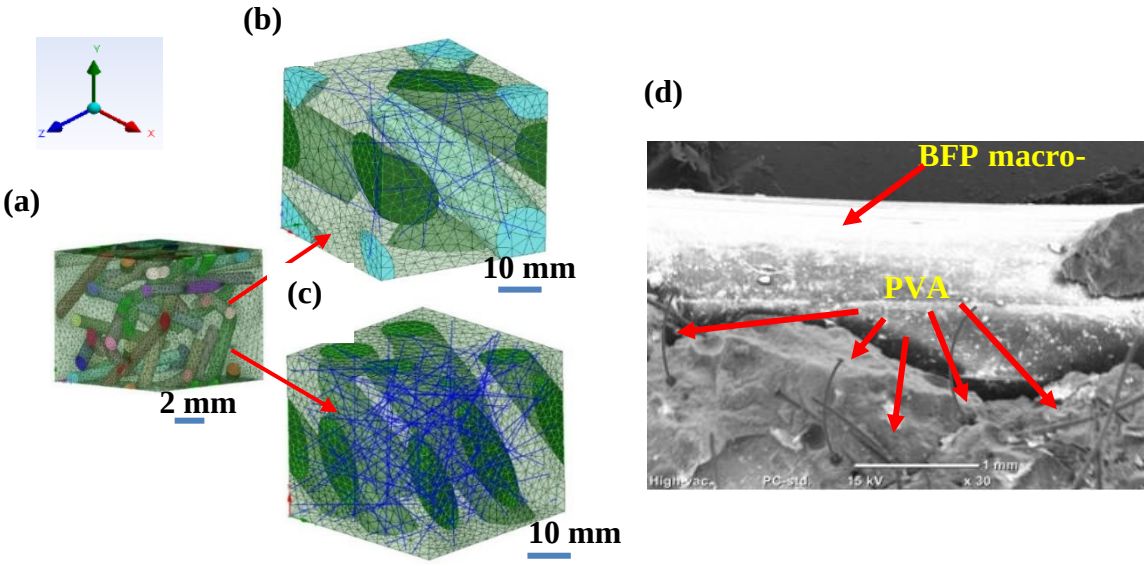


Figure 6.1: Homogenization RVEs: (a) meso-RVE$_0$ of mixture G-N-V1, (b) meso-RVE$_4$ of mixture G-N-B2.5-V1, (c) meso-RVE$_5$ of mixture G-N-B4.5-V1, and (d) SEM micrograph showing the interaction of BFP with PVA.

6.3.2 Phase II: Bond Evaluation for Laboratory Tests

6.3.2.1 Theoretical Formulation

The interfacial slant shear bond strength between HPFRCC and CC is based on Mohr–Coulomb's theory describing the relationship between the normal (σ_n) and shear (τ_n) bond stresses at the failure plane (**Equation 6.6)**. Also, σ_n and τ_n at the failure plane can be expressed as a function of the bond stress (σ_o) and angle of inclination at the interface with vertical (α) [**Equations 6.7-6.8**]. By substituting in **Equation 6.6**, the adhesion (c) and coefficient of friction (μ) can be determined using Mohr's circle, where $\sigma_o = F$ (compression force on slant cylinders)/A = (cross-sectional area of cylinders).

$$\tau_n = c + \mu\ \sigma_n \quad \textbf{(Equation 6.6)}$$

$$\sigma_n = \sigma_o\ sin^2\ (\alpha) \quad \textbf{(Equation 6.7)}$$

$$\tau_n = 0.5\ \sigma_o\ sin\ (2\alpha) \quad \textbf{(Equation 6.8)}$$

The interfacial pure shear bond between HPFRCC and CC is based on the general shear stress theory, describing the relationship between shear stress, and applied force at failure plane [Hosford, 2010], as described by **Equation 6.9**, where: τ is the interfacial shear bond strength, P is the utmost applied load, and A is the interfacial area.

$$\tau = P/2A \quad \textbf{(Equation 6.9)}$$

The interfacial bond-slip relationship between HPFRCC and steel rebar depends on the local stress-strain criterion at the failure zone [Yankelevsky *et al.*, 2008]. The relative displacement d_l of the steel rebar embedded in the HPFRCC is equal to the relative displacement of steel rebar δ_s and concrete δ_c as described in **Equations. 6.10-6.11**. However, the concrete displacement can be neglected due to low internal stresses and high volume relative to steel (**Equation 6.12**). Differentiating the relative displacement function with respect to d_y, **Equation 6.13** can be derived [Yankelevsky *et al.*, 2008], where E and σ are internal modulus of elasticity and stress, while c and s subscripts refer to concrete and steel, respectively.

$$d_l = \delta_s - \delta_c \quad \textbf{(Equation 6.10)}$$

$$d_l = (\frac{\sigma}{E})_s d_y - (\frac{\sigma}{E})_c d_y \quad \textbf{(Equation 6.11)}$$

$$\frac{d_l}{d_y} = (\frac{\sigma}{E})_s \quad \textbf{(Equation 6.12)}$$

$$\frac{d_l}{d_y} = \frac{1}{E_s}\frac{d_{\sigma_s}}{d_y} \quad \textbf{(Equation 6.13)}$$

The equilibrium condition across an infinitesimal element of the steel rebar-HPFRCC (*dy*) can be expressed through **Equation 6.14**, which can be simplified to produce **Eq. 15** [Yankelevsky *et al.*, 2008]:

$$(\sigma_s + d\sigma_s)\, A_s = \sigma_s A_s + \tau\, d_y\, \pi\, \mathrm{d} \qquad \textbf{(Equation 6.14)}$$

$$\frac{d_{\sigma_s}}{d_y} = \tau\, (\frac{\pi\, d}{A_s}) \qquad \textbf{(Equation 6.15)}$$

The interfacial contact surface between steel rebar-HPFRCC can be substantiated from **Equations 6.13-6.15** depending on the circumferential shear stress [Yankelevsky *et al.*, 2008], and modeled analytically by a force-slip relationship that can be expressed by **Equation 6.16**, where, τ_y represents the shear stress, L_y represents the slippage between steel and concrete in the direction of loading (y ordinate), whilst d and A_s are the steel rebar diameter as well as cross-section area, respectively.

$$\frac{d_l^2}{dy^2} = \tau_y\ \ (L_y)\ \ \frac{\pi\, d}{E_s\, A_s} \qquad \textbf{(Equation 6.16)}$$

6.3.2.2 Model Parameters and Numerical Simulation

Eighteen 3D FEM were developed through Phase II using ANSYS R19.2 Workbench [2020], to determine the interfacial shear bond parameters as well as rebar bond-slip relationship, which were integrated in Phase III as input data. Three different configurations [**Figure 6.2 (a)-(d)**], including slant shear, pure shear, and rebar pull-out models were developed, and verified with the experimental data. In the slant shear models, the cylinder was meshed at a size of 10 mm resulting in a total of 1660 nodes and 822 elements. In bi-shear test, the block was meshed at a size of 5 mm resulting in a total of 2560 nodes and 1989 elements. In the rebar pull-out models, the assembly was meshed at a size of 20 mm resulting in a total of 2760 nodes and 1402 elements. Moreover,

parametric studies were performed to assess the influence of different slant shear inclination angles with the vertical on the interfacial bond strength of HPFRCC.

The mechanical properties (compressive strength = 45 MPa, Poisson's ratio = 0.2, and Young's modulus = 31.3 GPa) of CC were added to the Phase II models. Mechanical properties of plain matrices (G, G-N) [**Table 6.2**], and homogenization parameters of fiber reinforced matrices (G-B2.5, G-N-B2.5, G-NB4.5, G-N-B2.5-V1, and G-N-B4.5-V1) [**Table 6.4**] were also integrated into the Phase II models. The Poisson's ratio and modulus of elasticity of steel rebar were taken as 0.3 and 200 GPa, respectively. The CC was simulated as a nonlinear elastic material by SOLID65 brick elements, with eight nodes located at its corners; where each node has three translational degrees of freedom in the *x*, *y*, and *z* directions [**Figure 6.2(e)**]. This element can simulate cracking and crushing in tension and compression, respectively. Solid185, eight nodes [**Figure 6.2(f)**], element was used to model the HPFRCC; this element supports stress stiffening, large deflection/strain, plasticity, and creep. The steel reinforced strands/rebars were modeled as linear-elastic media using LINK180 element, which is a 3D spar (bar) element defined by two nodes with three translational degrees of freedom at each node [**Figure 6.2(g)**]. This element supports creep, plasticity, stress stiffening as well as large deflections and strains.

The interfacial bond between HPFRCC and CC in the slant shear models was simulated as a bonded pair using CONTA175 and TARGE170 by a cohesive zone model (CZM) mixed-mode bilinear CZM model (combination of tangential and normal components of contact stress and displacement, if applicable) [**Equation 6.17**], where T_m^{max} and δ_m^* are the maximum equivalent bond stress and tangential contact stress slip at the onset of debonding, while δ_m^c, δ_m, *K*, *n*, *t*, and d_m are the slip at the completion of

debonding, displacement jump, stiffness parameter (slope of the line), normal vector, tangential vector, and the debonding parameter, respectively.

$$T_m = K\,\delta_m\,(1\text{-}d_m) \qquad m = t\,,\,n \qquad \textbf{(Equation 6.17)}$$

$$K = T_m^{max} \;/\; \delta_m^*$$

$$d_m = \begin{cases} 0 & \delta_m^{max} \le \delta_m^* \\ \left(\frac{\delta_m^{max}-\delta_m^*}{\delta_m^{max}}\right)\left(\frac{\delta_m^c}{\delta_m^c-\delta_m^*}\right) & \delta_m^* \le \delta_m^{max} \le \delta_m^c \\ 1 & \delta_m^{max} > \delta_m^c \end{cases} \quad , \quad \delta_m = (\delta_n + \delta_t)^{0.5}$$

The interfacial behavior between HPFRCC and CC in the pure shear and between HPFRCC and rebar in the pull-out models were modeled as a bonded pair using CONTA175 and TARGE170 by CZM governed by a bilinear-mode-II. The general profile for the traction-separation CZM mode-II cohesive law can be expressed by **Equation 6.18**. where, T_t^{max}, δ_t^*, δ_t^c, K, δ_t and d_t are the maximum equivalent tangential contact stress, tangential slip at the onset of debonding, tangential slip at the completion of debonding, stiffness parameter (slope of the line), tangential displacement jump (slip) and the debonding parameter, respectively.

$$\tau_t = K\,\delta_t\,(1 - d_t) \qquad \textbf{(Equation 6.18)}$$

$$K = \frac{T_{max}^t}{\delta_t^*}$$

$$d_t = \begin{cases} 0 & \delta_t^{max} \le \delta_t^* \\ \left(\frac{\delta_t^{max}-\delta_t^*}{\delta_t^{max}}\right)\left(\frac{\delta_t^c}{\delta_t^c-\delta_t^*}\right) & \delta_t^* \le \delta_t^{max} \le \delta_t^c \\ 1 & \delta_t^{max} > \delta_t^c \end{cases}$$

Table 6.4: Homogenized engineering properties of RVEs with a size of 40 mm

Homogenized Matrix	E_{11} (GPa)	E_{22} (GPa)	E_{33} (GPa)	G_{12} (GPa)	G_{13} (GPa)	G_{23} (GPa)	υ_{12}	υ_{13}	υ_{23}	τ_H (MPa)
G-B2.5 (RVE1)	26.2	26.8	26.7	9.1	9.2	9.1	0.21	0.20	0.20	2.4
G-N-B2.5 (RVE2)	31.2	31.2	31.2	10.6	10.8	10.7	0.20	0.20	0.21	3.7
G-N-B4.5 (RVE3)	30.6	30.5	30.1	9.9	9.6	9.7	0.20	0.20	0.21	3.3
G-N-B2.5-V1 (RVE4)	34.3	34.2	34.3	12.3	12.6	12.7	0.21	0.20	0.20	4.1
G-N-B4.5-V1 (RVE5)	32.5	32.8	32.3	11.6	11.7	11.3	0.21	0.20	0.20	3.9

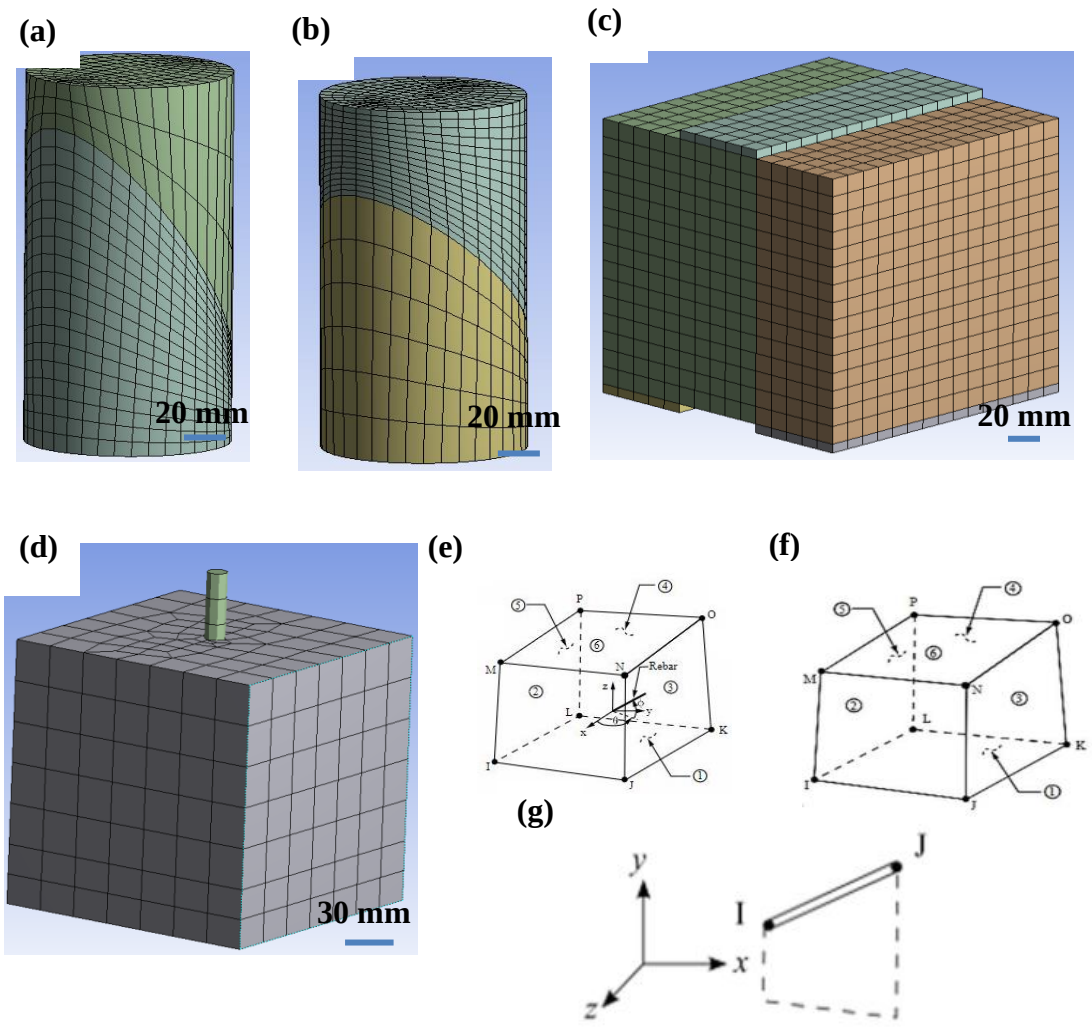


Figure 6.2: Finite element geometry: (a) slant shear model at 33.7°, (b) slant shear model at 45°, (c) bi-shear model, (d) rebar pull-out model, (e) SOLID65 element for CC, (f) SOLID185 element for HPFRCC, and (g) LINK180 element for the steel rebar.

6.3.3 Phase III: Predictive Model for the Shear Key Bridge Joint

6.3.3.1 Case Description

In this study, the bridge was a recent (2019) rehabilitation in Manitoba, Canada in 2019. The simulated mid-span has a length of 30.14 m and width of 9.60 m containing two lanes; the superstructure in the mid-span consisted of eight adjacent precast prestressed CC box girders, shear keys, and a deck slab. Each box beam is 1200 mm wide and deep (**Figure 6.3**). A total of 12.7 mm diameter seven-wire low relaxation strands with an ultimate strength of 1860 MPa were used in each beam. Transverse stressing ducts of 25 mm diameter and ultimate tensile strength 1035 MPa equally spaced at 3400 mm in the longitudinal direction were used for lateral stressing of the beams.

Figure 6.4 shows the different components of the developed 3D FEM for the full-scale prestressed precast box beams (rehabilitated mid-span of the bridge) including an example of the shear key joint connecting them. The HL-93 design truck load consisted of the live load and 33% dynamic load allowance according to article 3.6.2 in AASHTO LRFD [2020]. The design lane load consisted of a uniformly distributed load of 9.3 kN/m in the longitudinal direction and transverse direction over a 3000 mm, as specified by article 3.6.1.2.4 in AASHTO LRFD [2020]. For one lane design, the effect of one HL-93 design truck load was rested at the shear key interface away for the edge of the loaded lane by 906 mm (not closer than 609.6 mm (2 ft) from the edge of the design lane according to article 3.6.1.3.1 in AASHTO LRFD [2020] in the transverse direction) to produce maximum shear at the interfacial zone (shear key location). Each steel dowel has 125 mm embedment length in the shear key joint with 16 mm diameter equally spaced at 166.7 mm in the longitudinal direction.

6.3.3.2 Numerical Simulation and Model Parameters

Six 3D FEM were simulated in ANSYS R19.2 Workbench (2020) to predict the effect of various HPFRCC joint fillers on the maximum shear capacity of the shear key bridge joint under truck load HL-93. Each component was meshed in the longitudinal direction at a size of 100 mm with total of 270,006 nodes and 160,809 elements. The cross section in the transverse direction was meshed at a size of 40 mm with total of 480,178 nodes and 200,745 elements. The shear key section was individually meshed with a finer size of 13 mm at the contact between HPFRCC and precast box beams of total of192,070 nodes and 80,298 elements. To represent the boundary conditions of the bridge in the model, a fixed remote point was used at one bottom end of each box beam girder, whilst the other end of each box beam girder was supported by a roller remote point. Two loading steps were developed to simulate the effect of the prestressing force of the seven-wire low relaxation strands in the longitudinal direction and integrated as a constant deformation with HL-93 truck loads into the second loading step.

The compressive strength and Young's modulus of prestressed CC beams were 45 MPa and 31.3 GPa, respectively. Homogenization results (**Table 6.4**) were taken from Phase I to model the mechanical properties of HPFRCC and integrated into Phase III model. The Young's modulus of the shear dowels and strands were 200 GPa and 196 GPa, respectively. The Poisson's ratio for concrete and steel components were 0.2 and 0.3, respectively. The interaction between CC beams and steel reinforcement strands was modeled as embedded constraint to minimize slippage. Moreover, the interaction between HPFRCC and prestressed precast beams was modeled as a bonded pair using CONTA175 and TARGE170 via a CZM model, which requires that the shear key joint parameters (i.e., coefficient of friction and adhesion) be defined based on the Mohr-Coulomb friction

model (**Equation 6.6**). Accordingly, normal-shear stress relationship curves were fitted through simulating different slant shear inclination angles from Phase II sensitivity analysis. In addition, the interaction between HPFRCC and shear dowels in the shear key joint was modeled as a bonded pair using CONTA175 and TARGE170 by CZM governed by a bilinear-mode-II (**Equation 6.16**), which required the CZM parameters to be defined based on the verification of fitted bond-slip relationship for rebar pull-out models with the experimental results (Phase II).

6.4 Results and Discussion

6.4.1 Phase I: Homogenization

Based on applying the non-linear multi-scale homogenization theory, the homogenized stiffness coefficient k_{ij} was determined for different HPFRCC reinforced with single BFP and hybrid PVA/BFP using **Equation 6.4**. For instance, **Equation 6.19** shows the coupling term k_{ij} for a 40 mm RVE4 (comprising PVA/BFP). The coupling term k_{ij} indicates the even dispersion of PVA/BFP in RVE4, in which the elastic moduli k_{11}, k_{22} *and* k_{33} were comparable.

$$k_{ij} = \begin{bmatrix} 34.35 & 9.08 & 8.98 & 0 & 0 & 0 \\ & 34.23 & 8.18 & 0 & 0 & 0 \\ & & 34.36 & 0 & 0 & 0 \\ & Symmetry & & 12.37 & 0 & 0 \\ & & & & 12.63 & 0 \\ & & & & & 12.70 \end{bmatrix} \quad \textbf{(Equation 6.19)}$$

It was observed that the 40 mm size was suitable to yield the elastic moduli for different RVEs comprising single BFP and hybrid PVA/BFP.

Table 6.4 lists the results for the homogenized Young's modulus, shear modulus, Poisson's ratio, and tensile strength for the different RVEs (comprising BFP and PVA/BFP) in different directions (1, 2, 3), relative to the global axes *x*, *y*, *z*, respectively.

The homogenized models (**Table 6.4**) could simulate the elastic properties in terms of tensile strength and Young's modulus with an error less than 10% relative to the direct tension test results (**Table 6.2**).

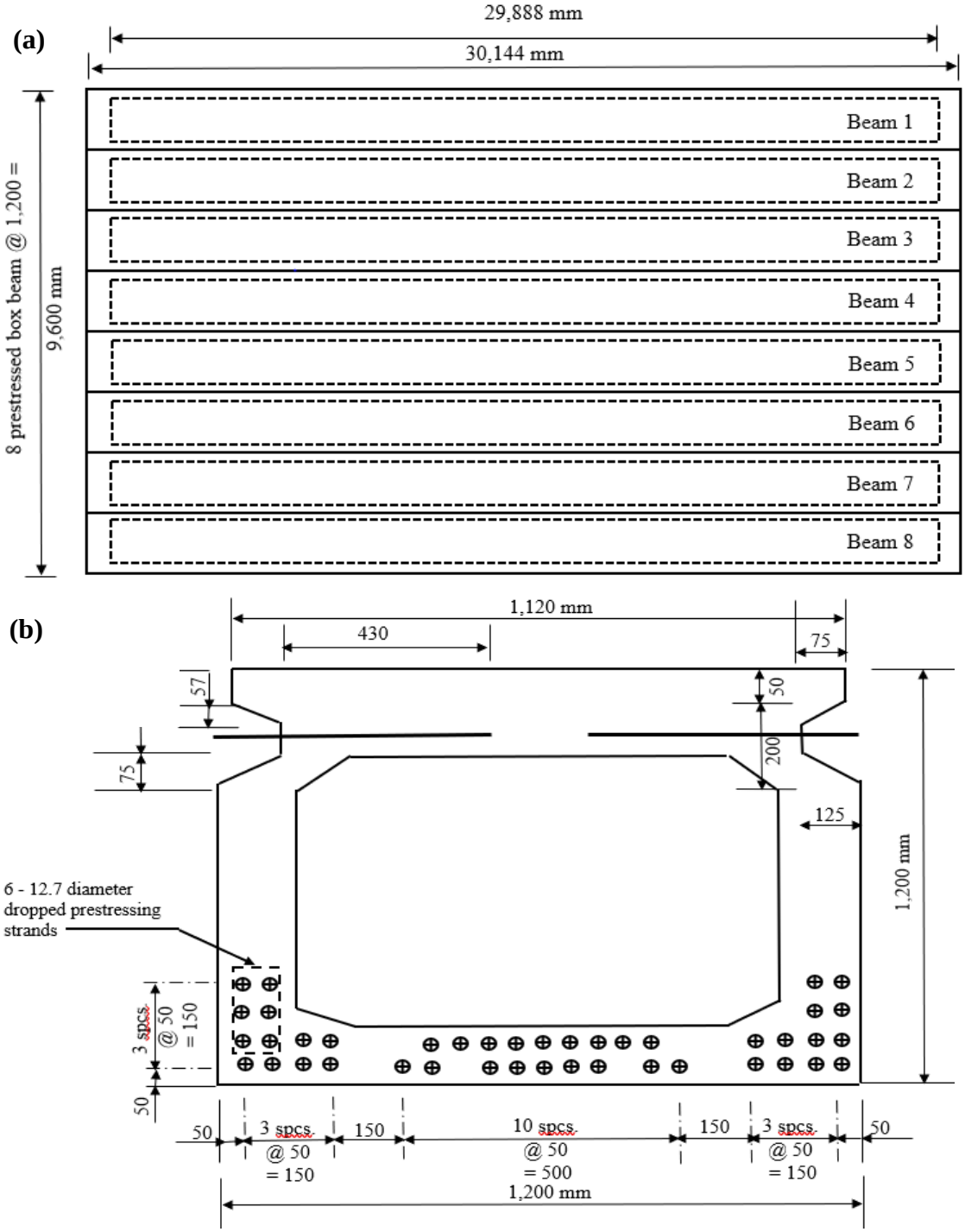


Figure 6.3: Mid-span bridge details: (a) top view, and (b) precast CC beam cross-section. (Note: all dimensions are in millimeter).

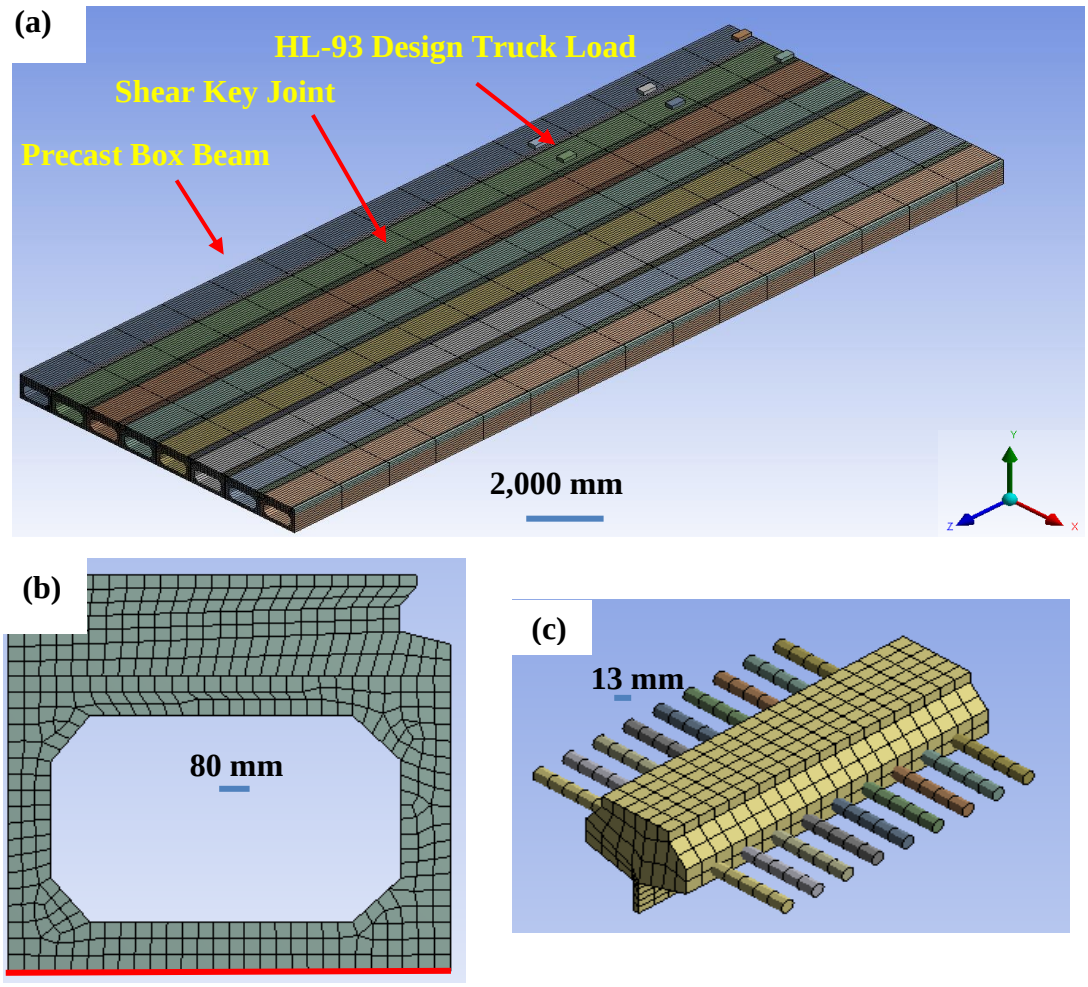


Figure 6.4: FEM for the bridge mid-span: (a) model's parts and loading, (b) beam boundaries, and (c) shear key meshing.

6.4.2 Phase II: Bond Evaluation

The parameters implemented in Phase II for the HPFRCC included the experimental mechanical properties for the plain matrices (i.e., G., and G-N) [**Table 6.2**], and the homogenized results obtained from Phase I (**Table 6.4**) for the mixtures comprising single BFP and hybrid PVA/BFP (G-B2.5, G-N-B2.5,G-N-B4.5,G-N-B2.5-V1, G-N-B4.5-V1). The experimental parameters for the CC layer including compressive strength, tensile strength, and Young's modulus were also integrated in the models. The predicted bond strength and debonding energy for the slant shear, bi-shear, and rebar pull-out

models were in good agreement (average of 8%, 6%, and 5% error, respectively) with the corresponding experimental values (**Tables 6.5-6.8**), indicating the reliability of the modeling approaches implemented in this study.

Table 6.5: Experimental slant shear test parameters

Mixture ID	33.7°		Mode of Failure	45°		Mode of Failure
	Shear Stress τ_n (MPa)	Normal Stress σ_n (MPa)		Shear Stress τ_n (MPa)	Normal Stress σ_n (MPa)	
G-N	10.1(0.8)	6.7 (0.8)	Interface	21.3 (0.4)	21.3 (0.4)	CC
G-B2.5	7.5 (0.7)	5.0 (0.7)	Interface	21.1 (0.3)	21.1 (0.3)	CC
G-N-B2.5	9.5 (0.8)	6.4 (0.8)	Interface	21.6 (0.5)	21.6 (0.5)	CC
G-N-B4.5	8.2 (0.7)	5.5 (0.7)	Interface	21.5 (0.4)	21.5 (0.4)	CC
G-N-B2.5-V1	13.3(1.4)	8.8 (1.4)	Interface+ CC	22.5 (0.3)	22.5 (0.3)	CC
G-N-B4.5-V1	11.5(1.2)	7.7 (1.2)	Interface+ CC	22.6 (0.6)	22.6 (0.6)	CC

Note: Values in parentheses are standard deviations

Table 6.6: Experimental versus modeling results for the slant shear test at 33.7°

Mixture ID	Slant Bond Strength σ_O (MPa)		Error (%)	De-bonding Energy (J)		Error (%)
	Experimental	Modeling		Experimental	Modeling	
G-N	22.4	24.8	10%	15.4	14.7	5%
G-B2.5	16.5	18.0	9%	9.9	10.8	9%
G-N-B2.5	20.8	23.2	12%	14.0	13.0	8%
G-N-B4.5	17.8	19.5	10%	12.7	11.5	10%
G-N-B2.5-V1	28.5	28.8	1%	25.5	27.5	8%
G-N-B4.5-V1	25.0	23.3	7%	22.4	20.8	8%

Table 6.7: Experimental versus modeling results for the bi-shear test

Mixture ID	Pure Shear Bond Strength, τ (MPa)		Error (%)	De-bonding Energy (J)		Error (%)
	Experimental	Modeling		Experimental	Modeling	
G-N	3.8	4.1	8%	18.8	16.9	11%
G-B2.5	3.0	2.8	7%	11.9	12.8	8%
G-N-B2.5	3.6	3.5	3%	16.9	15.2	11%
G-N-B4.5	3.2	3.4	6%	14.8	14.2	4%
G-N-B2.5-V1	4.5	4.2	7%	23.2	24.9	7%
G-N-B4.5-V1	4.0	3.8	5%	20.7	22.9	11%

Table 6.8: Experimental versus modeling results for the rebar pull-out test

Mixture ID	Bond Strength, τ_b (MPa)		Error (%)	De-bonding Energy up to 12 mm (J)		Error (%)
	Experimental	Modeling		Experimental	Modeling	
G-N	14.2	15.2	7%	5.4	5.9	9%
G-B2.5	21.6	22.7	5%	8.7	9.2	6%
G-N-B2.5	26.1	27.3	5%	12.5	13.2	6%
G-N-B4.5	29.1	29.8	2%	14.8	14.5	2%
G-N-B2.5-V1	31.4	33.1	5%	16.1	15.4	5%
G-N-B4.5-V1	33.2	35.1	6%	18.8	20.7	10%

6.4.2.1 Slant Shear

Figures 6.5-6.7 show three different modes of failure of the composite specimens tested under slant shear, including stress distributions at the HPFRCC/CC interface. Crushing/compression failure took place in all specimens bonded at 45º (**Figure 6.5**) with equivalent shear and normal stress components (ratio of 1.0) at the interface [**Table 6.5**], which led to enhanced friction at the interface and improved the degree of bonding between the two layers. From the simulation trends at 33.7°, the shear bond stress reached its maximum peak value at the last stage of de-bonding (red zone in the contour plots), which coincided with interface slippage (**Figure 6.6**), or partial interface failure followed by CC cracking (**Figure 6.7**). This could be attributed to the higher shear stress at the interface relative to the normal stress component (ratio of approximately 1.5, **Table 6.5**), which promoted sliding at the interfacial plane, depending on the mix design of HPFRCC. Accordingly, the analysis herein is done for this critical scenario at 33.7°. The simulation analysis indicated that for the composite specimens with nano-silica and reinforced with single BFP, visible crack formation appeared when the average loads reached approximately 53% of the peak values. Comparatively, adding 1% PVA micro-fibers in the hybrid nano-modified composites (G-N-B2.5-V1, and G-N-B4.5-V1) led to

localized interface cracks at approximately 72% of the peak load level, and then deviated towards the CC part at 88% of the peak loads.

The absence of nano-silica in the reference binder (i.e., G-B2.5) showed lower slant bond strength and de-bonding energy by 29%, and 20% respectively relative to G-N-2.5, both specimens displayed interface failure. The improvement of C-N-2.5 could be attributed to the precipitation of additional/secondary C-S-H at the interfacial plane (pozzolanic reactivity), associated with the particle filling effect of nano-silica that densified the microstructure at the interface, which resulted in matrix refinement similar to the MIP trends (**Table 6.3**) and enhancement in the adhesive capacity. Hence, SEM and EDX analyses showed that the addition of NS led to the deposition of pozzolanic cementitious gel at the interface with an average *Ca/Si* of 1.21, relative to reference matrix (G) with an average *Ca/Si* of 1.78 [e.g., **Figure 6.8**].

Increasing the dosage of BFP in the nano-modified cementitious composites up to 4.5% decreased the slant bond strength and de-bonding energy of the composites (**Table 6.6**). For instance, the slant bond strength and de-bonding energy for G-N-B4.5 were 21% and 22%, respectively lower relative to that of the reference mixture G-N, which were 24.8 MPa, and 14.7 J. This behavior could be linked to the stress concentration effect of the created ITZs due to the existence of BFP at the interface with CC, which reduced the bonding capacity. Comparatively, the presence of 1% PVA micro-fibers with BFP macro-fibers in the composites markedly enhanced interfacial bonding. The average slant bond strength and de-bonding energy of composite G-N-B2.5-V1 and G-N-B4.5-V1 specimens were 21% and 97%, respectively higher than that of the G-N-B2.5 and G-N-B4.5 specimens. This was associated with the fracture plane change from interface to localized interfacial cracks followed by cracking of the CC substrate (**Figure 6.7**). This could be

linked to the hydrophilic nature and chemical bonding through hydroxyl groups (OH^-) on the PVA surface with the cement paste at the HPFRCC/CC contact surface [Zanotti *et al.*, 2018], enhancing the refinement of the matrix similar to the MIP trends (**Table 6.3**). Accordingly, SEM micrographs [e.g., **Figure 6.9**] showed that PVA micro-fibers were bound to the HPFRCC layer with fracture edges at the contact zone towards CC.

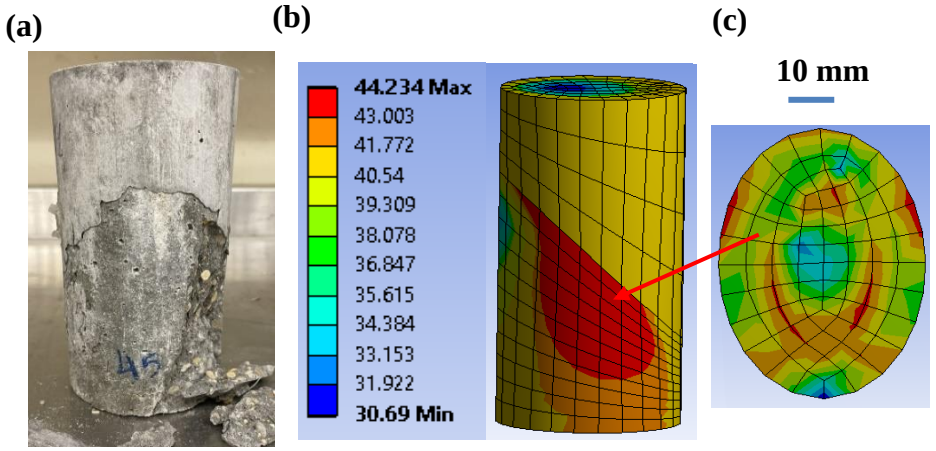


Figure 6.5: Crushing failure in the CC specimen cast with G-N-B2.5 at 45°: (a) experimental failure, (b) modeling simulation, and (c) bond stress (MPa) distribution at the interface.

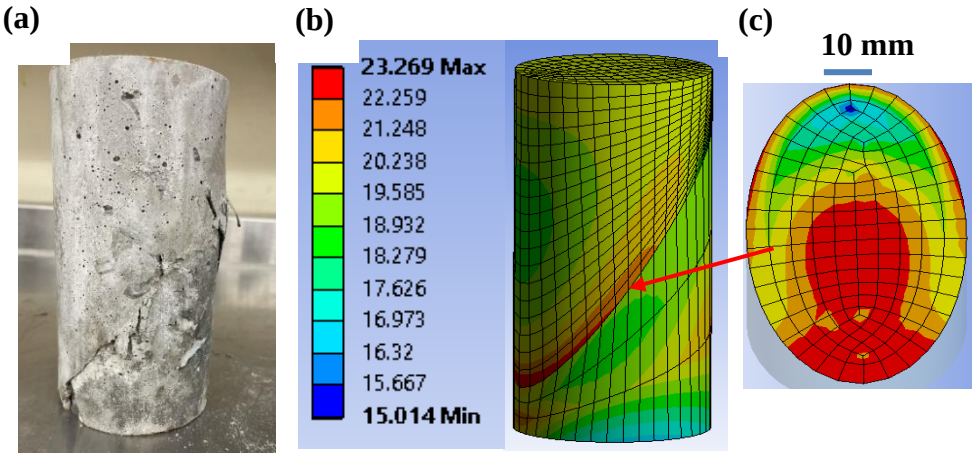


Figure 6.6: Interface failure in specimens cast with G-N-B2.5 at 33.7°: (a) experimental failure, (b) modeling simulation, and (c) bond stress (MPa) distribution at the interface.

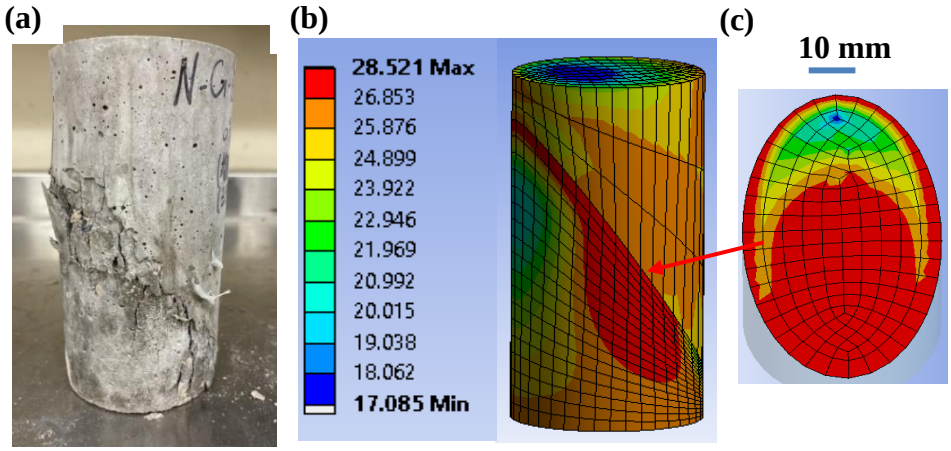


Figure 6.7: Interfacial and CC failure in specimens cast with G-N-B2.5-V1 at 33.7°: (a) experimental failure, (b) modeling simulation, and (c) bond stress (MPa) distribution at the interface.

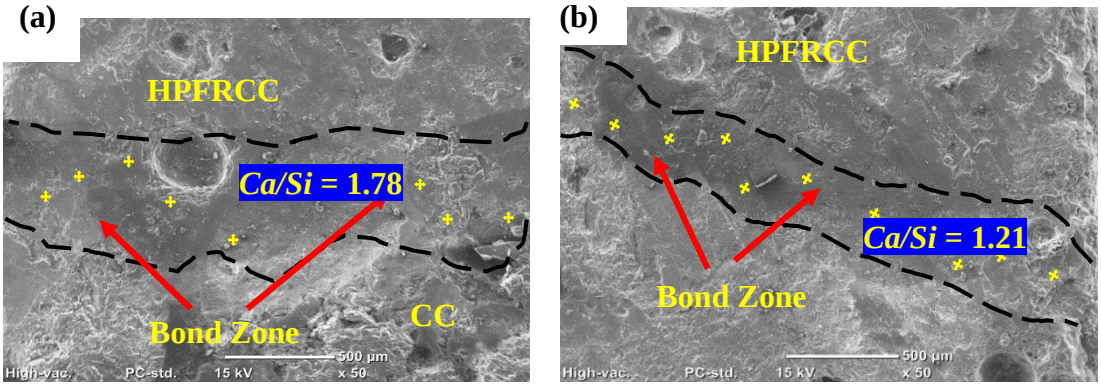


Figure 6.8: Exemplar SEM micrographs and EDX at the indicated locations in the interface between HPFRCC and CC: (a) G, and (b) G-N specimens.

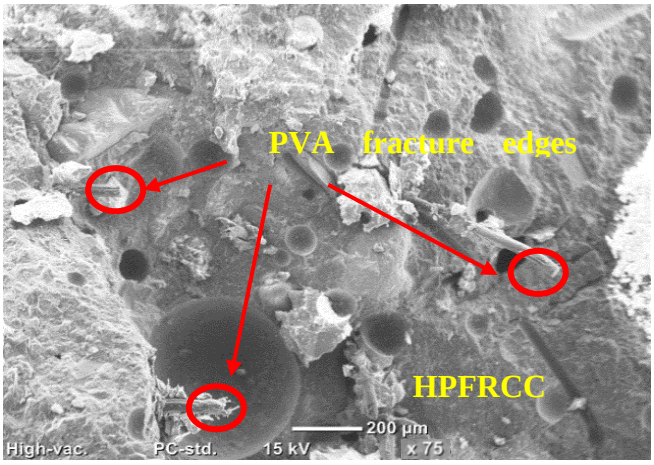


Figure 6.9: Exemplar SEM micrograph of fracture edges of PVA in the HPFRCC towards the CC layer.

6.4.2.2 Direct Shear

Figures 6.10-6.11 show the two modes of failure in the specimens cast with HPFRCC side-by-side with CC under direct shear, including stress distributions at interface zone. Simulation predictions indicated that in specimens without/with nano-silica and BFP, coalescence of visible appeared when the average applied loads reached 46% of the peak values, and then propagated along the interface until complete failure at the peak stress value [red zone in the contour plots, **Figure 6.10(b)**]. Comparatively, the localized interface crack for specimens comprising hybrid PVA/BFP (G-N-B2.5-V1, G-N-B4.5-V1) appeared when the average applied load was approximately 78% of the peak loads, and then deviated towards CC cracking at 94% of the peak loads [red regions in the contour plots, **Figure 6.11(b)**].

The incorporation of 6% NS in the reference mixture G-B2.5 to produce G-N-B2.5 significantly improved the adhesion with CC surface under direct shear, but the mode of failure in the specimens still displayed interface failure [**Figure 6.10**]. For example, the direct shear bond strength and the de-bonding energy for mixtures G-N-B2.5 were 25% and 19% higher than that of the G-B2.5 specimens, which were 2.8 MPa and 12.8 J, respectively (**Table 6.7)**. This could be attributed to the role of NS in the additional participation of cementitious products in the contact zone area with CC as discussed in Section 4.2.1.

Adding single BFP macro-fibers in the nano-modified matrix led to reduction in the adhesive capacity of the composites (**Table 6.7**). For instance, the average direct shear bond strength and de-bonding energy for G-N-B2.5 and G-N-B4.5 decreased by 16%, and 13%, respectively relative to that of the G-N composite, which were 4.1 MPa, and 16.9 J, respectively. This behavior could be linked to the effect BFP in creating

additional ITZs at the interface with CC, which led to reduction in the bonding capacity. However, the addition of 1% PVA micro-fibers to BFP macro-fibers had a significant effect on improving the bonding capacity as the average direct shear bond strength and de-bonding energy increased by 16%, and 60%, respectively relative to that of corresponding specimen with single BFP. Moreover, PVA fibers deviated the fracture plane towards the CC layer [**Figure 6.11**], due to the role of PVA in improving the adhesion at the interface between the two layers, as discussed in the Section 4.2.1. The coexistence of PVA micro-fibers with BFP macro-fibers synergistically restrained and arrested cracks at the interface, which improved bonding and diverted the failure towards the weaker CC substrate.

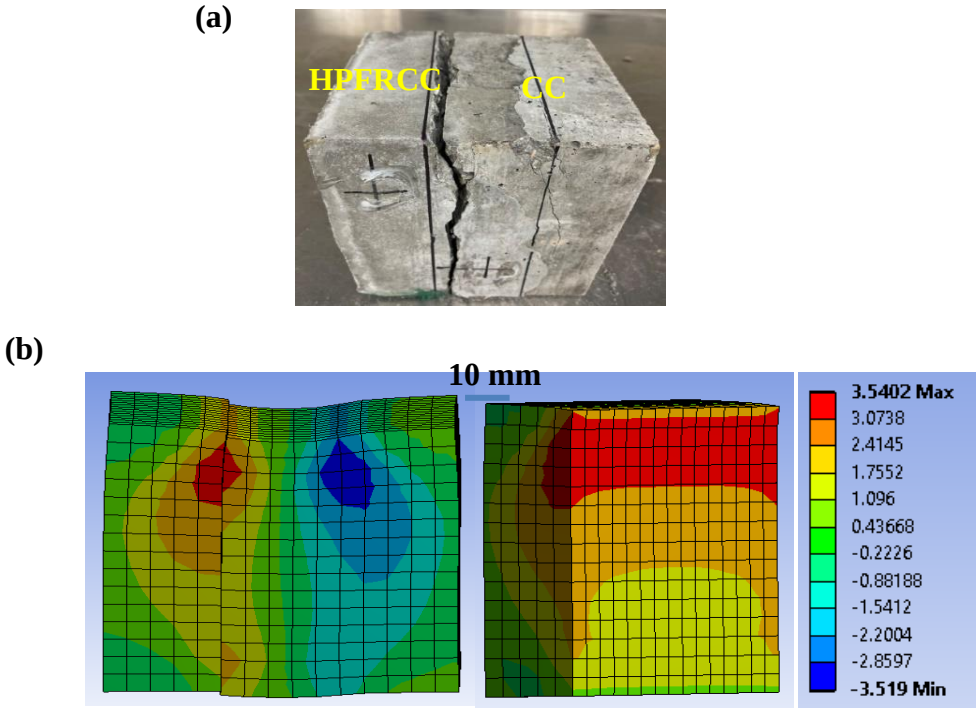


Figure 6.10: Direct shear failure in specimen G-N-B2.5: (a) experimental failure, and (b) predicted failure associated with shear stress (MPa) distribution at the interface between HPFRCC/CC.

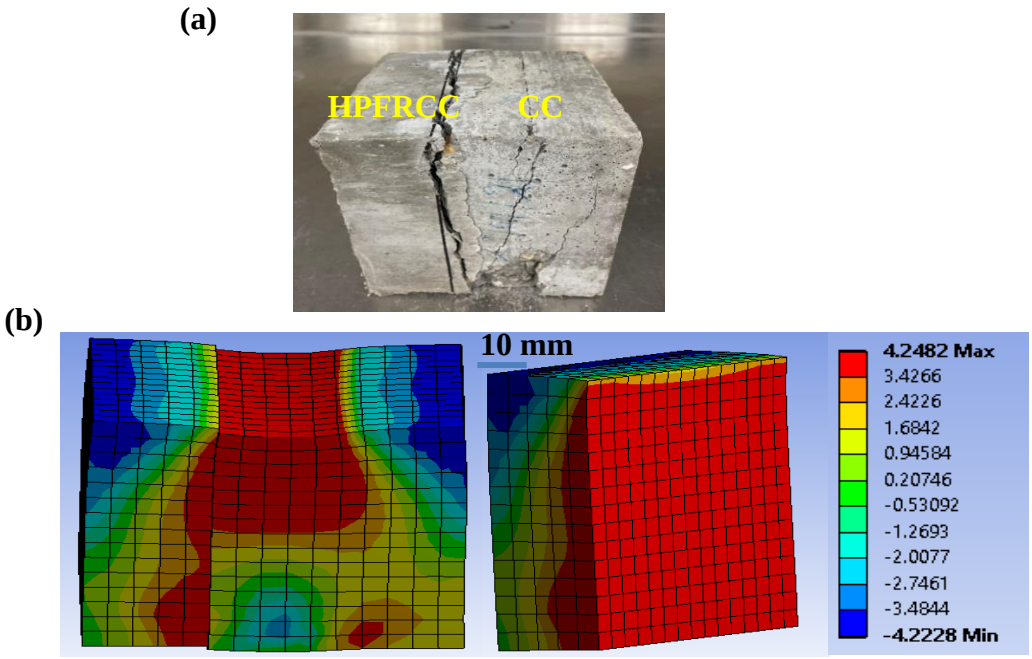


Figure 6.11: Direct shear failure in specimen G-N-B2.5-V1: (a) experimental failure, (b) predicted failure associated with shear stress (MPa) distribution at the interface between HPFRCC/CC.

6.4.2.3 Coefficient of Friction and Adhesion

ACI 318 [2019] stipulates that the shear forces can be resisted by friction only at the interface, which is taken as 1 and 0.6 for rough and smooth concrete surfaces, respectively. Comparatively, AASHTO LRFD Bridge Design Specifications [2020] stipulate that the coefficient of friction and adhesion should be 1 and 1.65 Mpa, respectively for rough surfaces and 0.6 and 0.52 Mpa, respectively for surfaces with no roughness. To determine the coefficient of friction (μ), different theoretical slant shear angles with the vertical (25°, 30°, 35°,40°) were simulated based on the slant shear model developed and verified in this study at 33.7°. **Figure 6.12** shows the predicted normal-shear stress interaction and linear trends at these angles, with a coefficient of determination of at least 0.93, based on Mohr's principle and fitted to **Equation 6.1**. Predications of the shear parameters [coefficient of friction (μ) and adhesion ©] obtained from the various slant shear angles [**Figure 6.12(b)**] were in good agreement (maximum

8%, and 6% error, respectively) with the experimental values, which were obtained from the combination of experimental slant shear at an angle of value 33.7° and bi-shear tests [**Figure 6.12(a)**], indicating the reliability of the modeling approaches implemented in this study.

The amplitude of the coefficient of friction ranged from 0.89 to 1.08, with a corresponding friction angle [$\tan^{-1}(\mu)$] that ranged between 41.7° to 47.2°. This parametric analysis indicated that all mixtures achieved higher adhesion ranging from 3.2 to 4.6 Mpa than that required by AASSHTO LRFD [2020], indicating high degree of surface roughness between the CC and HPFRCC layer, irrespective of its mixture design. In particular, the nano-modified specimens incorporating PVA/BFP (G-N-B2.5-V1 and G-N-B4.5-V1) met the AASHTO LRFD and ACI 318 interface code design stipulations, in terms of coefficient of friction (1.08 and 1.05), for rough surfaces.

6.4.2.4 Rebar Pull-Out

Figure 6.13 shows an example of the mode of failure (rebar slippage/debonding) that occurred in all composites after the pull-out test with no signs of damage in the concrete block. The load was progressively transferred from the steel rebar to the surrounding HPFRCC with corresponding increase in the cumulative displacement up to 12 mm. According to the stress distributions at the interface zone, it was observed that the bond stress reached its peak value with the last stage of de-bonding (red zone in the contour plot at the interface zone) coinciding with marked interface slippage. Moreover, the developed models could simulate the propagation and distribution of cracks in the HPFRCC during rebar pull-out [**Figures 6.14(a-d)**].

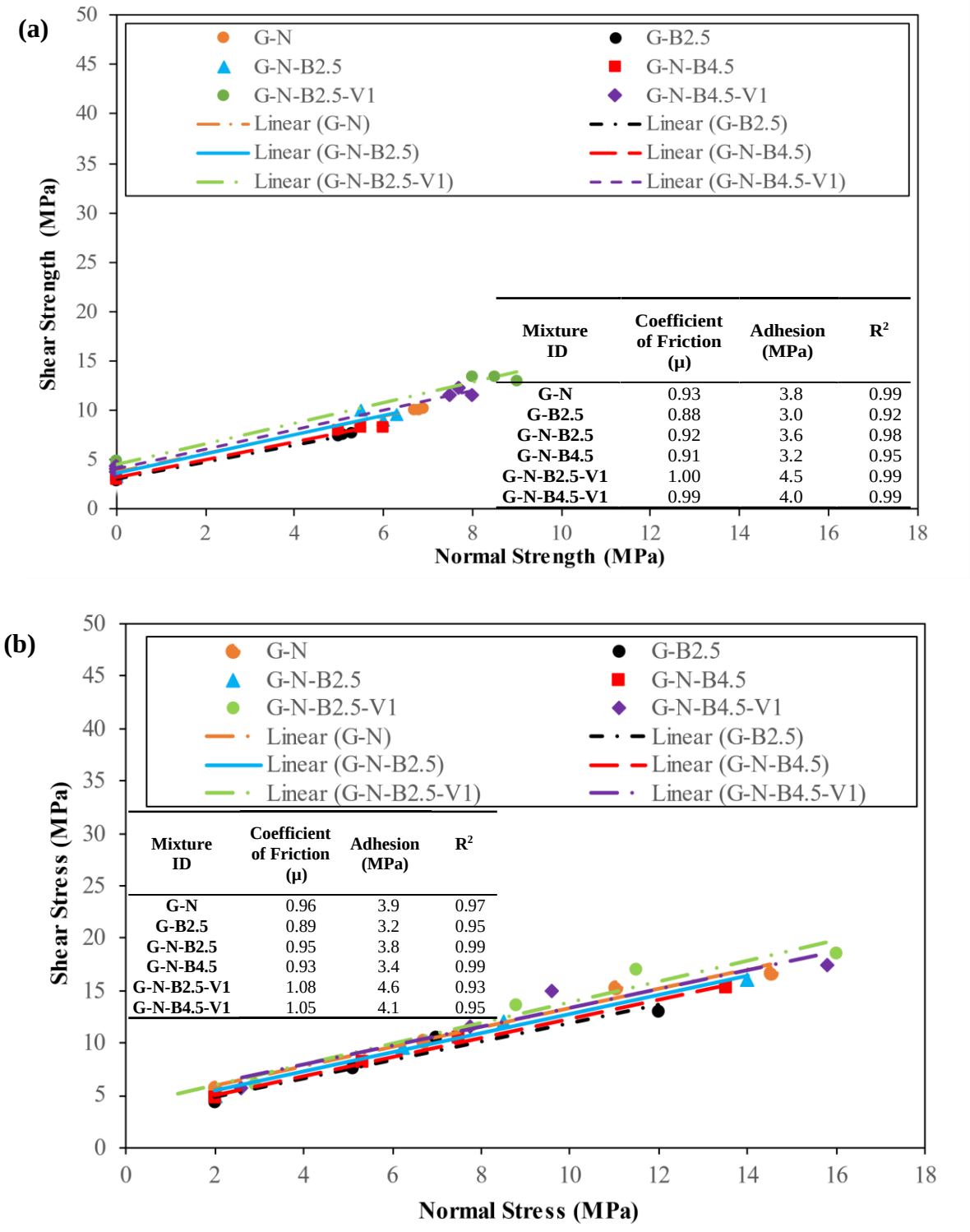


Figure 6.12: Shear-normal stresses interaction (fitted to Eq. 6) of the composite HPFRCC/CC specimens: (a) combination of experimental slant shear (at 33.7°) and bi-shear results, (b) FEM predictions for various slant shear angles (25°, 30°, 35°, 40°).

Adding PVA to BFP led to further improvement of the resistance of rebar to pull-out from the NS-modified cementitious composites compared with composites reinforced with single BFP; the pull-out bonding strength and de-bonding energy of G-N-B2.5-V1 and G-N-B4.5-V1 were 21% and 17%, and 18% and 43%, respectively higher than that of mixture G-N-B2.5 and G-N-B4.5 (**Table 6.8)**. The contribution of randomly distributed PVA micro-clusters surrounding BFP [**Figure 6.1(d**)] controlled the nucleation and coalescence of micro-cracks, while BFP macro-fibers bridged and arrested macro-cracks in the matrix. This increased the likelihood of concrete confinement and friction surrounding the ribs of the steel rebar, and hence enhancing the resistance to rebar pull-out from the composites. Accordingly, **Figures 6.14(c-d)** show the patterns of de-bonding failure of steel rebar from the G-N-B4.5-V1, which occurred after generation of multiple and sequential cracks parallel and perpendicular to the loading direction in the plan and elevation views, substantiating the role of PVA micro-fibers and their contribution with BFP macro-fibers in restraining the growth of cracks in HPFRCC. The FEM predicted that the first crack started to initiate when the applied load reached 33% of the peak load. Afterwards, the second, third and fourth cracks formed when the applied loads reached 44%, 74%, and 97%, respectively, of the peak loads till rebar pull-out failure.

6.4.3 Phase III: Predictions of Shear Key Behavior

The predictive shear key bridge models showed the possibility of two modes of failure for the HPFRCC shear key joints: interface cracking failure (**Figure 6.15**), and partial interface failure, followed by crushing of precast CC beams (**Figure 6.16**). The shear resistance force transferred from the adjacent CC beams represents a percentage of the

ultimate loads (a combination of concentrated and distributed truck loads HL-93). The interface crack formation progress for all joints without/with nano-silica, and single BFP commenced from the bottom at the side of truck loading when the average shear resistance force reached 52% of the ultimate force and propagated upwards at the interface [**Figure 6.15(a)**]. Subsequently, the crack gradually widened and propagated upwards till interface failure took place coinciding with the peak force [**Figure 6.15(b)**]. For the joints reinforced with the hybrid fiber system (PVA/BFP), the first-crack commenced from the bottom at the interface between precast CC and HPFRCC, when the average shear resistance force was approximately 85% of the ultimate load [**Figure 6.16(a)**]. By increasing the shear load, the cracks deviated into the CC beam forming diagonal cracks at approximately 45° with the horizontal [**Figure 6.16(b)**]. Afterwards, the CC crushed, when the load reached the maximum resistance force.

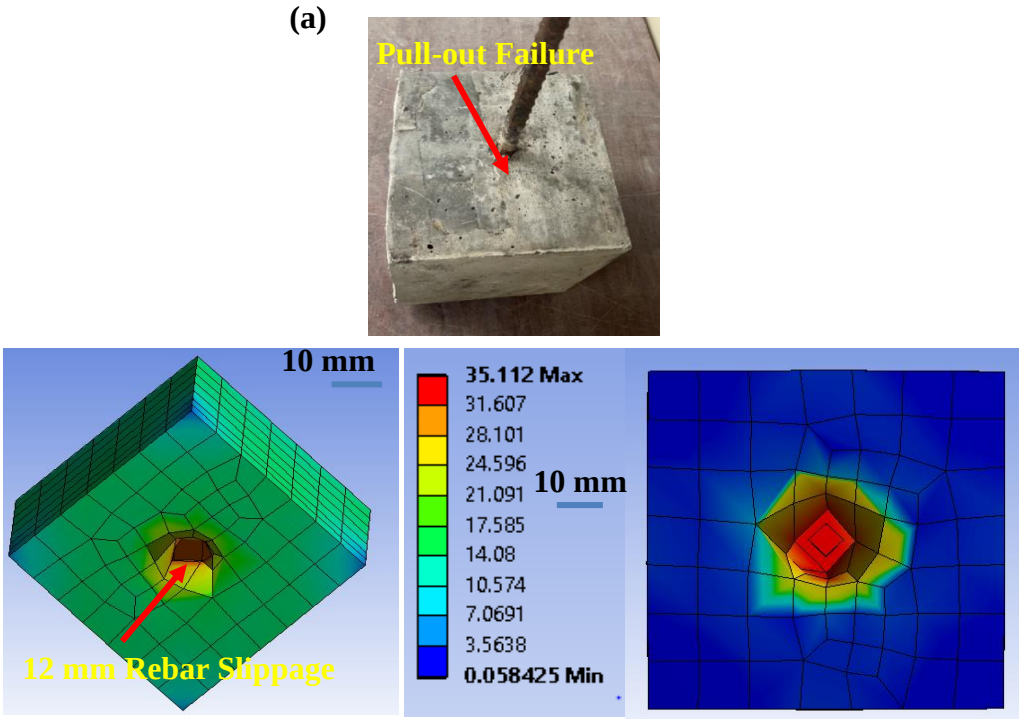


Figure 6.13: Rebar pull-out failure from G-N-B4.5-V1: (a) experimental failure, and (b) simulated rebar pull-out associated with bond stress (MPa) distribution around the rebar.

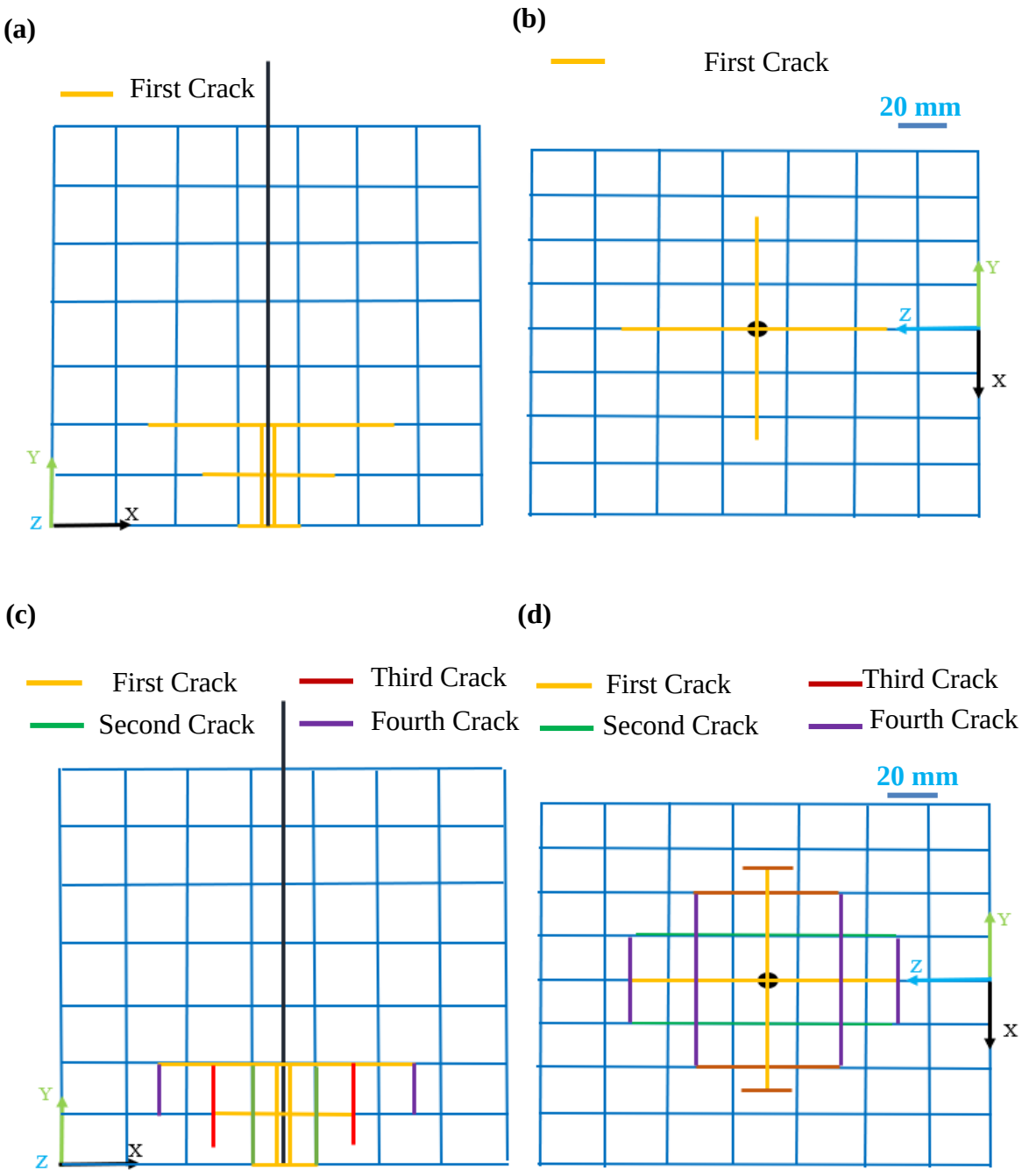


Figure 6.14: Predicted crack distributions during debonding of the rebar from HPFRCC: (a) plan view of mixture G-N-B4.5, (b) elevation view of mixture G-N-B4.5, (c) plan view of mixture G-N-B4.5-V1, and (d) elevation view of mixture G-N-B4.5-V1.

Figure 6.17 shows the predicted shear resistance force versus the vertical displacement for all HPFRCC shear key simulated joints. For all curves, the process consists of three stages including a linear stage, nonlinear ascending stage, and nonlinear descending stage. At the first stage, displacement increased with truck load assemblies, which was associated the crack formation process when the shear resistance force approximately reached 52% to 85% of ultimate loads depending on the mix design of HPFRCC. By further increasing the truck loads, the cracks widened with the shear resistance force at non-steady state relationship (secondary stage) due to the reduction in section stiffness with the rapid propagation of cracks. After reaching the maximum shear resistance force, all specimens entered the descending branch of the curve (tertiary stage) with increase in the displacement and reduction in the shear resistance force, due to shear key failure.

This predictive model showed that the nano-modified cementitious composites reinforced with either single BFP or hybrid PVA/BFP were able to resist the shear force up to or greater than the ultimate standard loads (HL-93), except for composites G-N, and G-B2.5 with corresponding shear resistance force of 80%, and 92% of the ultimate standard loads. Similar to Phase II trends, the inclusion of NS in the nano-modified cementitious composites led to marked improvement in the shear resistance of the joints. For instance, the shear capacity of joint G-N-B2.5 increased by 13% relative to that of the reference joint G-B2.5 with a shear strength of 3.2 MPa. This corresponded to a shear resistance force of approximately 102% of the standard loads. This trend can be attributed to the improvement of the matrix maturity (**Table 6.2**) and pore structure (**Table 6.3**) brought by NS, at the interfacial zone, as explained earlier [**Figures 6.8(a)-(b)**]. Increasing the dosage of single BFP in the nano-modified matrix slightly improved the

shear resistance force of the shear key bridge joints. For instance, the shear strength of joint G-N-B4.5 was 8% higher relative to that of joint G-N-B2.5, which was 3.6 MPa. However, the initial interface cracks developed earlier in G-N-B4.5 when the shear resistance force was 12% lower, relative to that in G-N-B2.5 (56% of ultimate loads), due to the stress concentration effect of the created ITZs due to the existence of BFP at the interface with precast CC. This behaviour was partially offset by the crack bridging effect and abundance of BFP macro-fibers interlocking with the shear reinforcing dowels, resulting in restoring load carrying capacity till reaching the ultimate load, thus enhancing the overall shear capacity of the connection.

In addition, the presence of 1% PVA micro-fibers with BFP macro-fibers had a significant effect at improving the maximum shear resistance force of the shear key joint. For instance, the shear resistance force of joints G-N-B2.5-V1 and G-N-B4.5-V1 increased by 20%, and 23%, respectively relative to that of G-N-B2.5 and G-N-B4.5 joints. These joints achieved a maximum shear resistance force of 119%, and 130%, respectively relative to the ultimate standard highlighting their efficiency. Moreover, these composites were able to blunt the propagation of cracks at the interface and deviate them to CC at these high loads (**Figure 6.16**). This can be attributed to the role of PVA micro-fibers at enhancing the adhesive capacity at the interfacial zone with CC and interlocking with BFP around shear dowels, as discussed in previous sections. Hence, complying with the trends from Phase II, G-N-B2.5-V1 and G-N-B4.5-V1 are the most promising composites for this shear key application.

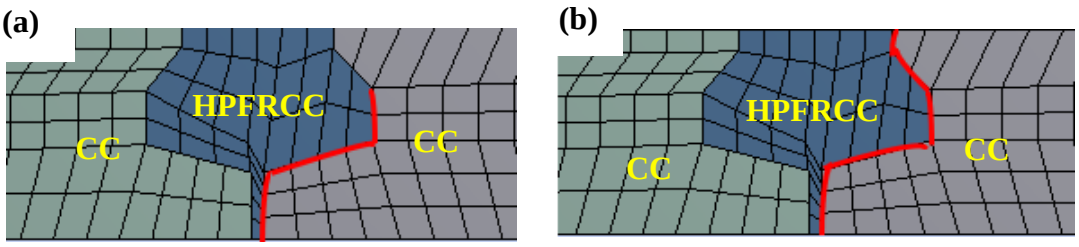


Figure 6.15: Development of cracking at the interface in shear key joints incorporating HPFRCC with single BFP: (a) initial crack at approximately 55% of ultimate load, and (b) crack propagation up to failure.

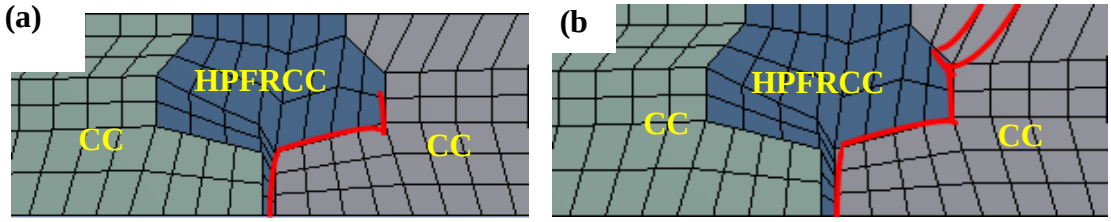


Figure 6.16: Development of cracking in shear key joints incorporating HPFRCC with PVA/BFP: (a) initial interface crack at approximately 85% of ultimate load, and (b) crack deviation at approximately 45° into CC.

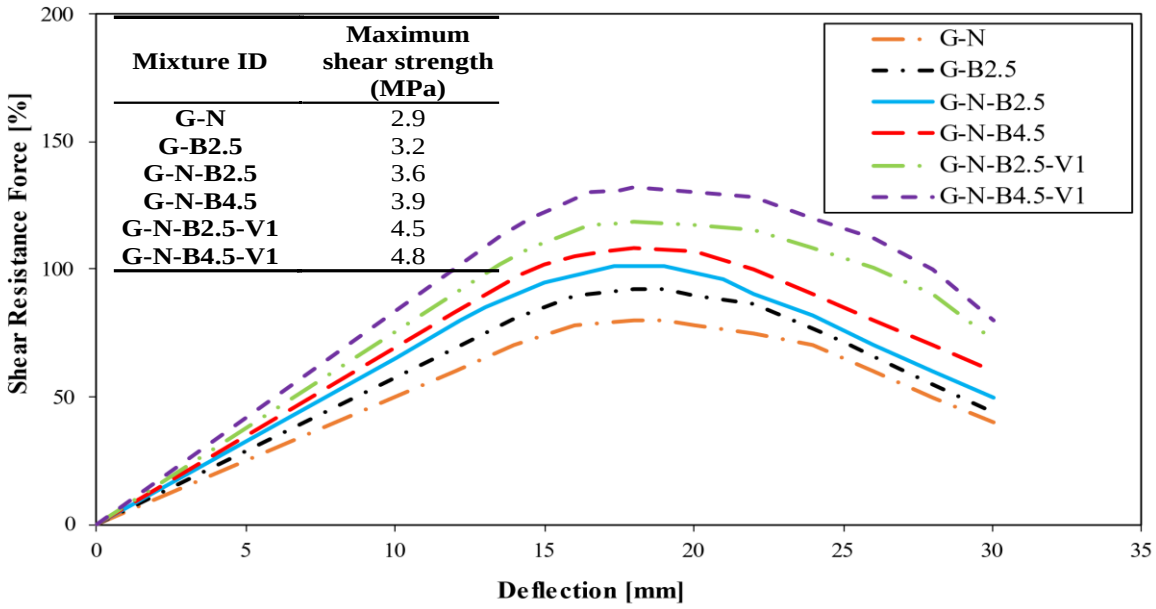


Figure 6.17: Shear resistance force relative to the standard truck loading HL-93 vs. vertical deflection for all composites in the shear key joint.

CHAPTER 7: SUMMARY, CONCLUSIONS, AND RECOMMENDATIONS

7.1 Summary

Nano-modified cementitious composites represent a new class of high-performance fiber reinforced cementitious composites (HPFRCC) that can be a feasible option for repair/overlay, or as a filler material in different infrastructure applications. In this thesis, integrated experimental and finite element modeling studies were conducted in order to capture the factors affecting the properties of these cementitious composites (e.g., binder formulation, fiber' dosage, types and system); particularly identifying their suitability for shear key bridge jointing applications.

The experimental program was designed to provide fundamental data on nano-modified cementitious composites comprising high volume of slag and reinforced with single (macro-BFP or micro-PVA) and hybrid system (micro-PVA and macro-BFP) fibers. The effect of fiber dosage, system, and type on the fresh, hardened and durability properties were investigated. Seven mixtures were prepared and tested for mortar flow test, air content, and setting time of the mixtures using standard needles at regular time intervals. The mechanical performance was evaluated through compressive strength at different ages and flexural performance. The resistance to freezing-thawing cycles (total of 300 cycles) was evaluated according to ASTM C666, based on the durability factor (*DF*). In addition, the features of pore structure of the mixtures were assessed by mercury intrusion porosimetry (MIP). Furthermore, thermal and microscopy studies were performed to assess the hydration evolution and microstructure of the composites.

The BFP interfacial bonding with various matrices was evaluated for fundamental understanding of the performance of nano-modified cementitious composites, with respect to crack bridging and load transferring mechanisms, as well as correlating bond strength of the pellet/matrices interface with the flexural properties. Fourteen mixtures were investigated to evaluate various nano-modified cementitious composites under single pellet pull-out and flexural tests, coupled with scanning electron microscopy and thermal studies. Besides, a complementary modeling (homogenization/FEM) approach using ANSYS software package was developed to determine the homogenized stiffness coefficient $k_{ij}$of nano-modified cementitious composites and interfacial single BFP bond strength. The FEM approach introduced herein had high reliability with the experimental data. The models could capture evolution of micro-cracks, and stress-strain distributions around the pellet in the nano-modified matrices comprising PVA (micro-fibers) and NFC, respectively. Parametric analyses were conducted to show the effect of different fibers volume fractions on the homogenized stiffness coefficient k_{ij} and BFP interfacial bond strength τ_t.

Owing to the superior performance of the cementitious composites, the suitability of these composites as a filler material in shear key bridge joints was examined. The interfacial bonding capacity between HPFRCC and parent conventional concrete (CC) under shear configurations, as well as its interaction with reinforcing rebars were evaluated. Six mixtures were prepared and tested under compression and tension tests to evaluate the bonding performance of HPFRCC by slant shear (combination of compressive and shear stresses at the interface), bi-shear (pure shear stresses at the

interface), and rebar pull-out tests. This was coupled with thermal and microstructure studies to verify the elucidate trends.

Based on the previous outcomes of bonding characterization of cementitious composites under various loading configurations, the efficiency of HPFRCC in shear key bridge joints was predicted using FEM. Six mixtures were simulated to evaluate the bonding stress distribution, modes of failures, crack pattern/formation process between these composites and precast CC beams, as well as steel rebars. Subsequently, based on the validated model outcomes with relevant experimental results, a full-scale 3D FEM for predicting the performance of shear key joint filled with various HPFRCC under HL-93 design truck loads according to AASHTO LRFD [2020] was analyzed.

7.2 Conclusions

7.2.1 Factors Affecting Properties of Nano-Modified Cementitious Composites (Chapter 3)

- The addition of 6% nano-silica to the high-volume slag-based binder significantly enhanced the performance (shortened setting times and increased compressive strength, flexural strength, toughness, and resistance to freezing-thawing cycles) of the composites. The synergistic effects of nano-silica, cement and slag enhanced the binder reactivity/maturity and produced dense microstructure.
- Increasing the dosage of macro-BFP (single system) led to reduction in the mechanical capacity and durability to frost action of the composites, due to increasing air contents and creation of additional of ITZs in the matrix. However, the BFP improved the flexural performance in terms of post-cracking behavior and toughness of the composites, due to the improved bonding with the matrix (precipitation of hydration/pozzolanic products in the pellets' micro-groves).

- The hydrophilic nature and chemical effect of micro-PVA fibers improved the mechanical properties and resistance to frost action of the composites with PVA (single system); however, a brittle failure occurred after reaching the first-peak flexural strength due to the 1% dosage used that was inadequate to restrain the macro-cracks propagation.
- Addition of 1% micro-PVA fibers to 2.5% or 4.5% macro-BFP (hybrid system) led to balanced performance of the composites in terms of refined pore structure, mechanical capacity, ductility, and durability to frost action. Micro-PVA fibers produced more tortuous pore structure and impeded the coalescence of micro-cracks, while macro-BFP restrained the propagation of macro-cracks, thus improving performance of the composites.
- The overall results from this study indicated that nano-modified high-volume slag-based cementitious composites comprising hybrid micro-PVA fibers and macro-BFP can be a viable option for various construction applications serving under freezing-thawing exposures and also requiring high mechanical capacity and ductility.

7.2.2 Evaluation of Single Pellet Interfacial Bond Strength with Various Cementitious Composites (Chapters 4)

- Nano-modified cementitious composites incorporating NS (G-N) had balanced performance in terms of enhancing the first-cracking flexural capacity, post-cracking residual strength and toughness relative to that of the reference binder (G), due to the synergetic effects of NS with slag, which increased the degree of matrix maturity, produced dense microstructure, led to extensive deposition of cementitious gel/products in the BFP micro-groves, and consequently enhancement of BFP/matrix friction and interfacial bonding.

- The hydroxyl groups (OH^-) on NCC and spindle geometry creating a pathway for transporting water in the matrix improved the hydration development of G-NCC matrix, and thus its first-cracking flexural capacity relative to that of the reference matrix (G). However, the post-cracking residual strength and overall toughness of G-NCC had less improvement compared to that of the G-N counterpart, due to the similar deposition pattern as the reference matrix G at the interface with BFP micro-groves.
- Increasing the dosage of BFP macro-fibers decreased the first-peak flexural strength of the composites due to increasing the air content and creation of additional ITZs in the matrix; however, the 4.5% BFP contributed to enhancing the flexural performance of the composites in terms of post-cracking deflection-hardening and toughness, especially with the presence of NS, due to the resistance of abundant number of pellets in the failure plane to pull-out.
- The hydrophilic and chemical effects of 1% PVA micro-fibers with 2.5% or 4.5% BFP macro-fibers (hybrid system) led to improvement in the first-peak flexural strength of the NS-modified matrix (G-N). Randomly distributed micro-PVA clusters in the G-N matrix surrounding BFP promoted the likelihood of interlocking, which increased friction, bond strength and de-bonding energy. This was reflected by enhancement in the flexural deflection-hardening behavior of these composites, and achievement of the highest toughness.
- Addition of 0.2% NFC (nano-fibres) with 2.5% or 4.5% BFP macro-fibers (hybrid system) to the matrix modified with NCC (G-NCC-NFC) increased its first-cracking flexural strength, owing to the hydrophilic/hygroscopic features of NFC acting as an internal curing aid. However, these composites had reduced toughness, due to

deposition of NFC patches in the textured micro-grooves of BFP which acted as separation zones with the matrix leading to easier slippage of the pellets, as verified by the single pellet pull-out tests.

- The mesoscopic RVEs developed herein (0.5 mm for G-NCC-NFC and 12 mm for G-N-V) showed accurate predictions for the homogenized Young's modulus and tensile strength of nano-modified matrices comprising nano- or micro-fibers, in comparison to the direct tension test results. Also, the FEM approach introduced herein had high reliability in predicting the bond-slip relationships of the single BFP pull-out from all matrices, showing the evolution of cracks and stress/strain distributions in the vicinity of BFP. The FEM parametric analysis indicated that BFP interfacial bond strength and de-bonding energy could be improved by increasing the content of PVA up to 2% in the G-N matrix, whereas reduction in these interfacial metrics could be obtained by increasing the NFC dosage up to 0.3%.
- The compendious results from this study indicated that nano-modified slag-based cementitious composites comprising hybrid PVA/BFP fibers (G-N-V1-B2.5 and G-N-V1-B4.5) can be a viable option for a suite of construction applications requiring balance between mechanical capacity, interfacial bonding and ductility, with the potential for increasing the dosage of PVA micro-fibers up to 2% by volume. The proposed computational multiscale analysis can efficiently predict the behavior of materials with complex microstructure, with the capability of parametric analysis instead of laborious experiments.

7.2.3 Bonding Evaluation of Nano-Modified Cementitious Composites (Chapter 5).

- The synergistic effects of nano-silica, cement, and high-volume slag improved the maturity of the paste and created very dense microstructure, leading to improvement in the compressive strength (up to 15%) at earlier ages (7 and 28 days), and tensile strength (up to 20%), which make them practical for field applications.
- The nano-modified composites comprising 6% NS had noticeable improvement in terms of interfacial bond strength (more than 20%), and de-bonding energy (more than 40%), with the CC (slant shear, direct shear) and steel rebar (pull-out) due to the nucleation, pozzolanic reactivity and filling effects of NS, which resulted in intensive participation of additional cementitious products at the interface zone.
- Increasing the BFP dosage in the cementitious composites decreased the mechanical capacity of HPFRCC (up to 20 % drop) determined at first-cracking, and the interfacial bond strength (up to 21 % drop) with CC (slant-shear, bi-shear tests) due to the creation of additional ITZs in the matrix.
- Conversely, BFP contributed to enhancing the post-cracking tensile performance in terms of strain-hardening modulus (up to 394%) and energy absorption/toughness (up to 41%), due to the resistance of abundant number of pellets in the failure plane to pull-out, especially with the presence of NS which promoted precipitation of cementitious products in the microgrooves. Moreover, randomly distributed BFP in the matrix increased the likelihood of composites' confinement and interlock surrounding the steel rebar, which enhanced the rebar bond strength and de-boding energy up to 105% and 174%, respectively.
- The superficial hydroxyl groups, hydrophilic nature and micro-crack bridging effects of PVA micro-fibers enhanced the mechanical capacity of HPFRCC comprising BFP.

The coexistence of 1% PVA micro-fibers with 2.5% or 4.5% BFP macro-fibers led to improvement in the interfacial bond strength (up to 40%) and de-bonding energy (more than 80%) with CC, due to increasing adhesion and friction, and micro-crack deviation/blunting at the interface with CC; in addition, the hybrid fibers increased the rebar bond strength and de-boding energy up to 20% and 29%, respectively due to additional confinement and interlocking around the ribs of the rebar.

- The compendious results from this study determined that nano-silica modified slag-based cementitious composites including hybrid fibers (G-N-V1-B2.5 and G-N-V1-B4.5) can be a feasible option for partial depth repair/overlay in concrete pavements/bridges, or as a filler material in bridge deck shear key joints applications requiring balance of mechanical capacity, interfacial bonding and ductility.

7.2.4 Potential of Nano-Modified Cementitious Composites in Shear Key Joints (Chapter 6)

- The meso-scale RVEs homogenization models developed herein were capable of predicting the elastic properties of HPFRCC as verified by comparison to the direct tension test results. Also, the FEM approach introduced herein had high reliability in predicting the HPFRCC interfacial bonding behaviour with precast CC and steel rebar, showing the evolution of cracks formation in the matrix relative to the peak load and bond stress distributions along the interface with CC and rebar.
- The pozzolanic reactivity and filling effects of nano-silica increased the interfacial bond strength (more than 29%), and de-bonding energy (more than 43%), with CC and steel rebar, as well as the shear capacity of the shear key joint (by 13%), due to intensive participation of secondary cementitious products at the interface zone.

- The FEM predicted two modes of failure for HPFRCC shear key joints including interface cracking failure and partial interface failure followed by cracking/crushing of precast CC beams. The latter happened in the hybrid PVA/BFP composites, where the initial crack formation occurred up to 85% of ultimate loads, and diagonal cracks' deviation into the precast beams was at approximately 45° with the horizontal.
- The FEM showed that addition of BFP in the nano-modified composites decreased the interfacial bond strength (up to 21 %), and debonding energy (up to 22%), due to the creation of additional ITZs at the interface between HPFRCC and precast CC. However, increasing the dosage of BFP macro-fibers in the composites improved the rebar bond strength (up to 88%), and debonding energy (up to 135%). Thus, the net effect of BFP led to slightly improving the shear of bridge joints (up to 34%), owing to the dominant crack bridging effect of BFP macro-fibers and interlocking/friction around the shear dowels.
- The hydrophilic nature, hydroxyl groups, and crack bridging effects of PVA micro-fibers improved the interfacial bond strength (up to 21%), and debonding energy (up to 97%) with CC and steel rebar. Accordingly, the FEM showed that the hybrid PVA/BFP system (G-N-B2.5-V1 and G-N-B4.5-V1) improved the shear resistance force of the joint by up to 130% of the standard load, due to improving the adhesive capacity and friction at the interfacial zone with CC and efficient interlocking with BFP around steel reinforcement, meeting the AASHTO LRFD interface coefficient of friction and adhesion parameters for rough surfaces.
- The overall results from this study suggest that nano-silica modified HPFRCC comprising hybrid fibers (G-N-V1-B2.5 and G-N-V1-B4.5) can be a practicable option for shear key joints with enhanced bonding capacity with CC and shear

reinforcement. Moreover, the developed finite element models herein could efficiently project the expected full-scale behavior of complex composites such as HPFRCC including its shear capacity, crack formation process, and modes of failure.

7.3 Recommendations

- Increasing the micro-PVA dosage up to 2% by volume in HPFRCC is recommended for a future study to evaluate the magnitude of improvement with respect to ductility properties and multiple cracking phenomenon.
- Laboratory fatigue experimental testing is recommended for future research to investigate the effect of HPFRCC developed in this thesis under cyclic loading, particularly in shear key bridge joints.
- The application of nano-modified cementitious composites as a filler in shear key bridge joints is recommended in a field trial to substantiate the predicted behavior by the FEM developed herein.
- Large-scale field trials including realistic cost/performance analysis of HPFRCC developed herein, especially when producing bulk amounts of BFP, relative to other cementitious composites commercially available in the construction sector are recommend for future research, to substantiate the findings obtained from this study.

REFERENCES

AASHTO LRFD, 2020. *American Association of State Highway and Transportation Officials LRFD Bridge Design Specifications (8th ed)*, Washington, DC, USA.

ACI (American Concrete Institute). (2014), *Building code requirements for structural concrete*, ACI 318-14, Farmington Hills, MI.

Ahmad, F.S., Foret, G. and Le Roy, R., 2011. "Bond Between Carbon Fibre-Reinforced Polymer (CFRP) Bars and Ultra High-Performance Fibre Reinforced Concrete (UHPFRC): Experimental Study." *Construction and Building Materials*, 25(2), pp.479-485.

Al-Aljaberi, Z., Myers, J.J., and Chandrashekhara, K., 2018. "Behavior of EB FRP Masonry Bond under Service Temperature." *Advance Material Letters*, Linkoping, Sweden., 9(11), pp. 753-769.

Al-Jaberi, Z., Myers, J.J., and Chandrashekhara, K., 2019. "Effect of Direct Service Temperature Exposure on The Bond Behavior Between Advanced Composites and CMU Using NSM and EB Techniques." *Composite Structures*, 211, pp. 63-75.

Al-Jaberi, Z.K., and Myers, J.J., 2019. "Effect of Different Temperatures on Epoxy Adhesive Used in Near Surface Mounted FRP Bars Strengthened Concrete Masonry Unit Under Direct Shear Test." *In Advances in Engineering Materials, Structures and Systems: Innovations, Mechanics and Applications*, pp. 1560-1565.

Al-Khafaji, A.W., Tooley, J.R. and Al-Khafaji, A.W., 1986. *Numerical Methods in Engineering Practice*. (190), Holt, Rinehart and Winston, New York (NY), USA.

Al-Madani, M.K., Al-Osta, M.A., Ahmad, S., Khalid, H.R. and Al-Huri, M., 2022. "Interfacial Bond Behavior Between Ultra-High-Performance Concrete and Normal Concrete Substrates." *Construction and Building Materials*, 320, pp.126229-14.

ANSYS Inc., 2020. "Ansys Workbench 19 R2." Pennsylvania, USA.

Arslan, M. E., 2016. "Effects of Basalt and Glass Chopped Fibers Addition on Fracture Energy and Mechanical Properties of Ordinary Concrete: CMOD measurement." *Construction and Building Materials*, 114, pp. 383-391.

Arafa, A., Farghaly, A.S., Ahmed, E.A. and Benmokrane, B., 2016. "Laboratory testing of GFRP-RC panels with UHPFRC Joints of the Nipigon River cable-stayed bridge in Northwest Ontario, Canada. *Journal of Bridge Engineering*, 21(11), pp.05016006-14.

Arjomandi, H. and Asl, A.F., 2021. "Pull-out Strength between Nano-SiO 2 Contained Light-Weight Self-Consolidating Concrete and GFRP and Steel bars", *Computer and Concrete*, 27(6), pp. 563-574.

ASTM (American Society for Testing and Materials), 2019. *Standard Test Method for Flexural Performance of Fiber-Reinforced Concrete (using beam with third-point loading)*. ASTM C1609/C1609M-19, West Conshohocken, PA, USA

ASTM (American Society for Testing and Materials), 2020. *Standard Test Method for Bond Strength of Epoxy Resin Concrete by Slant Shear*. C882/C882M-20, West Conshohocken, PA, USA

ASTM (American Society for Testing and Materials), 2015. *Standard Test Method for Resistance of Concrete to Rapid Freezing and Thawing*. ASTM C666/C666M-15, West Conshohocken, PA, USA

ASTM (American Society for Testing and Materials), 2017. *Standard Specification for Chemical Admixtures for Concrete*. ASTM C494/C494M-17, West Conshohocken, PA, USA.

ASTM (American Society for Testing and Materials), 2016. *Standard Test Method for Time of Setting of Concrete Mixtures by Penetration Resistance*. ASTM C403/C403M-16, West Conshohocken, PA, USA.

ASTM (American Society for Testing and Materials), 2017. *Standard Test Method for Air Content of Freshly Mixed Concrete by the Pressure Method*. ASTM C231/C231M-17, West Conshohocken, PA, USA.

ASTM (American Society for Testing and Materials), 2020. *Flow Table for Use in Tests of Hydraulic Cement*. ASTM C230/C230M-20, West Conshohocken, PA, USA.

ASTM (American Society for Testing and Materials), 2019. *Standard Test Method for Fundamental Transverse, Longitudinal and Torsional Resonant, Frequencies of Concrete Specimens*. ASTM C215/C215M-19, West Conshohocken, PA, USA.

ASTM (American Society for Testing and Materials), 2018. *Standard Test Method for Compressive Strength of Cylindrical Concrete Specimens*. ASTM C39/C39M-18, West Conshohocken, PA, USA.

Ayub, T. Shafiq, N. and Nuruddin, M. F., 2014. "Mechanical Properties of High-Performance Concrete Reinforced with Basalt Fibers." *Procedia Engineering*, 77, pp. 131-139.

Azzam, A., Bassuoni, M.T. and Shalaby, A., 2022. "Flexural Performance of Nanomodified Cementitious Composites Reinforced with BFP in Bonded Overlays." *Journal of Materials in Civil Engineering*, 34(8), pp. 04022169-14.

Azzam, A. Bassuoni, M. T. and Shalaby, A., 2021. "Nanomodified Cementitious Composites Incorporating Basalt Fiber Pellets under Tensile and Impact Loads." *Journal of Materials in Civil Engineering*, 33(10), pp. 04021260-14.

Azzam, A. Bassuoni, M. T. and Shalaby, A., 2019. "Properties of High-Volume Fly Ash and Slag Cementitious Composites Incorporating Nanosilica and Basalt Fiber Pellets." *Advance in Civil Engineering Materials*, 8(3), pp. 255-274.

Balamirzoev, A. G., Abdullaev, A. R., and Selimkhanov, D. N., 2021. Elastic-Plastic Model of Concrete Damage and Its Main Design Parameters. *In Environmental and Construction Engineering: Reality and the Future, Springer*, pp. 37-44.

Bandelt, M. J., and Billington, S. L., 2016. "Impact of Reinforcement Ratio and Loading Type on the Deformation Capacity of High-Performance Fiber-Reinforced

Cementitious Composites Reinforced with Mild Steel." *Journal of Structural Engineering*, 142(10), pp. 04016084-14.

Banholzer, B., Brameshuber, W., and Jung, W., 2005. "Analytical Simulation of Pull-out Tests—the Direct Problem." *Cement and Concrete Compos*ites, 27(1), pp. 93-101.

Bediwy, A.G. and El-Salakawy, E.F. 2021. "Bond Behavior of Straight and Headed GFRP Bars Embedded in a Cementitious Composite Reinforced with Basalt Fiber Pellets." *Journal of Composites for Construction*, 25(5), pp. 04021038-14.

Bediwy A., and El-Salakawy E.F., 2021. Mechanical Properties of Hybrid Structures Incorporating Nano-Silica and Basalt Fiber Pellets. *Civil Eng*ineering, 2(4), pp. 909-928.

Bentur, A., Mindess, S, 2006. Fibre Reinforced Cementitious Composites, CRC Press, London, UK.

Benveniste, Y., 1987. "A New Approach to the Application of Mori-Tanaka's Theory in Composite Materials." *Mechanics of Materials*, 6(2), pp. 147-157.

Branston J., Das S., Kenno S.Y., and Taylor, C., 2016. Mechanical Behaviour of Basalt Fibre Reinforced Concrete. *Construction and Building Materials*, 124, pp. 878-886.

Cao, Y., Zavaterri, P., Youngblood, J., Moon, R., and Weiss, J., 2015. "The Influence of Cellulose Nano Crystal Additions on the Performance of Cement Paste." *Cement and Concrete Composites*, 56, pp. 73-83.

Cao, Y., Zavattieri, P., Youngblood, J., Moon, R., and Weiss, J., 2016. "The Relationship between Cellulose Nano Crystal Dispersion and Strength." *Construction and Building Materials*, 119, pp. 71-79.

Carbonell Muñoz, M. A., Harris, D. K., Ahlborn, T. M., and Froster, D. C., 2013. Bond Performance between Ultrahigh-Performance Concrete and Normal-Strength Concrete. *Journal of Materials in Civil Engineering*, 26(8), pp. 04014031-14.

Christensen, R. M., and Lo, K., 1979. "Solutions for Effective Shear Properties in Three Phase Sphere and Cylinder Models." *Journal of Mechanics and Physics of Solid.*, 27(4), pp. 315-330.

Chu, S.H. and Kwan, A.K.H., 2018. A new Method for Pull out Test of Reinforcing Bars in Plain and Fibre Reinforced Concrete. *Engineering Structures*, 164, pp. 82-91.

CSA, 2019. Concrete Materials and Methods of Concrete Construction/ Test Methods and Standard Practices for Concrete. *CSA-A23.1/A23.2:19,* Canadian Standards Association, Mississauga, ON, Canada.

CSA, 2018. Cementitious Materials for Use in Concrete. *CSA-A3001-18*. Canadian Standards Association, Mississauga, ON, Canada.

Craig, R.R. and Taleff, E.M., 1996. *Mechanics of Materials*. (Vol. 2), Wiley New York (NY), USA.

Dawood, E. T., & Ramli, M., 2011. "High Strength Characteristics of Cement Mortar Reinforced with Hybrid Fibres." *Construction and Building Materials,* 25(5), pp. 2240-2247.

Detwiler, R., Bhatty, J., and Bhattacharja, S., 1996. *Supplementary Cementing Materials for Use in Blended Cements*. (103), Portland Cement Association, Skokie, IL.

Da Costa Correia, V., Santos, S.F., Teixeira, R.S., and Junior, H.S., 2018. "Nanofibrillated Cellulose and Cellulosic Pulp for Reinforcement of the Extruded Cement-Based Materials." *Construction and Building Materials*, 160, pp. 376-384.

Douglas, K.S. and Billington, S.L., 2005, May. Rate Dependence in High-Performance Fiber Reinforced Cement Based Composites for Seismic Applications. In *Proceedings, HPFRCC-2005 international workshop, Honolulu, Hawaii, USA*.

Dalalbashi, A., Ghiassi, B., Oliveira, D.V. and Freitas, A., 2018. "Effect of Test Setup on the Fiber-to-Mortar Pull-out Response in TRM Composites: Experimental and Analytical Modeling." Composites Part B: Engineering, 143, pp.250-268.

Elhadary, R., and Bassuoni, M. T., 2021. "Mechanical Properties of Nano-Modified Cementitious Composites Reinforced with Single and Hybrid Fibers." *Transportation Research Record*, 2675(9), pp. 56-64.

El-Remaily, A., Tadros, M. K., Yamane, T., and Krause, G., 1996. "Transverse Design of Adjacent Precast Prestressed Concrete Box Girder Bridges." *PCI journal*, 41(4), pp. 96- 113.

Flores, J., Kamali, M., and Ghahremaninezhad, A., 2017. "An Investigation into the Properties and Microstructure of Cement Mixtures Modified with Cellulose Nanocrystal." *Materials*, 10(5), pp. 498-16.

Fu, J. Yuan, A. and Wan, S., 2021. "Behavior of Fiber Reinforced Key Joints in Precast Concrete Segmental Bridge: Experimental and Numerical Analysis", *Journal of Bridge Engineering*, 26(8), pp. 04021053-14.

Fu, T., Montes, F., Suraneni, P., Youngblood, J., and Weiss, J., 2017. "The Influence of Cellulose Nanocrystals on the Hydration and Flexural Strength of Portland Cement Pastes." *Polymers*, 9(9), pp. 424-440.

Flores, E.Y., Varbel, J., Toledo, W.K., Newtson, C.M. and Weldon, B.D., 2021. "Ultrahigh-Performance Concrete Shear Keys in Concrete Bridge Superstructures", *Transportation Research Record.*, 2675(2), pp. 108-120.

Ghazy A, Bassuoni MT, Shehata E, and Burmey, D., 2019. "Comparison of Different Approaches for Determining the Tesidual Post-Cracking Strength Index of Fiber Reinforced Concrete for Bridges". *Canadian Journal of Civil Engineering*, 46(5), pp. 462-465.

Ghazy, A., Bassuoni, M. T., and Shalaby, A., 2016. "Nano-Modified Fly Ash Concrete: A Repair Option for Concrete Pavements." *ACI. Materials Journal*, 113(2), pp. 231-42.

Ghazy, A., Bassuoni, M. T., Maguire, E., and O'Loan, M., 2016. "Properties of Fiber-Reinforced Mortars Incorporating Nano-Silica." *Fibers*, 4(1), 1-16.

Gomaa, E., Gheni, A. and ElGawady, M.A., 2020. "Repair of Ordinary Portland Cement Concrete Using Ambient-Cured Alkali-Activated Concrete: Interfacial behavior." *Cement and Concrete Research*, 129, pp.105968.

Grace, N. F., Jensen E. A., Enomoto T., Matsagar V. A., Soliman E. M., and Hanson J. Q., 2010. "Transverse Diaphragms and Unbonded CFRP Posttensioning in Box Beam Bridges". *PCI Journal,* 55(2), pp. 109-122.

Griffiths, G.and Thom, N., 2007. *Concrete Pavement Design Guidance Notes.* London and New York (NY): Taylor and Francis Group. 168 p. CRC Press. ISBN 978-0-203-96206-0.

Haile, B. F, Jin, D. W., Yang, B., Park, S., and Lee, H. K., 2019. "Multi-level Homogenization for the Prediction of the Mechanical Properties of Ultra-High-Performance Concrete." *Construction and Building Materials*, 229, pp. 116797-17.

Halvaei, M., Jamshidi, M. and Latifi, M., 2014. Application of Low Modulus Polymeric Fibers in Engineered Cementitious Composites. *Journal of industrial textiles*, *43*(4), pp.511-524.

Hanif, A., Parthasarathy, P., Lu, Z., Sun, M. and Li, Z., 2017. Fiber-Reinforced Cementitious Composites Incorporating Glass Cenospheres–Mechanical Properties and Microstructure. *Construction and Building Materials*, *154*, pp.529-538.

Hanna, K. E., Morcous, G., and Tadros, M. K., 2009. "Transverse Post-Tensioning Design and Detailing of Precast, Prestressed Concrete Adjacent-Box-Girder Bridges". *PCI journal*, 54(4), pp. 160-174.

Hisseine, O.A., Wilson, W., Sorelli, L., Tolnai, B., and Tagnit-Hamou, A., 2019. "Nanocellulose for Improved Concrete Performance: A Macro-to-Micro

Investigation for Disclosing the Effects of Cellulose Filaments on Strength of Cement Systems." *Construction and Building Materials*, 206, pp. 84-96.

Hisseine, O. A., Omran, A. F., and Tagnit-Hamou, A., 2018. "Influence of Cellulose Filaments on Cement Paste and Concrete. *Journal of Materials in Civil Engineering*, 30(6), pp. 04018109-14.

Hoyos, C. G., Cristia, E., and Vázquez, A., 2013. "Effect of Cellulose Microcrystalline Particles on Properties of Cement-Based Composites." *Materials and Design*, 51, pp. 810-818.

Hussein, H. H., Sargand, S. M., Khoury, I., & Al-Jhayyish, A. K., 2017b. "Environment-Induced Behavior of Transverse Tie Bars in Adjacent Prestressed Box-Girder Bridges with Partial Depth Shear Keys". *Journal of Performance of Constructed Facilities*, 31(5), pp. 04017074-14.

Hussein, H. H., Sargand, S. M., Al-Jhayyish, A. K., & Khoury, I., 2017a. "Contribution of Transverse Tie Bars to Load Transfer in Adjacent Prestressed Box-Girder Bridges with Partial Depth Shear Key". *Journal of Performance of Constructed Facilities*, pp. 04016100-14.

Hussein, H.H., Sargand, S.M., Al Rikabi, F.T. and Steinberg, E.P., 2017. "Laboratory Evaluation of Ultrahigh-Performance Concrete Shear Key for Prestressed Adjacent Precast Concrete Box Girder bridges", *Journal of Bridge Engineering*, 22(2), pp. 04016113-14.

Hu, M., Han, Q., Wu, S. and Du, X., 2021. "Shear Capacity of Precast Concrete Shear Keys with Ultrahigh-Performance Concrete for Connections", *Journal of Bridge Engineering,* 26(7), pp. 04021036-14.

Hosford, W.F., 2010. *Solid Mechanics*. Cambridge University Press, Cambridge, UK

Iyer, P., Kenno, S. Y., and Das, S., 2016. "Performance of Fiber-Reinforced Concrete Made with Basalt-Bundled Fibers." *Advance in Civil Engineering Materials,* 5(1), pp. 107-123.

Iyer, P., Kenno, S. Y., and Das, S., 2015. "Mechanical Properties of Fiber-reinforced Concrete Made with Basalt Filament Fibers." *Journal of Material in Civil Engineering*, 27(11), pp. 04015015-8.

Yang, E.H. and Li, V.C., 2014. Strain-Rate Effects on the Tensile Behavior of Strain-Hardening Cementitious Composites. *Construction and Building materials*, 52, pp.96-104.

Jalasutram, S., Sahoo, D.R. and Matsagar, V., 2017. Experimental Investigation of the Mechanical Properties of Basalt Fiber-Reinforced Concrete. *Structural Concrete*, *18*(2), pp. 292-302.

Jia, J. Zhang, K. Saiidi, M.S. Guo, Y. Wu, S. Bi, K. and Du, X., 2020. "Seismic Evaluation of Precast Bridge Columns with Built-in Elastomeric Pads." *Soil Dynamics and Earthquake Engineering*, 128, pp. 105868-14.

Jiang, H., Chen, L., Ma, Z.J. and Feng, W., 2015. "Shear Behavior of Dry Joints with Castellated Keys in Precast Concrete Segmental Bridges." *Journal of Bridge Engineering,* 20(2), pp. 04014062-12.

Jiang, C., Fan, K., Wu, F., and Chen, D., 2014. "Experimental Study on the Mechanical Properties and Microstructure of Chopped Basalt Fibre Reinforced Concrete." *Materials and Design*, 58, pp. 187-193.

Jongvisuttisun, P., Negrello, C., and Kurtis, K. E., 2013. "Effect of Processing Variables on Efficiency of Eucalyptus Pulps for Internal Curing." *Cement and Concrete Composites,* 37, pp. 126-135.

Julander, J.L. 2009. *Finite Element Modeling of Full Depth Precast Concrete Transverse Bridge Deck Connections*. Utah State University, USA.

Kanit, T., Forest, S., Galliet, I., Mounoury, V., and Jeulin, D., 2003. "Determination of the Size of the Representative Volume Element for Random Composites: Statistical and Numerical Approach." *International Journal of Solids and Structures,* 40(13-14), pp. 3647-3679.

Kawashima, S. and Shah, S.P., 2011. Early-Age Autogenous and Drying Shrinkage Behavior of Cellulose Fiber-Reinforced Cementitious Materials. *Cement and Concrete Composites, 33*(2), pp.201-208.

Khaksefidi, S., Ghalehnovi, M. and De Brito, J., 2021. "Bond Behaviour of High-Strength Steel Rebars in Normal (NSC) and Ultra-High-Performance Concrete (UHPC)." *Journal of Building Engineering,* 33, pp.101592-16.

Kim, B., Doh, J.H., Yi, C.K. and Lee, J.Y., 2013. "Effects of Structural Fibers on Bonding Mechanism Changes in Interface Between GFRP Bar and Concrete." *Composites Part B: Engineering*, 45(1), pp. 768-779.

Kong, D., Du, X., Wei, S., Zhang, H., Yang, Y., and Shah, S. P., 2012. "Influence of Nano-Silica Agglomeration on Microstructure and Properties of the Hardened Cement-based Materials." *Construction and Building Materials*, 37, pp. 707-715.

Kuder, K.G., Ozyurt, N., Mu, E.B. and Shah, S.P., 2007. Rheology of Fiber-Reinforced Cementitious Materials. *Cement and Concrete Research*, *37*(2), pp.191-199.

Laranjeira, F., Molins, C., & Aguado, A., 2010. "Predicting the Pullout Response of Inclined Hooked Steel Fibers." *Cement and Concrete Research*, 40(10), 1471-1487.

Lee, J.J., Song, J. and Kim, H., 2014. "Chemical Stability of Basalt Fiber in Alkaline Solution." *Fibers and Polymers*, *15*(11), pp.2329-2334.

Lenz, R. W., 2011. *Pavement Design Guide*. Texas Department of Transportation, Texas, USA, pp. 428

Lepech, M.D., and Li, V.C., 2010. "Sustainable pavement overlays using engineered cementitious composites." *International Journal of Pavement Research and Technology*, 3(5), 241-250.

Li, V.C., 2004. Strategies for high-performance fiber reinforced cementitious composites development, Fiber Reinforced Concrete: From Theory to Practice. In *Proceedings of the North American/European, Workshop on Advances in Fiber Reinforced*

Concrete, S. Ahmad, M. di Prisco, C. Meyer, G. A. Plizzari, and S. Shah, eds., Bergamo, Italy; pp. 93-98.

Li, Q., Gao, X., and Xu, S., 2016. "Multiple Effects of Nano-SiO2 and Hybrid Fibers on Properties of High Toughness Fiber Reinforced Cementitious Composites with High-Volume Fly Ash". *Cement and Concrete Compos*ites, 72, pp. 201-212.

Li, V. C., Wang, S., and Wu, C., 2001. "Tensile Strain-Hardening Behavior of Polyvinyl Alcohol Engineered Cementitious Composite (PVA-ECC)." *ACI Materials Journal*, 98(6), pp. 483-492.

Li X, Wang J, Bao Y, and Chen, G., 2017. "Cyclic Behavior of Damaged Reinforced Concrete Columns Repaired with High-Performance Fiber-Reinforced Cementitious Composite". *Engineering Struct*ures,136, pp. 26-35.

Li, Y., and Li, Y., 2019. "Evaluation of Elastic Properties of Fiber Reinforced Concrete with Homogenization Theory and Finite Element Simulation." *Construction and Building Materials*, 200, pp. 301-309.

Liu, T., Wang, Z., Guo, J. and Wang, J., 2019. "Shear Strength of Dry Joints in Precast UHPC Segmental Bridges: Experimental and Theoretical Research", *Journal of Bridge Engineering*, 24(1), pp. 04018100-16.

Liu, S. G., He, C., Yan, C. W., and Zhao, X. M., 2011. "Water Permeability of Polyvinyl Alcohol (PVA) Fiber Reinforced Cementitious Composites." *Advanced Materials Research*, 150, pp. 1009-1012.

Loh, Z.P., Mo, K.H., Tan, C.G., & Yeo, S.H., 2019. "Mechanical Characteristics and Flexural Behaviour of Fibre-Reinforced Cementitious Composite Containing PVA and Basalt Fibres". *Sādhanā.*, 44(4), pp. 1-9.

Lubliner, J., Oliver, J., Oller, S., and Onate, E., 1989. "A Plastic-Damage Model for Concrete." *International Journal of Solids and Structures*, 25(3), pp. 299-326.

Lubliner, J. and Papadopoulos, P. 2016. Introduction to Solid Mechanics. Springer-Verlag, New York, USA.

Ma, H., Qian, S., Zhang, Z., Lin, Z. and Li, V.C., 2015. "Tailoring Engineered Cementitious Composites with Local Ingredients." *Construction and Building Materials, 101*, pp.584-595.

Mahmoud, K., Ghazy, A., Bassuoni, M. T., and El-Salakawy, E., 2017. "Properties of Nanomodified Fiber-reinforced Cementitious Composites." *Journal of Material in Civil Engineering*, 29(10), pp. 04017173-12.

Mechtcherine, V., 2013. Novel Cement-Based Composites for the Strengthening and Repair of Concrete Structures. *Construction and Building Materials*, 41, pp.365-373.

Meng, D., Huang, T., Zhang, Y. X., and Lee, C. K., 2017. "Mechanical Behaviour of a Polyvinyl Alcohol Fibre Reinforced Engineered Cementitious Composite (PVA-ECC) using Local Ingredients." *Construction and Building Materials*, 141, pp. 259-270.

Model Code 2010. First complete draft – vol. 1. Comité Euro-International du Béton, Secretariat permanent, Case Postale 88, CH-1015 Lausanne, Switzerland.

Mori, T., and Tanaka, K., 1973. "Average Stress in Matrix and Average Elastic Energy of Materials with Misfitting Inclusions." *Acta Metallurgica*, 21(5), pp. 571-574.

Neville, A.M., 2011. *Properties of Concrete.* Prentice Hall. London, UK.

Noushini, A., Samali, B., and Vessalas, K., 2013. "Effect of Polyvinyl Alcohol (PVA) Fibre on Dynamic and Material Properties of Fibre Reinforced Concrete". *Construction and Building Materials*, 49, pp. 374-383.

Nye, J. F., 1985. *Physical Properties of Crystals: Their Representation by Tensors and Matrices*. Oxford University Press, New York (NY), USA.

Onuaguluchi, O., Panesar, D. K., and Sain, M., 2014. "Properties of Nano-Fibre Reinforced Cement Composites. *Construction and Building Materials*, 63, pp. 119-124.

Ondova, M., Stevulova, N., and Meciarova, L., 2013. "The Potential of Higher Share of Fly Ash as Cement Replacement in the Concrete Pavement". *Procedia Eng*ineering, 65, pp. 45-50.

Özkan, Ş., and Çoban, Ö., 2021. The Hybrid Effects of Basalt and PVA Fiber on Properties of a Cementitious Composite: Physical Properties and Non-Destructive Tests. *Construction and Building Materials*, 312, pp. 125292-17.

Özkan, Ş., and Demir, F., 2020. "The Hybrid Effects of PVA Fiber and Basalt Fiber on Mechanical Performance of Cost-Effective Hybrid Cementitious Composites. *Construction and Building Materials*, 263, pp. 120564-16.

Pan, Z. Wu, C. Liu, J. Wang, W. and Liu, J., 2015. "Study on Mechanical Properties of Cost-effective Polyvinyl alcohol Engineered Cementitious Composites (PVA-ECC)." *Construction and Building Materials*, 78, pp. 397-404.

Park, S. H., Kim, D. J., Ryu, G. S., and Koh, K. T., 2012. "Tensile Behavior of Ultra-High-Performance Hybrid Fiber Reinforced Concrete." *Cement and Concrete Compos*ites, 34(2), pp. 172-184.

Poorhosein, R. and Nematzadeh, M., 2018. "Mechanical Behavior of Hybrid Steel-PVA Fibers Reinforced Reactive Powder Concrete", *Computer and Concrete.*, 21(2), pp. 167-179.

Porter, S. D., Logan Julander, J., Halling, M. W., and Barr, P. J., 2011. "Shear Testing of Precast Bridge Deck Panel Transverse Connections." *Journal of Performance of Constructed Facilities*, 26(4), PP. 462-468.

Qu, J., 1993. "Eshelby Tensor for an Elastic Inclusion with Slightly Weakened Interface." *Journal of Applied Mechanics*, 60(4), pp. 1048-1050.

Ramezanianpour, A.A., 2014. *Cement Replacement Materials*. Springer, New York (NY), USA.

Ranade, R. Li, V. C. Stults, M. D. Rushing, T.S. Roth, J. and Heard, W. F., 2013. "Micromechanics of High-strength, High-Ductility Concrete." *ACI Materials Journal*, 110(4): 375-384.

RILEM 7-II-128 RC6., 1994. Bond Test for Reinforcing Steel, 1. *Pull-out Test for Reinforcement, RILEM (Technical Recommendations for the Testing and Use of Construction Materials)*, London: UK.

Ronanki, V.S., Aaleti, S. and Valentim, D.B., 2018. "Experimental Investigation of Bond Behavior of Mild Steel Reinforcement in UHPC." *Engineering Structures*, 176, pp. 707-718.

Russell, H. G., 2011. Adjacent Precast Concrete Box-Beam Bridges: State of the practice. *PCI journal*, 56(1), pp. 75-91.

Russell, H. G., 2009. *Adjacent Precast Concrete Box-Beam Bridges*: Connection details. (Vol. 393), Transportation Research Board, Washington, DC.

Sahmaran, M., Li, M. and Li, V.C., 2007. Transport Properties of Engineered Cementitious Composites under Chloride Exposure. *ACI Materials Journal*, *104*(6), pp.604-611.

Şahmaran, M., Özbay, E., Yücel, H.E., Lachemi, M. and Li, V.C., 2012. Frost Resistance and Microstructure of Engineered Cementitious Composites: Influence of Fly Ash and Micro Poly-vinyl-Alcohol Fiber. *Cement and Concrete Composites*, *34*(2), pp.156-165.

Said, A. M., Zeidan, M. S., Bassuoni, M. T., and Tian, Y. 2012. "Properties of Concrete Incorporating Nano-Silica." *Construction and Building Materials*, 36, pp. 838-844.

Semendary, A.A. and Svecova, D., 2020. "Factors Affecting Bond between Precast Concrete and Cast in Place Ultra High-Performance Concrete (UHPC)." *Engineering Structures*, 216, pp.110746.

Shi, F.J., 2012. A Study on Structure and Properties of Basalt Fiber. In *Applied Mechanics and Materials*, 238, pp. 17-21.

Sim, J. and Park, C., 2005. Characteristics of Basalt Fiber as a Strengthening Material for Concrete Structures. *Composites Part B: Engineering*, *36*(6-7), pp.504-512.

Sindu, B. S., and Sasmal, S., 2019. "On the Development and Studies of Nano-and Micro-fiber Hybridized Strain Hardened Cementitious Composite." *Archives of Civil and Mechanical Engineering*, 19(2), pp. 348-359.

Smith, T., Eng, P. and Works, P., 2010, September. Concrete Pavement Rehabilitation Techniques and Canadian Based Case Studies. In *paper presentation, Annual Conference of the Transportation Association of Canada, Halifax, Nova Scotia*.

Smolcic, Z. and Ozbolt, J., 2017. "Meso Scale Model for Fiber-Reinforced-Concrete: Microplane Based Approach", *Computer and Concrete*, 19(4), 375-385.

Sui, L., Luo, M., Yu, K., Xing, F., Li, P., Zhou, Y. & Chen, C., 2018. "Effect of Engineered Cementitious Composite on the Bond Behavior Between Fiber-Reinforced Polymer and Concrete." *Composite Structures*, 184, pp. 775-788.

Sun, C. T., and Vaidya, R. S., 1996. "Prediction of Composite Properties from a Representative Volume Element." *Composites Science and Technology*, 56(2), pp. 171-179.

Sun, Z., Garboczi, E. J., and Shah, S. P., 2007. "Modeling the Elastic Properties of Concrete Composites: Experiment, Differential Effective Medium Theory, and Numerical Simulation." *Cement and Concrete Compos*ites, 29(1), pp. 22-38.

Tayeh, B.A. and Magbool, H.M. (2021), "Influence of Substrate Roughness and Bonding Agents on the Bond Strength between Old and New Concrete", *Advance in Concrete Construction*, 12 (1), 33-45.

Teng, T. L., Chu, Y. A., Chang, F. A., and Chin H. S., 2004. "Calculating the Elastic Moduli of Steel-fiber Reinforced Concrete using a Dedicated Empirical Formula." *Computational Materials Science,* 31(3-4), pp. 337-346.

Toutanji, H, Xu, B., Gilbert, J., and Lavin, T., 2008. Fracture Toughness Model for Poly (vinyl alcohol) Fiber Reinforced High-Performance Cementitious Material. *In Proceedings of the 8th International Symposium on Utilization of High-Strength and High-Performance Concrete,* Tokyo, Japan.

Thong, C.C., Teo, D.C.L., and Ng, C.K., 2016. "Application of Polyvinyl Alcohol (PVA) in Cement-Based Composite Materials: A review of its Engineering Properties and Microstructure Behavior". *Construction and Building Materials,* 107, pp. 172-180.

Tran, Q.T., Toumi, A. and Turatsinze, A., 2007. "Modelling of Debonding between Old Concrete and Overlay: Fatigue Loading and Delayed Effects. *Materials and Structures*, *40*(10), pp.1045-1059

Wang, S., 2005. *Micromechanics based matrix design for engineered cementitious composites*, The University of Michigan, PhD Thesis, Civil Engineering, pp. 222.

Wang, H., Sun, X., Peng, G., Luo, Y. and Ying, Q., 2015. "Experimental Study on Bond Behaviour between BFRP Bar and Engineered Cementitious Composite." *Construction and Building Materials*, 95, pp. 448-456.

Wang, Q., Yi, Y., Ma, G., and Lui, H., 2019. "Hybrid Effects of Steel Fibers, Basalt Fibers and Calcium Sulfate on Mechanical Performance of PVA-ECC Containing High-Volume Fly Ash". *Cement and Concrete Compos*ites, 97, pp. 357-368.

Wang, Z.B., Han, S., Sun, P., and Wang, Q., 2021. "Mechanical Properties of Polyvinyl Alcohol-Basalt Hybrid Fiber Engineered Cementitious Composites with Impact of Elevated Temperatures". *Journal of Central South University of Technology*, 28(5): pp. 1459-1475.

Wang, Z. Li, T. Qu, H. Wei, H. and Li, Y., 2019. "Seismic Performance of Precast Bridge Columns with Socket and Pocket Connections Based on Quasi-Static Cyclic Tests: Experimental and Numerical Study." *Journal of Bridge Engineering*, 24(11), pp. 04019105-12.

Weber, E.D. Pantelides, C.P. and Reaveley, L.D., 2015. "Performance of CFRP Posttensioned Transverse Grouted Joints for Full-Depth Precast Concrete Panels." *PCI Journal*,60(3), pp. 39-49.

Wu, C. Y., Tang, C. Y., and Lee, W., 2010. "Electro-Optical and Capacitive Characteristics of Stratified Polymer/liquid Crystal Composite Devices under DC Electric Field." *Journal of Applied Physics Express*, 3(11), pp. 111701-13.

Wu, S., 2019. "Investigation on the Connection Forces of Shear Keys in Skewed Bridges during Earthquakes", *Engineering Structure*, 194, 334-343.

Xu B, Toutanji HA, Lavin T, and Gilbert, J.A., 2011. "Characterization of Polyvinyl Alcohol Fiber Reinforced Organic Aggregate Cementitious Materials". *Key Engineering Materials*, 466, pp. 73-83.

Xu, M., Song, S., Feng, L., Zhou, J., Li, H. and Li, V.C., 2021. Development of Basalt Fiber Engineered Cementitious Composites and its Mechanical Properties. *Construction and Building Materials*, *266*, p.121173.

Yang, I. H., Joh, C., and Kim, B. S., 2010. "Structural Behavior of Ultra-High Performance Concrete Beams Subjected to Bending." *Engineering Structure*, 32(11), pp. 3478-3487.

Yankelevsky, D.Z., Jabareen, M. and Abutbul, A.D., 2008. "One Dimensional Analysis of Tension Stiffening in Reinforced Concrete with Discrete Cracks", *Engineering Structure*, 30(1), pp. 206-217.

Yu, J., Yao, J., Lin, X., Li, H., Lam, J.Y., Leung, C.K., Sham, I.M., and Shin, K., 2018. "Tensile Performance of Sustainable Strain-Hardening Cementitious Composites with Hybrid PVA and Recycled PET Fibers". *Cement and Concrete Res*earch, 107, pp. 110-123.

Yuan, J. and Graybeal, B., 2015. "Bond of Reinforcement in Ultra-High-Performance Concrete." *ACI Structural Journal*, 112(6), pp. 851-860.

Zanotti, C., Rostagno, G. and Tingley, B., 2018. "Further Evidence of Interfacial Adhesive Bond Strength Enhancement Through Fiber Reinforcement in Repairs." *Construction and Building Materials*, 160, pp. 775-785.

Zhang, C., and Cao, M., 2014. "Fiber Synergy in Multi-scale Fiber-reinforced Cementitious Composites." *Journal of Reinforced Plastics and Composites*, 33(9), pp. 862-874.

Zhang, M.H., Islam, J., & Peethamparan, S., 2012. Use of Nano-Silica to Increase Early Strength and Reduce Setting Time of Concretes with High Volumes of Slag. *Cement and Concrete Compos*ite, 34(5), pp. 650-662.

Zhang, J., Gong, C., Guo, Z. and Zhang, M., 2009. Engineered Cementitious Composite with Characteristic of Low Drying Shrinkage. *Cement and Concrete Research, 39*(4), pp.303-312.

Zhu, Y., Yang, Y. and Yao, Y., 2012. Use of Slag to Improve Mechanical Properties of Engineered Cementitious Composites (ECCs) with High Volumes of Fly Ash. *Construction and Building Materials, 36*, pp.1076-1081.

Zhou, J., Qian, S., Ye, G., Copuroglu, O., van Breugel, K. and Li, V.C., 2012. Improved Fiber Distribution and Mechanical Properties of Engineered Cementitious Composites by Adjusting the Mixing Sequence. *Cement and Concrete Composites, 34*(3), pp.342-348.

APPENDIX A: SUPPLEMENTAL RESULTS FOR CHAPTER 3

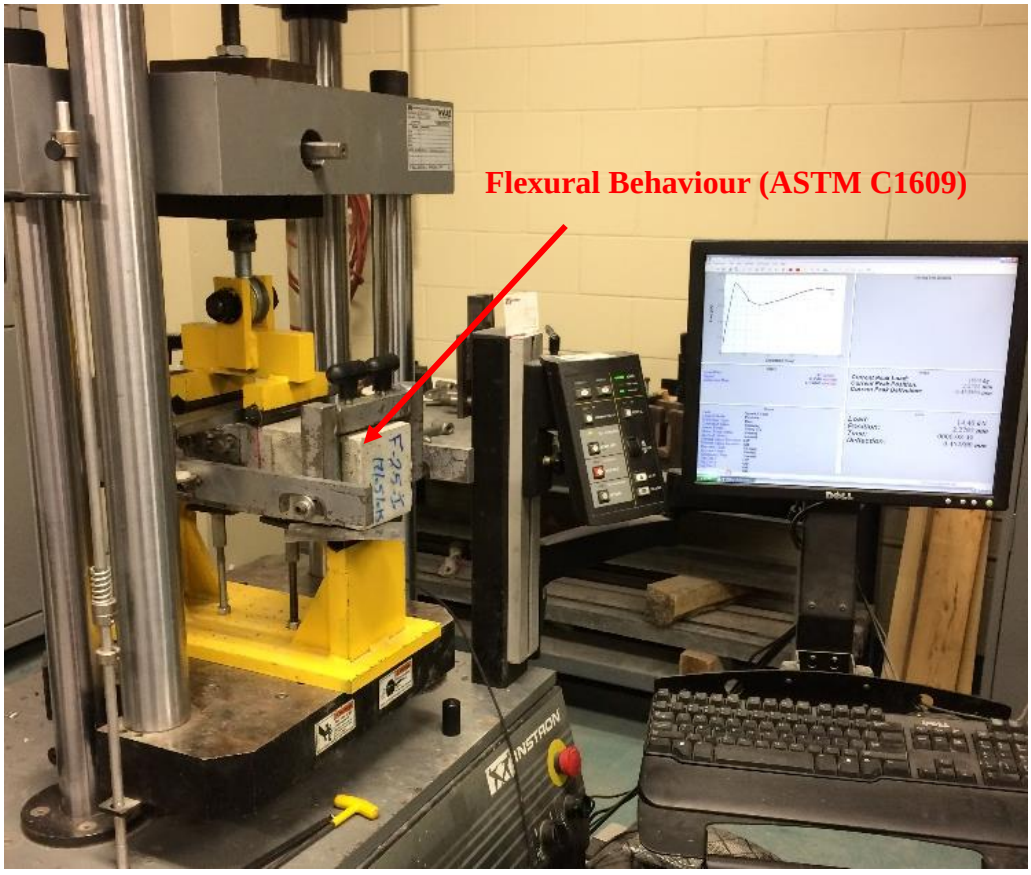


Figure A.1: Flexural test setup.



Figure A.2: Target flow for all specimens of 170±10 mm.

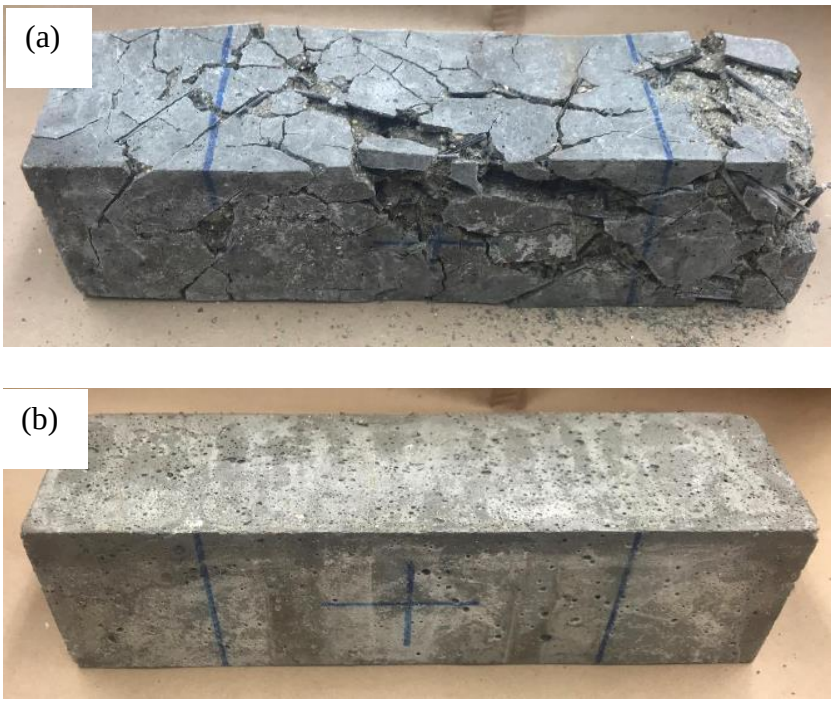


Figure A.3: Resistance to frost damage after 300 cycles: (a) G-N-B4.5 and (b) G-N-B4.5-V1.

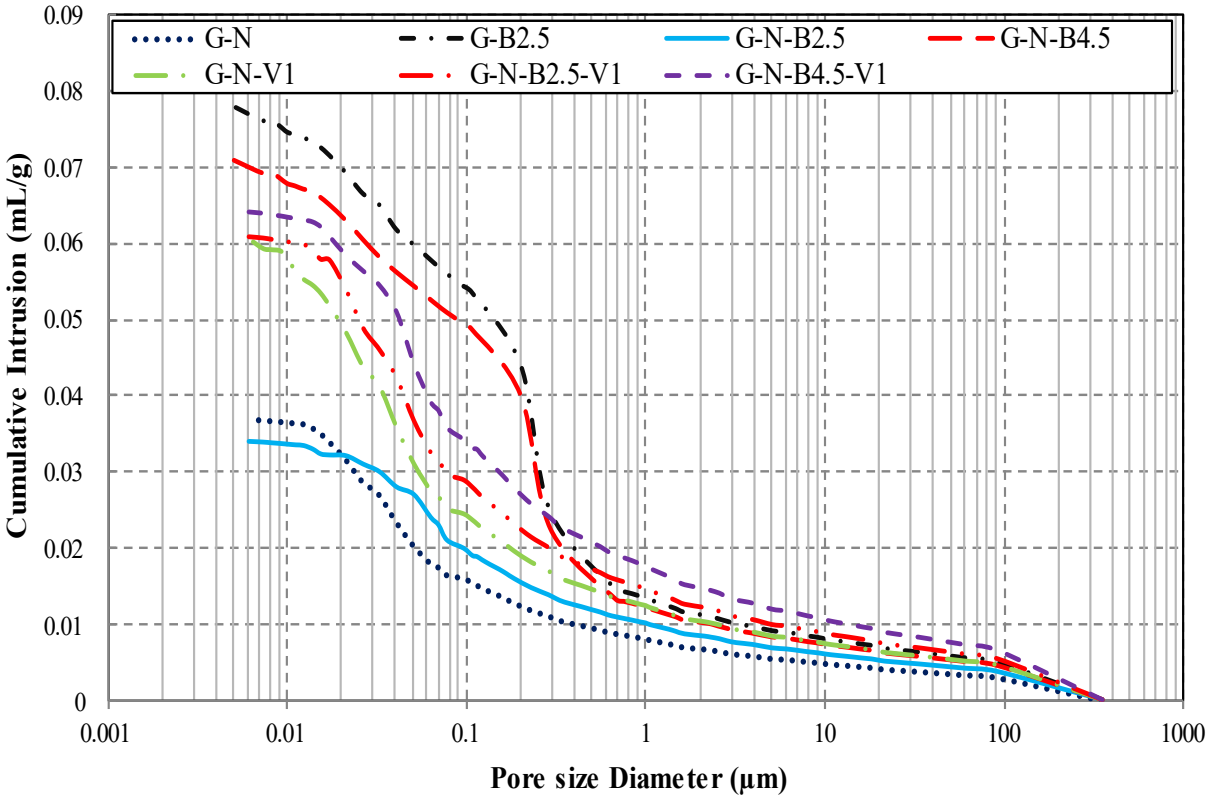


Figure A.5: Cumulative intrusion vs. Pore size diameter.

APPENDIX B: SUPPLEMENTAL RESULTS FOR CHAPTER 4

$$k_{ij} = \begin{bmatrix} \frac{1-\nu_{23}\nu_{32}}{E_{22}E_{33}\Delta} & \frac{E-E}{\frac{\nu_{21}+\nu_{23}\nu_{31}}{E_{22}E_{33}\Delta}} & \frac{E-S}{\frac{\nu_{31}+\nu_{21}\nu_{32}}{E_{22}E_{33}\Delta}} & 0 & 0 & 0 \\ & \frac{1-\nu_{13}\nu_{31}}{E_{11}E_{33}\Delta} & \frac{\nu_{32}+\nu_{12}\nu_{31}}{E_{22}E_{33}\Delta} & 0 & 0 & 0 \\ & & \frac{1-\nu_{12}\nu_{21}}{E_{11}E_{22}\Delta} & 0 & 0 & 0 \\ & Symmetry & & G_{23} & 0 & 0 \\ & & & & G_{13} & 0 \\ & & S-S & & & G_{12} \end{bmatrix}$$

$\Delta = \frac{1-\nu_{23}\nu_{32}-\nu_{21}\nu_{12}-\nu_{13}\nu_{31}-2*\nu_{23}\nu_{12}\nu_{13}}{E_{11}E_{22}E_{33}}$, and

Figure B.1: The homogenized stiffness coefficients k_{ij} equation.

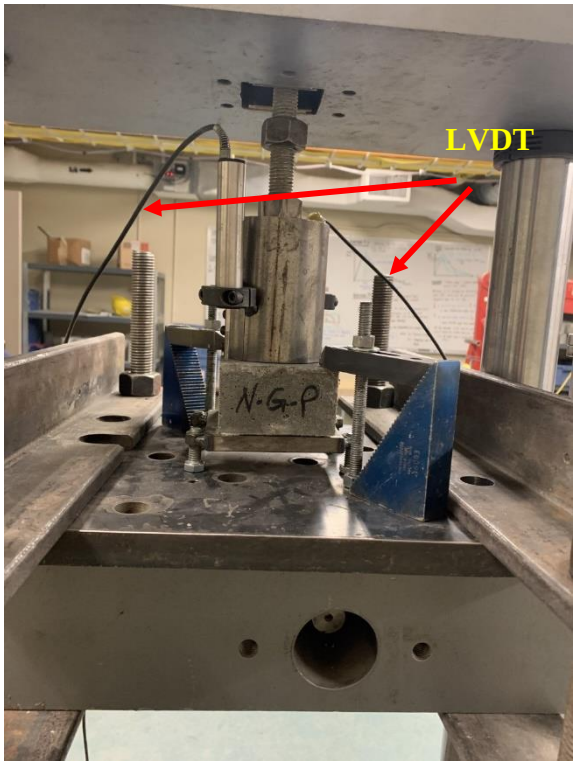


Figure B.2: The pellet pull-out test set up.

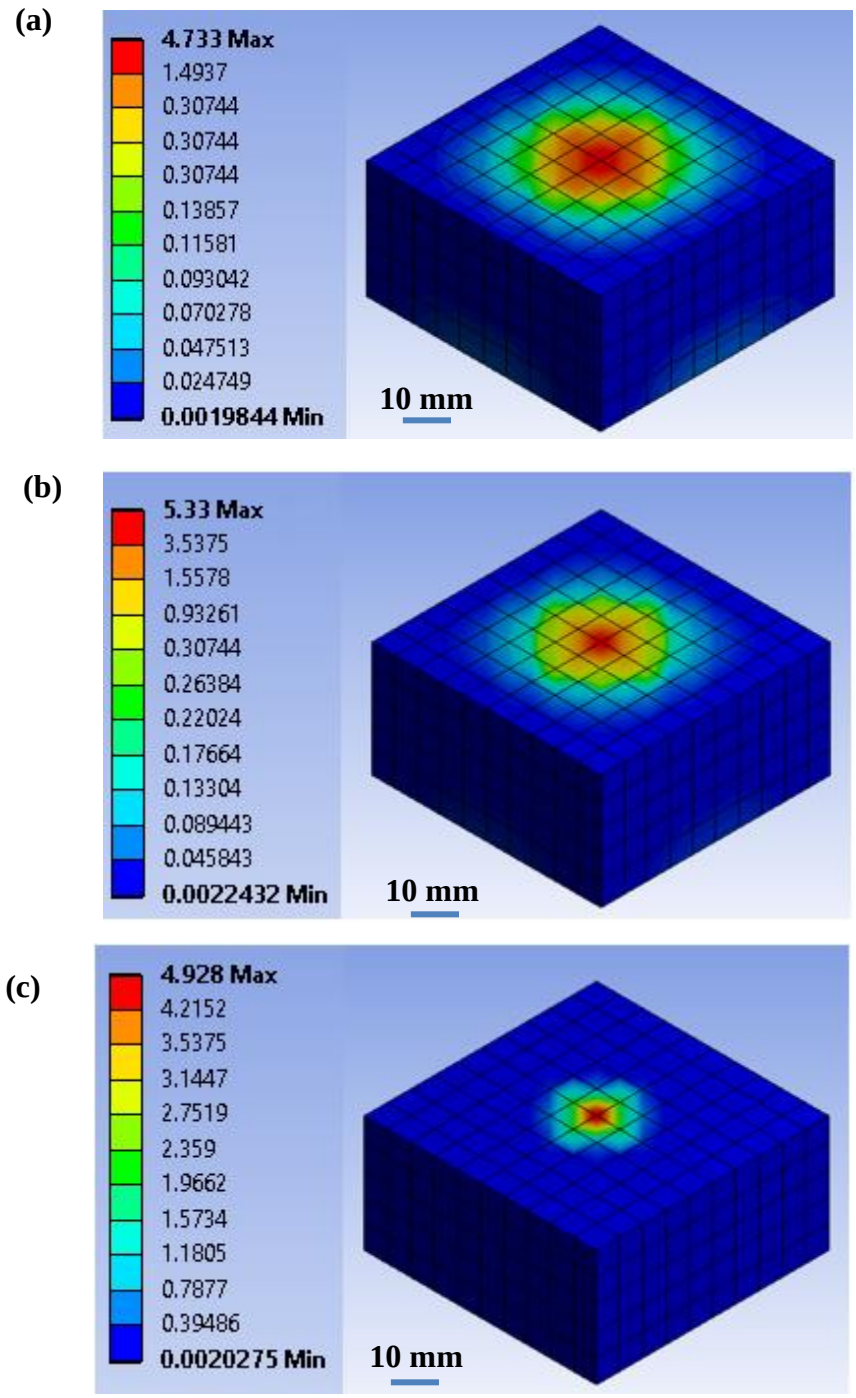


Figure B.3: Examplear stress distributions from the models for the single pellet pull-out tests: (a) G, (b) G-N, and (c) G-NCC.

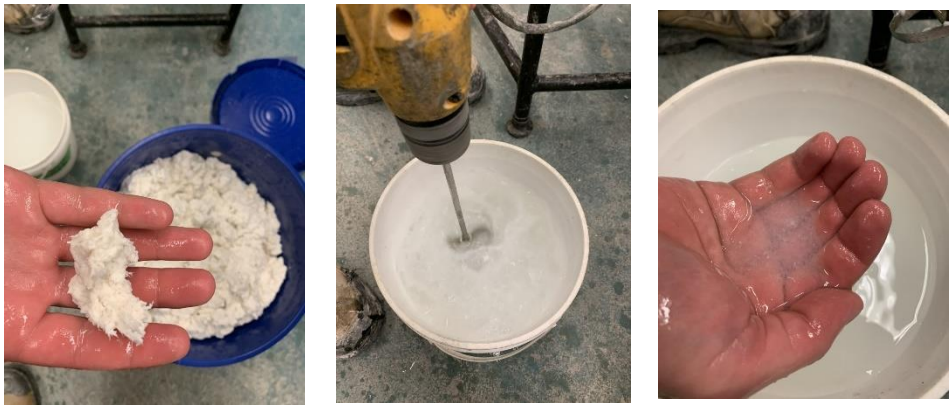


Figure B.4: Nano-fibrillated Cellulose: (a) solid state, (b) homogenizer at 2000 rpm for 4 min and (b) Liquid state (homogenization in water).

$$k_{ij} = \begin{bmatrix} 32.80 & 10.54 & 10.12 & 0 & 0 & 0 \\ & 32.84 & 10.18 & 0 & 0 & 0 \\ & & 32.83 & 0 & 0 & 0 \\ & Symmetry & & 11.64 & 0 & 0 \\ & & & & 11.54 & 0 \\ & & & & & 11.84 \end{bmatrix}$$

Figure B.5: The homogenized stiffness coefficients k_{ij} equation for G-NCC-NFC0.2 (RVE1).

APPENDIX C: SUPPLEMENTAL RESULTS FOR CHAPTER 5



Figure C.1: Preparations for the CC half cylinder for all specimens at 45°.



Figure C.2: Preparations for the CC half cylinder for all specimens at 33.7°.



Figure C.3: Slant Shear test set up.

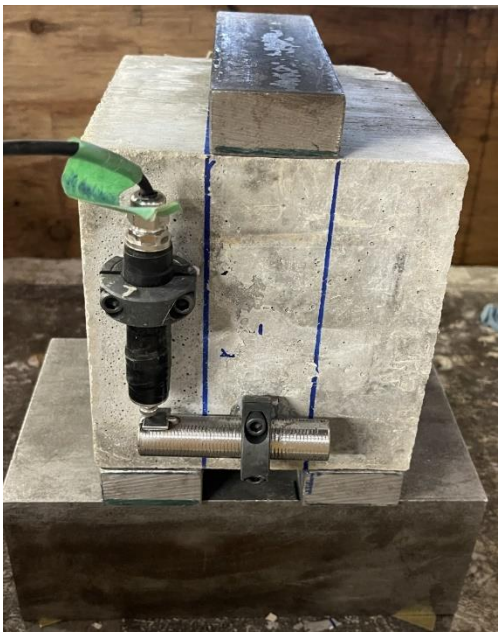


Figure C.4: Bi-Shear test set up.



Figure C.5: Quasi-static tensile test specimen failure in the middle.

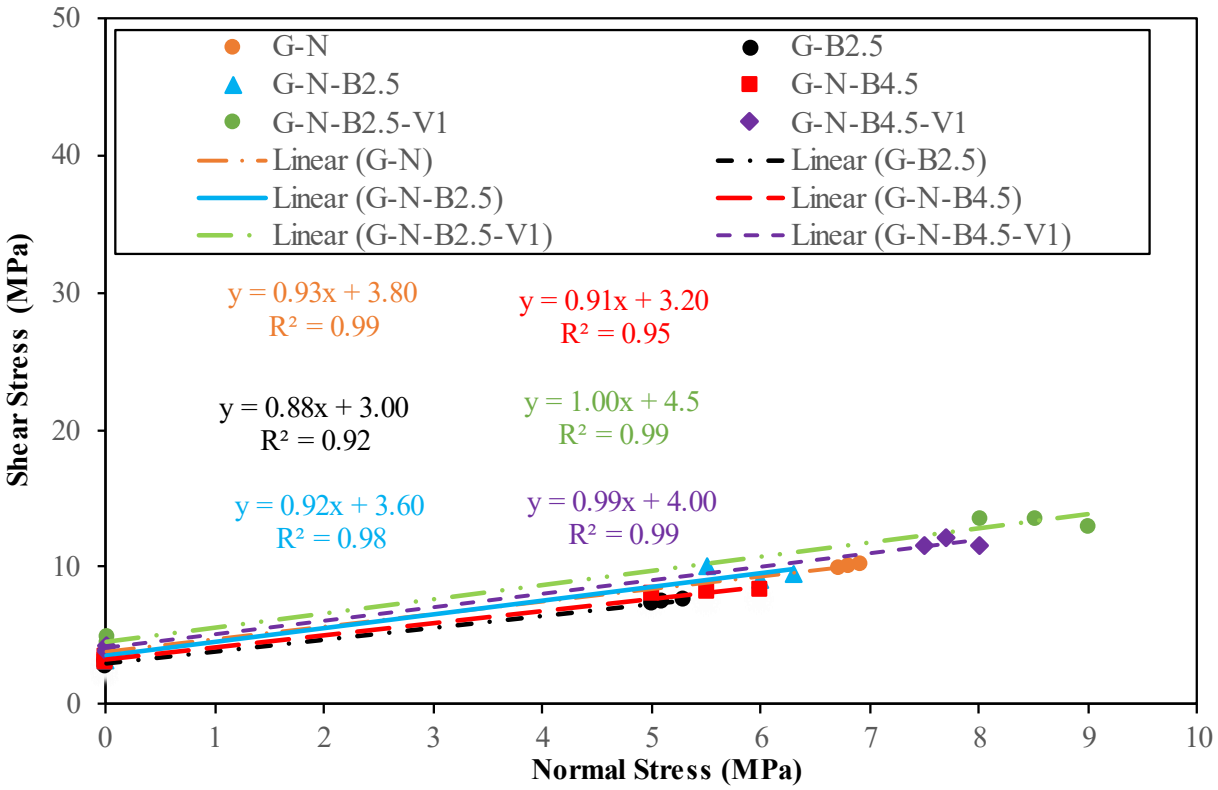
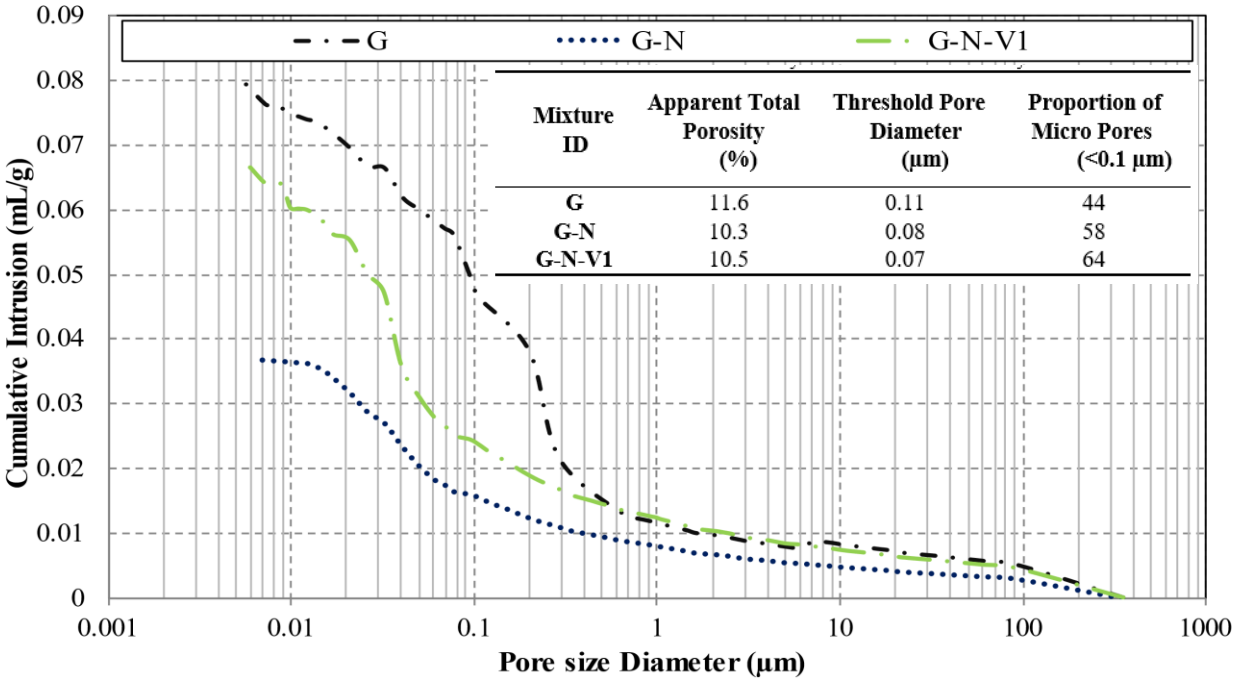


Figure C.6: Shear-normal stresses interaction of the composite HPFRCC/CC specimens for combination of experimental slant shear (at 33.7°) and bi-shear results.

APPENDIX D: SUPPLEMENTAL RESULTS FOR CHAPTER 6



Mixture ID	Apparent Total Porosity (%)	Threshold Pore Diameter (µm)	Proportion of Micro Pores (<0.1 µm)
G	11.6	0.11	44
G-N	10.3	0.08	58
G-N-V1	10.5	0.07	64

Figure D.1: Cumulative intrusion vs. pore size diameter.

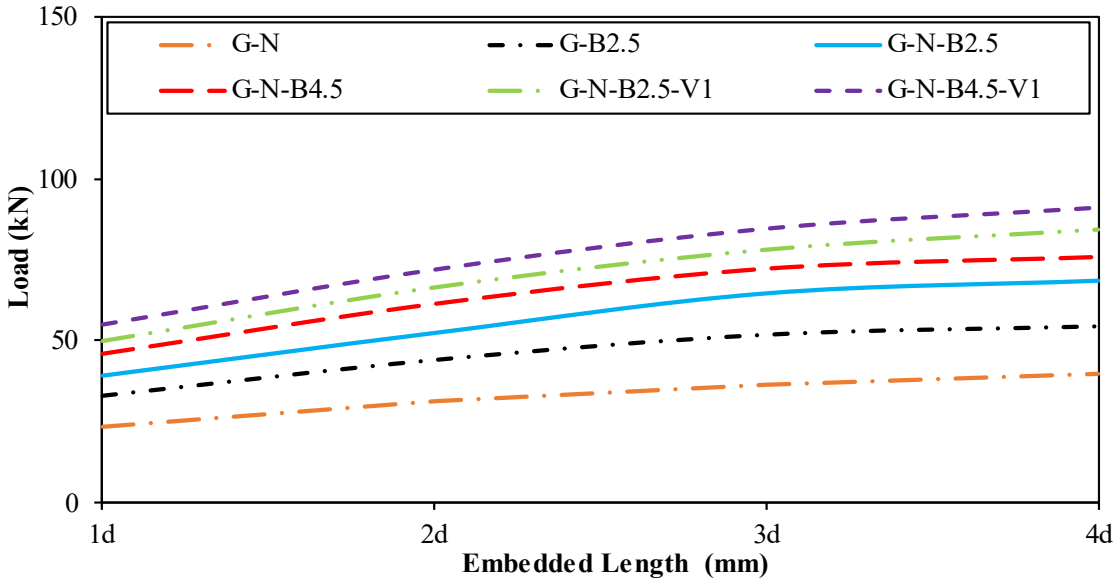


Figure D.2: Predicted peak load-embedded rebar length relationships for all composites.

$$k_{ij} = \begin{bmatrix} 26.20 & 8.55 & 8.75 & 0 & 0 & 0 \\ & 26.82 & 8.77 & 0 & 0 & 0 \\ & & 26.75 & 0 & 0 & 0 \\ & Symmetry & & 9.1 & 0 & 0 \\ & & & & 9.2 & 0 \\ & & & & & 9.1 \end{bmatrix}$$

Figure D.3: The homogenized stiffness coefficients k_{ij} equation for G-B2.5 (RVE1).

$$k_{ij} = \begin{bmatrix} 31.25 & 10.34 & 10.12 & 0 & 0 & 0 \\ & 31.25 & 10.18 & 0 & 0 & 0 \\ & & 31.25 & 0 & 0 & 0 \\ & Symmetry & & 10.64 & 0 & 0 \\ & & & & 10.85 & 0 \\ & & & & & 10.78 \end{bmatrix}$$

Figure D.4: The homogenized stiffness coefficients k_{ij} equation for G-N-B2.5 (RVE2).

$$k_{ij} = \begin{bmatrix} 30.60 & 10.12 & 10.31 & 0 & 0 & 0 \\ & 30.58 & 10.24 & 0 & 0 & 0 \\ & & 30.17 & 0 & 0 & 0 \\ & Symmetry & & 9.97 & 0 & 0 \\ & & & & 9.60 & 0 \\ & & & & & 9.74 \end{bmatrix}$$

Figure D.5: The homogenized stiffness coefficients k_{ij} equation for G-N-B4.5 (RVE3).

$$k_{ij} = \begin{bmatrix} 32.50 & 10.51 & 10.12 & 0 & 0 & 0 \\ & 32.84 & 10.53 & 0 & 0 & 0 \\ & & 32.83 & 0 & 0 & 0 \\ & Symmetry & & 11.64 & 0 & 0 \\ & & & & 11.74 & 0 \\ & & & & & 11.34 \end{bmatrix}$$

Figure D.6: The homogenized stiffness coefficients k_{ij} equation for G-N-B4.5-V1 (RVE5).

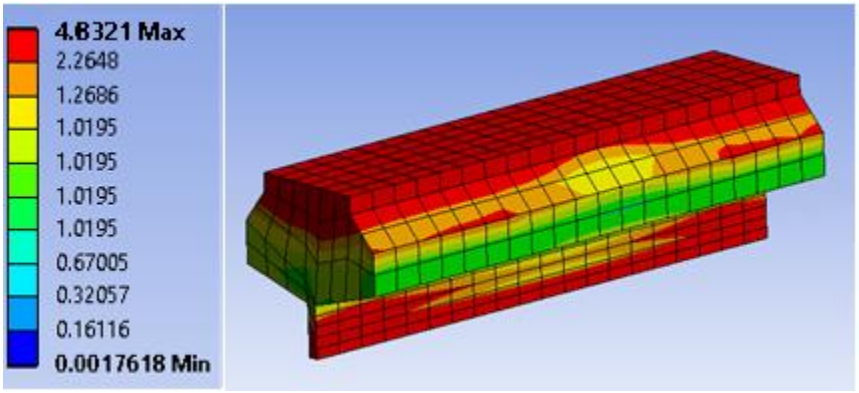


Figure D.7: Shear stress distribution for shear key bridge joint filled with G-N-B4.5-V1.

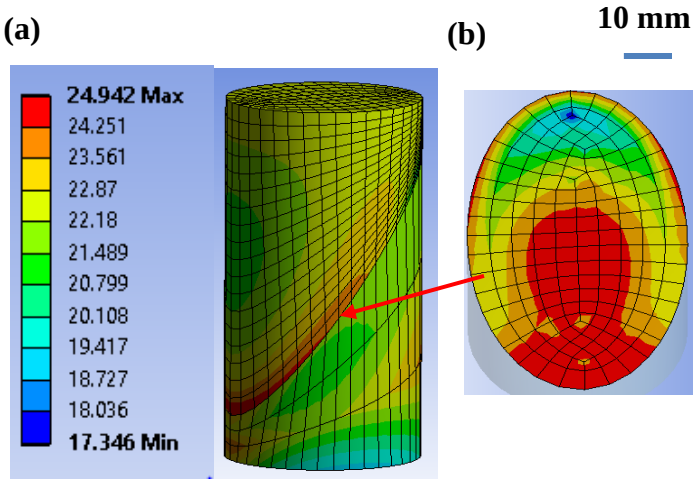


Figure D.8: Interface failure in specimens cast with G-N at 33.7°: (a) modeling simulation, and (b) bond stress (MPa) distribution at the interface.

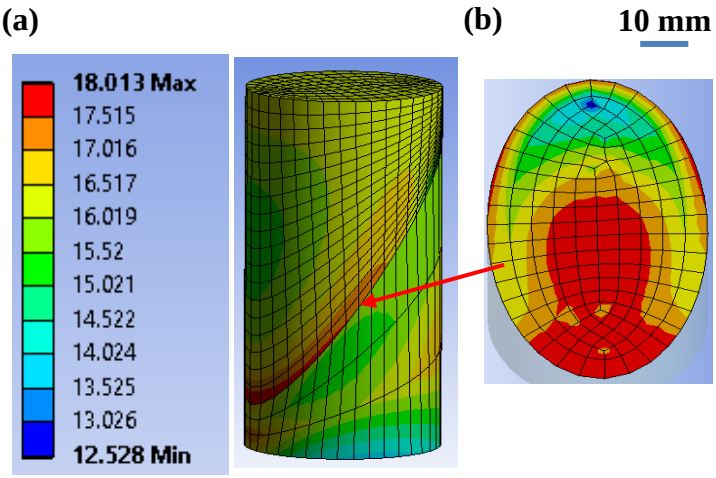


Figure D.9: Interface failure in specimens cast with G-N at 33.7°: (a) modeling simulation, and (b) bond stress (MPa) distribution at the interface.

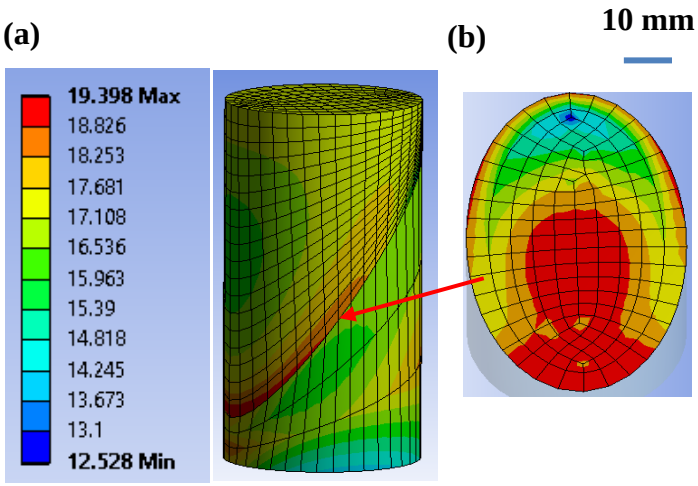


Figure D.10: Interface failure in specimens cast with G-N-B4.5 at 33.7°: (a) modeling simulation, and (b) bond stress (MPa) distribution at the interface.

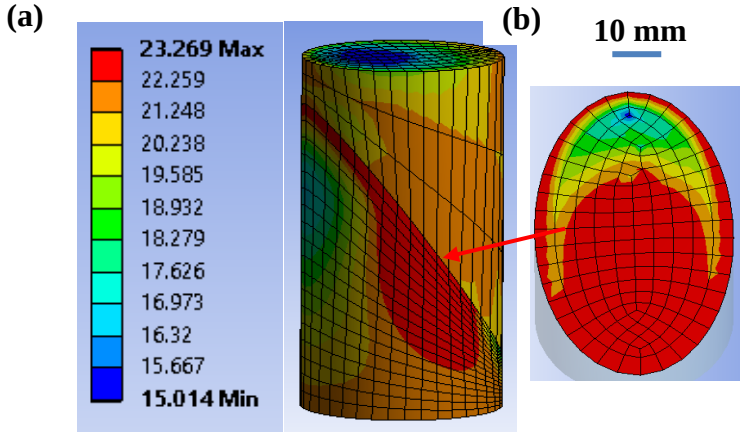


Figure D.11: Interface failure in specimens cast with G-N-B4.5-V1 at 33.7°: (a) modeling simulation, and (b) bond stress (MPa) distribution at the interface.

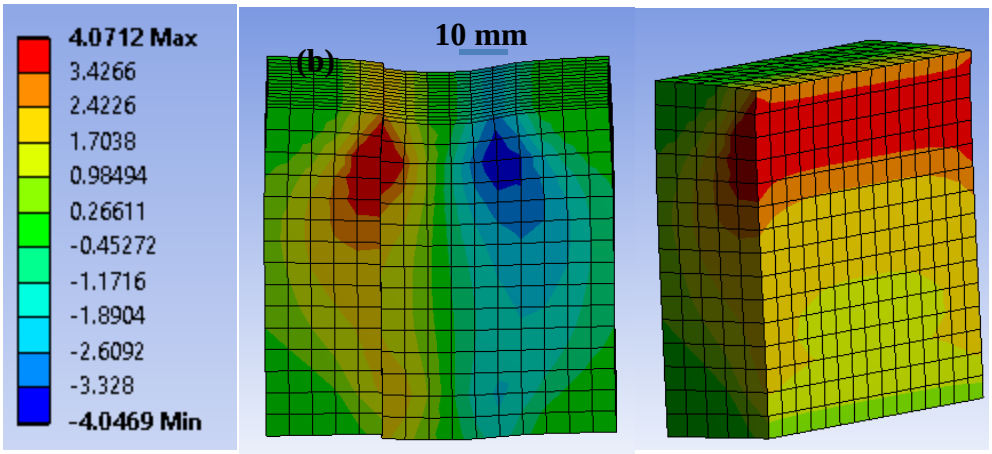


Figure D.12: Direct shear failure in specimen G-N associated with shear stress (MPa) distribution at the interface between HPFRCC/CC.

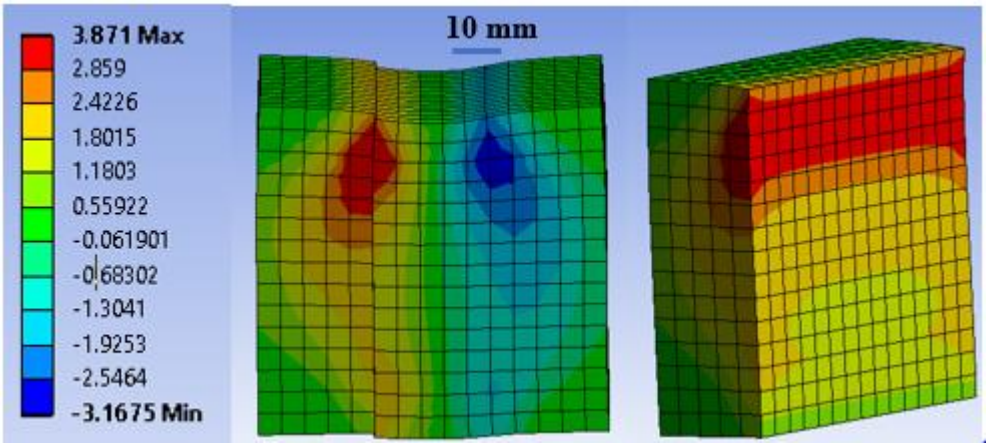


Figure D.13: Direct shear failure in specimen G-N-B4.5-V1 associated with shear stress (MPa) distribution at the interface between HPFRCC/CC.

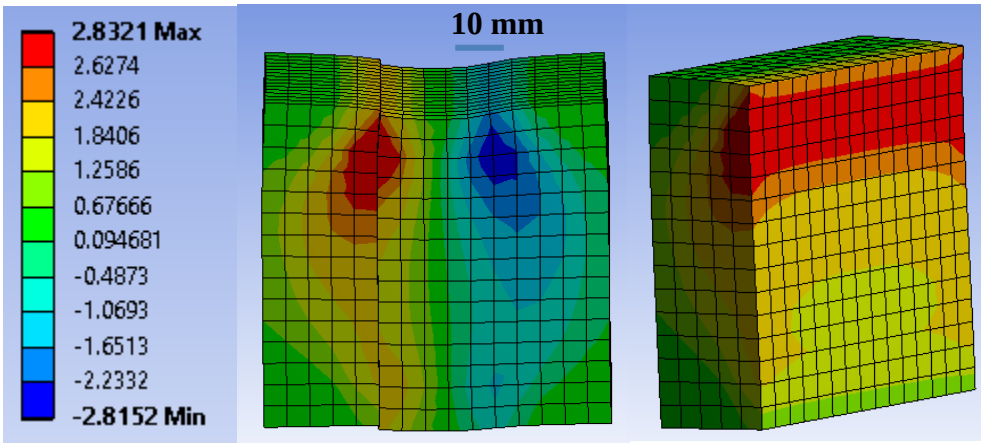


Figure D.14: Direct shear failure in specimen G-B2.5 associated with shear stress (MPa) distribution at the interface between HPFRCC/CC.

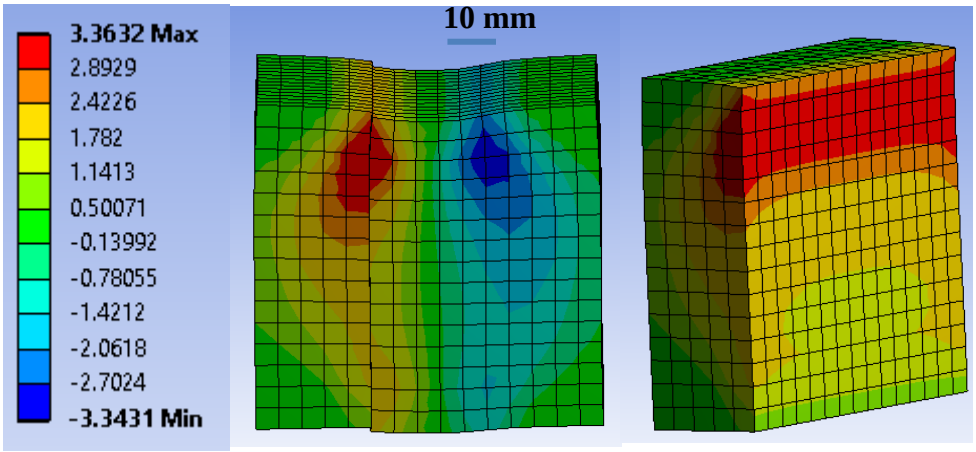


Figure D.15: Direct shear failure in specimen G-N-B4.5 associated with shear stress (MPa) distribution at the interface between HPFRCC/CC.